NORTHWESTERN UNIVERSITY

Thermodynamic insights and microscopic models for characterizing vibrations in solids

A DISSERTATION

SUBMITTED TO THE GRADUATE SCHOOL
IN PARTIAL FULFILLMENT OF THE REQUIREMENTS

for the degree

DOCTOR OF PHILOSOPHY

Materials Science & Engineering

By

Matthias T. Agne

EVANSTON, ILLINOIS

June 2020

Abstract

Given directives such as the UN Global Goals targeting sustainable development, the research presented herein makes but a small contribution to the advancement of alternative energy technologies. Nevertheless, the present work was largely motivated to address specific points of intrigue within the thermoelectrics community. The general principles demonstrated, however, may be directly applicable to other areas of solid-state research.

Thermoelectric materials, which can convert heat to electricity through the Seebeck effect, require a complex optimization of their electronic and thermal properties. For the past 2 decades, great strides have been made to improve their energy conversion efficiency—and many successes in doing so can be attributed to reductions in the thermal conductivity. In the long-standing phonon gas model of thermal transport, where atomic vibrations carry heat in a manner analogous to gas particles, the strategy has been to introduce scattering mechanisms that impede transport. This works well in many materials. Recently, however, we have demonstrated that the thermal conductivity of materials like lead telluride may be engineered by controlling their bulk elastic properties, effectively controlling the speed of the phonons, which is a fundamentally different mechanism than scattering.

Another proposed method of reducing thermal conductivity was to utilize phase transitions, with the hope of introducing additional phonon scattering. In fact, there are many reports of reduced thermal conductivity (and improved thermoelectric performance) through both solid-solid and solid-liquid (analogous to ice melting) phase transitions. Here, a reassessment of the underlying thermodynamic relationship between thermal conductivity and thermal diffusivity demonstrates that thermal conductivity is likely underestimated from thermal diffusivity measurements when latent heats from phase transformations are not taken into account. In several well-characterized material systems it is shown that thermal conductivity is not greatly impacted by phase transitions, whereas thermal diffusivity is. This relates to a need for the accurate characterization of the heat capacity of materials at high temperature. For materials not undergoing a phase transition a simple equation was developed to describe high temperature heat capacity that is likely more accurate than experiments in many cases.

Although phase transitions may not result in ultralow thermal conductivity, there are materials (and materials still to be discovered) with intrinsically high anharmonicity that results in high phonon scattering rates and low thermal conductivity. Here, anharmonic-

ity is an aspect of bonding in materials that deviates from Hooke's Law, i.e. there are non-linear interactions between atoms. Anharmonicity is also used to explain thermal expansion. Thus, characterizing anharmonicity has widespread repercussions. Here, it is proposed that the harmonic (e.g. elastic) properties of solids can be thermodynamically related to higher order anharmonic effects of bonding. Specifically, a physical model of thermal expansion is developed by considering that harmonic phonons produce a pressure pushing the solid outwards, while the elasticity of the atomic bonds compensates the phonon pressure to achieve mechanical equilibrium. Besides fundamentally reconsidering the nature of anharmonic behaviors in solids, this simple model provides accessible estimates of thermal expansion and the thermodynamic Grüneisen parameter that may be used for thermodynamic modeling and high-throughput screening of anharmonicity, both necessary for next-generation computational materials design.

The desire to reduce thermal conductivity for improved thermoelectric efficiency is summarized well by the "phonon-glass electron-crystal" mantra. Here, the thermal properties of the material are desired to be glass-like (amorphous-like) since glasses are known to exhibit some of the lowest thermal conductivities of all solids. However, glasses are not typically good electronic conductors, and so crystallinity is desirable for this aspect of thermoelectrics optimization. Indeed, this concept has been demonstrated in some solids like semiconducting clathrates, zinc antimonide and skutterudites. Nevertheless, the atomic vibrations in crystals are often only discussed in terms of the phonon gas model. Only recently has it has it been shown that vibrations in crystals and those in glasses can be described in the same mathematical framework, and that crystalline materials can transition to more glass-like behavior under certain circumstances. In this work, a phenomenological model of thermal transport by *diffusons* (the primary mechanism of heat transport in glasses) is developed for applications to crystalline materials. This study was one of the first to promote a reclassification of vibrations in crystals and gives an estimate of the so-called "minimum" thermal conductivity that can be used to benchmark experimental observations. Specifically, the model gives an estimate for thermal conductivity in the case where all vibrations in the material behave as diffusons. Again, characterizing the fundamental nature of vibrations in solids has far reaching implications for energy materials beyond thermoelectrics.

So far, both thermodynamic analysis and microscopic models have been used to characterize the thermal properties of solids. In this work, they were also utilized to assess the stability of materials for device-level operation. In one case, it is shown that there are thermodynamic stability criteria in a subclass of thermoelectric materials called mixed

ionic-electronic conductors. Their stability depends on the atomic chemical potential of the mobile atom. Importantly, this means that there is a critical voltage above which the material can decompose. This is related to, but not the same as, the prevalent idea that these materials cannot sustain high current densities. In fact, it is shown experimentally that the superionic material copper sulfide can sustain high current densities when the voltage is kept below the thermodynamic critical voltage of the material.

Lastly, an estimate for the fracture toughness of solids is proposed that is based on ideal-strength calculations. Modern computational methods in materials science provide a unique opportunity to investigate fracture at the level of local atomic structures. The integral of the ideal stress-displacement curve is used to approximate the work of fracture. That is, to estimate the total energy required to make new surfaces. This computational method is shown to reproduce the magnitude of experimental results quite well, indicating that the relevant physics of fracture are being captured. This method is easily generalized to defect structures in materials and may be useful for atomic scale materials design.

Although this body of work is but a humble offering to the scientific community, when research is coupled with international collaboration and education outreach, great strides can be made in small steps. It is my passion to explore material properties, to build the energy sciences community and to share knowledge with others.

Acknowledgements

As far as I know, or it has been reminded to me, this journey began in the 3rd or 4th grade. When asked what I wanted to be when I grew up, the answer was “physicist” or, somewhat later, “engineer.” I feel now that I have achieved a reasonable degree of both likenesses. This success in attaining my childhood desire is only the direct result of the positive impact that so many people have had on my life. My family – Mel, Suzi, Melissa, Graham, and (recently) Scarlett and Nova – constitute a family unit like no other. In many ways, my being *here* is “their fault.” We joke that I was raised in a museum, and their facilitating my curiosities led me down an unobstructed path to academia. My grandparents, especially my grandmothers, known to me as Amma and Granny, filled my childhood with imagination and an appreciation for nature and art. I would like to dedicate this thesis to their memory.

As for the many other people I am grateful for, I will attempt here to name as many as reasonably possible. Know that I am truly grateful to have met so many wonderful people so far, with even small interactions having potentially large consequences.

It has been a true pleasure to learn from and work towards this degree with Jeff Snyder. His passion for science and his ability to communicate findings in an engaging manner has made me realize that science does not have to be boring. I hope you find some of that reflected here. In addition, he has provided father-like guidance for a man in his mid-twenties deciding his future and, in fact, the lab group is better described as a research family. The iteration of the Snyder group family that I was a part of includes fellow Ph.D. students: Riley Hanus (my research "partner in crime"), Kazuki Imasato, Shashwat Anand, Ian Witting, Max Wood, Max Dylla, Jimmy Kuo, Ramya Gurunathan, James Male, Saneyuki Ohno, Stephen Kang, Sam Miller, Moath Al-Malki, Madison Brod, and Michael Toriyama. All of whom I know I can always count on to brighten my day, wonder with about the nature of the universe, and enjoy a beer or two. Your friendship has made this an awesome experience. Leah Borgsmiller, thank you for your help this year and best of luck beginning graduate school. The constant flux of visitors (mostly international) also made for a wonderful extension of the research family. Stefan Maier, Stefan Schwarzmüller, and Freddie Reissig, I hope to see you in Germany soon. Alex Lin too, if just to ski.

To my larger friend group at Northwestern and in Chicago, you all have been wonderful. Matt and Edu (and Franklin and Monte), thank you for taking me in and continually looking out for me. Lupo, you are my life coach and a great friend. You and Kazu make

the best housemates anyone could ask for! Blake and Robby, the band Cold Turkey and the Fruitcakes gave me much-needed sanity many Wednesday nights. Long live CDW. Also, Tad and Jen, Ryan, Kazi, Megan, Nick, David, Jann, Xia, Nathan, Matt, and so many others in my cohort and those above and below me, you were great companions to go through this whole process with. Amin, Jake and Curt, it was great to have friends outside of materials science. The passing mention of my fellow JUAMI fellows, Sheel, Danielle, Julie and Josh, cannot describe how much I have enjoyed our energy science outreach in Africa together. I must also acknowledge a large degree of support and encouragement from Emily, Claudia and Hayley, whose strength and ambition I continue to admire.

I owe a great deal of my scientific development to Michel Barsoum and Babak Anasori, who first taught me how to research. As did Richard Underwood and Judd Day, who helped me publish my first scientific paper. My long-term Drexel and Philly friends, thank you for your continued support. Especially, Janette, Emily, Eric and Evan (the "study group") who always have my back, as well as Devin Marlin who willingly proofread this thesis. Michael Ghidu, I'm happy our paths continue to cross. Also... GUYS! Sankalp Kota, I'm glad we managed to collaborate a few times these past few years.

As for my formative years, Eric Schwartz, Lance Yunkin, Ed Sykes, Mr. Day, and other Dayspring teachers invested a lot of time in teaching me to think critically. Along with fellow students Eric Pettis and Matt Day, who are among my oldest friends, we took advantage of the opportunities we had in high school. I certainly am indebted to the ASM Materials Camp program that first introduced me to materials science and engineering. Ed Garrity was a large inspiration in my becoming a materials scientist.

I would like to acknowledge the invaluable contributions of all of the many collaborators that I share authorship with on academic papers, many of whom I have not met in person but have the utmost respect for. And for the guidance of my thesis committee, including Peter Voorhees, Chris Wolverton and John Ketterson, I have learned a great deal from your classes, research, and friendly discussion. I must also express my thanks for Sossina Haile, who has shown me much kindness and has given me many opportunities for scientific outreach, as well as the other Northwestern faculty who have been very approachable and willing to brainstorm and discuss scientific questions.

Also, to the many people I have met in my travels these past four years. Dinner conversations, conferences, etc., these are excellent opportunities to talk science. Raphael Hermann, Mike Manley, Eric Toberer, Vladan Stevanović, Joseph Heremans, Peter and Gerda Rogl, Dave Johnson, David Cahill, Takao Mori, Gang Chen, and many others, who

provided interesting discussion and friendly advice to a young scientist, I thank you.

Finally, this document was compiled entirely during my quarantine in Charleston, SC, as the result of the COVID-19 pandemic. I am indebted to my brother, Graham, his puppy, Nova, and his housemate, Jeff, for hosting me and providing continual support. Also, I am very happy to have gained new friends as a result of my time here – Sam, Summer, Bray, Anna and Emily – thank you for some illusions of normalcy during this strange time.

Notation Conventions

This text is written with the philosophy that a certain level of notational detail may be omitted explicitly so that the reader can focus on higher level concepts. Particularly as there are many equations, the goal is to communicate the essential thermodynamics and physics without being overbearing with superscripts, subscripts, or tensor math. Consequently, they are included in the text to the extent that they are essential to communicate the main idea.

With this in mind, it should be noted that many equations are written in a way that references the tensor form, but looks to relate scalar quantities. In so much as thermal conductivity, thermal expansion, elastic constants, etc. are in fact tensors, any discussion of these quantities as scalars can be thought of as either one particular direction or an appropriate average over all directions such that the property can be considered isotropic.

A separate comment on notation is related to the complexity associated with working in such diverse topics as thermal transport to fracture mechanics. Given the limited number of variables to choose from some are bound to be repeated. This may partially reflect a desire to retain notations familiar to each respective subtopic. Unfortunately, this results in situations like: V is used to denote volume and also the electric potential (voltage). In situations such as this distinctions will be made in the text, where appropriate, to avoid confusion. Although, in many cases, the particular definition should be apparent contextually.

Lastly, the nomenclature page is provided for reference, but is not exhaustive. Its primary aim is to provide quick access to variables that are used consistently throughout the text.

Nomenclature

α	thermal expansion coefficient
C_{P}	heat capacity at constant pressure
c_{p}	mass specific heat at constant pressure
C_{V}	heat capacity at constant volume
ΔH	enthalpy of transformation
ϵ	strain
γ	thermodynamic Grüneisen parameter
$\hbar$	reduced Planck constant
κ_{e}	electronic thermal conductivity
k_{B}	Boltzmann constant
κ_{diff}	diffuson thermal conductivity
κ_{L}	lattice thermal conductivity
κ_{ph}	phonon thermal conductivity
$\mathcal{D}$	thermal diffusivity (microscopic)
μ	chemical potential
$\widetilde{\mu}$	electrochemical potential
M_{W}	molecular weight
ω	angular frequency of vibration
ϕ	order parameter
ρ	density
σ	stress

σ_e	electonic conductivity, sometimes denoted as σ
θ_D	Debye temperature
v_l	longitudinal speed of sound
V_m	molar volume
v_s	appropriate average speed of sound
v_t	transverse speed of sound
B	bulk modulus
D	thermal diffusivity (thermodynamic)
F	Faraday constant
H	enthalpy
J_Q	heat flux
J_e	electonic flux (current density), sometimes denoted as J
n	number density (per volume) of atoms or electrons
P	pressure
R	gas constant
S	entropy
T	absolute temperature
t	time
U	internal energy
V	electric potential
V	volume
z	assigns sign and magnitude of electric charge
zT	thermoelectric figure-of-merit
γ_e	Sommerfeld coefficient of electronic heat capacity
κ	thermal conductivity
∇	gradient operator
e	elementary charge

Contents

List of Figures

List of Tables

Chapter 1

Introduction

Global climate change and resource scarcity mean that renewable energy sources must be adopted. As it is, current reports show that ~67% of energy produced in the United States is lost due to production, transmission and use inefficiencies (Fig. 1.1). Much of this unutilized energy is lost in the form of heat. In many respects, this is because heat is "slippery," or easily lost before utilization. Unlike electrical circuits, which act like water pipelines for electrons, there is not such an efficient process for directing the flow of heat. Thus, while many engineering processes generate heat due to thermodynamic losses (like friction), there is a fundamental inability to direct or harness that heat.

This is partly because there is no one mechanism of heat transport. Instead, there are three that have fundamentally different considerations:

1. *Conduction* - internal transport of heat within solids.
2. *Convection* - heat transport due to bulk movement of atoms or molecules (like those in gases and liquids).
3. *Radiation* - heat transported by light (the principle behind infra-red "night vision" goggles).

It is clear that each of these mechanisms is related to one or more technology relevant to everyday living, from gas turbine power generation to the boiling water on your kitchen stove top (Fig. 1.2). Due to the particular relevance of solids as engineering materials, much of the work presented herein will focus on characterizing and interpreting thermal conduction.

The desire to control and harness heat and utilize energy efficiently is driven in part by social responsibility. In order to be good stewards of our planet we should make use of our

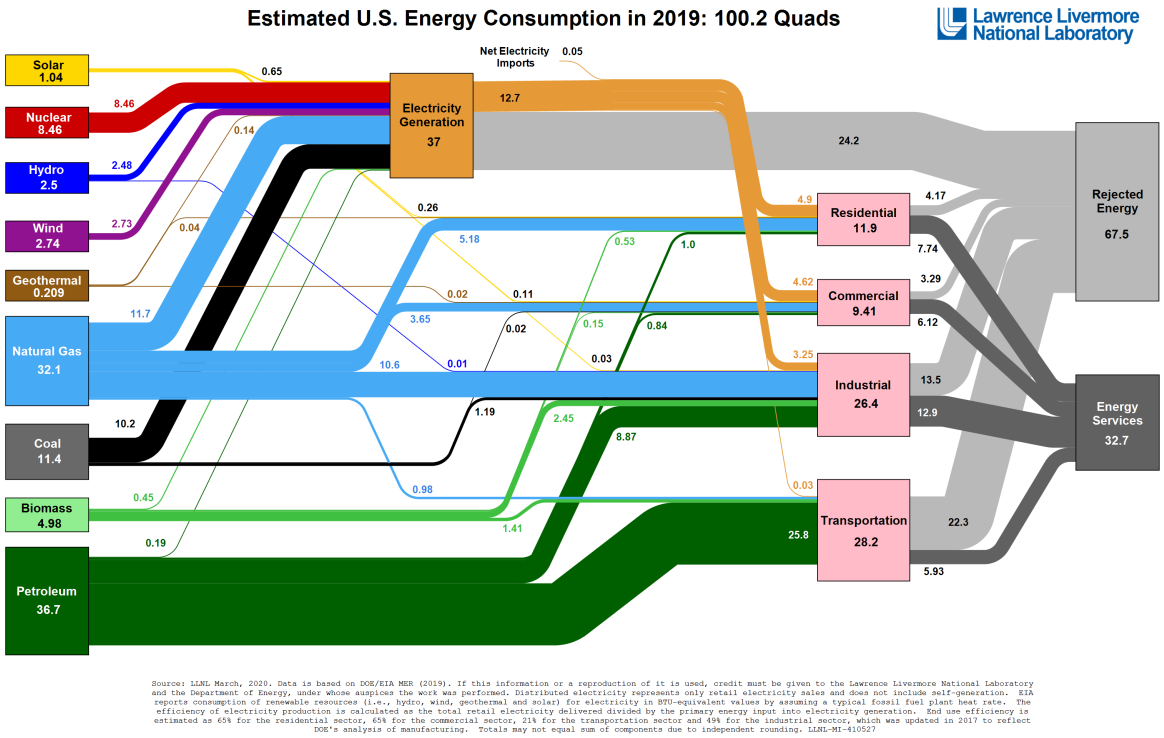

Figure 1.1: **Estimated U.S. Energy Consumption in 2019.** Energy production and use relations quantified by Lawrence Livermore National Laboratory. Original content can be found at `https://flowcharts.llnl.gov/`.

available resources in the most humanitarian way according to our technological capabilities. Given our current technological prowess, the ideal scenario would be to remove our dependence on fossil fuels, which have to be burned and inherently require thermal losses to maximize power output, and utilize alternative energy production methods (e.g. solar, wind, etc.) in conjunction with next-generation, thermally-efficient, energy storage devices (e.g. batteries, fuel cells, etc.) to regulate and meet grid-level electricity demands [67].

Furthermore, renewable technologies provide a platform for the advancement of developing countries by providing independent energy ownership and driving local economies [68, 69]. The development of these next generation energy solutions will rely on the ability to engineer materials with specific electrical and thermal transport properties.

As far as thermal technologies are concerned, there is a desire to make new materials with either lower thermal conductivity (better thermal insulators) or higher thermal conductivity (better thermal conductors, so-called heat pipes). Thermal insulators are necessary

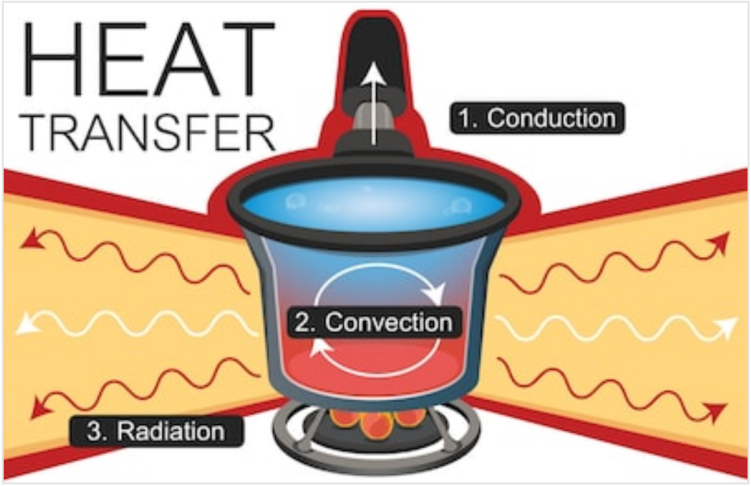

Figure 1.2: **An illustration of the primary mechanisms of heat transfer:** conduction, convection and radiation.

for containing heat, which can improve the efficiency of processes that inherently require high temperatures such as refractory processes [70]. Heat pipes serve to effectively direct the flow of heat, which is arguably more difficult. Nevertheless, directing heat flow on small length-scales is particularly important in computer technologies where computing efficiency and processor speeds are limited by the rate at which heat can be removed from the device [71, 72, 73]. The hope of making solid-state quantum computers is also likely to be limited by the ability to minimize thermal fluctuations, and thus requires careful temperature control on small length-scales [74].

Thermoelectric generators, which convert heat into electricity through the solid-state Seebeck effect, are one example of an energy harvesting device that could become prevalent if the energy conversion efficiency could be enhanced and devices can be made cost-effectively. This is largely a materials problem, as an optimized thermoelectric material requires high electrical conductivity and a large Seebeck coefficient, while thermal conductivity should be as low as possible [75]. These properties will be discussed in more detail later. A typical thermoelectric device is shown in schematic form in Fig. 1.3.

Although thermoelectric materials hold promise to reclaim some of the heat wasted in engineering processes, the primary application of thermoelectric generators to date has been for deep space exploration. Specifically, Radioisotope Thermoelectric Generators (RTG) are “atomic batteries” that currently power the Voyager Probes, Cassini, and the Curiosity Rover. These devices convert the heat from the radioisotope nuclear mate-

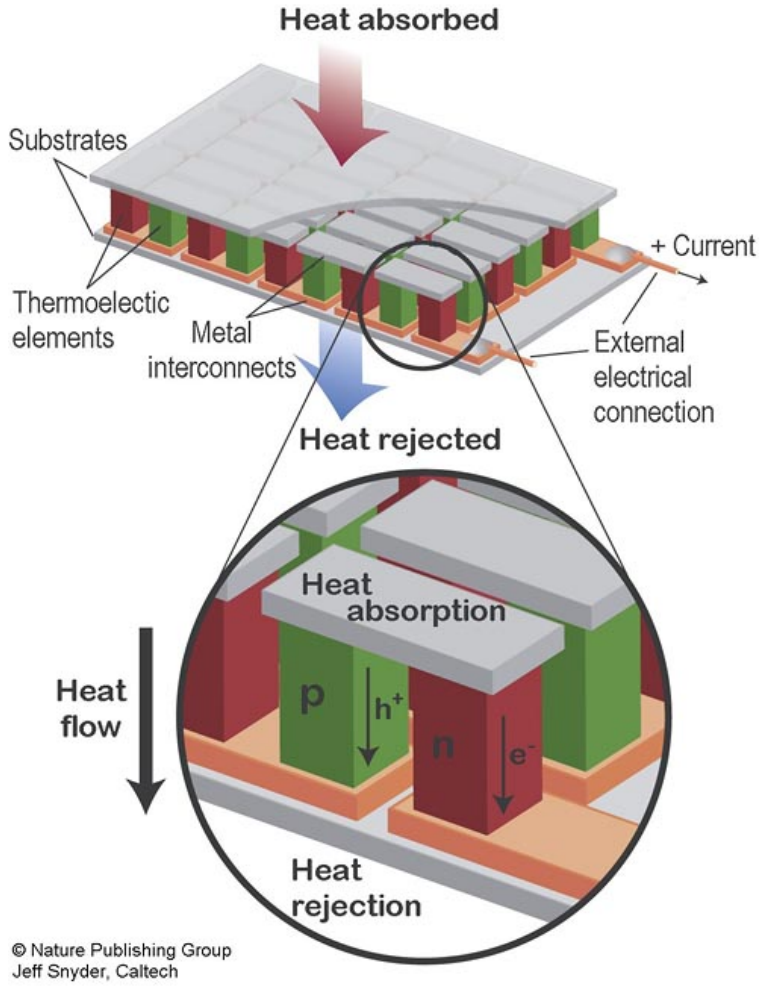

Figure 1.3: **Schematic construction of a thermoelectric module.** The thermoelectric device is constructed by connecting p- and n-type semiconductors (i.e. the thermoelectric materials) in series with a heat absorber on one side (the hot side) and a heat exchanger on the other (the cold side). The materials are thermally in parallel and electrically in series during operation, which causes a current to flow.

rial (e.g. Pu-238) into usable electricity to power the on-board electronics. Since these thermoelectric generators have no moving parts, they tend to be very reliable, as demonstrated by the 40+ years of continuous communication with the Voyager space probes. In return, the constant operating conditions of space are ideal for thermoelectrics. Part of the trouble in finding terrestrial applications for thermoelectric generators is the diverse temperature ranges of waste heat. Thermoelectrics have to be optimized for the

operational temperature of interest, making the transference of one device to multiple applications difficult.

Due to the symmetry of physics, however, thermoelectric devices can also run in reverse. This is to say that, instead of converting heat (via a temperature difference) into electricity, an electric current can be used to generate a temperature difference. This has large implications for efficient, small scale (low volume) cooling near room temperature. While compressor-based refrigeration becomes increasingly more efficient for large volumes, the efficiency of thermoelectric devices is constant (volume independent). Thus, at small volumes there is a crossing point. Then, a thermoelectric device would be more efficient for cooling a volume than a compressor-based system. Couple this with the realization that we cool entire buildings (a large volume) just for the comfort of the humans inside the structure (a fractionally small volume). The ability of thermoelectric devices to provide efficient local cooling has yet to be fully explored. But, these considerations may drastically reduce energy consumption and waste.

For technological applications, it is also necessary to consider material and device stability during operation. This includes chemical stability and mechanical stability of materials and interfaces [76, 77, 78, 79, 80]. For example, continual observations of chemical decomposition led the National Aeronautics and Space Administration to discontinue development of a new thermoelectric device based on copper selenide after nearly a decade of research [81, 82]. The ability of a material to resist fracture is also fundamental to device design and implementation.

It is with these motivations in mind that the present work aims to contribute towards the progression of thermoelectric technologies. However, it would be remiss not to mention that there is a vast degree of overlap between the materials science topics relevant to the development of thermoelectric materials and those of other energy materials. This is to say that, while the present studies were "thermoelectrics motivated" there are, in many cases, direct implications for the design and characterization of other energy materials. Specific examples are given throughout the text. In particular, the results presented here to aid in the interpretation of thermal conductivity behaviors through phase transitions will be important to battery materials as their thermal transport properties are further characterized, as these materials typically undergo phase transitions during charge and discharge cycles. The relation of thermal transport in these materials to "thermal runaway" and device failure is presently the topic of much scientific investigation [83]. The thermodynamic stability criterion developed for mixed ionic-electronic conducting thermoelectric materials is also expected to be fundamental to engineering the stability of

halide perovskite solar cells. Lastly, the novel insights presented here in rethinking the fundamental nature of vibrations in solids has profound implications for mechanistically understanding and quantifying thermal properties and thermal transport in materials regardless of application.

Chapter 2

Background

The materials science of solids is comprised of observations (measurements) and theory (models) that span many orders of magnitude. As atoms and their bonds dictate the bulk behavior of materials, there is a need to understand the atomic scale behavior of atoms in solids. However, the bulk properties that are observed at the macroscale (e.g. in engineering devices) are the culmination of many interactions at the atomic scale. This results in "emergent" phenomena that are the collective behavior of many complicated processes.

The inference here is that measurements of "bulk properties" necessarily includes some summation and/or averaging over all of the atomic-scale phenomena. That is, bulk measurements do not investigate individual atomic behavior in the individual sense. When the volume of material that is being measured is large enough (in a statistical sense), a thermodynamic framework can be used to describe the behavior of that volume element.

Thermodynamics has the generality to describe interdependent relations of material response(s) to experimental parameters. The goal of physics, in this case, is to then describe the underlying mechanism(s) that explains the thermodynamic observation. Consequently, the utility of both thermodynamic and physical models provides ample insights for engineering design.

In this perspective, there are thermodynamic truths (experimental observations) that may have more than one physics explanation, or progressive levels of the same physical theory. This chapter aims to outline fundamental aspects of both thermodynamic methods and measurements, as well as established physics in solids.

2.1 Equilibrium Thermodynamics

In order to learn something about a material, it is necessary to perturb it in some way. When the perturbation is relatively small, "uniform" throughout the material and time-independent, then equilibrium thermodynamics can characterize a large variety of material responses (from a reference state) due to external stimuli.

Free energy functions (e.g. Gibbs free energy or Helmholtz free energy) are constructed in order to define the energetic changes of the material given the relevant thermodynamic conditions of the experiment. For example, the Gibbs free energy describes the energy in the system that is available to do work when the system is held at constant temperature and pressure. Alternatively, the Helmholtz free energy can be used when temperature and volume are held constant. These functions describe the condition for equilibrium when they obtain their "minimum" value, or correspondingly, when their derivative goes to zero.

In differential form, the effects of perturbations (T, P, N, X) on the Gibbs free energy G are characterized as

$$dG = VdP - SdT + \sum_i \mu_i \, dN_i + \sum_j A_j dX_j, \tag{2.1}$$

where T is temperature having the conjugate variable entropy S, P is pressure having the conjugate variable volume V, μ_i is the chemical potential of species i that describes changes in the free energy when the number N_i of species changes, and, similarly, A_j is the coefficient that describes how G changes due to purturbation (external variable) X_j.

Similarly, the differential of the Helmholtz free energy F is written as

$$dF = V \sum_{ij} \sigma_{ij} d\epsilon_{ij} - SdT + \sum_a \mu_a dN_a + \sum_b A_b dX_b, \tag{2.2}$$

which has been written to emphasize that P and V can be abstracted (generalized) to include the full tensor relation of stress σ and strain ϵ. Again, the effects of other external variables can also be considered to change the free energy of the system, such as an electric or magnetic field.

In Figure 2.1 the interrelations of thermodynamic variables are considered from a materials perspective (see ref. [1]). For example, stress and strain are related by the elastic constants (elasticity) of the material. Temperature and entropy are related through heat

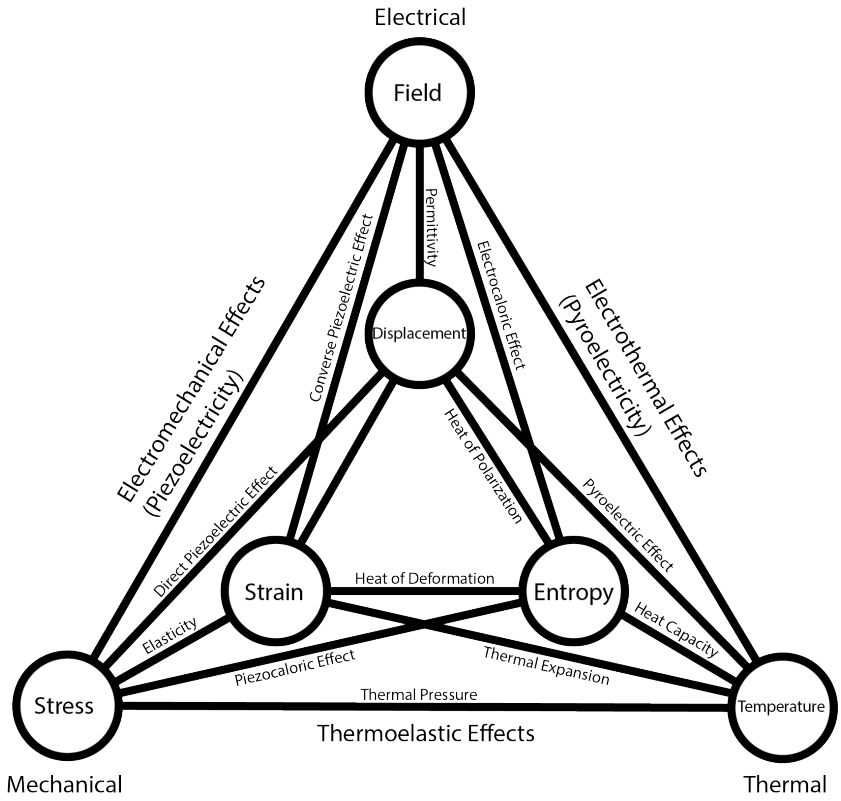

Figure 2.1: **Schematic of interconnections between thermodynamic variables.** Relations between thermodynamic variables are coupled by partial derivatives [1]. In most cases, these derivatives are used to define material properties (e.g. the elastic tensor, heat capacity and permittivity tensor).

capacity. If stress (pressure) is held constant when the temperature is changed, then entropy changes according to the heat capacity at constant stress. The conjugate variable to stress, that is strain, is expected to change according to the thermal expansion coefficient at constant stress. In this manner, the thermo-electro-mechanical interactions in solids can be visualized.

One of the most profound insights from thermodynamics is Maxwell's relations. They are derived simply from the calculus of differentials, such that the order of differentiation with respect to two variables does not matter. Considering the Gibbs and Helmholtz free energy functions as an illustration (and as functions of only two variables, i.e. all other

variables are held constant):

$$\frac{\partial}{\partial T}\left[\left(\frac{\partial G}{\partial N_i}\right)_{\mathrm{T}}\right]_{\mathrm{N}_i} = \frac{\partial}{\partial N_i}\left[\left(\frac{\partial G}{\partial T}\right)_{\mathrm{N}_i}\right]_{\mathrm{T}} \tag{2.3}$$

and

$$\frac{\partial}{\partial T}\left[\left(\frac{\partial F}{\partial \epsilon_{ij}}\right)_{\mathrm{T}}\right]_{\epsilon_{ij}} = \frac{\partial}{\partial \epsilon_{ij}}\left[\left(\frac{\partial F}{\partial T}\right)_{\epsilon_{ij}}\right]_{\mathrm{T}} \tag{2.4}$$

which, considering the definitions of the partial derivatives, can be written simply as

$$\left(\frac{\partial \mu_i}{\partial T}\right)_{\mathrm{N}_i} = -\left(\frac{\partial S}{\partial N_i}\right)_{\mathrm{T}} \tag{2.5}$$

and

$$\left(\frac{\partial \sigma_{ij}}{\partial T}\right)_{\epsilon_{ij}} = \left(\frac{\partial S}{\partial \epsilon_{ij}}\right)_{\mathrm{T}} \tag{2.6}$$

and similar relationships can be derived from other free energy functions. The profound implication of these thermodynamic (mathematical) relationships is that the temperature dependence of one thermodynamic variable is related to isothermal changes of a different thermodynamic variable. Since thermodynamic quantities, namely entropy, can be difficult to measure directly, Maxwell relations provide methods to relate experimental observations of measurable variables to those that cannot be measured.

Looking again at Figure 2.1 more carefully, there is a simple way of determining which variables have a Maxwell relation. If the line that connects two variables (say A and B) has a crossing, then there is a Maxwell relation of those variables (A,B) with the two variables associated with the intersecting line (C and D). If the line connecting two variables (A and B) does not have a crossing, then it only has a Maxwell relation if there are a pair of variables (C and D) that are connected by a line that runs parallel to the AB line. Of course, this only indicates which variables have Maxwell relations and not the exact relationship. Nonetheless, it is straightforward to consider the mathematical construct of the free energy functions and determine the Maxwell relations directly from there.

Throughout the text, thermodynamic variables and associated material properties will be defined as necessary. As will necessary thermodynamic relations. Here, it is only important to illustrate the general energetic principles and versitility of a thermodynamic perspective.

2.2 Transport Thermodynamics

The "uniform" perturbations considered in the previous section may very well be non-uniform in real materials. This is to say that spatial variations can exist such there are gradients in thermodynamic variables. Inherently, this means that the material is not-at-equilibrium. The extent to which this matters depends on which thermodynamic variable, the magnitude of the spatial variation, and the underlying material physics related to the thermodynamic property. Nevertheless, a general consequence of non-uniformity (spatial gradients) in materials is a flow of matter and/or energy that seeks to bring the material to equilibrium, so-called *transport*.

All transport phenomena are inherently non-equilibrium effects. In other words, systems not-at-equilibrium attempt to equilibrate via transport. For typical (small) deviations from equilibrium, transport can be described by the phenomenological linear flux equations of non-equilibrium thermodynamics [84]. Just as free energy functions were written to describe changes in energy due to perturbations in thermodynamic variables, the linear flux equations describe the "desire" of a thermodynamic quantity to move (transport) in response to a gradient in a thermodynamic variable. If this "desire" is not otherwise impeded, there will be a flux. In general, the net flux J of a thermodynamic quantity throughout the material will depend on all of the available transport mechanisms i and all of the gradients in thermodynamic variables X_j that relate to that thermodynamic quantity, written as

$$J = \sum_{i,j} \mathcal{L}_{i,j} \nabla X_j. \tag{2.7}$$

The coefficient $\mathcal{L}_{ij}$ is the material property that determines how quickly transport can occur by mechanism i due to a gradient in X_j.

While Eq. 2.7 is written somewhat abstractly in order to capture generality, simple cases where the flux of electronic charges is only due to gradients in electrical potential, heat flux is due only to the temperature gradient, and the flux of atoms is due to concentration (chemical potential) gradients are shown schematically in Figure 2.2.

2.2.1 Thermal Transport

In the case of conductive thermal transport, which is the mechanism by which solids can achieve thermal equilibrium (i.e. a uniform temperature throughout the material), Fourier [85] defined thermal conductivity as the proportionality between the heat flux density, $J_\mathcal{Q}$ [J s^{-1} m^{-2}], and the temperature gradient ∇T.

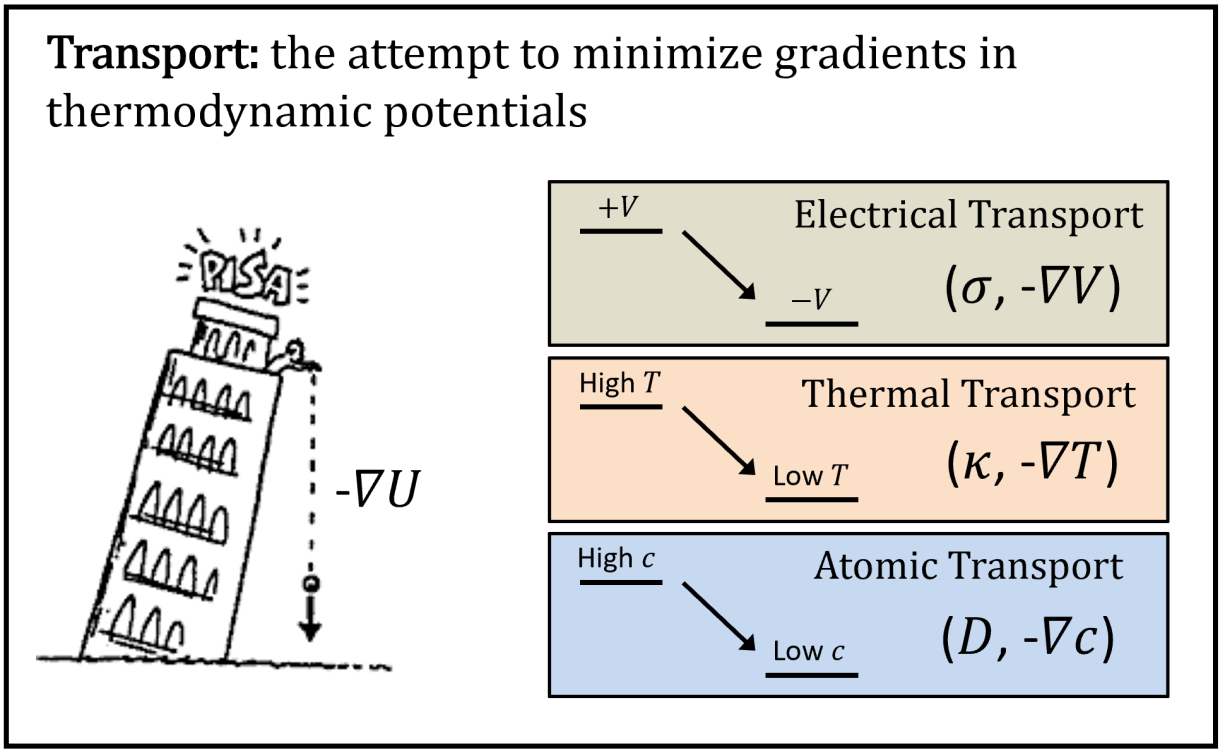

Figure 2.2: **The transport of mass (atoms and electrons) and energy (heat) in solids is driven by gradients in thermodynamic potentials.** These gradients in thermodynamic potentials are analogous to the gradient in potential energy (∇U in figure) that causes macroscopic masses to fall due to gravity. The material property that defines these particular relationships are the electrical conductivity σ, thermal conductivity κ and atomic diffusion coefficient D.

Thus, thermal conductivity κ, as it is measured, is a thermodynamic quantity. While experiments can be designed in order to investigate particular mechanisms of thermal conduction, the bulk property is strictly defined as the coefficient relating heat flux $J_{\mathcal{Q}}$ to the temperature gradient ∇T. In tensor notation,

$$J_{\mathcal{Q},i} = -\kappa_{ij}\, \nabla_j T \ . \tag{2.8}$$

where $J_{\mathcal{Q},i}$ is the component of the heat flux vector in the i-direction and $\nabla_j T$ is the component of the temperature field in the j-direction. Thus, κ_{ij} is a second rank tensor.

While the full tensor is certainly important in certain situations (e.g. in single crystal materials), bulk polycrystalline materials can often be considered isotropic. This is because the orientation dependence is averaged out by all of the randomly oriented crystallites

in the material. Thus, while recognizing that material properties like elastic modulus, thermal and electrical conductivity, etc. are tensors, it is often possible to consider their scalar (averaged) analogs for most theoretical purposes pertaining to bulk materials. This significantly reduces notation (subscripts and superscripts) that can be distracting. This is how we arrive at the simple form of heat flux as J_{Q},

$$J_{\mathrm{Q}} = -\kappa \nabla T \ , \tag{2.9}$$

which still alludes to the tensor form, but omits the subscripts.

Since the heat energy, Q [J], is a conserved quantity (in the absence of source terms), there is a continuity equation associated with Eq. 2.9 [84],

$$\frac{1}{V}\frac{\partial Q}{\partial t} + \nabla \cdot J_{\mathrm{Q}} = 0 \ , \tag{2.10}$$

relating the time derivative of Q to the divergence of J_{Q}. V [m^3] is the volume element of material being considered. Inherent in any thermodynamic model is that it is coarse grain enough (i.e. large enough volume) for thermodynamic quantities to be applicable. It is also important to realize that Eqs. 2.9 and 2.10 refer to Q as a thermodynamic quantity that is independent of any microscopic model of how heat is contained (stored or transported) by the solid.

Then the internal energy, U [J], having the differential form $dU = dQ + dW$, at constant volume (i.e., $dW = 0$), can be used to obtain

$$\left(\frac{\partial U}{\partial t}\right)_{\mathrm{V}} = \left(\frac{\partial Q}{\partial t}\right)_{\mathrm{V}} . \tag{2.11}$$

Similarly, at constant pressure,

$$\left(\frac{\partial H}{\partial t}\right)_{\mathrm{P}} = \left(\frac{\partial Q}{\partial t}\right)_{\mathrm{P}} \tag{2.12}$$

is obtained from a Legendre transform. Making use of the product rule,

$$\left(\frac{\partial H}{\partial t}\right)_{\mathrm{P}} = \left(\frac{\partial H}{\partial T}\right)_{\mathrm{P}} \left(\frac{\partial T}{\partial t}\right)_{\mathrm{P}} , \tag{2.13}$$

and substituting Eq. 2.9 into Eq. 2.10, then for conditions when $\nabla \kappa \approx 0$,

$$\left(\frac{\partial T}{\partial t}\right)_{\mathrm{P}} = \frac{\kappa}{\rho c_{\mathrm{p}}} \nabla^2 T \ , \tag{2.14}$$

where

$$\rho c_{\mathrm{p}} = \frac{1}{V}\left(\frac{\partial H}{\partial T}\right)_{\mathrm{P}} \tag{2.15}$$

defines the volumetric heat capacity from the density ρ and mass specific heat c_{p}.

Since thermal diffusivity, D, is defined as the coefficient of the Laplacian in the second order differential heat equation (in the absence of source terms),

$$\frac{dT}{dt} = D\nabla^2 T \ , \tag{2.16}$$

comparison of Eq. 2.14 and 2.16 gives the well-known relation

$$\kappa = \rho c_{\mathrm{p}} D \ , \tag{2.17}$$

remembering that, for experiments at constant pressure,

$$\frac{dT}{dt} = \left(\frac{\partial T}{\partial t}\right)_{\mathrm{P}} . \tag{2.18}$$

The thermal diffusivity D can be experimentally determined just from the time evolution of the temperature profile of the material when the solution of the boundary-value problem is known [86, 85]. In the laser flash method [87], $D \propto\ L^2/t_{1/2}$ is defined by the sample thickness, L, and the time required for the temperature evolution to reach half of its maximum value, $t_{1/2}$. Thus, D can be determined from the sample/experimental geometry and the time-dependent temperature profile, independent of the assumption of sample homogeneity or porosity, and implies the geometric density should be used in Eq. 2.14 [88]. The accuracy of thermal diffusivity measurements is within ~2-3% when the error in L is minimized.

This shows the intimate thermodynamic relation between thermal conductivity, heat capacity and thermal diffusivity. Particularly for measurements above room temperature, thermal diffusivity can be easily and reliably measured. Heat capacity and thermal conductivity, however, are more easily and reliably measured below room temperature. Thus, this thermodynamic relationship allows for one property to be estimated if the other two are known.

2.2.2 Charge Transport

The flux equation from linear non-equilibrium thermodynamics for any charged species of particles (mol m^{-2} s^{-1}) is given by:

$$j = -\mathcal{L}\left[\nabla\widetilde{\mu} + \left(\mathtt{s} + \frac{\mathtt{Q}}{T}\right)\nabla T\right], \tag{2.19}$$

where the coefficient, $\mathcal{L}$, obeys the Onsager reciprocity relations, and is related to the conductivity, σ, of the species by

$$\mathcal{L} = \frac{\sigma}{(zF)^2}\ , \tag{2.20}$$

and z specifies the sign/magnitude of the charge. The electrochemical potential ($\widetilde{\mu}$) is related to the chemical potential (μ) and electric potential (V) as $\widetilde{\mu} = \mu + zFV$. Then the current flux density (C m^{-2} s^{-1}) contributed by that species is

$$J = zFj = -\frac{\sigma}{zF}\ [\nabla\widetilde{\mu} + s\ \nabla T]\,, \tag{2.21}$$

and we have used the convenient shorthand

$$s = \left(\mathtt{s} + \frac{\mathtt{Q}}{T}\right), \tag{2.22}$$

where $\mathtt{s}$ and $\mathtt{Q}/T$ have units of entropy, $\mathtt{s}$ is the specific entropy, and $\mathtt{Q}$ is the so-called heat of transport [89]. This equation can then be applied to any charged species.

Considering the case for electronic carriers ($z_e = \pm 1$),

$$J_e = -\frac{\sigma_e}{z_e F}\left[\nabla\widetilde{\mu}_e + s_e\ \nabla T\right], \tag{2.23}$$

Considering the case for ionic carriers, from Eq. 2.21, explicitly,

$$J_{\text{ion}} = -\frac{\sigma_{\text{ion}}}{z_{\text{ion}}F}\left[\nabla\widetilde{\mu}_{\text{ion}} + s_{\text{ion}}\ \nabla T\right]. \tag{2.24}$$

When ion-blocking electrodes are used (i.e., there can be no ion flux) and $J_{\text{ion}} = 0$. In this case, the total electrochemical potential is the open circuit electrochemical potential,

$$\nabla\widetilde{\mu}_{\text{ion}} = (\nabla\widetilde{\mu}_{\text{ion}})_{J_{\text{ion}}=0} = -s_{\text{ion}}\ \nabla T\ . \tag{2.25}$$

2.3 Thermoelectric Effect and Figure-of-Merit

The thermoelectric effect responsible for thermoelectric technologies is the voltage that is caused when any material is placed in a temperature gradient. Simply, this is due to the fact that more electronic states will be populated at higher temperatures than at lower temperatures. Any charged ionic species that are mobile may also diffuse as the result of a temperature difference (e.g. the Soret effect), however this case will not be considered here. Regardless, the non-uniform distribution of electric charges results in a net electric potential across the material. So, when the material is not at constant temperature (i.e. there is a "hot side" and a "cold side") a net voltage develops across the material.

While this occurs in every material (yes, think about holding your hand over a candle - there will be an ever-so-small voltage across your hand), some materials that we call "thermoelectrics" have relatively high voltages ΔV that develop for the same temperature difference ΔT. The magnitude of this effect is defined by the Seebeck coefficient S that can be defined simply as

$$S = \frac{\Delta V}{\Delta T} \ . \tag{2.26}$$

Strictly speaking, the Seebeck coefficient is defined under open circuit conditions and, analogous to Eq. 2.25, this is found by setting $J_e = 0$ in Eq. 2.23.

With this definition of the Seebeck coefficient, all of the relevant thermodynamic properties needed to determine the thermoelectric efficiency of a material have been discussed. The so-called material figure-of-merit zT is thus defined as

$$zT = \frac{\sigma S^2}{\kappa} T, \tag{2.27}$$

which indicates that the electrical conductivity σ and Seebeck coefficient S should be maximized, while thermal conductivity κ should be minimized. Implicitly all of these terms are temperature dependent.

It should be reiterated that, in this context, the figure-of-merit is defined by thermodynamic measurements of materials properties. Thus, when evaluating zT the requisite thermodynamic implications of measurement methods and approximations should be thoroughly considered before the underlying physics can be assessed.

2.4 Microscopic Physics

In this body of work, the object of microscopic physics is to describe the underlying mechanisms of the thermodynamic quantities that are determined from bulk (thermodynamic) measurements. While contemporary computational materials science techniques have the capabilities to provide exact values (in many cases), analytical theories aim to mathematically describe the primary mechanisms underlying the material property in a mechanistic and tangible way. Thus, analytic theory is the focus here, for conceptual reasons, with the understanding that computational methods can be utilized (where appropriate) when accurate values of materials properties are to be ascertained.

2.4.1 Thermal Transport

The thermal conductivity that is measured directly, or estimated from its thermodynamic relation to thermal diffusivity, is in fact a total. That is, it contains the contributions of every mechanism that is available to transport heat in the material. For any arbitrary number of mechanisms,

$$\kappa = \sum_i \kappa_i. \tag{2.28}$$

Typically, however, other information about the material is known that provides hints as to what mechanisms are likely to contribute to the total thermal conductivity. For the majority of engineering solids, it is only necessary to consider two primary contributions to κ, namely,

$$\kappa = \kappa_{\mathrm{L}} + \kappa_{\mathrm{e}}, \tag{2.29}$$

which includes the contribution from atomic vibrations (i.e. the lattice) κ_{L} and from electronic carriers κ_{e}. Again, we are breaking from the thermodynamic quantity κ and now attempt to understand the underlying mechanisms responsible for the measured value.

Electronic Thermal Conductivity

It was first noticed by Wiedemann and Franz in the 1850s that the thermal conductivity of metals was linearly related to their electrical conductivity when appropriately normalized by temperature. Later this relationship could be derived using an elementary theory of electrons in conjunction with the Boltzmann transport equation. These details are not

particularly relevant for the main discussion of this text, so it is enough to simply state that:

electrons carry both electric charge and thermal energy (heat).

It is not surprising then, that the bulk measurements of electrical and thermal conductivity made by Wiedemann and Franz were proportional given that electrons carry most of the heat in metals.

As it turns out, the heat carried by electrons is always proportional to the corresponding electrical conductivity since both quantities are carried by the same particles. The general relationship between κ_{e} and σ_{e} is

$$\kappa_{\mathrm{e}} = L_{\mathrm{e}}\sigma_{\mathrm{e}}T. \tag{2.30}$$

where the coefficient L_{e} is the Lorenz number. For metals, $L_{\mathrm{e}} = 2.44 \times 10^{-8}$ W Ω K^{-2}, but it does depend to a certain degree on the number of electronic carriers [90].

Importantly, the independent relation of κ_{e} on the electrical conductivity is what allows for the estimation of the lattice contribution,

$$\kappa_{\mathrm{L}} = \kappa - L_{\mathrm{e}}\sigma_{\mathrm{e}}T. \tag{2.31}$$

Lattice Thermal Conductivity

The heat carried by atomic vibrations tends to be negligible in most metals (i.e. $\kappa_{\mathrm{L}} \ll \kappa_{\mathrm{e}}$), but is a comparable contributor in many semiconductors (i.e. $\kappa_{\mathrm{L}} \approx \kappa_{\mathrm{e}}$) and is the dominant mechanism of thermal transport in electrical insulators (i.e. $\kappa_{\mathrm{L}} \gg \kappa_{\mathrm{e}}$). Indeed, the primary focus of this work will pertain to the latter two cases. Here, understanding the underlying physics of κ_{L} can be utilized to devise engineering design principles that directly impact the total thermal conductivity κ.

In this section, discussions about thermal conductivity κ assume $\kappa \approx \kappa_{\mathrm{L}}$. Furthermore, the description of κ_{L} may also be comprised of multiple terms depending on the specific nature of the vibrations being considered. With foresight to the rest of the text, the general construction of κ_{L} can include contributions from both phonons κ_{ph} and diffusons κ_{diff},

$$\kappa_{\mathrm{L}} = \kappa_{\mathrm{ph}} + \kappa_{\mathrm{diff}}. \tag{2.32}$$

This is a somewhat new concept [36, 91, 92, 93, 94].

Phonon Gas Model

The kinetic theory of gases is often a starting point for describing the physics of transport. In the case of thermal conductivity the kinetic theory phenomenologically describes the transport of heat in solids as

$$\kappa_{\mathrm{L}} = \frac{1}{3} C v \ell \tag{2.33}$$

where C is the heat capacity per unit volume (i.e. the thermal energy being transported), v is the average speed of a collective lattice vibration (i.e. phonon) and ℓ is the average phonon mean free path (i.e. distance traveled between scattering events), where collectively $v\ell$ describes how "fast" heat diffuses through the material. In this perspective phonons behave like gas particles and, hence, is called the "phonon gas model." Thus, κ_{L} written in Eq. 2.33 is more aptly named as the phonon thermal conductivity κ_{ph}.

The extension of the phonon gas model to consider how individual vibrations contribute to the thermal conductivity tensor can also be considered. Then, $\kappa_{\mathrm{ph},ij}$ can be obtained by solving the Peierls-Boltzmann transport equation in the relaxation time approximation. In standard notational form:

$$\kappa_{\mathrm{ph},ij} = \sum_{\mathbf{k}s} C_{\mathrm{ph}}(\mathbf{k}s)\, v_{\mathrm{g},i}(\mathbf{k}s)\, v_{\mathrm{g},j}(\mathbf{k}s)\, \tau(\mathbf{k}s), \tag{2.34}$$

where specific phonon modes are indexed by their wavevector $\mathbf{k}$ and branch index s, denoted by the compound label $\mathbf{k}s$. Then $C_{\mathrm{ph}}(\mathbf{k}s)$ is the heat capacity of the phonon mode, $v_{\mathrm{g},i}(\mathbf{k}s) = d\omega(\mathbf{k}s)/dk_i$ is the component of the phonon group velocity vector pointing in the i direction, $\tau(\mathbf{k}s)$ is the lifetime of the phonon (i.e. time between scattering events).

Modern computational techniques are typically capable of calculating κ_{ph} directly for structures that are not too complicated. Recently, a unified approach to calculate both κ_{ph} and κ_{diff} has been developed [92]. The results of these calculated κ_{L} are comparable to experimental values when the measured material does not have a significant number of defects (atomic or microstructural), as these are difficult to account for in current computational methods.

Spectral Thermal Conductivity

Although explicit consideration of individual vibrational modes is possible, analytically it is much easier to group vibrations according to their frequency (i.e. energy $\hbar\omega$) and assign "average" behaviors to the vibrations at that frequency. In this manner the high-level

physics can be captured mathematically, without tediously worrying about the behavior of individual vibrations. Since this looks at thermal transport phenomena as a function of frequency, it is termed "spectral thermal conductivity." Of course, this approach has major limitations. Even so, spectral theories typically capture the correct magnitude of thermal conductivity and predict trends with experimental variables that are useful for engineering design.

In this perspective, any model for the thermal conductivity carried by the atomic vibrations of a solid must consider three components:

1. the number of vibrations of a particular energy that are available to carry heat, i.e. the vibrational density of states, $g(\omega)$,
2. the quantity of heat that can be carried by each vibration, i.e. the heat capacity per mode, $C(\omega)$, and,
3. the propagation behavior of these vibrations through the material, i.e. the thermal diffusivity for each vibration, $\mathcal{D}(\omega)$.

Therefore, the total thermal conductivity can be written as the frequency-dependent integral

$$\kappa = \int_0^\infty g(\omega)\ C(\omega)\ \mathcal{D}(\omega)\quad d\omega\ . \tag{2.35}$$

The spectral heat capacity $C(\omega)$ for lattice vibrations follows from Bose-Einstein statistics, explicitly

$$C(\omega) = \frac{\partial}{\partial T}\left(\frac{\hbar\omega}{e^{\frac{\hbar\omega}{k_{\mathrm{B}}T}}-1}\right), \tag{2.36}$$

and saturates to $C(\omega) = k_{\mathrm{B}}$ in the $T \to \infty$ limit.

Consequently, the primary difference between thermal conductivity models is in the choice of physics used to characterize the propagation behavior, $\mathcal{D}(\omega)$. In the phonon gas model,

$$\mathcal{D}(\omega) = v(\omega)^2\tau(\omega), \tag{2.37}$$

as expected from a spectral averaging of the terms in Eq. 2.34. Lastly, it should be noted that a different form of $\mathcal{D}(\omega)$ will be developed for diffusons later in the text.

2.4.2 Charge Transport

This body of work does not explicitly consider the microscopic mechanisms of charge transport in solids other than by assigning individual contributions to electronic charge carriers (electrons) and to mobile ionic species. Otherwise, charge transport is discussed in a thermodynamic context. Nevertheless, a brief discussion is included here to, again, draw parallels between thermodynamic descriptions and microscopic mechanisms, as well as to identify key physical parameters relevant to engineering design.

Electronic Transport

It is again possible to begin with a kinetic model. The well-known Drude theory of electrical conductivity is conveniently written as

$$\sigma = \frac{n_{\mathrm{e}} e^2 \tau_{\mathrm{e}}}{m_{\mathrm{e}}^*}, \tag{2.38}$$

to explicitly include the so-called "effective mass" m^* that may or may not differ from the rest mass of an electron, but describes the characteristic inertial mass of electron quasi-particles that describe the collective behavior of electrons in a solid. The electronic conductivity also depends on the number of carriers n_{e} and their characteristic time τ_{e} between scattering events.

As with thermal conductivity, the simple Drude model can be expanded upon to consider the specific electronic band structure of the material and contributions from individual electronic states. These are foregone considerations here. Computational techniques like BoltzTraP [95] make investigations of electronic properties accessible for many materials.

The total charge transport due to electronic species (electrons and holes) is, of course, the sum of both. In metals and intrinsic semiconductors typically both charge carriers should be considered. Degenerate semiconductors (heavily doped with either electrons or holes) are ideal for thermoelectric applications since they have a large electronic conductivity due to only one carrier type, which is necessary to prevent the Seebeck coefficient from being reduced.

A simple derivation of the Seebeck coefficient by Mott [96] shows the inherent relation to electronic conductivity through the number of carriers and effective mass. Explicitly,

$$S \propto \left(\frac{k_{\mathrm{B}}}{z_{\mathrm{e}} e}\right) m^* n_{\mathrm{e}}^{-2/3} T. \tag{2.39}$$

Here it is seen that the Seebeck is negative for electrons and positive for holes. The total Seebeck is the sum of the contributions from both carriers, and is subsequently reduced (approaches zero) when there are an equal number of both electrons and holes.

Ionic Transport

A separate contribution to the total charge transport can come from any charged mobile ions in the solid. The subset of solids known as superionic conductors are particularly relevant for sensor and battery applications. Some of these materials are also electronic conductors and have low thermal conductivity, making them desirable for thermoelectrics applications.

Although the equations presented for the microscopic picture of thermal and electronic conductivity were somewhat simplified in order to better communicate the essential elements of the theory, the same cannot be said for ionic conduction. In the present state, ionic transport is largely defined phenomenologically, without a deeper underlying transport model that is "fully" (more) predictive of ionic behavior. This is likely the result of the complexity of interactions associated with moving an entire ion through a solid. As opposed to the behavior of atomic vibrations or electrons, which already require a quite detailed theory to describe, the behaviors of ionic transport are still being investigated and the theoretical understanding that is needed for predictive power and modeling is still under development.

However, the phenomenological transport model does provide some insights into the likely nature of ionic transport. The general form of ionic conductivity is given as

$$\sigma_{\text{ion}} = \frac{\sigma_0}{T} \exp\left(-\frac{\Delta H_{\text{m}}}{k_{\text{B}} T}\right) \tag{2.40}$$

and, clearly, there is an activation barrier to transport that is governed by the enthalpy of migration ΔH_{m}. However, most of the essential physics is hidden within the prefactor σ_0. Expanding this term,

$$\sigma_0 = \frac{(z_{\text{ion}} e)^2}{k_{\text{B}}} n_{\text{ion}} \Gamma a_0^2 \omega_0 \exp\left(\frac{\Delta S_{\text{m}}}{k_{\text{B}}}\right) \tag{2.41}$$

which includes the concentration of mobile ions n_{ion}, a geometric factor Γ that describes what positions are available for the average mobile ion to move to, the characteristic length a_0 that an ion travels when it moves, as well as the characteristic frequency of vibration ω_0

that facilitates the hopping-like transport and the entropic term that is associated with transport ΔS_{m}. In practice, both σ_0 and ΔH_{m} are fit to experimental measurements. Theoretically and computationally there is a predictive understanding of the migration barrier ΔH_{m}. Understanding the prefactor σ_0 at a more rigorous and predictive level is currently the subject of much attention in solid-state ionics [97, 98].

2.4.3 Comment on the Disparity in Conductivity

A large motivation for studying the thermal properties of materials, especially those properties related to thermal transport, is due to the fundamental disparity between electronic and thermal conductivity. While materials were very quickly categorized according to their electronic conductivity (which is also related to their optical properties), thermal properties and thermal conductivity do not provide such a stark contrast between materials.

To illustrate, consider the electrical conductivity of silicon and the thermal conductivity of silicon (Fig. 2.3). The electrical conductivity can easily span 6 orders of magnitude. Thermal conductivity can only span about 1, or maybe 2 orders of magnitude if amorphous silicon is included ($\kappa \sim 1$ W m^{-1}K^{-1} at 300 K). This is primarily due to the fact that materials can have electronic carrier concentrations that vary by many orders of magnitude (even though changes in composition may be subtle [99]), whereas the heat capacity of solids is generally fairly constant, spanning 1-2 orders of magnitude at most. Thus, whatever advantages can be gained by maximizing or minimizing the diffusion of thermal energy by vibrational modes, either by tuning the elastic properties of the material (controlling the speed of sound or phonon velocity [2]) or by introducing scattering mechanisms [100, 101, 102, 103], these effects are highly sought after.

In the case of thermoelectric materials, where electronic structure is also essential to the thermoelectric performance, it is essential to explore all possible avenues to reduce thermal conductivity while retaining the electronic structure. This is to say that it is not so simple as to simply switch to a material with lower thermal conductivity.

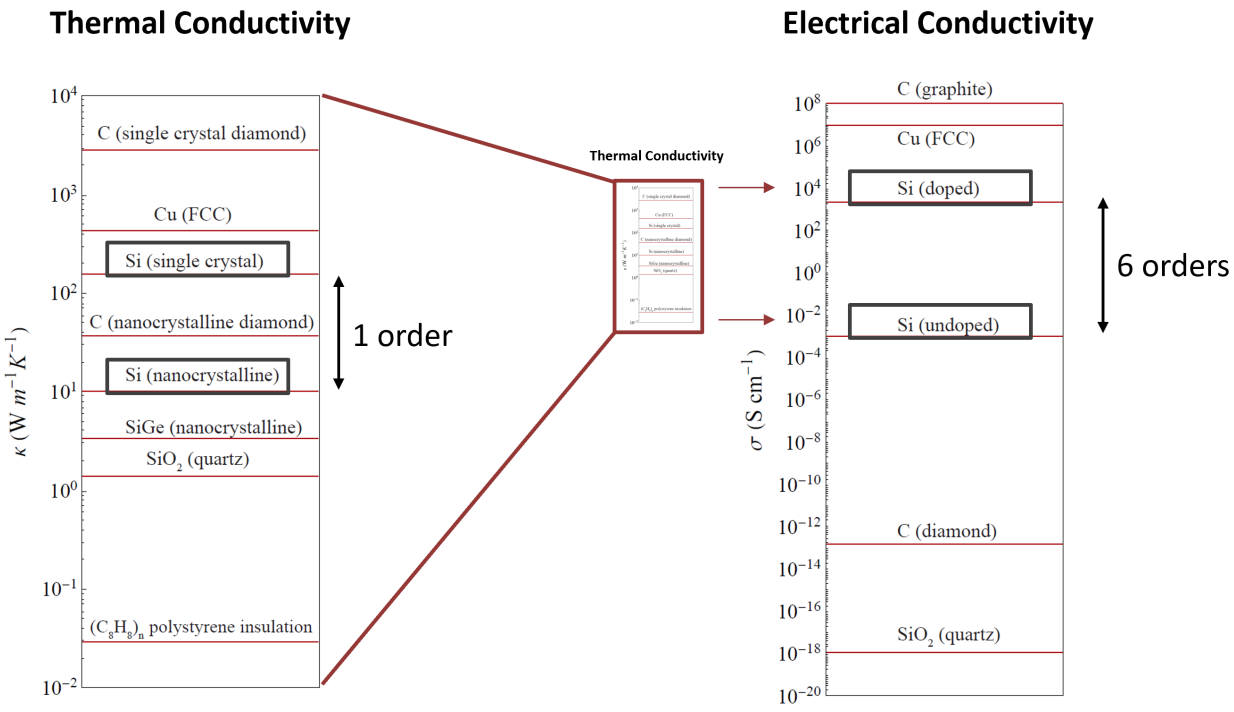

Figure 2.3: **Illustration of the disparity between electrical and thermal conductivity in solids.** Here, silicon is shown as an exemplary case, where electrical conductivity spans ∼6 orders of magnitude (largely due to the ability to control the number of electronic carriers), whereas thermal conductivity spans ∼1–2 orders of magnitude, and even that requires significant effort to control both phonon speed and mean free path [2]. Figure modified from the original developed by Riley Hanus.

Chapter 3

Characterization of Heat Capacity

3.1 Overview

The ability of a material to store thermal energy is defined by its heat capacity. In solids, this quantity is fairly consistent between different materials at room temperature, as first noted by Dulong and Petit in the early 1800s. Here, temperature considerations of heat capacity are discussed, as are phenomena that can lead to additional heat storage. Simple models and equations are developed to give accessible and accurate descriptions of heat capacity for engineering purposes.

This chapter largely draws from content contained within the published works:

Agne, Matthias T., et al. "Heat capacity of Mg_3Sb_2, Mg_3Bi_2, and their alloys at high temperature." Materials Today Physics 6 (2018): 83-88.
Agne, Matthias T., Peter W. Voorhees, and G. Jeffrey Snyder. "Phase Transformation contributions to heat capacity and impact on thermal diffusivity, thermal conductivity, and thermoelectric performance." Advanced Materials 31.35 (2019): 1902980.

3.2 Thermodynamic Description

The differential enthalpy (in units of Joules) of a single phase material having natural variables of entropy, S, and pressure, P, is

$$dH = TdS + VdP. \tag{3.1}$$

Since S is a function of (T,V), then at constant pressure

$$C_{\mathrm{P}} = \left(\frac{\partial H}{\partial T}\right)_{\mathrm{P}} = T\left(\frac{\partial S}{\partial T}\right)_{\mathrm{V}} + T\left(\frac{\partial S}{\partial V}\right)_{\mathrm{T}}\left(\frac{\partial V}{\partial T}\right)_{\mathrm{P}} = C_{\mathrm{V}} + VB\alpha^2 T. \tag{3.2}$$

Here, $T\left(\frac{\partial S}{\partial T}\right)_V = C_{\mathrm{V}}$ is the heat capacity at constant volume; $T\left(\frac{\partial S}{\partial V}\right)_T\left(\frac{\partial V}{\partial T}\right)_{\mathrm{P}} = VB\alpha^2 T$ is the dilation contribution calculated from the volume, V, isothermal bulk modulus, B, and volumetric thermal expansion, α. Eq. 3.2 very clearly demonstrates the progressive levels for approximating C_{P}:

- Using $C_{\mathrm{P}} \approx C_{\mathrm{V}}$, or the Dulong-Petit limit ($3k_{\mathrm{B}}$/atom) at high temperature, is a good first approximation.
- Including the dilation contribution (e.g. the effects of anharmonicity) is the first order correction, which becomes more important above the Debye temperature [104].

For a multi-phase material system, however, the total enthalpy of the system is a volume-weighted average of the enthalpies of each phase and the additional molar enthalpy h_i required to change the molar quantity n_i of component i in each phase. Then the differential enthalpy should be written as

$$dH = TdS + VdP + \sum_i h_i dn_i \ . \tag{3.3}$$

Taking a two-phase system of α and β as an example, then $S = \phi_\alpha S^\alpha + \phi_\beta S^\beta$ and $n_i = \phi_\alpha n_i^\alpha + \phi_\beta n_i^\beta$. Here, ϕ is the phase fraction of each phase, such that $\phi_\alpha + \phi_\beta = 1$. The differentials are: $dS = \phi_\alpha dS^\alpha + \phi_\beta dS^\beta$ (at constant ϕ) and $dn_i = \left(n_i^\beta - n_i^\alpha\right) d\phi_\beta$ (at constant n_i) since $d\phi_\alpha = -d\phi_\beta$. Now Eq. 3.3 can be rewritten as

$$dH = T(\phi_\alpha dS^\alpha + \phi_\beta dS^\beta) + Vdp + \Delta H^{\alpha\to\beta}\, d\phi_\beta \tag{3.4}$$

where $\Delta H^{\alpha\to\beta} = \sum_i h_i \left(n_i^\beta - n_i^\alpha\right)$ is the total enthalpy of transforming α into β. Since, entropy is a function of (T,V) and ϕ_β is a function of (T,P), the total heat capacity at constant pressure is then given by

$$C_{\mathrm{P}} = \left(\frac{\partial H}{\partial T}\right)_{\mathrm{P}} = \phi_\alpha \left(C_{\mathrm{V}}^\alpha + \Gamma_\alpha T\right) + \phi_\beta \left(C_{\mathrm{V}}^\beta + \Gamma_\beta T\right) + \Delta H^{\alpha\to\beta} \left(\frac{\partial \phi_\beta}{\partial T}\right)_{\mathrm{P}} . \tag{3.5}$$

where $\Gamma = VB\alpha^2$ is the dilation correction for the indicated phase in the composite system. Again, $\Delta H^{\alpha\to\beta}$ is the total enthalpy of transforming α to β. Since $\Delta H^{\alpha\to\beta}$ can often be considered to be a constant (independent of ϕ and T), large changes in phase fraction with temperature give rise to large contributions to the heat capacity. Eq. 3.5 is an excellent description for C_{P} in two phase systems, and the method can be applied to multi-phase systems of any size. Obviously, Eq. 3.5 reduces to Eq. 3.2 when the material is single phase (i.e. $\phi_\beta = 0$).

3.3 Physical Contributions to Heat Capacity

The first-order difference between C_{P} and the heat capacity at constant volume, C_{V}, is the contribution due to dilation of the material via thermal expansion,

$$C_{\mathrm{P}} = C_{\mathrm{V}} + B\alpha^2 T = C_{\mathrm{V}}(1 + \gamma\alpha T) , \tag{3.6}$$

where α is the volumetric thermal expansion coefficient, B is the isothermal bulk modulus, $\gamma = B\alpha/C_{\mathrm{V}}$ is the thermodynamic Grüneisen parameter and T is the absolute temperature. Note that Eq. 3.6 has implicitly been normalized by volume (unlike the previous section). Additional contributions to C_{P} from electronic carriers and vacancies can also be considered. As can the effects of phase transformations in multi-phase materials. Since thermodynamic quantities are additive, the total heat capacity of the material is the sum of all contributions. However, the relative contribution of each of these different "degrees-of-freedom" (i.e. the available mechanisms by which the solid can store heat) in the system will depend on the specific physics at play, some of which are considered here.

3.3.1 Phonon Heat Capacity

The dominant contribution to the heat capacity of solids at high temperature (e.g. near and above room temperature) is due to atomic vibrations (phonons). When the phonon

density of states, $g(\omega)$, can be considered as temperature independent, C_{V} can be calculated using

$$C_{\mathrm{V}} = 3nk_{\mathrm{B}} \int_0^{\infty} \left(\frac{g(\omega)}{3n}\right) \left(\frac{\hbar\omega}{k_{\mathrm{B}}T}\right)^2 \left(e^{\frac{\hbar\omega}{k_{\mathrm{B}}T}}\right) \left(e^{\frac{\hbar\omega}{k_{\mathrm{B}}T}} - 1\right)^{-2} d\omega, \tag{3.7}$$

where n is the number density of atoms and $g(\omega)/3n$ is the normalized phonon density of states ($\int_0^{\infty} [g(\omega)/3n]\, d\omega = 1$). Thus, C_{V} can be evaluated when $g(\omega)$ is known or can be approximated. In turn, C_{P} can be modeled from the perspective of Eq. 3.6 using the C_{V} determined by Eq. 3.7 and values of α and B (or the Grüneisen parameter γ), which may be determined experimentally or computationally.

A common approximation for $g(\omega)$ is the Debye model, which assumes phonons are an elastic continuum with a linear dispersion relation ($\omega = vk$). Specifically,

$$g(\omega) = \frac{3\omega^2}{2\pi^2 v_{\mathrm{s}}^3}, \tag{3.8}$$

which allows for the density of states to be approximated from the average speed of sound in the material v_{s}. Since materials really are an elastic continuum in the low frequency limit, measurements of heat capacity at low temperature often capture the approximately linear portion of the phonon dispersion, facilitating a measurement of the material speed of sound. In fact, the Debye model predicts $C_{\mathrm{V}} = \beta T^3$ in the $T \to 0$ limit, where β is related to the Debye temperature through the relation:

$$\theta_{\mathrm{D}} = \left(\frac{12}{5}\pi^4 NR\right)^{1/3} \beta^{-1/3}, \tag{3.9}$$

when β has units of J mol^{-1}K^{-4}, N is the number of atoms per formula unit and R is the gas constant. In turn, the Debye temperature is related to v_{s} as

$$\theta_{\mathrm{D}} = (\hbar/k_{\mathrm{B}})(6\pi^2 n)^{1/3} v_{\mathrm{s}}, \tag{3.10}$$

which connects the thermal and elastic properties of materials.

Although the Debye model can be used in Eq. 3.7 to estimate the temperature dependence of C_{V} from 0 K, a simple description of the temperature dependence as C_{V} saturates to the Dulong-Petit value can be obtained by fitting a Maier-Kelly [105] polynomial to the Debye model C_{V}. The obtained polynomial is accurate for $T > \theta_{\mathrm{D}}/2$. When substituted

into Eq. 3.6 this gives a reasonable estimate of C_{P} at high temperatures ($T > \theta_{\mathrm{D}}/2$),

$$c_{\mathrm{p}}\left[\mathrm{J\ g^{-1}K^{-1}}\right] \approx \frac{3NR}{M_{\mathrm{W}}}\left[1+\frac{1}{10^4}\left(\frac{T}{\theta_{\mathrm{D}}}\right)-\frac{1}{20}\left(\frac{T}{\theta_{\mathrm{D}}}\right)^{-2}\right]+A\left(\frac{T}{\theta_{\mathrm{D}}}\right)\ , \tag{3.11}$$

where A is primarily the dilation term in units of J g^{-1}K^{-1}, i.e.

$$A = BV_{\mathrm{m}}\alpha^2\theta_{\mathrm{D}}/M_{\mathrm{W}}\ . \tag{3.12}$$

Alternatively, A can be found directly from the slope (dc_{p}/dT) of high temperature heat capacity measurements.

3.3.2 Electrons and Vacancies

Electronic contributions to the heat capacity are not expected to be discernible for semiconductors where carrier concentrations are typically less than 10^{21} cm^{-3}. This is demonstrated by the Sommerfeld model of electronic heat capacity,

$$c_{\mathrm{V,el}} = \frac{\pi^2}{3}k_{\mathrm{B}}^2 g_e(E_{\mathrm{F}})T\ , \tag{3.13}$$

where $g_e(E_{\mathrm{F}})$ is the density of electronic states evaluated at the Fermi level. In the parabolic band approximation,

$$g_e(E) = \frac{1}{2\pi^2}\left(\frac{2m^*}{\hbar^2}\right)^{3/2}E^{1/2}, \tag{3.14}$$

and the Fermi level is related to the carrier concentration n_e as

$$E_{\mathrm{F}} = \frac{\hbar^2}{2m^*}\left(3\pi^2 n_e\right)^{2/3}, \tag{3.15}$$

showing that the magnitude of electronic heat capacity scales linearly with the effective mass m^* and is proportional to the number of electronic carriers as $n_e^{1/3}$ (Fig. 3.1). Not to be confused with the Grüneisen parameter, the so-called Sommerfeld coefficient is typically denoted as γ (eg. in Fig. 3.1) or γ_e (to distinguish it from Grüneisen γ) and defines the linear relation between $c_{\mathrm{V,el}}$ and T in Eq. 3.13.

The determination of γ_e from low temperature heat capacity measurements is possible by considering the $T \to 0$ limit, where electronic contributions to the heat capacity dominate

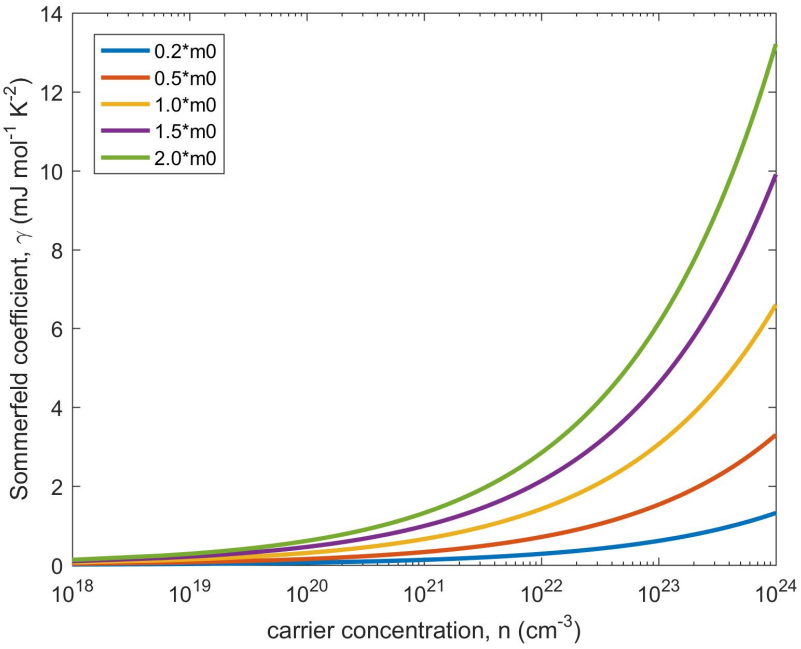

Figure 3.1: **The Sommerfeld coefficient of electronic heat capacity.** The contribution to heat capacity (C_{V}) due to electrons according to the Sommerfeld model increases linearly with temperature as γT. The magnitude of heat capacity depends on the carrier concentration and effective mass of the charge carriers (defined relative to the mass of a free electron m_0 in figure).

over phonon contributions. In this regime, $C_{\mathrm{P}} = C_{\mathrm{V}}$ and can be written as

$$C_{\mathrm{V}} = \gamma_e T + \beta T^3, \tag{3.16}$$

such that a plot of C_{P}/T vs T^2 gives a straight line, with the y-intercept equal to the value of γ_e.

Furthermore, the contribution due to vacancies can be estimated in the dilute limit as

$$C_{\mathrm{p,vac}} \approx R\left(\frac{\Delta H_{\mathrm{vac}}}{RT}\right)^2 e^{-\frac{\Delta H_{\mathrm{vac}}}{RT}}, \tag{3.17}$$

where ΔH_{vac} is the vacancy formation energy. This term is also typically small, e.g. $\sim$53 kJ mol^{-1} for Mg vacancies in degenerate n-type Mg_3Sb_2 material [106], resulting in $C_{\mathrm{p,vac}}$<0.2% of the Dulong-Petit value at 800 K. However, vacancy effects near the melting temperature may become important in some materials.

3.3.3 Two-phase Considerations

For the case of two-phase materials, where phase transformations can occur and there is an additional contribution to C_{P} according to Eq. 3.5, the magnitude of this additional heat capacity may be estimated from the equilibrium phase diagram. Consider the order parameter ϕ as the fractional quantity of the phase of interest (i.e. phase fraction). The equilibrium phase fraction can be determined from the phase diagram. Here, a schematic phase diagram having a miscibility gap is used for demonstration (Fig. 3.2a). In general, however, many thermoelectric alloys and composites have been made in systems having more complicated phase diagrams [15, 107, 108, 11, 109, 110, 111, 112, 113, 114, 115, 116, 117, 118, 119, 120, 121, 122, 123, 124, 125, 126].

For a fixed nominal composition, x_0, the equilibrium phase fraction changes with temperature according to the inverse lever rule (Fig. 3.2b). When kinetics are fast enough, the phase fraction is able to maintain the equilibrium value as the temperature is changed. According to Eq. 3.5, the excess heat capacity is not only determined by the energy associated with the transformation ΔH, but also by the rate of change of the transformation $(\partial\phi/\partial T)_{\mathrm{P}}$ (Fig. 3.2b). Thus, rapid changes in solubility with temperature can lead to substantial contributions to heat capacity. For typical values of $\Delta H \approx 10^4$ J mol^{-1} and values of $(\partial\phi/\partial T)_{\mathrm{P}} \approx 10^{-3}$ K^{-1} (see Fig. 3.2b), then latent heat contributions to c_{p} on the order of tens of J mol^{-1} K^{-1} are easily possible. This can be an appreciable fraction of the Dulong-Petit value. Specific values of $(\partial\phi/\partial T)_{\mathrm{P}}$ are, of course, phase diagram dependent. In the case of Cu_2Se, values of $(\partial\phi/\partial T)_{\mathrm{P}} \approx 10^{-1}$ K^{-1} can occur (see Section 3.7).

3.4 Case Study of Magnesium Antimonide

The high thermoelectric performance reported for n-type $Mg_3(Sb,Bi)_2$ compounds has attracted much interest and has initiated a great effort to optimize this material [127, 128, 129, 130, 131, 132, 133, 106, 134, 135, 136, 5, 137, 138, 139, 140, 141, 142, 143, 144]. One of the origins of this high performance in the $Mg_3(Sb,Bi)_2$ system is its anomalously low thermal conductivity, which is attributed to the undersized Mg cation and the corresponding soft, anharmonic Mg-Sb bonds [145, 134]. Because of the high thermoelectric performance, this material possesses a large potential to be utilized for practical thermoelectric applications, such as power generation for space probes and also refrigeration devices near room temperature.

However, the heat capacity values of $Mg_3(Sb,Bi)_2$, which are required to calculate ther-

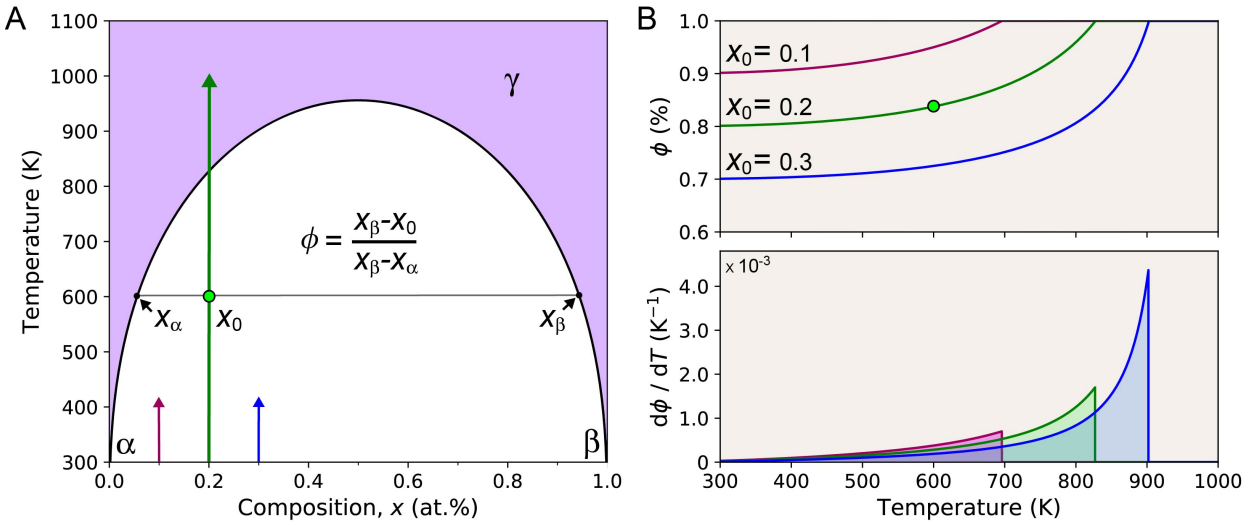

Figure 3.2: **Equilibrium values of ϕ and dϕ/dT can be calculated from the phase diagram.** (a) In this example miscibility gap system, the area below the solvus line is a two-phase mixture of α and β with the equilibrium phase fraction ϕ at each temperature defined by the inverse lever rule. Above the solvus line (shaded region) the single phase γ is formed. (b) The equilibrium phase fraction of the α phase is shown as a function of temperature for several x_0, and the corresponding derivative dϕ/dT, which becomes larger in magnitude approaching the solvus temperature and can contribute significantly to the heat capacity of the solid.

mal conductivity, are inconsistent between studies [6, 7, 4, 5]. At high temperature, the deviation of heat capacity data is more than 10% among previous reports. Before thermoelectric applications can be considered, it is vital to obtain reliable and consistent thermal conductivity data in this system. Temperature dependent heat capacity data is required to calculate thermal conductivity, κ through the relation:

$$\kappa = \rho c_{\mathrm{p}} D, \tag{3.18}$$

where D [m^{2}s^{-1}] is the thermal diffusivity and $C_{\mathrm{P}} = \rho c_{\mathrm{p}}$ is the volumetric heat capacity [J m^{-3}K^{-1}], typically calculated from experimental bulk density, ρ [kg m^{-3}], and the mass specific heat c_{p} [J kg^{-1}K^{-1}]. Although the various reports all rely on the laser flash method to measure D, different reports have used different values of C_{P}. These different values of heat capacity directly correspond to an over/underestimation of the thermoelectric figure of merit, zT, and leads to a loss of consistency among data reported from different groups.

The problem with experimentally obtained C_{P} lies in the uncertainty of the heat capacity measurement at high temperature due to the difficulty of the calibration and temperature

control [88, 146]. Because of this uncertainty, it is often more accurate to use the Dulong-Petit value of heat capacity which is temperature independent. The Dulong-Petit value is often discussed as a specific heat at constant volume, C_{V}, because it does not contain contributions to the specific heat from anharmonic effects [147] (e.g., thermal expansion), but also ignores the heat capacity due to electronic carriers, formation of vacancies, etc. Near room temperature these effects are typically smaller than 5% of the Dulong-Petit value. At higher temperatures, however, these temperature dependent contributions to C_{P} can become appreciable, such that estimates of zT can be affected by 10-20%. For example, a $\sim$15% difference in zT at 725 K was obtained for a $Mg_3(Sb,Bi)_2$ alloy depending if the Dulong-Petit or an experimental heat capacity was used (compare zT in Refs. [106, 137]). Thus, for systems like $Mg_3(Sb,Bi)_2$ where 10% accuracy in thermal conductivity (and zT) is desired, it is imperative to obtain reliable heat capacity values for precise evaluation of the thermoelectric performance, as has been done for PbTe [148].

In this study, we successfully establish a physics-based model to evaluate values of C_{P} at high temperature by considering the contribution from thermal expansion combined with experimentally measured low temperature heat capacity. It is found that the high temperature heat capacity of the entire solid solution range can be simply described by a single polynomial equation which should be a new standard for calculating the thermal conductivity of $Mg_3(Sb,Bi)_2$.

3.4.1 Low Temperature Analysis

The Mg_3Sb_2 and Mg_3Bi_2 compounds are known to have soft shear moduli and highly anharmonic bonding compared with other isostructural compounds (e.g., $CaMg_2Sb_2$) [134, 149]. These characteristics contribute to the low lattice thermal conductivity that makes $Mg_3Sb_{2-x}Bi_x$ alloys promising for thermoelectric applications. However, the high anharmonicity present in these compounds means that the use of the Dulong-Petit heat capacity is likely a significant underestimate at high temperatures.

This study utilized low temperature heat capacity measurements to determine the Debye temperature for a series of $Mg_3Sb_{2-x}Bi_x$ compounds (x = 0, 0.5, 1.0, 1.5, 2). By plotting C_{P}/T^3 vs T it is possible to determine the so-called Debye level, β. This horizontal plateau is observed when atomic vibrations dominate the heat capacity in the $T \rightarrow 0$ K limit (i.e., $g(\omega) \propto \omega^2$) and is related to the Debye temperature through the relations discussed in Section 3.3.1. In Fig. 3.3a, the experimental values of C_{P}/T^3 are plotted along with corresponding Debye model fits of β. The Debye temperatures obtained from pulse-echo

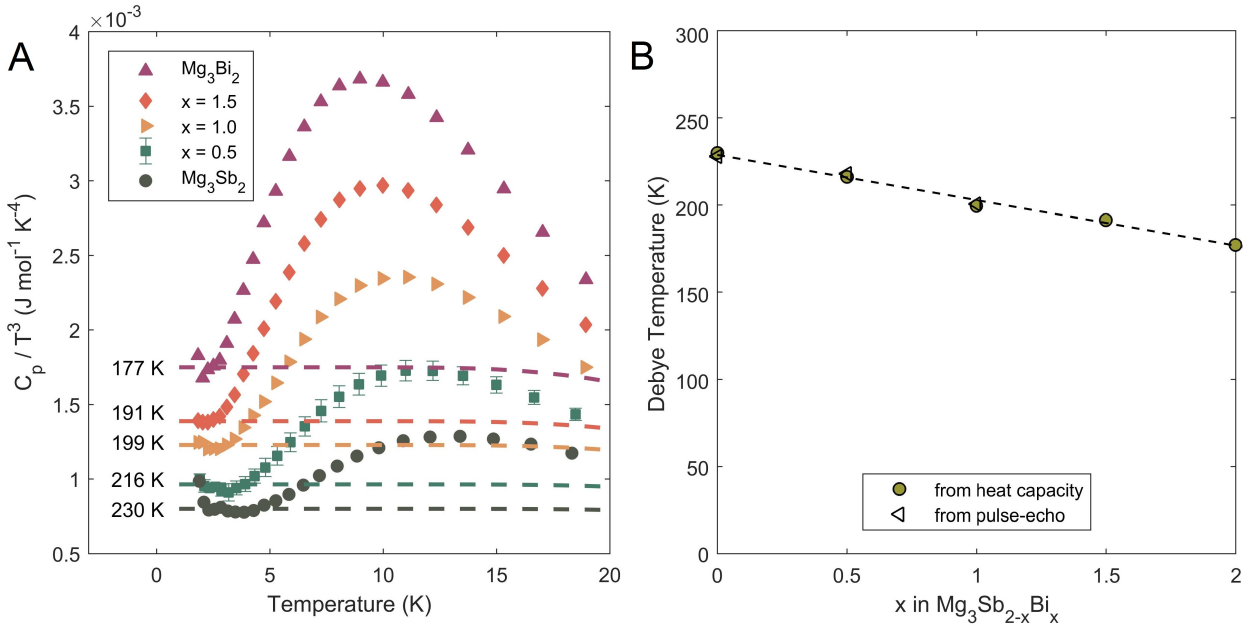

Figure 3.3: **Debye temperature of $Mg_3Sb_{2-x}Bi_x$ alloys.** Measured values of molar heat capacities plotted as C_P/T^3 vs T (markers) for several compositions in the $Mg_3Sb_{2-x}Bi_x$ system, with corresponding Debye model curves (dashed lines); as well as, (b) the Debye temperatures obtained from the data shown in panel (a) and from pulse-echo speed of sound data, plotted vs nominal composition.

speed of sound measurements are in excellent agreement with those determined from heat capacity (Fig. 3.3b).

Clearly there is an elastic softening as Mg_3Sb_2 is alloyed with Mg_3Bi_2 that appears to follow a linear relation (Vegard's law) with composition. Interestingly, although the Debye temperature decreases by 23%, the bulk modulus remains nearly constant across the compositional range (Table 3.1). This indicates that it is predominantly the shear modes that soften during alloying.

Thermal expansion is an inherently anharmonic effect, such that more anharmonicity tends to result in larger thermal expansion coefficients. The volumetric thermal expansion coefficient,α, determined via dilatometry ($66.9\times10^{-6}K^{-1}$) is comparable to other anharmonic thermoelectric materials like PbTe ($59.1\times10^{-6}K^{-1}$) and SnTe ($63.9\times10^{-6}K^{-1}$) [151]. However, temperature dependent X-ray diffraction results obtained herein gave a 37% lower absolute magnitude of α, likely resulting from a systemic error in the temperature control. Nevertheless, the X-ray measurements indicate that the thermal expansion coefficient is independent of composition, within 10%. Previous experimental and

Table 3.1: Physical properties of the $Mg_3Sb_{2-x}Bi_x$ alloy system

Compound:	Mg_3Sb_2 (x=0)	$Mg_3Sb_{1.5}Bi_{0.5}$ (x=0.5)	Mg_3SbBi (x=1.0)	$Mg_3Sb_{0.5}Bi_{1.5}$ (x = 1.5)	Mg_3Bi_2 (x=2)
Bulk Modulus, B (GPa)	45.9 36.4 [134] 42 [150]	47.5	45.3	–	– 38.4 [134] 37 [150]
Shear Modulus, G (GPa)	16.0 15.7 [134] 19 [150]	16.4	15.5	–	– 13.4 [134] 15 [150]
Poisson ratio, ν	0.34 0.32 [150]	0.34	0.35	–	– 0.32 [150]
Molar volume, V_m (m^3mol^{-1})	7.86E-05	7.98E-05	8.09E-05	8.23E-05	8.35E-05
Debye temperature, θ_D (K)	230 ± 2 228 ± 4	216 ± 4 218 ± 3	199 ± 2 201 ± 3	191 ± 1 –	177 ± 2 –

computational work on Mg_3Sb_2 reported α values of $51.9\times10^{-6}K^{-1}$and $61.7\times10^{-6}K^{-1}$, respectively, at 300 K [134]. These values are larger than those for the isostructural compounds $CaMg_2Sb_2$ and $CaMg_2Bi_2$ (and the Yb analogues), again due to the larger anharmonicity of $Mg_3(Sb,Bi)_2$. Computational values as large as almost $90\times10^{-6}K^{-1}$ were reported for Mg_3Sb_2 at 600 K [134]. However, experimentally, there is no indication of a significant increase in α from 300 to 720 K.

Experimental heat capacities of Mg_3Sb_2 and Mg_3Bi_2 from 2 to 220 K can be well described using Eq. 3.6 (Fig. 3.4a). The DFT calculated density of states (Fig. 3.4b, used in Eq. 3.7) also shows that Mg_3Bi_2 is softer than Mg_3Sb_2, in agreement with the trend in Debye temperatures (Fig. 3.3b). A constant value of $B\alpha^2 = 206.9$ J $m^{-3}K^{-2}$ is used, based on the average measured value of bulk modulus (46.2 GPa) and the high temperature value for the volumetric thermal expansion coefficient ($66.9\times10^{-6}K^{-1}$). The temperature dependence of α, which is constant at high temperature but goes to zero at 0 K, can be neglected because the $B\alpha^2$ term is already relatively small and is multiplied by the absolute temperature (Eq. 3.6), effectively suppressing the dilation contribution below 150 K. As T increases, however, the dilation term is necessary to account for the deviation of the measured C_P from C_V (compare dashed and solid lines in Fig. 3.4).

3.4.2 Extension to High Temperature

The success of using the physics-based model (Eq. 3.6) to describe the low temperature heat capacity (Fig. 3.4) provides validation for using the model to describe the heat ca-

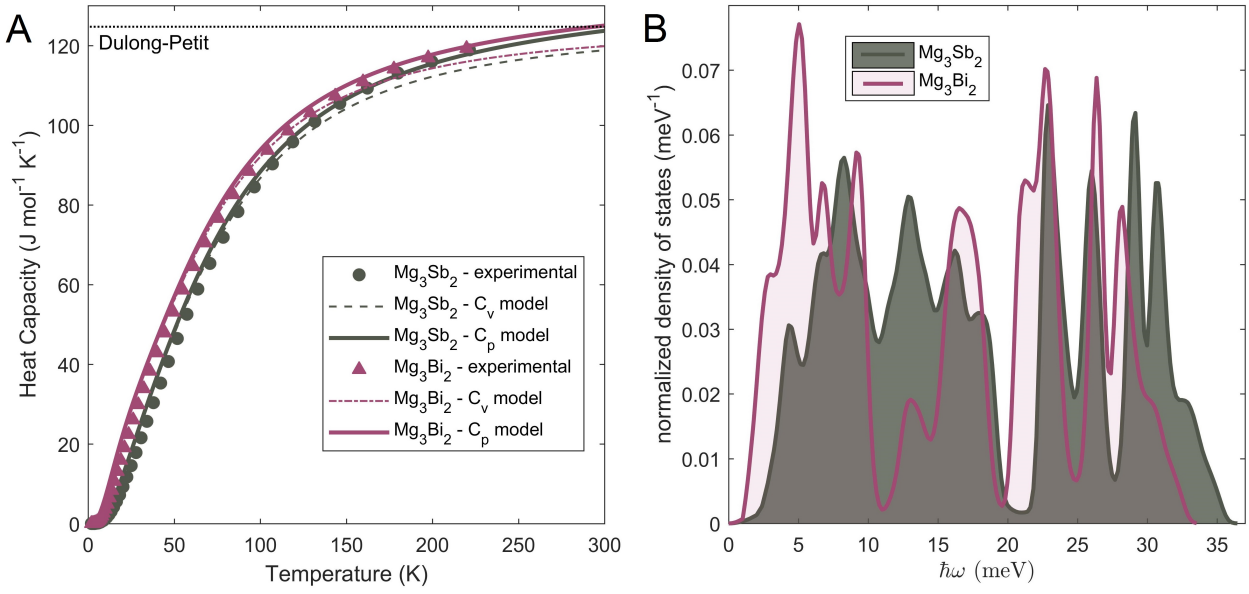

Figure 3.4: **Heat capacity and vibrational density of states of Mg_3Sb_2 and Mg_3Bi_2.** Measurements of low temperature molar heat capacities of Mg_3Sb_2 (grey circles) and Mg_3Bi_2 (purple triangles) modeled by Eq. 3.6 (solid lines), using the linear dilation term discussed in text and the constant volume heat capacity (dashed lines) calculated using (b) the DFT phonon densities of states of Mg_3Sb_2 (grey shaded) and Mg_3Bi_2 (purple line) in Eq. 3.7.

pacity over the full temperature range (Fig. 3.5). Particularly, by demonstrating that the model correctly captures the magnitude and curvature of C_P leading up to 300 K means that extrapolation to higher temperatures is self-consistent with low temperature measurements. Since the molar heat capacities of the entire compositional range ($0 \leq x \leq 2$) are similar at low temperatures (e.g., the spread in values is $< 5\%$ of the mean at 220 K), the C_P model for Mg_3Sb_2 can be used as a good approximation for the entire system. For temperatures from 100 to 220 K, the model is within 1% of the average of the experimental values. Then the error of the model can be estimated from the range of the 5 data sets as approximately $\pm 3\%$. As can be seen in Fig. 3.5, measurements of high temperature (>300 K) heat capacity in the $Mg_3Sb_{2-x}Bi_x$ system vary substantially in magnitude ($\approx$20% at 400 K, see Fig. 3.5). This is likely the result of the sensitivity of measurement techniques (e.g., differential scanning calorimetry) to baseline corrections/calibration. Nonetheless, the high temperature slopes of the measured C_P values (dC_P/dT) are qualitatively consistent with that predicted from the bulk modulus and thermal expansion. This supports the idea that measurements are prone to systemic errors that lead to differing absolute magnitudes between studies, whereas relative magnitudes (i.e., dC_P/dT)

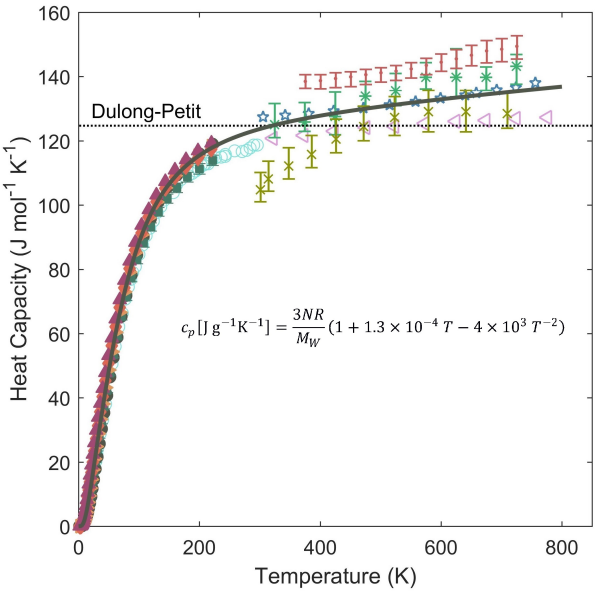

Figure 3.5: **The heat capacity of $Mg_3Sb_{2-x}Bi_x$ alloys.** A compilation of experimental heat capacity values for $Mg_3Sb_{2-x}Bi_x$ alloys over the full temperature range. The low temperature values (<300 K) measured herein: x=0 (grey circles), x = 0.5 (green squares), x = 1.0 (yellow triangles), x = 1.5 (orange diamonds), x = 2.0 (purple triangles), have magnitudes within ±3% of the Mg_3Sb_2 model curve (grey line) below 220 K. The experimental results of this study agree with the low temperature values reported for Mg_3Sb_2 by Yoon [3] (open blue circles). The reported values at higher temperature (>300 K) are more scattered, with the measured values of this study (red dots) having the largest magnitude, but a slope in agreement with theory. The experimental values of Shuai, et al. [4] (open blue stars) and Tamaki, et al. [5] (green asterisk markers) agree best with both the magnitude and slope of the model curve. Bhardwaj and Misra [6] (open triangle markers) and Chen, et al. [7] (gold X markers) report values somewhat lower in magnitude, but with similar slopes as the others. Note that the linear dilation term is responsible for increasing C_P ≈5% above the Dulong-Petit value by 600 K.

agree. Thus, the model is likely a better estimate of the magnitude of the high temperature C_P since it is consistent with the low temperature values and reproduces the linear slope observed in the high temperature measurements.

In recognizing that the molar heat capacities of the $Mg_3Sb_{2-x}Bi_x$ system are similar (Fig. 3.5) and can be estimated by a simple model (Eq. 3.6) over the full temperature range (grey line in Fig. 3.5), it is advantageous to make the model values of C_P accessible for engineering applications. Herein, a Maier-Kelly [105] polynomial expression was found to describe the model curve (normalized RMS error of 0.2%), and thus estimate the mag-

nitude of experimental heat capacity ±3% for the range 200 K $\leq$ T $\leq$800 K:

$$c_{\mathrm{p}}\left[\mathrm{J\ g^{-1}K^{-1}}\right] = \frac{3NR}{M_{\mathrm{W}}}\left(1 + 1.3\times10^{-4}\ T - 4\times10^{3}\ T^{-2}\right), \tag{3.19}$$

where $3NR$=124.71 J mol^{-1}K^{-1} since N=5 (number of atoms per formula unit) and R is the gas constant. M_{W} is the molecular weight of the formula unit being considered (in units of g mol^{-1}). By the Neumann-Kopp rule, this same expression is expected to hold when dopants/substitutions are introduced. In that case, an appropriate M_{W} should be used accordingly. Also note that Eq. 3.19 is written in a way that the unit dimensions may be easily changed. The dimensionless heat capacity $C_{\mathrm{P}}/3nk_{\mathrm{B}}$ is the polynomial term in parenthesis in Eq. 3.19.

The excellent agreement of Eq. 3.19 even for the full solid solution from Mg_3Sb_2 to Mg_3Bi_2 and its closeness to the Dulong-Petit value ($3NR/M_{\mathrm{W}}$) suggests that Eq. 3.19 should be a good estimate even for doped (such as Te, La n-type dopants or Na, Li p-type dopants) or alloyed (Ca, Zn, Cd, etc. up to ∼30%) samples.

The equivalence of Eq. 3.11 (θ_{D}=282 K) with Eq. 3.19 for $Mg_3Sb_{2-x}Bi_x$ compounds provides compelling justification for the use of Eq. 3.11 to accurately estimate the heat capacity of other compounds at high temperature. In fact, Eq. 3.11 is likely more accurate than even experimental measurements, not only for $Mg_3Sb_{2-x}Bi_x$, but also for other single phase materials [88].

3.4.3 Summary

Including the first-order anharmonic correction to the harmonic phonon heat capacity provides an accurate description of experimental heat capacity of $Mg_3(Sb,Bi)_2$ up to 800 K. The self-consistency of the C_{P} model with both low and high temperature experimental results provides validation that it can be used to estimate the magnitude of high temperature C_{P} where experimental results are scattered. The model is likely to be more accurate for a given new material than an individual measurement considering the typical uncertainties of high temperature heat capacity measurements. A simple polynomial expression is given for the suggested heat capacity values over the 200 K$\leq$ T $\leq$800 K range that is expected to be accurate within ±3% for $Mg_3(Sb,Bi)_2$ solid solutions even when considering dopant and alloying additions. The high anharmonicity of $Mg_3(Sb,Bi)_2$ compounds leads to deviations of C_{P} from the Dulong-Petit limit at high temperatures. We recommend the suggested values of C_{P} be used so that thermal conductivity is not ap-

preciably underestimated and to improve accuracy of comparing results among different laboratories.

3.5 Characterization of MAB Phases

The MAB phases are atomically laminated transition metal (M) borides, whose crystal structures are comprised of transition metal boride (M-B) layers separated by a bilayer or monolayer of Al (A) atoms. As electrically conductive, high-temperature layered ceramics, they resemble the MAX phases [152]. Their bulk synthesis has only recently been realized [153], and thus their thermophysical characterization is important for classifying these materials for potential technological applications.

3.5.1 Determination of Electronic Heat Capacity

In the characterization of the heat capacity of the MAB phases, like the MAX phases [154], it is necessary to include the electronic heat capacity for an accurate description across the full temperature range.

In the case of the MAB phase MoAlB [8], it has a non-negligible electronic heat capacity, determined here to be $\gamma_e = 1.94$ mJ mol^{-1} K^{-2} (Fig. 3.6). This makes use of the strategy of determining the Sommerfeld coefficient γ_e as discussed in Section 3.3. It is important to note that the value of γ_e depends on the region that is linearly fit (e.g. the blue region in Figure). Further discussion on determining the Sommerfeld coefficient γ_e can be found in Appendix A.

The Mn_2AlB_2 and Fe_2AlB_2 MAB phases are somewhat different than the MoAlB case, in that there is a net magnetic moment at low temperature that adds an additional contribution to the heat capacity. Thus, while the low temperature ($T \to 0$) limit is not linear when C_P/T is plotted versus T^2, the y-intercept is still a reasonable estimate of γ_e (see Appendix B).

3.5.2 Estimation of High Temperature Heat Capacity

Since the magnetic phase transition in Mn_2AlB_2 and Fe_2AlB_2 is around room temperature, the high temperature heat capacity does not have a magnetic component. Thus, the simple description of high temperature heat capacity (Eq. 3.11) can be used for MoAlB,

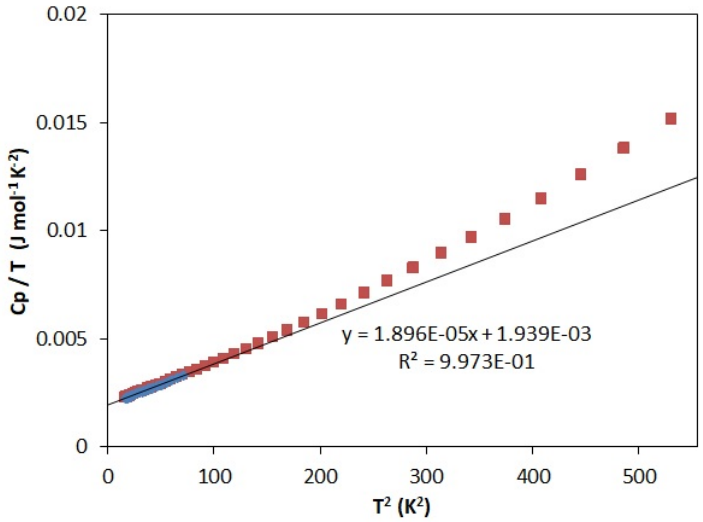

Figure 3.6: **Determination of the coefficient of electronic heat capacity γ_e from low temperature heat capacity measurements.** The y-intercept is γ_e and the linear slope is β as discussed in Section 3.3.

Mn_2AlB_2 and Fe_2AlB_2. However, the linear term A has to be adapted to include the electronic contribution as,

$$A = \frac{\theta_{\mathrm{D}}}{M_{\mathrm{W}}}(BV_{\mathrm{m}}\alpha^2 + \gamma_e). \tag{3.20}$$

In all cases, the dilation contribution to C_{P} can be estimated in the same manner as for the Mg_3Sb_2 materials (Section 3.4) using the experimentally determined bulk modulus and thermal expansion coefficient.

It was then possible to estimate the high temperature heat capacity according to Eq. 3.11 using the A coefficient defined by Eq. 3.20 (Fig. 3.7).

3.6 Characterization of Zinc Antimonide

The thermoelectric material Zn_4Sb_3 is a remarkable example of the "phonon-glass electron-crystal" philosophy and has an exceptional zT in the ~400–700 K range [155]. At lower temperature ~250 K it undergoes a phase transition, which is relevant to a later discussion in this work.

Here, it is demonstrated how Eq. 3.11 provides a simple and accurate description of the temperature dependent heat capacity outside of the phase transition region. In three

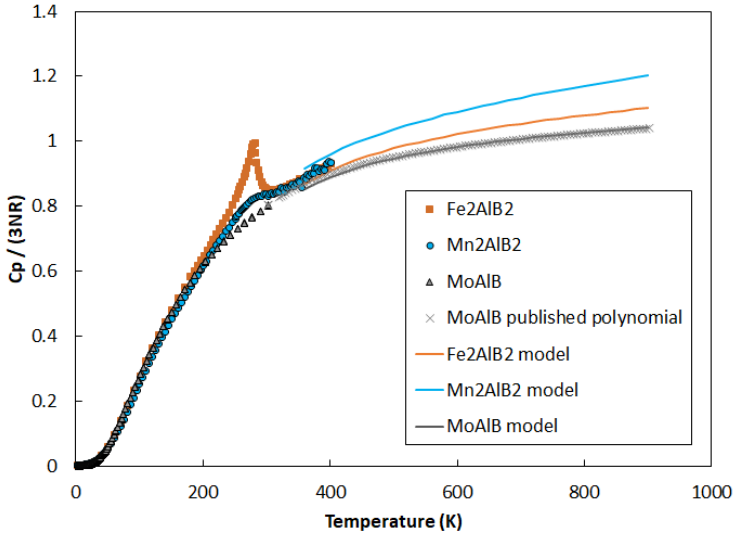

Figure 3.7: **Heat capacity of the MAB phases.** Experimental measurements of heat capacity (markers) and high temperature model (solid lines) of the MAB phases MoAlB, Mn_2AlB_2 and Fe_2AlBe. The excellent agreement of this model with previously reported high temperature results [8] provides confidence in the model for the other compounds. The model makes use of the experimentally measured speed of sound to estimate the Debye temperature θ_D and bulk modulus B, as well as experimentally measured thermal expansion to account for the dilation contribution to C_P. The electronic contribution made use of the linear Sommerfeld term as discussed in text. Magnetic terms are not expected to contribute above the phase transition, which is the peak (or plateau) in the experimental data near 300 K.

easy steps:

1. Calculate the Dulong-Petit heat capacity.

   The value $\frac{3NR}{M_W} = 0.2785$ J g^{-1}K^{-1} was calculated using $N = 7$ (atoms per formula unit) and $M_W = 626.84$ g mol^{-1}.

2. Determine the Debye temperature θ_D.

   In this case, a value of the Debye temperature $\theta_D = 237$ K was taken from literature [156]. Experimentally, it can be obtained by the methods discussed in Section 3.3.1.

3. Estimate the linear term A.

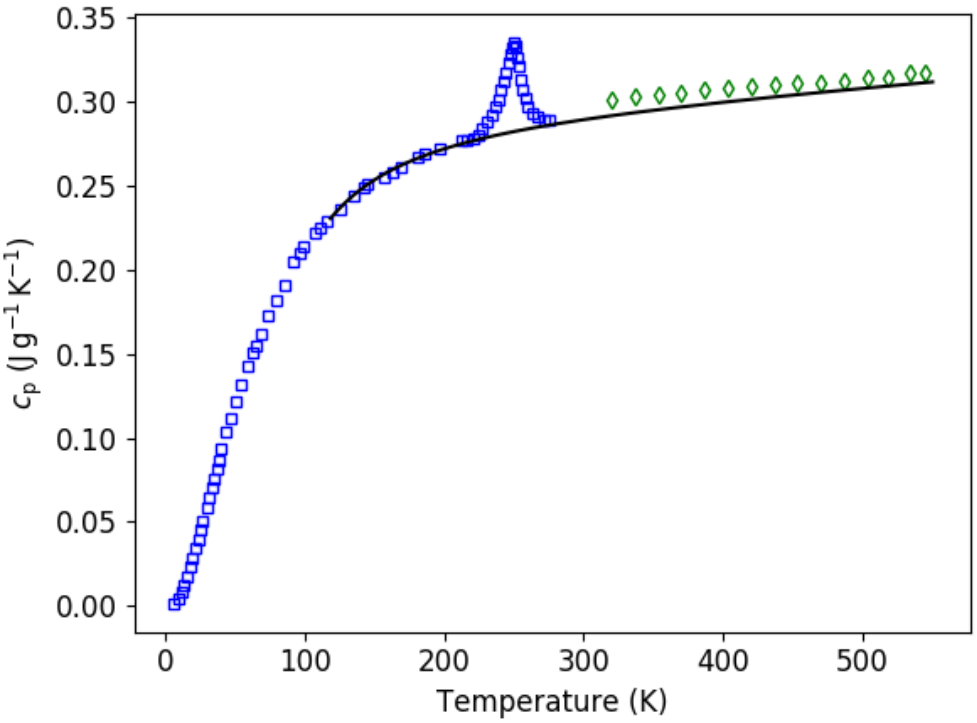

Figure 3.8: **Heat capacity of zinc antimonide.** Experimental heat capacity reported at low temperature by Bhattacharya et al [9] (blue squares), and at high temperature by Toberer et al [10] (green diamonds), compared with the model defined by Eq. 3.11 (black line).

> If the material properties needed to calculate A (as in Eq. 3.20) are unknown, it is also possible to use the slope of experimental heat capacity measurements which are generally more reliable than their absolute magnitude. Here, the coefficient $A = \theta_{\mathrm{D}} \times 6.521 \times 10^{-5}$ J g^{-1}K^{-1} was determined using dc_{p}/dT found from a linear regression of the experimental data given by Toberer, et al. [10] (green diamonds in Fig. 3.8).

Using these values in Eq. 3.11 accurately captures the temperature dependent heat capacity for temperatures greater than $\theta_{\mathrm{D}}/2$ (black line in Fig. 3.8). Again, effects of the phase transition on heat capacity were not considered here.

3.7 Characterization of Copper Selenide

There are many similarities between Cu_2Se and Zn_4Sb_3. Both are p-type semiconductors due to the large number of cation (copper or zinc) vacancies. Both undergo phase transitions in which the high temperature phase has a high ionic mobility of the cations. And both have a high thermoelectric performance that is generally limited by their chemical stability during operation. In the case of Cu_2Se, it is generally accepted to have high thermoelectric performance at high temperature ($\sim$1000 K) [157], but it is highly debated if (or to what degree) the thermoelectric efficiency peaks at the phase transition $\sim$400 K. Here, the phase transformation contribution to heat capacity is considered.

Examination of the $Cu_{2-\mathrm{d}}Se$ region of the phase diagram [11] shows a two phase region (Fig. 3.9a), from which ϕ_β and $\left(\partial\phi_\beta/\partial T\right)_\mathrm{p}$ can be calculated (Fig. 3.9b). This is done using the inverse lever rule as shown in Fig. 3.2.

Then, Eq. 3.5 can be used to estimate the heat capacity including the phase transformation contribution. For simplicity, the Dulong-Petit value can be used for the c_v component and the dilation term can be neglected (for both phases) in the temperature range of interest. The latent heat contribution for the $Cu_{1.985}Se$ nominal composition is estimated using $\left(\partial\phi_\beta/\partial T\right)_\mathrm{p}$ determined from the phase diagram and $\Delta H^{\alpha\rightarrow\beta} = 30$ J g^{-1} [11].

This model for the heat capacity is in good overall agreement with carefully measured experimental values [12] (Fig. 3.9c). However, there is thermal broadening associated with the experimental method that is not captured in the model c_p. In other words, there is not a discontinuity in the experimental c_p but a more gradual decrease above $\sim$410 K (compare blue squares with black curve in Fig. 3.9c).

3.8 Characterization of Elastic Softening

The recently noted importance of elastic softening for tuning thermal conductivity in bulk solids is a new mechanism for improving thermoelectric performance. In a model PbTe system, the thermal conductivity could be reduced by $\sim$20% with a reduction in the bulk speed of sound by only $\sim$7% [2]. This demonstrates the subtle dependence of transport properties on the elastic properties of materials (e.g. the speed of sound).

Similarly, the connection of elastic properties to the ionic conductivity of Li ion batteries makes the characterization of elastic properties essential to understanding transport in

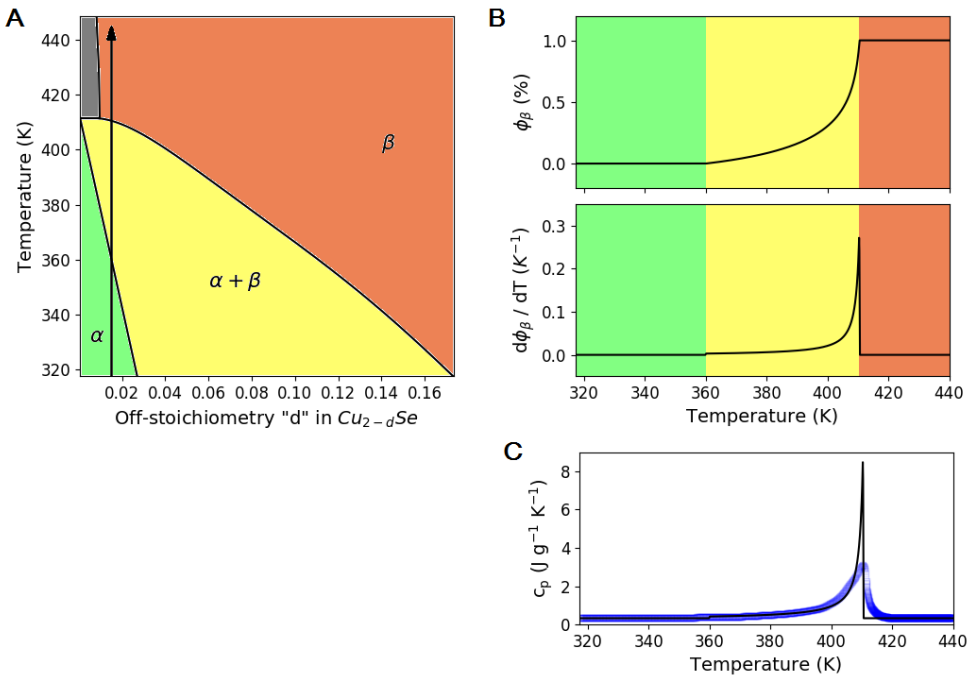

Figure 3.9: **Phase diagram and heat capacity of copper selenide.** Section of the Cu-Se phase diagram showing (a) the $\alpha \rightarrow \beta$ phase transition region [11] of $Cu_{2-d}Se$, as well as, (b) the temperature dependent equilibrium phase fraction of β, ϕ_β, and the temperature derivative $d\phi_\beta/dT$ for the nominal $Cu_{1.985}Se$ composition defined by the path of the arrow in panel a. Thermal properties for the nominal $Cu_{1.985}Se$ composition including (c) the experimental heat capacity [12] (blue points in top panel) measured by differential scanning calorimetry and the model heat capacity (black line in top panel) calculated using $d\phi_\beta/dT$ shown in panel b.

a general sense. Thus, characterization of the speed of sound (or elastic modulus) is of utmost importance for characterizing and assessing these new transport phenomena.

Low temperature heat capacity, which can thermally probe the elastic continuum of materials (at low enough temperatures), is an excellent resource for determining the elastic properties of materials. While bulk solids (nominally fully dense) may use ultrasonic methods (pulse echo or resonant) to characterize the elasticity of the material, highly anisotropic materials, porous materials, or even powders can utilize heat capacity measurements to extract thermally averaged elastic properties.

3.8.1 Evaluation of Elasticity in Lead Telluride

The low temperature heat capacity results of Mg_3Sb_2 materials (Fig. 3.3) demonstrate the principle perfectly. In that case, the elastic softening was due to alloying. In the

case of the bulk PbTe materials considered here (Fig. 3.10), the elastic softening is strain induced [2].

It should be noted that the traditional C_{P}/T vs T^2 plot is difficult to analyze since the linear region spans a small temperature range. In fact, had the present study not made measurements as low as 1.8 K, the Debye-like elastic region would have been missed entirely. It is typical for low temperature heat capacity measurements to begin $\sim$4 K. If that had been the case, the plot of C_{P}/T vs T^2 would have still looked fairly linear (see $T^2 > 20$ K^2 in Fig. 3.10a), which one may erroneously interpret as being the Debye-like region. However, C_{P}/T can never be negative as both C_{P} and T can only be positive. Thus, if the y-intercept of the C_{P}/T vs T^2 linear regression is significantly less than zero (beyond typical errors in regression analysis) this would indicate that the Debye region has been missed, or is not the dominant contribution to C_{P} if other physics is at play.

Instead, the plot of C_{P}/T^3 vs T is used as it was in the case of Mg_3Sb_2. The horizontal plateau ($\sim$ 2 K in Fig. 3.10b) clearly shows the so-called "Debye level" needed to extract the speed of sound (see Section 3.3.1). The deviation of the heat capacity due to the quick rise in the phonon density of states (due to the low frequency transverse modes) is clearly seen as a hump centered around $\sim$10 K. This hump does not necessarily mean there is a "rattling" mode, as is often inferred in other materials, but rather there is a large density of states at low frequency that is not accounted for by the Debye model.

3.8.2 Phenomenological Description of Elastic Softening

As an illustration of the nature of softening, and how transverse acoustic phonons can give rise to the peak observed in the low temperature plot of C_{P}/T^3, consider the simple phonon dispersion shown in Fig. 3.11a that was constructed using the Brillouin zone boundary condition (BZBC) model described by Kaviany [13, 14]. The flattening of the transverse acoustic branch around 4 meV gives rise to a peak in the density of states at this same point (Fig. 3.11b). As the longitudinal branch is essentially linear (Debye-like) it would produce a horizontal plateau in the C_{P}/T^3 plot as shown in Fig. 3.10. However, due to the presence of the transverse branch, the peak in low temperature heat capacity is reproduced (Fig. 3.11c). Thus, this simple model captures the main elements observed experimentally:

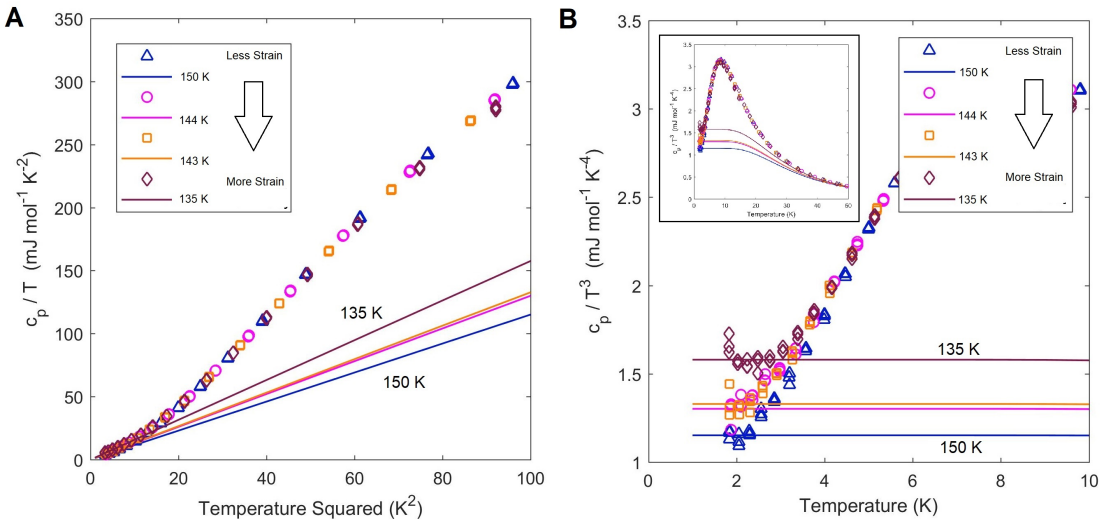

Figure 3.10: **Experimental characterization of elastic softening in lead telluride by low temperature heat capacity measurements.** Debye model fits to the lowest temperature data are used to extract the thermally averaged speed of sound through its relation to the Debye temperature ($\theta_{\mathrm{D}} \sim v_{\mathrm{s}}$). (a) The plot of C_{P}/T vs T^2 is not recommended for materials like PbTe that have substantial contributions to the phonon density of states at low frequencies that cause a rapid rise in the heat capacity that is not expected from the Debye model, as determination of the Debye region may be difficult. For example, compare the temperature range of the linear region ($T^2 < 20$ K^2) with that in Fig. 3.6. (b) A plot of C_{P}/T^3 shows softening as a change in the so-called Debye level, the horizontal plateau at the lowest temperatures. This plot further emphasizes deviations from the Debye model (i.e. the peak ~10 K, see inset) that is more more distinguishable than the change in slope observed in panel a.

1. The shift in Debye level is indicative of a change in the bulk speed of sound (larger value of C_{P}/T^3 means smaller θ_{D}).

2. The subtle shift of the peak in C_{P}/T^3 to lower temperature is explained by a corresponding shift in the frequencies of the transverse phonon modes.

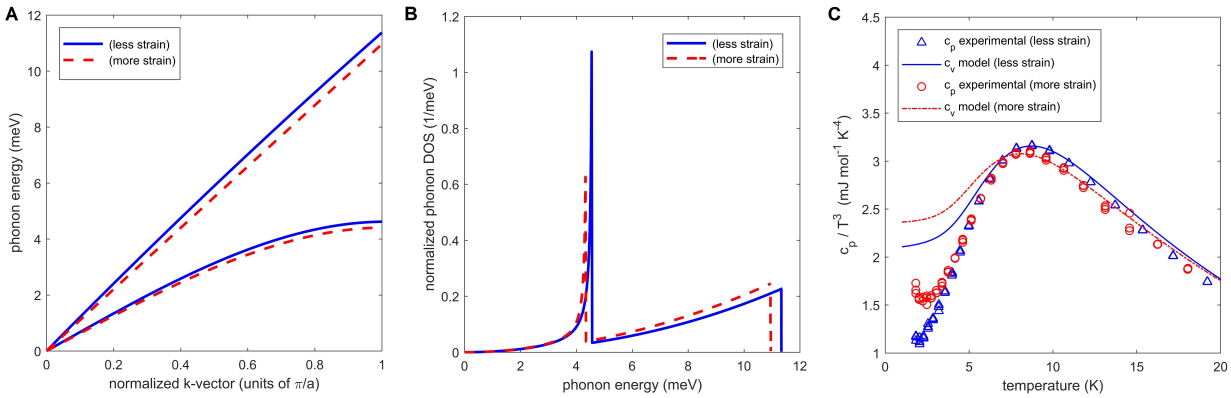

Figure 3.11: **Illustration of softening and its impact on low temperature heat capacity.** (a) Example phonon dispersion demonstrating the shift in phonon modes to lower frequency that is meant by "softening". This phonon dispersion is sketched using the BZBC model described by Kaviany [13, 14]. (b) The corresponding phonon density of states from which heat capacity can be calculated. (c) The heat capacity determined from the density of states shown in panel b, illustrating both the change in Debye level and subtle shift of the hump due to the transverse acoustic phonons.

Chapter 4

Thermal Conductivity Through Phase Transitions

4.1 Overview

The accurate characterization of thermal conductivity κ, particularly at high temperature, is of paramount importance to many materials, thermoelectrics in particular. The ease and access of thermal diffusivity D measurements allows for the calculation κ of when the volumetric heat capacity, ρc_{p}, of the material is known. However, in the relation $\kappa = \rho c_{\mathrm{p}} D$, there is some confusion as to what value of c_{p} should be used in materials undergoing phase transformations. Herein, it is demonstrated that the Dulong-Petit estimate of c_{p} at high temperature is not appropriate for materials having phase transformations with kinetic timescales relevant to thermal transport. In these materials, there is an additional capacity to store heat in the material through the enthalpy of transformation ΔH. It is shown experimentally in Zn_4Sb_3 that the decrease in D through the phase transition at 250 K is fully accounted for by the increase in c_{p}, while κ changes smoothly through the phase transition. Consequently, reports of κ dropping near phase transitions in widely studied materials such as PbTe and SnSe have likely overlooked the effects of excess heat capacity and overestimated the thermoelectric efficiency, zT [158].

The bulk of this chapter was published as:

> Agne, Matthias T., Peter W. Voorhees, and G. Jeffrey Snyder. "Phase Transformation contributions to heat capacity and impact on thermal diffusivity, thermal conductivity, and thermoelectric performance." Advanced Materials 31.35 (2019): 1902980.

4.2 Motivations

Well characterized thermophysical properties, especially thermal conductivity, κ, are crucial for modern engineering design and applications. Both low κ (e.g. thermoelectric and thermal barrier) and high κ (e.g. thermal management and heat sink) technologies rely on accurate thermal property measurements to evaluate material/device performance and efficiency. For thermoelectric materials, where the energy conversion efficiency is determined by the material figure-of-merit [75], $zT \propto \kappa^{-1}$, it is vital to obtain reliable and consistent thermal conductivity data before applications can be considered.

The drive to improve thermoelectric efficiency through reductions in thermal conductivity has been successful over the past two decades [159, 160, 161]. The general approach has been to reduce the lattice thermal conductivity κ_{L} through phonon scattering by introducing various defects in the material. Although it has also been demonstrated that controlling the elastic properties of the material may be equally or more important in some materials [2]. Beneficially, it seems that introducing microstructural defects can reduce thermal conductivity through both mechanisms (softening and scattering).

The use of phase transitions has been proposed as a method of improving zT through further reducing thermal conductivity (Fig. 4.1). Observations of κ_{L} approaching zero during phase transitions in some materials lead to the idea of "critical" phonon scattering as a mechanism for thermal conductivity suppression. However, it was later noted that a corresponding peak in heat capacity at the phase transition was also present causing some confusion as to which heat capacity to use in the estimation of thermal conductivity.

Although direct measurements of κ are possible [88], it is more frequent in measurement above room temperature to calculate thermal conductivity through the relation (Section 2.2.1)

$$\kappa = \rho c_{\mathrm{p}} D. \tag{4.1}$$

Here, D [m^2 s^{-1}] is the thermal diffusivity and $\rho c_{\mathrm{p}} = (\partial H/\partial T)_{\mathrm{p}}$ is the constant pressure heat capacity [J m^{-3}K^{-1}] typically calculated from experimental bulk density, ρ [kg m^{-3}] and the mass specific heat c_{p} [J kg^{-1} K^{-1}]. Eq. 4.1 is utilized largely because measurements of thermal diffusivity, D, are accurate (within $\sim$3%) and easily accessible [88].

Thus, the uncertainty in calculating κ (often 10% or more) is frequently attributed to measurement of heat capacity [88, 146]. Due to the uncertainty in the absolute magnitude of high temperature heat capacity measurements, it is often more accurate to use

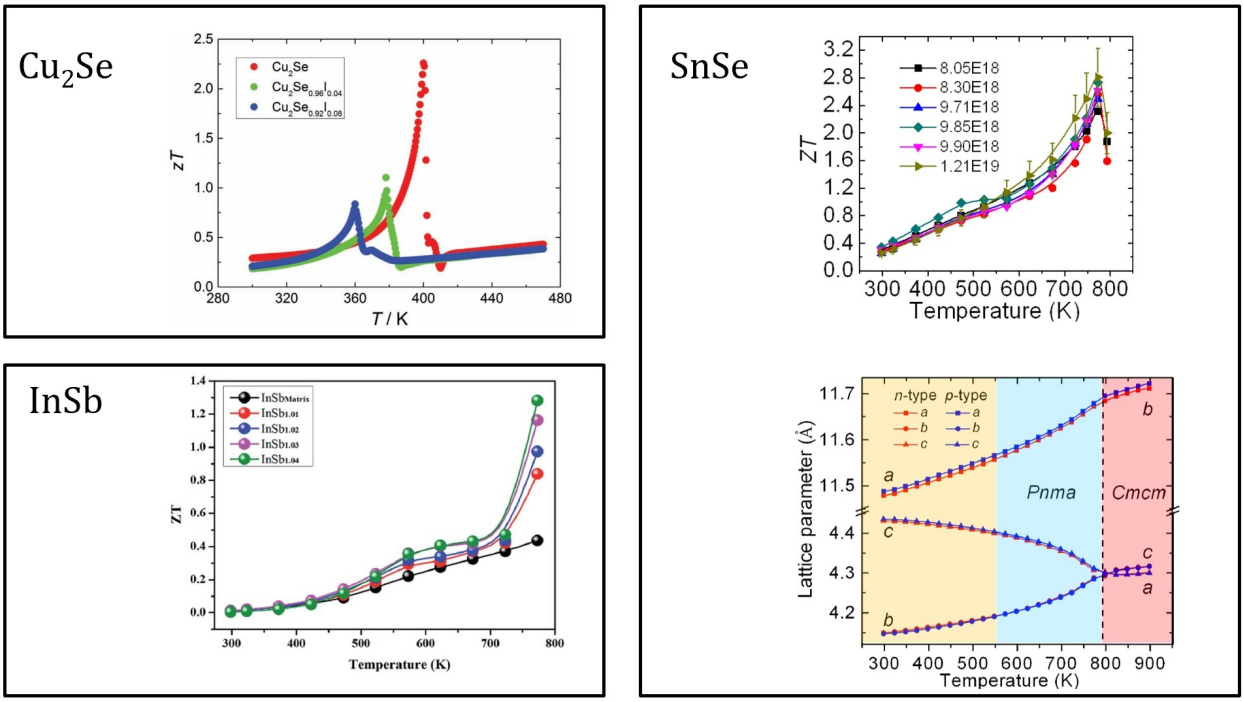

Figure 4.1: **Thermoelectric efficiency at phase transitions.** Experimental reports suggest that the thermoelectric figure-of-merit zT increases sharply at phase transitions in various materials [15, 16, 17]. In all cases, the increase in zT can be largely attributed to a drastic reduction in thermal conductivity.

a model. Usually, the temperature independent Dulong-Petit heat capacity is a good approximation (within ∼5%) near room temperature. At higher temperatures, a model that incorporates a linear temperature dependence may be appropriate [104, 88, 8].

However, an incomplete understanding of heat capacity measurements and models can lead to inaccurate estimations of κ in some systems, especially those having substantial latent heats (e.g. during phase transitions). The recent debate surrounding the thermoelectric material, Cu_2Se, is an excellent example [12, 162, 11, 16, 163, 164]. In this material, and others [17, 15, 18], the thermal diffusivity drops markedly as the material undergoes a phase transition. Depending on the heat capacity used to calculate κ, a maximum zT between 0.6 [12] to 2.3 [16] has been reported due to the superionic phase transition in Cu_2Se. As exemplified in Fig. 4.2, the choice of heat capacity can have a drastic impact on zT values.

To properly characterize the behavior of thermal conductivity through a phase transition, it is paramount to understand the concurrent behavior of heat capacity. Recognizing that the total capacity of a material to absorb heat includes both the intrinsic heat capacity

of the phases present and the enthalpy (heat) of transformation ΔH that is required to maintain equilibrium (characterized by the order parameter ϕ) as the temperature is changed,

$$\rho c_{\mathrm{p}} = \left(\frac{\partial H}{\partial T}\right)_{\mathrm{p}} = C_{\mathrm{p}\phi} + \Delta H \left(\frac{\partial \phi}{\partial T}\right)_{\mathrm{p}}. \tag{4.2}$$

Here, $C_{\mathrm{p}\phi} = (\partial H/\partial T)_{\mathrm{p},\phi}$ is the intrinsic heat capacity of the phases present. It can be approximated as the Dulong-Petit value of $3k_{\mathrm{B}}$/atom, or a temperature dependent model can be used. Note that Eq. 4.2 is essentially a generalized form of Eq. 3.5 written in a consolidated notation, a detailed description can be found in Section 3.2. The second term, which includes the enthalpy of transformation ΔH (the heat associated with a complete phase transformation) that can be estimated from an integrated peak in heat capacity measurements, is not typically considered. This is understandable as one could argue that $(\partial \phi/\partial T)_{\mathrm{p}}$ should be zero in the steady-state measurement of κ. However, we show theoretically why this term is non-zero and should be included in the calculation of κ when transformation kinetics are fast on the timescale of thermal transport. Not including the enthalpy of transformation can lead to significantly underestimated values of κ in the region of peak zT for many important cases, such as Cu_2Se, PbTe and SnSe, where exceptional $zT > 2$ has been reported.

This work examines the relevant thermodynamic definitions for the estimation of thermal conductivity from thermal diffusivity, while considering the non-equilibrium and kinetic aspects of materials during experiments. It is demonstrated that latent heat can contribute significantly to the total heat capacity in some cases, including several material systems with high reported thermoelectric performance.

4.3 Time Dependent Heat Capacity

The relation of thermal conductivity to thermal diffusivity (Eq. 4.1) comes from a derivation of the heat equation from linear non-equilibrium thermodynamics [84] (see Section 2.2.1). In this derivation, the heat capacity is obtained by applying the chain rule, and is actually a ratio of two time dependent derivatives. Explicitly,

$$\rho c_{\mathrm{p}} = \left(\frac{\partial H}{\partial T}\right)_{\mathrm{P}} = \left(\frac{\partial H}{\partial t}\right)_{\mathrm{P}} / \left(\frac{\partial T}{\partial t}\right)_{\mathrm{P}} \tag{4.3}$$

is the ratio of the time rates of change of enthalpy to temperature. Thus, the timescale of the processes is relevant. In fact, Eq. 4.2 can be written to include the time dependence

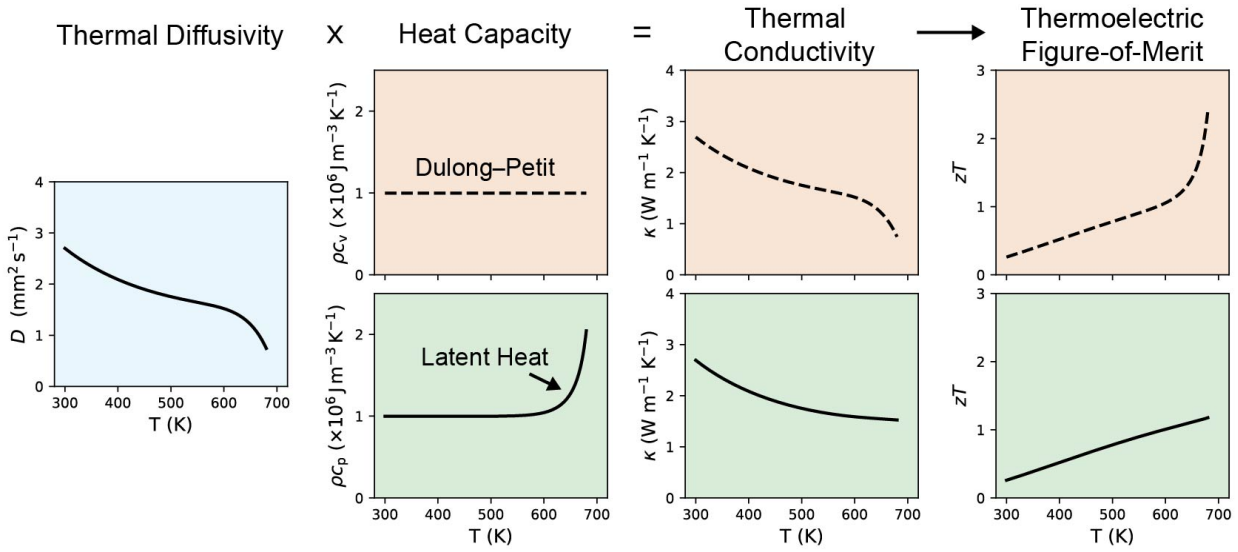

Figure 4.2: **The process of estimating thermal conductivity and thermoelectric performance.** Two possible pathways for calculating thermal conductivity κ (and zT) from thermal diffusivity D and volumetric heat capacity ρc_p are shown. One possibility (upper panels) is to use the Dulong-Petit heat capacity, i.e. $c_\mathrm{p} \approx c_\mathrm{v}$, resulting in $zT > 2$ for this hypothetical material. The other possibility (lower panels) is to include the enthalpy of transformation in the heat capacity, i.e. ρc_p according to Eq. 4.2, resulting in $zT < 2$.

as [165]

$$\rho c_\mathrm{p} = \left(\frac{\partial H}{\partial T}\right)_\mathrm{P} = C_{\mathrm{p}\phi} + \Delta H \frac{(\partial\phi/\partial t)_\mathrm{P}}{(\partial T/\partial t)_\mathrm{P}} \,, \tag{4.4}$$

in which the first term, $C_{\mathrm{p}\phi}$, depends on the instantaneous temperature $T(t)$ and the second term clearly demonstrates how the timescales of transformation and thermal transport are important to the total heat content in the material. Specifically, the transformation enthalpy contributes to the total heat capacity on timescales where changes in ϕ and T occur concurrently. When transformation kinetics are slow, i.e. $(\partial\phi/\partial t)_\mathrm{P} \to 0$, only the intrinsic heat capacity is relevant (blue region in Fig. 4.3). However, when transformation kinetics are fast, i.e. ϕ can respond "instantly" to temperature changes, additional heat is absorbed in order to maintain equilibrium (red region in Fig. 4.3). Note that advanced study of time-dependent heat capacity may benefit from a transformation of Eq. 4.4 to frequency space, but this is not necessary to support the conclusions drawn herein.

As a brief aside, $C_{\mathrm{p}\phi}$ (the "intrinisic heat capacity") includes the contributions from the atomic vibrations, electrons, etc. that determine C_V and Γ for each phase (see Eq. 3.5). These mechanisms to store heat respond "instantaneously" to temperature changes, as opposed to the transformation term in Eq. 3.5 which generally has an activation barrier

(i.e. for diffusion-mediated transformations). At high temperatures (i.e. above the Debye temperature) $C_{\mathrm{p}\phi}$ is dominated by the Dulong-Petit heat capacity and is therefore largely independent of temperature and ϕ (because $\sum \phi_i = 1$ and each phase tends to have about the same number of atoms/volume). The dilation term Γ is only a small correction, and it is often sufficient to treat it as a constant (independent of T and ϕ) using room temperature values of B and α [104]. Thus, $C_{\mathrm{p}\phi}$ has little to no dependence on $\phi(t)$ for the cases discussed herein.

Atomic rearrangement often has a slower response to changes in temperature than the atomic vibrations or electrons. Thus, the primary time dependence of heat capacity is due to the kinetics of transformation. In Eq. 4.4, however, it may not be immediately obvious what happens as $(\partial T/\partial t)_{\mathrm{P}} \to 0$. The confusion may arise because $(\partial T/\partial t)_{\mathrm{P}}$ can be interpreted both as a "heating rate" which can be set by the experimenter, but also as the temperature fluctuations when the macroscale temperature is constant. By the fluctuation-dissipation theorem these two interpretations are linked, and may be best considered by a spectral analysis.

Nevertheless, to identify systems where latent heat may be expected to contribute to the total heat capacity, the characteristic time of atomic rearrangement at a given temperature can be compared to the characteristic time of thermal transport (Fig. 4.3). Using the atomic diffusion coefficient, D_a [m^2 s^{-1}], and the number density of atomic sites, n [m^{-3}], the characteristic time of atomic rearrangement is defined here as $t_a = D_a^{-1} n^{-2/3}$. Some examples are shown in Fig. 4.3 (values given in Appendix C). Many engineering materials, including good thermoelectric systems, can exhibit t_{a} values of similar magnitude to phonon relaxation times.

4.4 Impact of Heat Capacity on Thermal Diffusivity

In many instances, phase transformations in a material occur so slowly that they do not contribute significantly to the total enthalpy and so it is appropriate to use $\rho c_{\mathrm{p}} = C_{\mathrm{p}\phi}$. Steel at room temperature is one example (Fig. 4.3). Like many structural metals, steel is a complex mixture of phases where the microstructure and even some of the phases present are metastable. Under conditions where transformations do not occur $(\partial \phi/\partial T)_{\mathrm{P}} = 0$. Thus, these materials only have a capacity to store and conduct heat according to their available vibrational and electronic degrees of freedom. This is to say that heat capacity and thermal transport are facilitated by the same mechanisms.

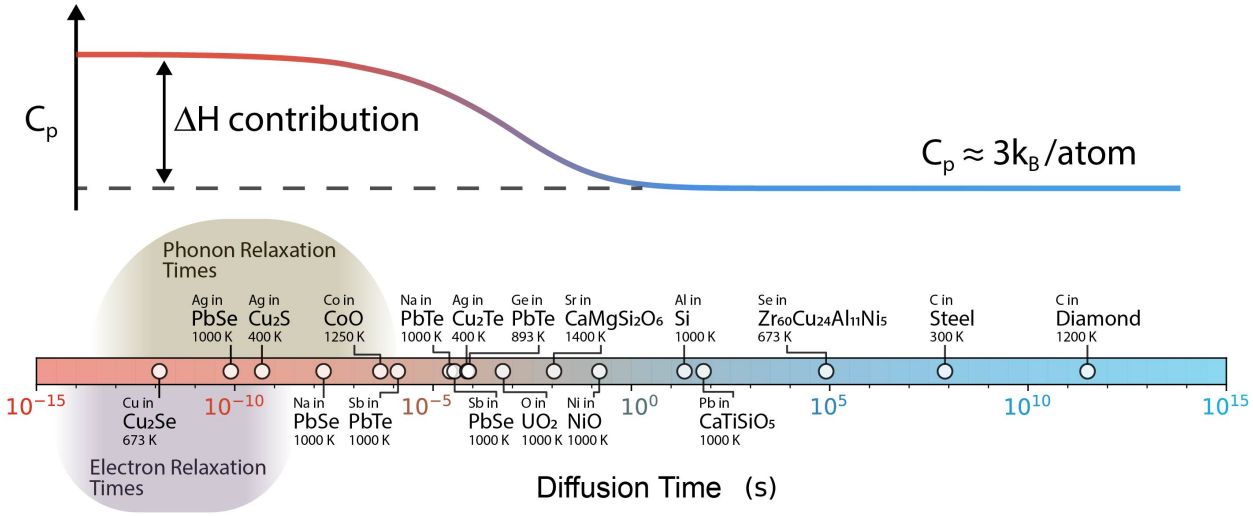

Figure 4.3: **Characteristic time scale for thermal and atomic diffusion and its effect on heat capacity.** When a phase transformation occurs so slowly it is effectively frozen (blue region) the phase transformation enthalpy (ΔH) need not be considered and the total heat capacity at high temperature is approximately the Dulong-Petit value of $3k_{\mathrm{B}}$/atom ("$C_{\mathrm{P}} \approx 3k_{\mathrm{B}}$/atom" in figure). When the atomic motion that facilitates such transformations occurs as fast as the relaxation time of the heat carrying phonons or electrons, the phase transformation enthalpy (ΔH) contributes to the total heat capacity ("ΔH contribution" in figure). In between these extremes the extent of the (ΔH contribution depends on the time dependent characteristics of the material property of interest and its measurement. Plotted values are described in Table C.1

This is not true, however, in systems with phase transformations having "fast" kinetics. Besides the heat capacity due to the mechanisms responsible for thermal transport (nominally $C_{\mathrm{p}\phi}$), there is simultaneously an additional heat capacity due to the dynamic transformation of ϕ (i.e. atomic rearrangement). The consequence of this additional heat capacity on measurement values is often overlooked. In particular, measurements of thermal diffusivity have been prone to misinterpretation because the total heat capacity is not often used in Eq. 4.1. In fact, the kinetic timescale of ϕ can also give rise to a time-dependent thermal diffusivity (substitute Eq. 4.4 in Eq. 4.1). For "instantaneous" transformations,

$$D = \frac{\kappa}{C_{\mathrm{p}\ \phi} + \Delta H\ \ (\partial\phi/\partial T)_{\mathrm{P}}}\ , \tag{4.5}$$

which clearly shows that experimentally measured thermal diffusivity, D, is expected to decrease when $(\partial\phi/\partial T)_{\mathrm{P}}$ is non-zero, independent of the behavior of κ. Thus, the interplay of heat capacity and thermal diffusivity, particularly near phase transitions, should be considered before changes in thermal conductivity can be attributed to structural, compositional or nano/microstructural features.

Undeniably, a sharp decrease in D is observed in phase transformation regions, followed by a step-wise increase above the maximum phase transition temperature (Fig. 4.4a). This does not mean that κ mimics the behavior of D. On the contrary, it is more likely that κ changes smoothly (or remains fairly constant) through the phase transition, and that the behavior of D is primarily due to changes in heat capacity.

This is well-demonstrated in Zn_4Sb_3, which undergoes an $\alpha/\alpha\prime \rightarrow \beta$ phase transition around 250 K [113]. Because the phase transition occurs below room temperature, steady-state measurements of κ are accessible and reliable. Careful measurements of κ and c_p across the phase transition have been previously reported [9, 20, 113, 19], which show a smooth change in κ even though a peak is observed in c_p (Fig. 4.4b and 4.5). From Eq. 4.5, it is expected that there should be a corresponding decrease in D due to the excess heat capacity. Indeed, low temperature thermal diffusivity measurements performed in this study confirm this hypothesis (Fig. 4.4b). Conversely, κ would be significantly underestimated through the phase transition if only $C_{p\phi}$ was used in Eq. 4.1 (dashed black line in top panel of Fig. 4.4b). Note that the behavior of κ, c_p and D in Zn_4Sb_3 are in qualitative agreement with complex measurements at the glass transition temperature of glycerol, which show strong frequency dependence of heat capacity and thermal diffusivity but constant thermal conductivity [166].

4.5 Comment on Zinc Antimonide

An important aspect of this work is that conclusions about the behavior of thermal conductivity can only be made after the effects of the total heat capacity on thermal properties measurements are considered. In particular, there is an explicit dependence of thermal diffusivity on the total heat capacity (Eq. 4.5). Thus, the observation of a peak in total heat capacity corresponds to a dip in thermal diffusivity for Zn_4Sb_3 around 250 K (Fig. 4.4b). Steady state measurements of κ show a smooth change across the phase transition region, and have no peak or valley, regardless of the absolute magnitude (Fig. 4.5). However, if the thermal conductivity is estimated as $\kappa = C_{p\phi}D$, ignoring the peak in the total heat capacity, then the behavior of κ through the phase transition would be misconstrued as having a valley (dashed black line in Fig. 4.5).

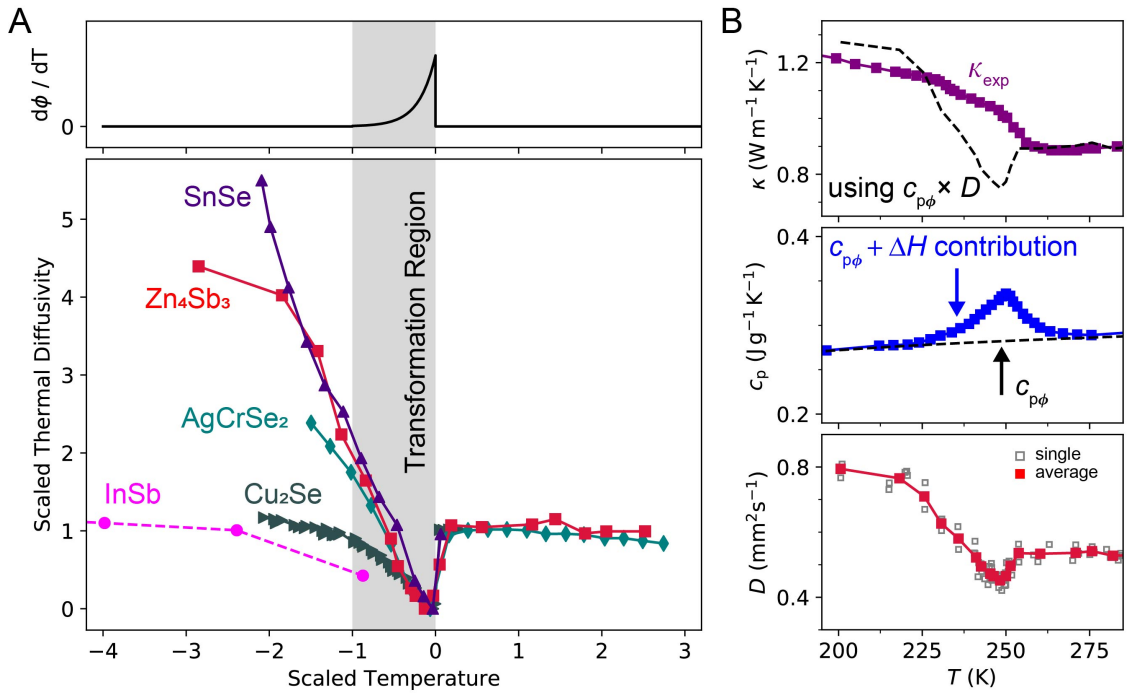

Figure 4.4: **Effect of heat capacity on thermal diffusivity through phase transformation regions.** Demonstration of the sharp decrease in thermal diffusivity for (a) InSb [15], Cu_2Se [12], $AgCrSe_2$ [18], SnSe [17], and Zn_4Sb_3 (this study) having temperature dependent phase transformations, i.e. $d\phi/dT \neq 0$; as well as, (b) the exemplary case of Zn_4Sb_3 which has a smooth change in thermal conductivity κ (measured using a steady-state method [19]), while a peak is observed in the heat capacity c_p [9] and a decrease is observed in thermal diffusivity D through the phase transition. The use of $c_{p\phi}$ and the experimental D results in an underestimation of κ through the phase transition. Further comparison with experimental κ of Zn_4Sb_3 is given in Fig. 4.5. The scaling used in panel a is discussed in Appendix D

4.6 Partial Melting of Indium Antimonide

Because of this impact from latent heat on heat capacity, thermal diffusivity measurements are affected and, can thereby lead to an overestimation of zT (Fig. 4.2). For example, InSb was reported to more than double its thermoelectric performance and achieve $zT > 1$ when in equilibrium with liquid Sb [15] (Fig. 4.6). However, the study used the Dulong-Petit value ($C_{p\phi}$) for the heat capacity to estimate thermal conductivity κ using Eq. 4.1 and the measured thermal diffusivity. Consequently, a negative (unphysical) value for the "lattice" thermal conductivity κ_L (obtained by subtracting the electronic contribution to thermal conductivity using the Wiedemann-Franz law [90], see Eq. 2.31) was calculated at 775 K (i.e. in the two-phase region).

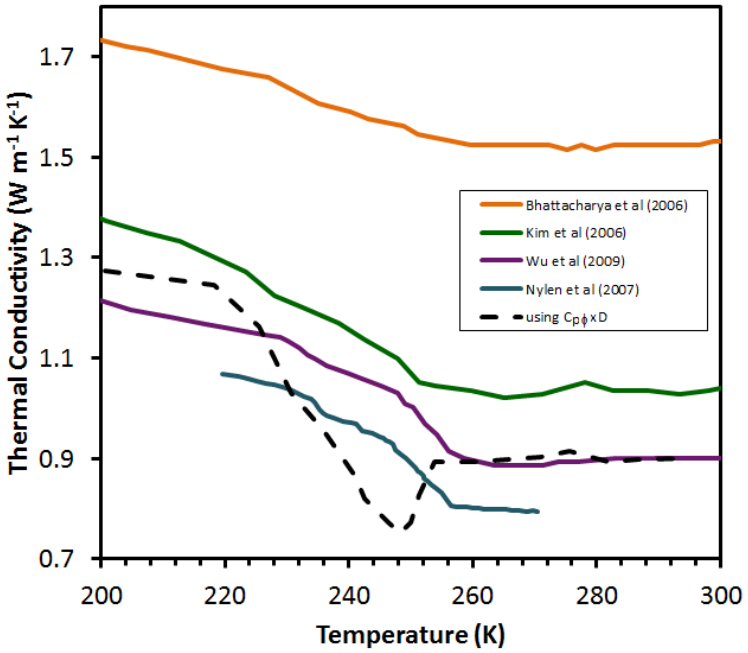

Figure 4.5: **Characterization of thermal conductivity through the phase transition of zinc antimonide.** Thermal conductivity of Zn_4Sb_3 measured by steady-state methods [9, 20, 21, 19] (solid curves) showing a smooth change in κ through the phase transition, with no peak or valley, unlike the thermal conductivity estimated from thermal diffusivity which ignores the transformation contribution to the total heat capacity, i.e. $C_{p\phi}D$, which leads to the incorrect conclusion that κ has a sharp drop through the phase transition (dashed black line).

The proposed method to improve the thermoelectric performance of InSb at high temperature was to melt an InSb−Sb eutectic secondary phase [15]. Indeed, above the eutectic temperature (∼765 K), a sharp drop in thermal diffusivity was observed. Using the Dulong-Petit value of heat capacity, the researchers concluded that the thermal conductivity dropped sharply as well, resulting in a 3× improvement in zT at 775 K. In calculating the lattice thermal conductivity negative values were obtained, and it was suggested that the Lorenz number may be the cause. However, a significant latent heat contribution to the heat capacity was overlooked by assuming the Dulong-Petit value. From the In-Sb phase diagram [22] (Fig. 4.7a), the equilibrium phase fraction and corresponding $\left(\partial\phi_{\text{Liquid}}/\partial T\right)_{\text{p}}$ at 775 K can be estimated for the sample with nominal composition $InSb_{1.04}$ (black point in Fig. 4.7). Using $\left(\partial\phi_{\text{Liquid}}/\partial T\right)_{\text{p}} = 1.4 \times 10^{-3}\ \text{K}^{-1}$ calculated from the phase diagram and the reported enthalpy of transformation (solid→liquid) $\Delta H^{s\to L} = 22$ kJ mol^{-1} [22], the latent heat contribution to the heat capacity can be estimated as ∼30 J mol^{-1}K^{-1}. The Dulong-Petit value is ∼50 J mol^{-1}K^{-1}. Thus, a more realistic total heat capacity at 775 K is at least 80 J mol^{-1}K^{-1}. A value of ∼110 J mol^{-1}K^{-1} would produce

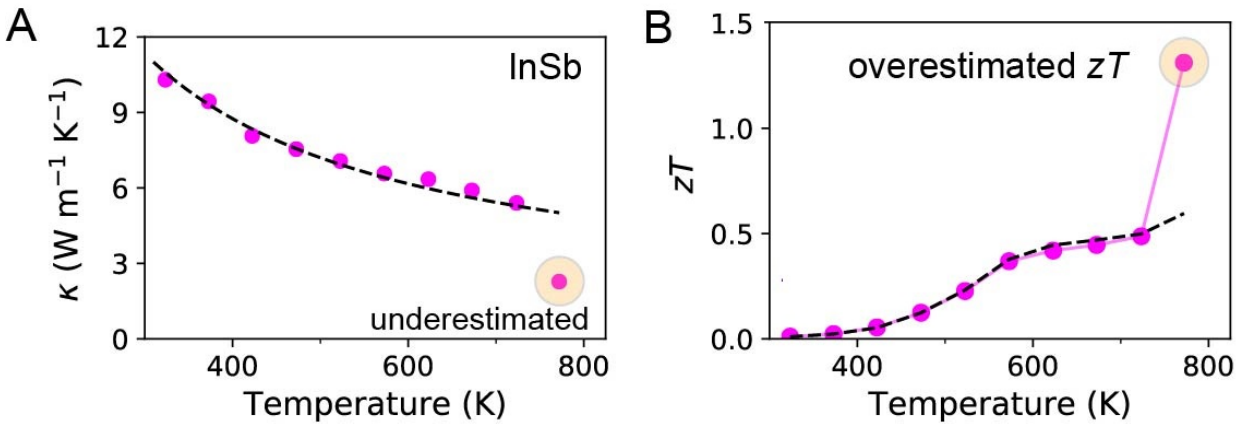

Figure 4.6: **Estimated thermal conductivity and thermoelectric figure-of merit zT of indium antimonide sample.**

the value of κ given by the trend line in Fig. 4.10a, which is reasonable given the estimation of $C_{\mathrm{p}\phi}$ as the Dulong-Petit value and the estimation of $\left(\partial\phi_{\mathrm{Liquid}}/\partial T\right)_{\mathrm{p}}$ from the phase diagram. These estimates of the total heat capacity lead to a positive value for the lattice thermal conductivity of the $\mathrm{InSb}_{1.04}$ material at 775 K, assessed here to be at least 0.8 W $\mathrm{m}^{-1}\mathrm{K}^{-1}$.

Thus, including the ΔH contribution to the total heat capacity, which can be estimated using the In-Sb phase diagram, gives a positive value for κ_{L} and a reasonable value for the total heat capacity at 775 K that is ~2.2 times the Dulong-Petit value gives the trend-line value for κ shown in Fig. 3.2a. This analysis is highly suggestive that the thermal conductivity of bulk InSb is not changing much in the presence of the liquid eutectic phase, such that partial melting is not suggested as a strategy for improving the high temperature efficiency of thermoelectric materials.

4.7 Beware of *T*-dependent Solubility

Dynamic doping, which relies on the temperature dependent solubility of a dopant atom to change the carrier concentration of a semiconductor with temperature, is a particular example where the transformation heat capacity should not be forgotten. In such a system the main semiconducting phase must be in equilibrium with a second phase containing the dopant.

The dynamic doping of PbTe by copper [23] or silver [115] has been reported to lead to high thermoelectric efficiency. However, negative values for κ_{L} would have been obtained

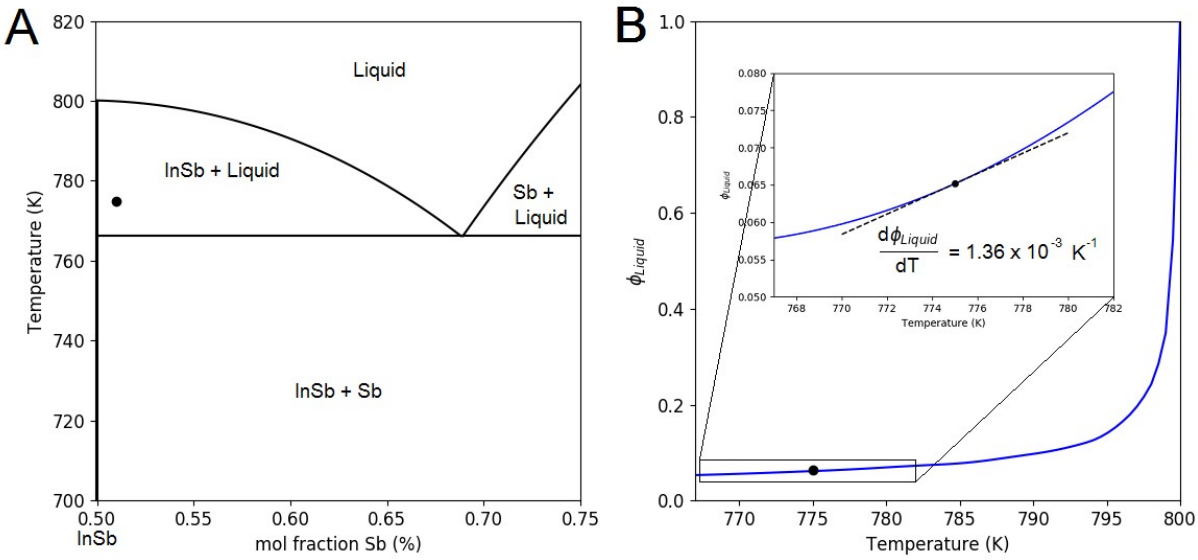

Figure 4.7: **Phase diagram and analysis of partial melting in indium antimonide.** Section of the In-Sb phase diagram [22] showing the InSb-Sb eutectic region (a) and the nominal $InSb_{1.04}$ composition at 775 K, as well as, (b) the temperature dependent equilibrium phase fraction of liquid for the $InSb_{1.04}$ composition in the InSb + liquid region of the phase diagram.

in the case of Cu-doped PbTe if experimental values of c_p (which are ~30% larger than pure PbTe at 600 K) had not been used in Eq. 4.1 (Fig. 4.8).

Again, this points to the drastic impact that temperature dependent solubility can have on heat capacity (Eq. 4.2) and, *ipso facto*, on measurements of thermal diffusivity (Eq. 4.5). In systems where precipitates are found at room temperature, e.g. sodium [125] and silver [115, 167] doped PbTe, heat capacity effects may be present at higher temperatures.

4.8 Settling the Copper Selenide Controversy

Past experience with Cu_2Se, and confirmed here with Zn_4Sb_3, demonstrates that even nominally single-phase materials can show a pronounced effect in thermal diffusivity that can lead to overestimates of zT. It is common for studies on thermoelectric materials to use the Dulong-Petit (or $C_{p\phi}$) value and measured diffusivity throughout the entire temperature range [88]. Although this may at first seem reasonable, a real compound semiconductor will have a small multiple-phase region (two or more phases in equilibrium) near the transition that will lead to $(\partial\phi/\partial T)_P \neq 0$ over a finite temperature range, as has been demonstrated for Cu_2Se [168, 11] and can be expected for Zn_4Sb_3 [113] and

SnSe [169].

Using Dulong-Petit, zT values greater than 2 can be estimated in Cu_2Se [16], as discussed by Brown et al. [12]. Later, measurements of thermal effusivity [170] and thermal conductivity directly [163], as well as a detailed analysis aiming to remove transformation effects from thermal properties measurements [162], confirm that the actual thermal conductivity and its impact on zT are much less affected than one would expect using Dulong-Petit. The generalized methodology for interpreting and modeling heat capacity and thermal diffusivity measurements presented here also indicates that the phase transition has little impact on zT or thermal conductivity in Cu_2Se.

Specifically, by making use of the heat capacity analysis presented in Section 3.7 it is possible to determine the corresponding impact on thermal diffusivity measurements. However, this requires an assumption about the temperature behavior of thermal conductivity. Since the temperature range is fairly narrow, and the thermal conductivity is fairly constant on either side of the phase transition (not the typical $1/T$ behavior expected for phonons), then a constant thermal conductivity through the phase transition is a reasonable first approximation. The expectation being that, if a drastic reduction in thermal conductivity is occurring, this analysis would show that.

Thus, when a constant thermal conductivity is assumed through the $\alpha \rightarrow \beta$ phase transition, the corresponding thermal diffusivity ($D = \kappa/\rho c_{\mathrm{p}}$, black line in bottom panel of Fig. 4.9) can be calculated from the model c_{p} (black line in top panel of Fig. 3.9c). The calculated D is expectedly similar to that measured experimentally. This analysis is highly suggestive that the thermal conductivity is not changing much (if at all) through the phase transition, in agreement with [170]. In any case, using only the Dulong-Petit value for heat capacity through the superionic phase transition of $Cu_{2-\mathrm{d}}Se$ would obviously result in an underestimated value of κ and erroneous high zT.

The new measurements reported herein for Zn_4Sb_3 corroborate the findings in Cu_2Se that thermal diffusivity is affected by the phase transition (Fig. 4.4), whereas thermal conductivity has a negligible impact on zT throughout the transformation region. The surprisingly small impact on zT and success of the generalized model with Zn_4Sb_3 suggests there might be other materials or materials systems with similar effects on thermal diffusivity and overestimated zT when Dulong-Petit is used throughout a phase transformation.

4.9 Sad News for Tin Selenide

Remarkable zT values, approaching and even exceeding 2, reported in SnSe [17, 171, 172, 173, 174, 175, 24, 176] coincide with a phase transition and are likely overestimated because of underestimated heat capacity (Fig. 4.10). The $\alpha \rightarrow \beta$ phase transition and other solubility effects are indicated in other recent studies of SnSe [177, 178, 179, 180, 181] and SnS [182, 183, 184]. Since the reported thermal conductivity increases and zT decreases after the phase transition, there is a good indication that thermal diffusivity is reduced by the total heat capacity through the phase transformation region (illustrated in Fig. 4.4a). Calorimetry measurements of SnSe materials (Fig. 4.11) show a peak in heat capacity through the phase transition [185, 26, 186, 187], which is expected since X-ray diffraction results [17, 186] indicate that $(\partial\phi/\partial T)_{\mathrm{P}} \neq 0$ in Eq. 4.2. The peak in the total heat capacity reported from calorimetry is $\sim$1.5 times the Dulong-Petit value, which can explain the difference between the reported κ and the trend-line in Fig. 4.10a.

Measurements of heat capacity obtained by the laser flash method used in ref. [17] did not show a peak, only a nearly constant value close to that of Dulong-Petit. This is likely due to the difficulties in measuring heat capacity by the laser flash method, particularly near phase transitions [188]. In addition to the effect on thermal diffusivity, a multi-phase transformation in a compound semiconductor can lead to changes in intrinsic defect concentrations, like in dynamic doping, which alter the Seebeck coefficient and electrical conductivity, as was also found in Cu_2Se [11].

Calorimetry results of SnSe consistently show a peak in heat capacity through the phase transition at around 800 K [189, 185, 25, 190, 26, 186, 191, 187], with some transitions sharper than others (Fig. 4.11). Further comparison is given in ref. [185]. A peak in heat capacity is expected (in accordance with Eq. 4.2) because there is a reported heat of transformation ΔH of $\sim$1–2 kJ mol^{-1} [189, 191] and a reported two-phase region (i.e. $d\phi/dT \neq 0$) [169].

The heat capacities reported in refs. [17, 24, 176] are all indirectly derived using the laser flash diffusivity instrument and a representative sample (e.g. Pyroceram standard). The result of their experimental methodology is a nearly constant value of heat capacity that resembles the Dulong-Petit value over the entire investigated temperature range. Note that while the thermal diffusivity values reported in ref. [17] were validated by Netzsch, the heat capacity values were not. Typically, the laser flash method to determine heat capacity is accurate within $\sim$8% [192], but difficulties in obtaining reliable values near phase transitions have been discussed [192, 188]. Furthermore, ASTM Standard E1461

for determining thermal diffusivity by the flash method warns against using the method to determine the heat capacity of inhomogeneous systems, including materials with high anisotropy. Nevertheless, heat capacity peaks corresponding to phase transitions have been characterized by laser flash using detailed methods [193, 188].

Given the totality of calorimetry observations which indicate a peak in heat capacity, the X-ray diffraction results [17, 186] that confirm $d\phi/dT \neq 0$ and the careful methods required to obtain reliable heat capacity values from laser flash instruments, it is highly likely that the heat capacity reported in refs. [17, 24, 176] is underestimated through the phase transformation region. Unfortunately, this results in a direct underestimation of thermal conductivity through the phase transition and corresponding overestimation of zT. Thus, while SnSe is still a high performing thermoelectric material (with $zT \sim 2$) it may not have the ground breaking efficiency (zT approaching 3) that was first reported.

4.10 Conclusions

In general, the examples presented herein suggest that thermal conductivity changes smoothly through phase transformations while thermal diffusivity can be greatly affected by the phase transformation enthalpy contribution to the heat capacity. Thus, even though these are steady-state materials properties where no net phase transformation may be taking place, microscale atomic fluctuations taking place at timescales of heat fluctuations give rise to an increase in the heat capacity that decreases the thermal diffusivity but has little effect on the thermal conductivity. This applies even to nominally isothermal transformations in single component systems, such as the HCP→BCC phase transition of zirconium at 1140 K [194].

Although this work gives guidance for how to interpret thermal diffusivity measurements by considering heat capacity effects, it still may not be an easy task to accurately estimate thermal conductivity. This is because accurate measurements of high temperature heat capacity are notoriously difficult with systemic errors and the generalized heat capacity model described herein requires accurate thermodynamic and kinetic information. Consequently, experimental reports of thermal conductivity in complex material systems should clearly state what heat capacity is used (e.g. the Dulong-Petit value) and indicate potential impacts of latent heat on the reported values, rather than using routine specific heat measurements that may be flawed.

Accurate evaluations of thermal conductivity from thermal diffusivity must utilize the total heat capacity contained by the solid on timescales of thermal transport. When it

contributes, the heat capacity contribution from the heat of transformation can be predicted using a generalized model and the equilibrium phase diagram. Although thermal diffusivity is suppressed, the effect of latent heat on thermal conductivity was found to be negligibly small, such that the thermal conductivity changes smoothly through phase transformations.

In many good thermoelectric materials at their operation temperatures, atomic rearrangement may be fast enough that latent heats will suppress the thermal diffusivity. An apparent increase in zT will result if a heat capacity is used that does not account for the latent heats. In particular, any discontinuity, spike, or sharp decrease that is found in thermal diffusivity measurements should be scrutinized before the same features are ascribed to the thermal conductivity. Even estimated values of lattice thermal conductivity κ_{L} which are substantially below estimates for the lower limit of thermal conductivity [195, 41] should be scrutinized (such as in Cu_3SbSe_3 [196]) as they may indicate that κ is underestimated, as was found in cases of dynamic doping. Substantial underestimates of κ and overestimates of zT, as demonstrated in Cu_2Se, are likely prevalent in other systems such as SnSe.

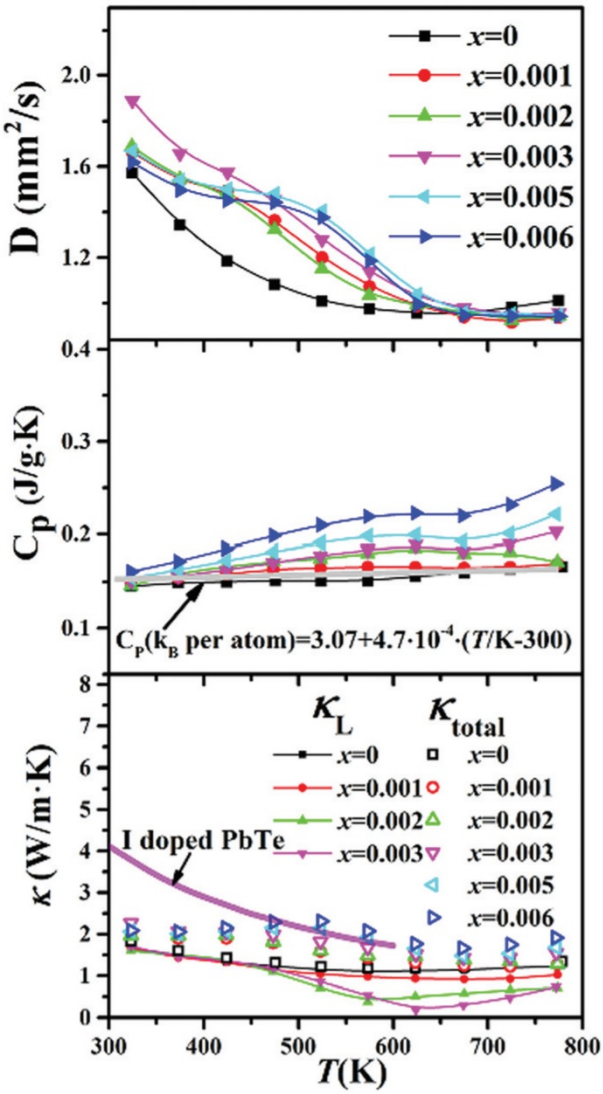

Figure 4.8: **Impact of dynamic doping of copper in lead telluride on thermal properties.** The subsequent rise in heat capacity with increasing Cu content is consistent with increased latent heat effects described by Fig. 4.3. The relevant phase diagram is characterized in ref. [23]. Here, it is important to recognize the behavior in thermal diffusivity as abnormal, particularly in the higher doped material, and suspect that heat capacity effects may be at play (possibly beyond the extent that the heat capacity measurements suggest).

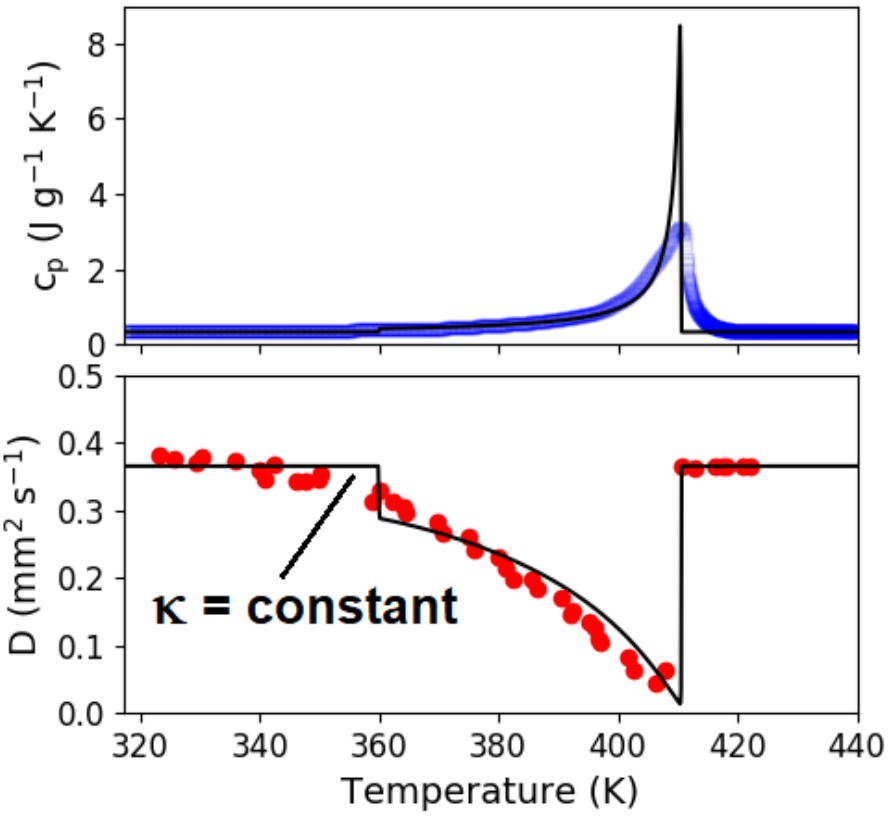

Figure 4.9: **Heat capacity effect on thermal diffusivity in copper selenide.** Using the model of heat capacity for Cu_2Se through the phase transition (black curve top panel) it is possible to model the thermal diffusivity (black curve bottom panel) and compare with the experimental thermal diffusivity determined by the laser flash method [12] (red points in bottom panel). In the thermal diffusivity model, the thermal conductivity κ is assumed to remain constant throughout the phase transition ("κ= constant" in figure), such that the entire temperature effect is attributed to the total heat capacity. The close agreement of the model thermal diffusivity to the experimental measurements is a strong indication that thermal conductivity is not changing much (if at all) through the phase transition.

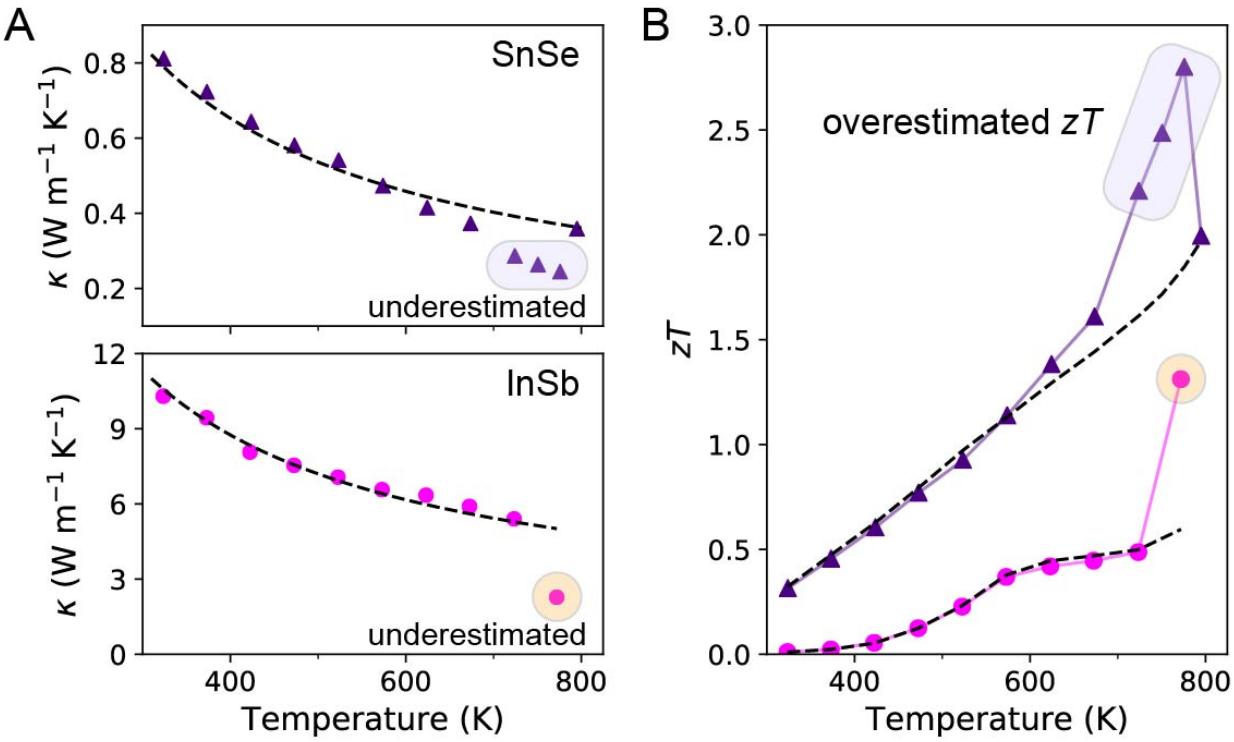

Figure 4.10: **Drastic impact of using a constant heat capacity in a temperature regime having a phase transition.** (a) The total thermal conductivity for SnSe [17] (purple triangles, top panel) and InSb [15] (pink circles, bottom panel), appears to be underestimated as compared with the dashed lines that illustrate typical $\kappa \propto T^{-1}$ behavior; as well as, (b) the thermoelectric figure of merit for SnSe [17] (purple triangles) and InSb [15] (pink circles), which is likely overestimated as compared with the dashed lines that illustrate zT if the thermal conductivity behaved as illustrated in panel a.

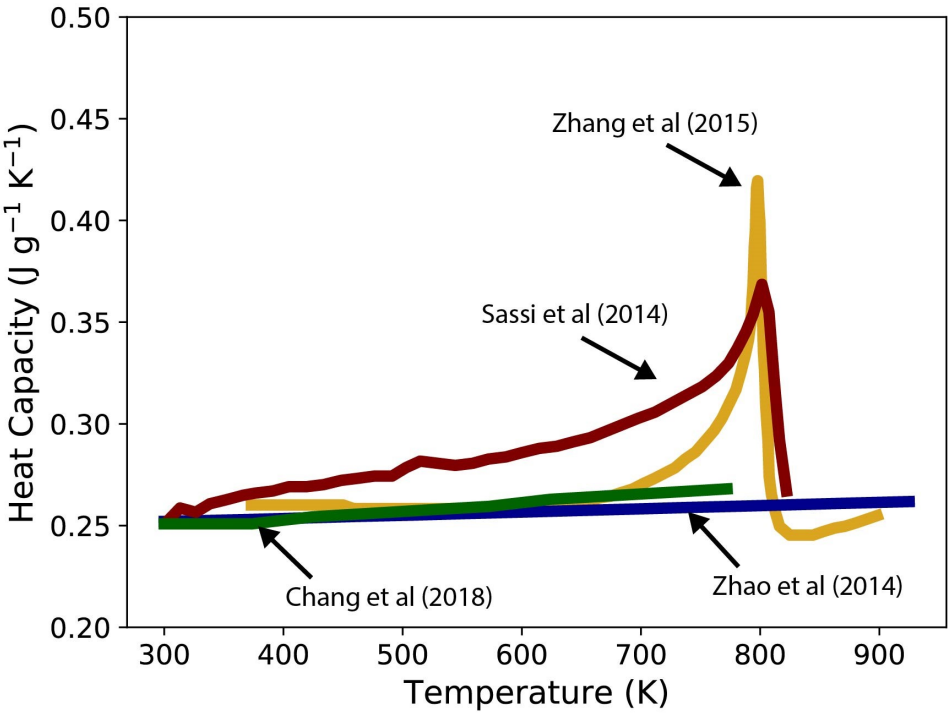

Figure 4.11: **The high temperature heat capacity of tin selenide.** Comparison between the linear estimates of heat capacity [17, 24] and calorimetry results that have a peak through the phase transition of SnSe [25, 26]. The magnitude of the peak in C_{P} can explain the deviation of estimated thermal conductivity from the trend line shown in Fig. 4.10.

Chapter 5

Inherent Anharmonicity of Harmonic Solids

5.1 Overview

Since the groundbreaking realization that atomic vibrations account for most of the capacity of a solid to store heat [197, 198], so-called "lattice dynamics" has given rise to foundational theories of the thermal behaviors of materials [199, 200, 201, 202, 203]. The frequencies and polarizations of these vibrations (i.e. phonons) are governed by the complex bonding between atoms, which is physically represented by a spring-mass model that can account for interactions (spring forces) between the atoms (masses) [199]. The lowest order "harmonic" approximation only considers linear forces between atoms and is thought incapable of explaining phenomena like thermal expansion and thermal conductivity [204], which are attributed to non-linear (anharmonic) interactions. It is tacitly assumed that the harmonic and anharmonic properties are entirely independent – even though no real material is found with very little anharmonicity. Here we show that harmonic vibrational pressure relates thermodynamically to thermal expansion and thus the Grüneisen parameter γ, a metric of anharmonicity. We derive a model of thermal expansion in solids where this vibrational or phonon pressure is balanced by the elastic pressure due to strain in the material (analogous to an elastic balloon membrane balancing the pressure of a gas). This model captures the magnitude and temperature dependence of thermal expansion in real solids and provides an estimation of γ that is comparable to values obtained using quantum mechanical methods. Furthermore, chemical intuition that γ should trend with bond type and atomic coordination [205, 206] is physically justified using a simplified analytical model. Our results indicate that harmonic and anharmonic interactions in solids are inherently linked. We anticipate that this model of phonon pressure can be used as a starting point for more sophisticated analysis and

may be useful in understanding other complicated material phenomena such as thermal transport in complex materials [207, 92, 93] and the nature of ionic transport in solid-state Li-ion battery materials [97]. Furthermore, this study provides a pathway for high-throughput screening of anharmonicity for computational materials design.

5.2 Thermodynamic Beginnings for Thermal Expansion Models

The spring-mass model of atomic bonding has been an indispensable tool, providing a clear conceptual link between classical and quantum mechanics [199]. In this model, the complicated interactions between atoms (masses) are attributed to spring-like forces. Specifically, the key aspects of bonding are described by an n-degree Taylor expansion of the interatomic potential about the equilibrium position of the atoms. Then the total potential energy of the material can be written in terms of the displacement u of atoms α, β, etc. from their equilibrium positions in cartesian coordinates (indexed by i,j,k) as [208]

$$U = U_0 + \sum_{\alpha}\sum_{i}\left(-f_i^{\alpha}\right)u_i^{\alpha} + \frac{1}{2!}\sum_{\alpha,\beta}\sum_{i,j} C_{ij}^{\alpha\beta}\; u_i^{\alpha}u_j^{\beta} + \frac{1}{3!}\sum_{\alpha,\beta,\gamma}\sum_{i,j,k} C_{ijk}^{\alpha\beta\gamma}\; u_i^{\alpha}u_j^{\beta}u_k^{\gamma} + \ldots . \tag{5.1}$$

Here, U_0 accounts for any initial potential energy already contained by the bonds (springs) at equilibrium and the linear term ($-f_i^{\alpha} = (\partial U/\partial u_i^{\alpha})_{u_i^{\alpha}=0}$) is zero since there is no net force on any atom at equilibrium (by definition). The "harmonic" term (with force constants $C_{ij}^{\alpha\beta}$) is the lowest order term that describes changes in the potential energy when an atom is displaced from its equilibrium position and can be used to obtain the fundamental frequencies of vibration (i.e. phonon eigenmodes). Cubic (i.e. $C_{ijk}^{\alpha\beta\gamma}$) and higher order "anharmonic" terms account for non-linear forces between atoms. Implicitly, each term (U_0, f, C and u) in Eq. 5.1 is temperature dependent since the force constants and equilibrium positions of the atoms can change with temperature.

The generality of Eq. 5.1 has made it the starting point for theoretical and computational assessments of diverse material behaviors [199, 208, 209]. But, it becomes computationally expensive to consider both higher order terms in atomic displacement and the temperature dependence of the potential. The thermodynamic Maxwell relation, however, between entropy S, pressure P, volume V and temperature T,

$$(\partial S/\partial V)_{\mathrm{T}} = (\partial P/\partial T)_{\mathrm{V}}\,, \tag{5.2}$$

subsequently shows that isothermal material properties can be related to temperature dependent properties (the subscripts indicate which variable is held constant). It is not surprising then that a description of thermal expansion (i.e. the quasi-harmonic model [210]) can be obtained using the Taylor expansion (Eq. 5.1) at 0 K, since $(\partial P/\partial T)_{\mathrm{V}}$ is directly related to the bulk modulus B and thermal expansion coefficient $\alpha = (\partial \ln V/\partial T)_{\mathrm{P}}$ as

$$(\partial P/\partial T)_{\mathrm{V}} = -(\partial P/\partial \ln V)_{\mathrm{T}} (\partial \ln V/\partial T)_{\mathrm{P}} = B\alpha. \tag{5.3}$$

In the quasi-harmonic approximation, the change in vibrational entropy with volume is attributed to changes in phonon frequencies ω_i with volume, i.e.

$$(\partial S/\partial V)_{\mathrm{T}} = \sum_i (\partial S/\partial \omega_i)_{\mathrm{T}} (\partial \omega_i/\partial V)_{\mathrm{T}} \, . \tag{5.4}$$

From this perspective (e.g. Fig. 5.1) anharmonic terms are necessary in Eq. 5.1 for $(\partial \omega_i/\partial V)_{\mathrm{T}} \neq 0$ [211], leading to the conclusion that harmonic solids cannot have thermal expansion.

Utilizing the phonon entropy (e.g. the quasi-harmonic approximation) however, is but one approach to modeling the physics of anharmonicity (Fig. 5.1). Alternatively, a mechanistic description of the pressure in solids could be used. This is easily done for an ideal gas but has not been considered for solids. The pressure exerted by an ideal gas is due to its kinetic energy. Atoms in a solid have the same form of kinetic energy as an ideal gas and should therefore have a similar pressure. Importantly, the kinetic energy of atoms inside a solid will change with temperature with or without any change in the vibrational frequencies. This is to say that a mechanical model of pressure in solids would not necessarily require anharmonic terms to be included in the potential.

Herein, we provide an intuitive (mechanical) understanding of thermal expansion that also suggests an inherent connection between harmonic and anharmonic aspects of bonding in real solids. The specific nature of thermal expansion, thermal conductivity, and other "anharmonic" material properties is at the forefront of solid-state materials research [212], as are methods to predict/calculate these properties en masse [213, 214]. Consequently, a mechanistic understanding of vibrational pressure in solids has broad implications for materials engineering and high-throughput screening of diverse material phenomena, such as negative thermal expansion, ultralow thermal conductivity and superconductivity.

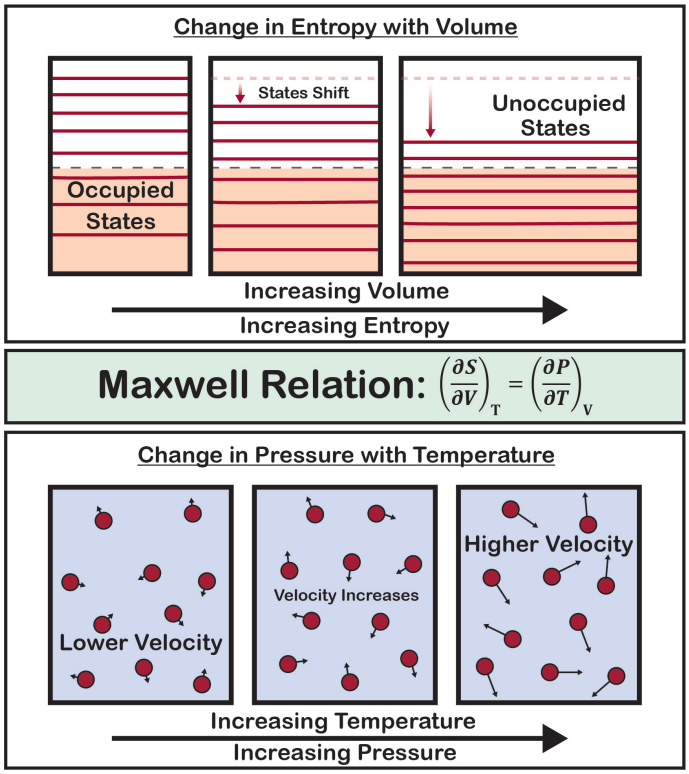

Figure 5.1: **Two different paths to understanding thermal expansion.** While thermodynamically equivalent (Eq. 5.2), the current explanation of thermal expansion is through the perspective that vibrational modes shift as the volume changes (top panel). In this picture, anharmonicity is required for vibrational states to shift. Alternatively, the change in pressure due to changes in temperature can be considered (bottom panel), as is often done for gases. Pressure is related to the kinetic energy (velocity) of the atoms and anharmonicity is not required in the lowest order description of atomic movement in solids.

5.3 Phonon Pressure in Solids

It is well-known that an ideal gas at volume V exerts a pressure P (force/area) that is proportional to its average internal energy, $PV = 2E/3$. When combined with the equipartition theorem ($E \sim k_B T$), this relation gives the microscopic origin of the ideal gas law, $PV = NRT$. In general, pressures arise as a result of the confinement of kinetic energy. Consequently, diverse physical systems from ideal gases to laser beams [215] and ultrasound acoustic waves [216] all produce pressures that are proportional to their kinetic energy density. Each of these pressures can be determined by considering the flux of linear momentum (i.e. kinetic energy) through an arbitrary plane representing a confining surface (Fig. 5.2a). In the realistic case where the kinetic particles are actually

confined by an elastic medium, there is an associated pressure (stress) provided by the medium as it deforms (i.e. strain $\neq 0$) in response to interacting with the particles.

For the same reasons, the kinetic energy of atomic vibrations gives rise to pressures in solids that can be thought of as phonon pressure. In fact, analogous to the ideal gas pressure, this phonon pressure is temperature dependent due to the change in kinetic energy with temperature. Thus, even for a harmonic solid, there is a pressure that can mechanistically facilitate thermal expansion (see Methods). For the sum of forces inside the solid to be zero at equilibrium (e.g. the linear term f_i^α in Eq. 5.1), the force exerted by the atomic vibrations must be compensated by an elastic restoring force that is proportional to the change in the equilibrium position. This is essentially the same physics that describes an elastic balloon filled with an ideal gas.

To illustrate, consider a gas kept at a finite pressure in equilibrium with an elastic environment as a filled balloon. The elastic response of the balloon is characterized by the bulk modulus B, it has a total pressure at volume V that can be related as

$$P_{\text{total}} = P_{\text{kinetic}} + P_{\text{elastic}} = \frac{NRT}{V} - \frac{B\left(V - V_0\right)}{V} = 0. \tag{5.5}$$

The volume that satisfies this equilibrium condition is $(V - V_0) = NRT/B$, which increases linearly with temperature. In other words, the thermal expansion coefficient is expected to be approximately constant (temperature independent). This is known to be the case according to Charles' law (i.e. at constant pressure) and is confirmed here for the case of elastic pressure (Fig. 5.2b). The volume of solids is also linearly proportional to temperature (Fig. 5.2c) when the kinetic energy of atomic vibrations increases linearly with temperature (i.e. at high temperature).

The expansion of a balloon with temperature is the natural result of balancing the temperature-dependent pressure of the kinetic gas with the elastic pressure in the balloon (Eq. 5.5). This equates to a minimization of the temperature dependent free energy of the system with respect to volume. Because vibrating atoms in a solid have the same form of momentum flux (kinetic energy) as a gas they must also produce an outward pressure to expand. Unlike a gas, which needs external confinement (e.g. the balloon), the balancing force creating the mechanical equilibrium (net force = 0) in a solid must be from the interatomic forces (represented by springs).

This is to say that thermal expansion can be described within the harmonic approximation. Specifically, the present theory uses the phonons found from the harmonic approximation to calculate the pressure exerted by atoms on the rest of the solid. There

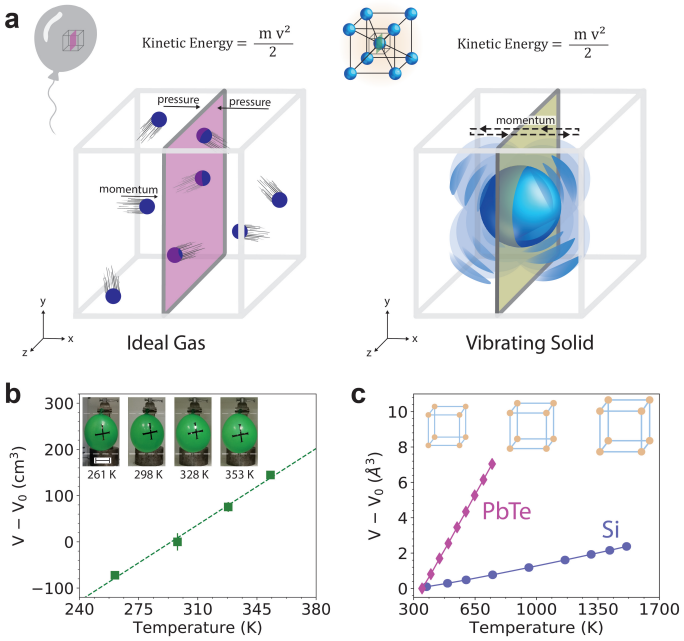

Figure 5.2: **Depiction of pressure due to kinetic energy and its effect on equilibrium volume with temperature.** (a) The pressure due to kinetic energy can be derived by considering the momentum flux through a fixed imaginary surface (e.g. pink and green planes in figure). Since the (time averaged) flux of momentum is equal in both directions, the (thermodynamic) pressure exerted on both sides of the surface is also equal. From this perspective, vibrating atoms in a solid exert a pressure on the rest of the solid just as gas particles exert a pressure on their container. (b) Equilibrium volume as a function of temperature for an argon filled balloon demonstrating that thermal expansion is linear due to the balance between the ideal gas (kinetic) pressure and the elastic response of the balloon (Eq. 5.5). (c) The equilibrium volume of solids [27, 28] also increases linearly with increasing temperature (at high temperature) and can be attributed to an analogous mechanical mechanism as the thermal expansion of the ideal gas in an elastic medium.

is a corresponding volume (strain) that satisfies the equilibrium condition at each temperature (analogous to Eq. 5.5). The thermal expansion coefficient is found from summing the individual contributions of all the vibrational modes (see Methods).

Remarkably, this intuitive picture of thermal expansion largely captures both the magnitude and temperature dependence of experimental observations (Fig. 5.3a). It should be reiterated that this estimation of the thermal expansion coefficient is determined solely using harmonic vibrational states in conjunction with the mechanical concept of phonon pressure (e.g. see inset of Fig. 5.3a). The relevance of lead telluride, PbTe, as a high-efficiency thermoelectric material makes this example particularly interesting, since understanding its vibrational properties is fundamental to engineering its thermal conductivity [2]. As PbTe is considered an archetype of anharmonic materials [217]

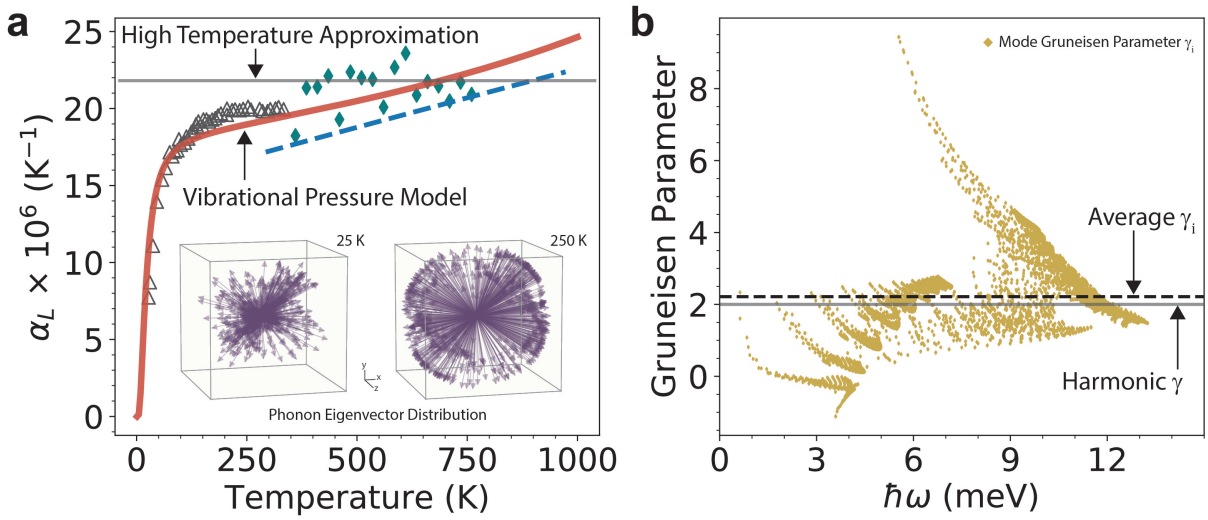

Figure 5.3: **Thermal expansion coefficient and Grüneisen parameters of lead telluride, PbTe.** (a) Coefficient of linear thermal expansion α_{L} for PbTe estimated using the "phonon pressure model" of thermal expansion (see Methods) calculated from harmonic eigenmodes and eigenvectors found from density functional theory (solid orange line) compared with experimental results (triangles [29], diamonds [27], dashed-line [30]). The "high temperature approximation" is found from a simplified analytical model (See Appendix E) and is defined as $\alpha_{\mathrm{L}} = 3k_{\mathrm{B}}/2\bar{m}v_{\mathrm{s}}^2$, where k_{B} is Boltzmann's constant, $\bar{m} = 2.8 \times 10^{-25}$ kg atom^{-1} is the average atomic mass and $v_{\mathrm{s}} = 1850$ m s^{-1} is the average speed of sound. The inset illustrates how phonon modes contribute to the vibrational pressure exerted by an atom differently at different temperatures due to the number of phonons that are excited. Here the real space direction of the atom vibrations (i.e. phonon eigenvectors) is shown by arrows. The length of the arrows is scaled by the heat capacity of the phonon mode. (b) Mode Grüneisen parameters γ_i of PbTe calculated from density functional theory (gold diamonds) and their average value, compared with the estimated "Harmonic Grüneisen parameter" (see Methods).

and is known to have complex (higher order) bonding interactions [218], it is unexpected that a harmonic model could capture an anharmonic property like the thermal expansion behavior so well. In the quasi-harmonic approximation, the large thermal expansion coefficient is attributed to the relatively large positive mode Grüneisen parameters ($\gamma_i = -(\partial \ln \omega_i / \partial \ln V)_{\mathrm{T}}$) at all frequencies (Fig. 5.3b). Here, the phonon pressure makes the solid expand, corresponding to $\gamma_i > 0$. The close agreement between the two perspectives (compare "harmonic γ" and "average γ_i" in Fig. 5.3b) is indicative of an underlying connection (e.g. Fig. 5.1). In the present perspective, the large thermal expansion coefficient in PbTe is thus explained by the large ratio of phonon pressure to the elastic restoring force.

It should be noted that, in the present calculations, atoms were considered to vibrate independent of each other. However, the coordinated movements of neighboring atoms are

likely important in some cases, particularly in negative or anomalous thermal expansion materials [219, 220]. The influence of higher order anharmonicity may also contribute to the behavior of thermal expansion [210]. Thus, further considerations of atomic structure and bonding could lead to a better understanding of the relation between the present phonon pressure perspective and the mode Grüneisen parameters found from quantum mechanics, which may provide insights to the origin of negative thermal expansion in some solids.

Complex bonding interactions in real solids necessarily include anharmonic terms (i.e. non-linear forces). Here we show that the lowest-order harmonic description is related to those higher order effects (Figs. 5.3 and 5.4), but does not preclude additional anharmonic considerations that may be important. Specifically, the harmonic theory of thermal expansion is thermodynamically connected to anharmonicity through the Grüneisen relation. The thermodynamic Grüneisen parameter γ is a restatement of Eq. 5.2 that can be written as [211]

$$\gamma = \frac{\alpha B}{C_{\mathrm{V}}}, \tag{5.6}$$

where the heat capacity C_{V} approaches the Dulong-Petit value ($3k_{\mathrm{B}}$/atom) at high temperature. Then the "harmonic Grüneisen parameter" can be calculated in the high temperature limit using the phonon pressure model of thermal expansion in conjunction with the bulk modulus determined by density functional theory (see Methods). This scalar "harmonic Grüneisen parameter" is compared with the scalar "DFT Grüneisen parameter" found by averaging the mode Grüneisen parameters γ_i (Fig. 5.4a). The overall agreement (within a factor of $\sim$2) corresponds to the agreement between their respective thermal expansion estimations. The important point, however, is that the vibrational properties of harmonic phonon modes can be related to their own anharmonicity at the thermodynamic level.

Using the theory of phonon pressure, it is also possible to show that the thermodynamic Grüneisen parameter (average γ_i) can be estimated from the ratio of the bulk-averaged transverse and longitudinal speeds of sound ($x = v_{\mathrm{t}}/v_{\mathrm{l}}$) (Fig. 5.4b), or equivalently the isotropic Poisson's ratio. The connection is plausible given that Poisson's ratio is a fundamental metric of materials behavior when strained elastically [221]. To arrive at this analytic result, we use a simplified form of the vibrational pressure model (see Methods) to obtain the thermal expansion coefficient α in terms of the heat capacity c_{V}, density ρ and speed of sound v_{s}, as

$$\alpha \approx \left(\frac{3}{2}\right) \frac{C_{\mathrm{V}}}{\rho v_{\mathrm{s}}^2} \quad . \tag{5.7}$$

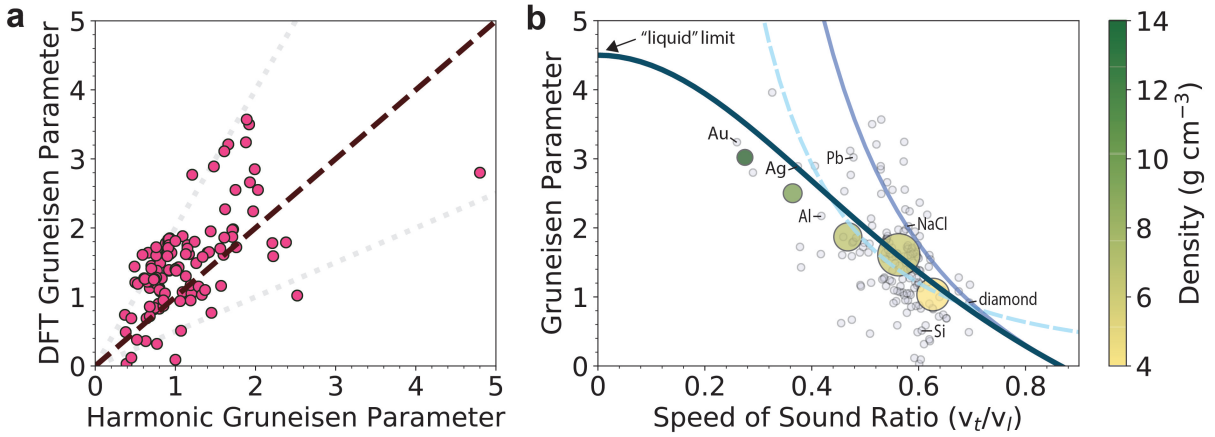

Figure 5.4: **Apparent relations between "anharmonic" and harmonic properties of solids.** (a) An equal plot comparing the 'DFT Grüneisen parameter' (i.e. the average mode Grüneisen parameter) with the 'Harmonic Grüneisen Parameter' (i.e. the thermodynamic Grüneisen parameter estimated from the harmonic model of thermal expansion) for 119 compounds. Light grey dashed lines indicate a factor of 2 from the equal line. (b) The thermodynamic Grüneisen parameter estimated from Eq. 5.8 in terms of the speed of sound ratio $x = v_\mathrm{t}/v_\mathrm{l}$ (using the RMS speed of sound, which is Eq. 5.9, gives the dark blue line and using the bulk modulus and v_s given by Anderson [31], gives the mid blue line, which diverges as $x \to 0$) compared with a previous theory given by Druyvesteyn [32] (dashed blue line) and the DFT calculated thermodynamic Grüneisen parameters (average γ_i) of individual materials (light grey circles) as well as the average Grüneisen parameters (yellow-green circles) of materials binned according to their speed of sound ratio (bins: [0.2,0.3), [0.3,0.4), [0.4,0.5), [0.5,0.6), [0.6,0.7)). The area of the marker is related to the number of materials it represents and the color represents the average density of those materials. The "liquid" limit for this model of solids is the case where the transverse speed of sound goes to zero (Poisson's ratio = 0.5). The other thermodynamic limit ($v_\mathrm{t}/v_\mathrm{l} = \sqrt{3}/2$, Poisson's ratio$= -1$) is the point where Eq. 5.9 gives $\gamma = 0$.

Substituting this result into the thermodynamic definition of the Grüneisen parameter (Eq. 5.6) yields

$$\gamma \approx \frac{3}{2}\frac{B}{\rho v_\mathrm{s}^2}, \tag{5.8}$$

which, when v_s is considered to be the root mean square speed of sound (i.e. $v_\mathrm{s}^2 = (2v_\mathrm{t}^2 + v_\mathrm{l}^2)/3$), can be written as

$$\gamma \approx \frac{3}{2}\frac{\left(3 - 4x^2\right)}{\left(1 + 2x^2\right)}, \tag{5.9}$$

where $x = v_\mathrm{t}/v_\mathrm{l}$. This form of the Grüneisen parameter (Eqs. 5.8 and 5.9) has been obtained previously [222, 223] but was based on a different assumption about the nature of vibrational pressure. In that work, the temperature dependence of vibrational pressure was not considered [222].

It is easily acknowledged that this approximation for the Grüneisen parameter (Eq. 5.9, dark blue line in Fig. 5.4b) is quite crude given the scatter in the data (grey circles in Fig. 5.4b). But its usefulness is more apparent when comparing with the average Grüneisen parameter of materials with similar speed of sound ratios (yellow-green circles in Fig. 5.4b), demonstrating that there is an intimate connection between material chemistry, elasticity, and anharmonicity that has not been fully explored. For one, Eq. 5.9 indicates that solids that are more "liquid-like" (i.e. $x \to 0$) are expected to be more anharmonic. This corresponds to the large Grüneisen parameter in metals like gold, silver and lead, where the atomic structure and bonding is often described as positively charged ions held together by a sea of negatively charged electrons. The reason being that the electrons are delocalized and can be easily rearranged like a liquid. Conversely, the Grüneisen parameter is much lower in highly directional, covalently bonded materials like diamond and silicon, when x is closer to the upper thermodynamic limit of $\sqrt{3}/2$. Another relation between γ and Poisson's ratio [32], derived from analytical considerations of an anharmonic interatomic potential, indicates γ diverges as $x \to 0$, but gives similar estimates as Eq. 5.9 for most materials ($0.4 < x < 0.7$, dashed light blue line in Fig. 5.4b). Using a different average v_s (i.e. a harmonic mean [31]) in Eq. 5.8 will also cause γ to diverge since $v_\mathrm{s} \to 0$ as $v_\mathrm{t} \to 0$ (mid-blue line in Fig. 5.4b), suggesting that the root mean square speed of sound better captures the nature of the elastic pressure.

Altogether, this relation (Eq. 5.9) provides a simple physical justification for the chemist's intuition that the anharmonicity of solids is related to the type of bond and atomic coordination (density) [205, 206, 224]. Nor would it be surprising if more intricate connections were found between elasticity, atomic structure and anharmonicity through modern machine learning methods.

This profound connection of the thermodynamic Grüneisen parameter with harmonic properties of solids means that transport phenomena like thermal conductivity and atomic diffusion may also be explained in terms of a harmonic potential. The temperature dependence of vibrational pressure corresponds to a temperature dependent potential energy landscape such that interactions between vibrational modes (e.g. phonon-phonon scattering) may be accounted for within perturbation theory. However, further investigations are needed to reconcile the relations between harmonic and anharmonic terms in the interatomic potential. Nevertheless, having accessible estimates for thermal expansion (e.g. Eq. 5.7) and the thermodynamic Grüneisen parameter allows for higher accuracy descriptions of the temperature dependent molar volumes and constant pressure heat capacity [225] needed for the thermodynamic modeling that is crucial to the design of

next generation materials [226].

The concept of phonon pressure provides a physical mechanism for "anharmonic" behavior (i.e. thermal expansion) that thermodynamically relates harmonic and anharmonic aspects of bonding in solids. That is, harmonic solids have an inherent anharmonicity. In this perspective, the harmonic potential shifts with temperature to be centered around the equilibrium position determined by the force balance between vibrational pressure and the elasticity of the material (analogous to Eq. 5.5). The success of the Temperature Dependent Effective Potential (TDEP) method developed by Hellman and coworkers [227, 228] further supports the idea that there are aspects of anharmonicity that can be represented by a harmonic potential that changes with temperature. In the TDEP method, the equilibrium atomic position also changes with temperature through a force balance procedure. Instead of explicitly using the theory of vibrational pressure, the residual forces between those calculated from the model potential and those obtained by molecular dynamics simulation are minimized. The necessity of a temperature dependent potential is apparent given that the Taylor expansion around equilibrium at 0 K is unable to reproduce finite temperature observations in some materials [227, 229].

5.4 Perspective

Although Brillouin [230] first proposed that thermal expansion in solids may be due to the vibrational pressure of elastic waves, the field of lattice dynamics largely left this mechanistic idea behind. As a result, it is commonly thought that harmonic solids cannot have thermal expansion and other properties assumed to be due entirely to anharmonic effects [204]. Here, the physical mechanism of phonon pressure leads to an explanation for thermal expansion based on only the lowest-order, harmonic approximation of solids. The connection of thermal expansion to the thermodynamic Grüneisen parameter, as well as other anharmonic behavior in solids, suggests that harmonic material descriptors may correlate with anharmonic properties more generally. The insights gained from this fundamental shift in thought-paradigm may be used to better understand both basic thermodynamic properties of solids, including melting (e.g. the Lindemann melting criteria), as well as the mechanisms of complex transport phenomena like superconductivity, ionic transport, and heat transport in defective materials.

Chapter 6

Diffuson Limit of Thermal Conductivity

6.1 Overview

A model for the thermal conductivity of bulk solids is proposed in the limit of diffusive transport mediated by diffusons as opposed to phonons. This diffusive thermal conductivity, κ_{diff}, is determined by the average energy of the vibrational density of states, $\hbar\omega_{\text{avg}}$, and the number density of atoms, n. Furthermore, κ_{diff} is suggested as an appropriate estimate of the minimum thermal conductivity for complex materials, such that (at high temperatures) this estimate κ_{min} gives values 37% lower than the widely-used Cahill result and 18% lower than the Clarke model for κ_{min}, on average. This model of diffuson-mediated thermal conductivity may thus help explain experimental results of ultralow thermal conductivity.

The bulk of this chapter was published as:

> Agne, Matthias T., Riley Hanus, and G. Jeffrey Snyder. "Minimum thermal conductivity in the context of *diffuson*-mediated thermal transport." Energy & Environmental Science 11.3 (2018): 609-616.

6.2 Where Phonons Fail

The classic phonon gas model of thermal conduction works well in many cases. In this perspective, phonon quasiparticles behave gas-like in that they carry thermal energy and physically scatter off of each other and defects in the material much like we can imagine a

gas. However a fundamental assumption that leads to the phonon gas model is sufficient periodicity of the material, such that the Bloch conditon is satisfied. In materials like nanomaterials, quasicrystals or crystals with very large unit cells there is an argument that sufficient periodicity may be lacking (at least on some length-scale).

It is well known that glassy materials do not behave according to the phonon gas model, but it was only recently that attempts to bridge the two perspectives have been undertaken [36, 231, 232, 92]. This work, particularly, was one of the first to reconsider the nature of vibrations in crystalline solids. From the perspective that crystalline materials can have vibrational character that is more similar to glassy materials than to the typical phonon gas model we arrive at this diffuson model of "minimum" thermal conductivity for solids.

6.3 Concept of Minimum Thermal Conductivity

The concept of a minimum thermal conductivity, κ_{min}, carried by the atomic vibrations of any solid material (crystalline or amorphous), is of practical technological importance. For example, materials screening and design for thermoelectric, thermal barrier and other thermal management applications often rely on models of κ_{min} to benchmark experimental observations or predict optimal material performance [233, 234, 40, 235, 236, 237]. Due to the complexity of thermal conductivity there is not a unique definition of κ_{min}, and one practical option is to take relevant models of thermal conductivity and assume some limiting condition(s) that results in a reasonable estimate of what κ_{min} could be. It may also be argued that amorphous materials are systems where the experimentally measured κ would be closest to a predicted κ_{min}.

Most previous models of κ_{min} have largely relied on the phonon description of thermal conductivity (Fig. 6.1). The form of phonon mediated thermal conductivity (analogous to a kinetic gas) is

$$\kappa = \frac{1}{3} C v \ell \tag{6.1}$$

where C is the heat capacity per unit volume, v is the average speed of a collective lattice vibration (phonon) and ℓ is the average phonon mean free path. The length scale of atomic disorder can be used to phenomenologically describe ℓ [238, 39]. In the Kittel [39] and Clarke [40] models, the minimum thermal conductivity can be thought of as the limit $\ell \rightarrow\ a$ (a is the interatomic spacing). The Cahill [239, 41] and Slack [42] models instead use a wavelength dependent mean free path to incorporate wave mechanics in the de-

scription of ℓ. Cahill uses $\ell = \lambda/2$, whereas Slack uses $\ell = \lambda$. These models work well for many materials and give an intuitive description of the phonon limit (at high temperature) of thermal conductivity (Fig. 6.1). However, as experimental thermal conductivities have been found below the Cahill and Clarke models, a different model/philosophy may provide insight into the limitations of phonon-based models and provide improved predictive power for experimentalists.

The mathematical description of lattice vibrations as phonons requires periodicity, which is not the case in amorphous materials or even nanomaterials and quasicrystals. Consequently, in the phonon picture of κ_{min} ($\ell \rightarrow \ a$, the so-called Ioffe-Regel limit [240] of phonons) the lattice vibration does not sample enough periodicity of the lattice to be a well-defined phonon or have the properties of such. Consequently, in this limit, it is technically more correct to define a diffusivity term, $\mathcal{D}$, which has the units of $v\ell$ (m^2/s) but v and ℓ are not independently defined, such that there is no need for a well-defined wavevector [241]. In the mechanism of diffusive thermal transport, heat is quantized by diffusons, characterized by a diffusivity. Diffusons can be present in any material, but may better describe atomic vibrations in materials with more atomic disorder (including crystals with large complex unit cells [242]).

Here we will use the diffuson theory of Allen and Feldman, thoroughly developed in refs. [34, 35, 36, 37, 38], to derive a phenomenological diffusive thermal conductivity, κ_{diff}, from the vibrational density of states. κ_{diff} is defined as the limit of entirely diffusive (diffuson mediated) thermal transport (Fig. 6.1). Even though the group velocity of phonons (measured by the speed of sound) is no longer the operative theoretical parameter, it can be incorporated post hoc by its correlation with the average frequency of the vibrational density of states. Lastly, by comparison of κ_{diff} with previous models of κ_{min} we suggest that κ_{diff} may be an appropriate estimation for κ_{min} in some cases. Whereby, κ_{diff} may help to explain materials with ultralow thermal conductivity.

6.4 Random Walk Diffuson Model

The diffuson theory of Allen and Feldman explains diffusive thermal transport as the harmonic coupling between non-propagating (i.e., not phonons or propagons), non-localized (i.e., able to transfer energy, not locons) atomic vibrations. It is in the spirit of diffuson theory that we construct this phenomenological model. The propagation behavior of diffusons is derived assuming each diffuson travels according to the path of a random walk. In random walk theory, the net distance, x_{N}, traveled by a quantum after N discrete

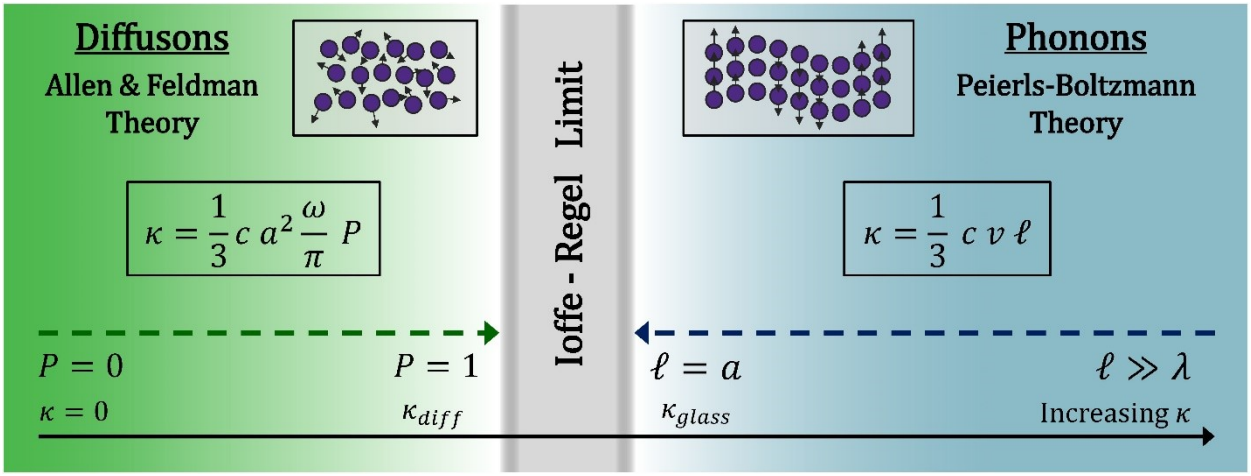

Figure 6.1: **Visual representation of the fundamental differences between phonon and diffuson models of thermal transport.** The defining characteristics of phonon-based models include the speed of sound (v) and mean free path (ℓ). Diffuson-based models of Einstein [33], formally defined by Allen and Feldman [34, 35, 36, 37, 38], and that described here rely on a thermal diffusivity coming from random walk considerations, which leads to the jump attempt frequency ($2\omega/2\pi$) and the probability of a successful jump (P) being the operative theoretical inputs. Kittel ($\ell = a$) [39], Clarke ($\ell = a$) [40], Cahill ($\ell = \lambda/2$) [41], and Slack ($\ell = \lambda$) [42] made estimations of κ_{min} from a phonon perspective.

steps of size α_l is $x_{\text{N}} = \alpha_l\sqrt{N}$. This is related to the random walk diffusivity, $\mathcal{D}_{\text{RW}}$, and the elapsed time, t, through the parabolic relation

$$\mathcal{D}_{\text{RW}} = \frac{x_{\text{N}}^2}{t} = \frac{\alpha_l^2 N}{t}. \tag{6.2}$$

Here, N/t (number of steps/unit time) may be interpreted as the frequency of energy transfer attempts multiplied by the probability of a successful transfer, P. Einstein [33], in his model for thermal conductivity (see also ref. [41]), inferred that each oscillator made 2 attempts to transfer energy in one period of oscillation, $N/t = (2\omega/2\pi)\ P$. From Eq. 6.2 we arrive at an isotropic approximation for the diffuson diffusivity,

$$\mathcal{D}_{\text{diff}}(\omega) = \frac{1}{3}\frac{n^{-\frac{2}{3}}\omega}{\pi}P, \tag{6.3}$$

by taking $\alpha = n^{-\frac{1}{3}}$ as the approximate jump distance between oscillators, where n is the number density of atoms. The factor of 1/3 comes from assuming a three dimensional system. Anisotropy may inhibit diffusion in certain directions and has ramifications discussed below. We also note that $P = 1$ is a theoretical maximum diffusivity for diffusons and is comparable to $\mathcal{D}_{\text{diff}}(\omega) = \frac{0.47}{3}n^{-\frac{2}{3}}\omega$ found by fitting N/t to MD results of

the diffuson contribution to thermal transport in amorphous Si [34]. The other limit, $P = 0$, phenomenologically describes the condition for locons (i.e., zero energy transfer). In the random walk diffuson picture, each oscillator acts completely independent from one another, resulting in a form of transport fundamentally different than that of phonons, where the phonon propagation is defined by a group velocity and relaxation time ($\mathcal{D} = \frac{1}{3} v_g^2 \tau$).

From Eqs. 2.36 and 6.3, Eq. 2.35 can be composed as the maximum ($P = 1$) diffusive thermal conductivity,

$$\kappa_{\text{diff}} = 3nk_{\text{B}} \int_0^\infty \left(\frac{g(\omega)}{3n} \right) \left(\frac{1}{3} \frac{n^{-\frac{2}{3}} \omega}{\pi} \right) d\omega \ , \tag{6.4}$$

which simplifies to

$$\kappa_{\text{diff}} = \frac{n^{\frac{1}{3}} k_{\text{B}}}{\pi} \frac{\int_0^\infty g(\omega) \ \omega \ d\omega}{\int_0^\infty g(\omega) \ d\omega} = \frac{n^{\frac{1}{3}} k_{\text{B}}}{\pi} \omega_{\text{avg}}. \tag{6.5}$$

Thus, it is the average oscillator frequency, ω_{avg}, which becomes the defining metric for the high temperature limit of diffuson-mediated thermal conductivity. In many cases ω_{avg} can be determined straightforwardly from inelastic neutron scattering experiments or computational methods. Furthermore, we will show that ω_{avg} may be approximated from speed of sound measurements and κ_{diff} may be appropriately used in the explanation of ultralow thermal conductivity materials. This approach to constructing κ_{diff} may also be used in the construction of a two-channel model of thermal transport [94] (i.e. $\kappa_{\text{L}} = \kappa_{\text{ph}} + \kappa_{\text{diff}}$).

By comparing Eqs. 5 and 6, it is possible to define the average diffuson diffusivity, $\bar{\mathcal{D}}_{\text{diff}}$, that is the weighted average of diffusivities, $\mathcal{D}_{\text{diff}}(\omega)$:

$$\bar{\mathcal{D}}_{\text{diff}} = \frac{\int_0^\infty g(\omega) \ \mathcal{D}_{\text{diff}}(\omega) \ d\omega}{\int_0^\infty g(\omega) \ d\omega} = \frac{n^{-\frac{2}{3}} \ \omega_{\text{avg}}}{3\pi} \ , \tag{6.6}$$

when P=1. Feldman, et al. [38] utilized molecular dynamics (MD) simulations to ascertain the spectral function $\mathcal{D}(\omega)$ for amorphous silicon. Thus, it is possible to compare the $\bar{\mathcal{D}}_{\text{diff}}$ calculated from Eq. 6.6 with the average diffusivity value calculated from the MD results. Using the MD data shown in Fig. 6.2 of ref. [38], the average diffusivity of amorphous silicon was determined to be $\bar{\mathcal{D}}_{\text{MD}} = \frac{\int g(\omega) \ \mathcal{D}(\omega) \ d\omega}{\int g(\omega) \ d\omega} = 4.9 \times 10^{-3}$ cm^2/s. The estimation using the average vibrational energy ($\hbar\omega_{\text{avg}} = 44$ meV [38]) and the number density of atoms for Si (Table 6.1) in Eq. 6.6 gives $\bar{\mathcal{D}}_{\text{diff}} = 5.2 \times 10^{-3}$ cm^2/s . The agreement between the MD

result and Eq. 6.6 is quite good and provides some validation for the use of Eq. 6.3. In fact, Allen and Feldman [34] use an equation with the same form as Eq. 6.3 to fit their MD results in the context of diffuson-mediated thermal transport. They suggest that the agreement between the phenomenological model and the MD result supports the idea of a microscopic definition of minimum thermal conductivity [34]. Here, the random walk derivation of κ_{diff} allows for inferences about the physics of ultralow thermal conductivity, whereas Refs. [242, 34] are limited to dimensional analysis arguments.

However, it is important to note that the more-extensive MD study [38] indicates that there are both propagating (low energy, see arrow in Fig. 6.2 of ref. [38]) and completely localized (high energy, see mobility edge line in Fig. 6.2 of ref. [38]) vibrations in their model of amorphous Si, accounting for about 7% of the vibrational density of states [36]. Diffusons are proposed as the non-propagating, non-localized heat-carrying vibrations at intermediate energies. In the derivation of κ_{diff} (Eq. 6.5) from $\mathcal{D}_{\text{diff}}(\omega)$ (Eq. 6.3), all vibrations contained within the density of states contribute to diffusive thermal transport, i.e. there are no propagating vibrations with larger contributions to thermal conductivity, and there are no localized vibrations that do not contribute to thermal conductivity. Consequently, κ_{diff} is the diffuson-mediated thermal conductivity. In using κ_{diff} as a type of κ_{min}, it should be recognized that experimental thermal conductivities found below κ_{diff} would tend to indicate that the material may have a significant number of localized vibrations (locons) that do not conduct heat; or, other exceptional physics may be at play, such as phonon focusing [243].

6.5 Debye Relation with Experimental Density of States

Although the derivation shows that it is possible to estimate κ_{diff} directly from $g(\omega)$, it is recognized that $g(\omega)$ is not always easily accessible experimentally or computationally, especially if the material system is complex (multi-phase, large unit cell, etc.). During the course of this study, it was found heuristically that the Debye temperature, θ_{D}, defined here by

$$k_{\text{B}}\theta_{\text{D}} = \hbar\omega_{\text{D}} = \hbar(6\pi^2 n)^{1/3} v_{\text{s}} \ , \tag{6.7}$$

can be used as a metric to estimate the experimentally determined ω_{avg}. It is important to recognize that, in the context of diffuson theory, θ_{D} may be regarded as a proxy for the influence of bond strength, atomic mass, and average atomic separation on the spectral distribution of the density of states. Specifically, by compiling $g(\omega)$, the arithmetic average speed of sound, $v_{\text{s}} = \frac{1}{3}(2v_{\text{t}} + v_{\text{l}})$ and number density of atoms, n, for 24 compounds

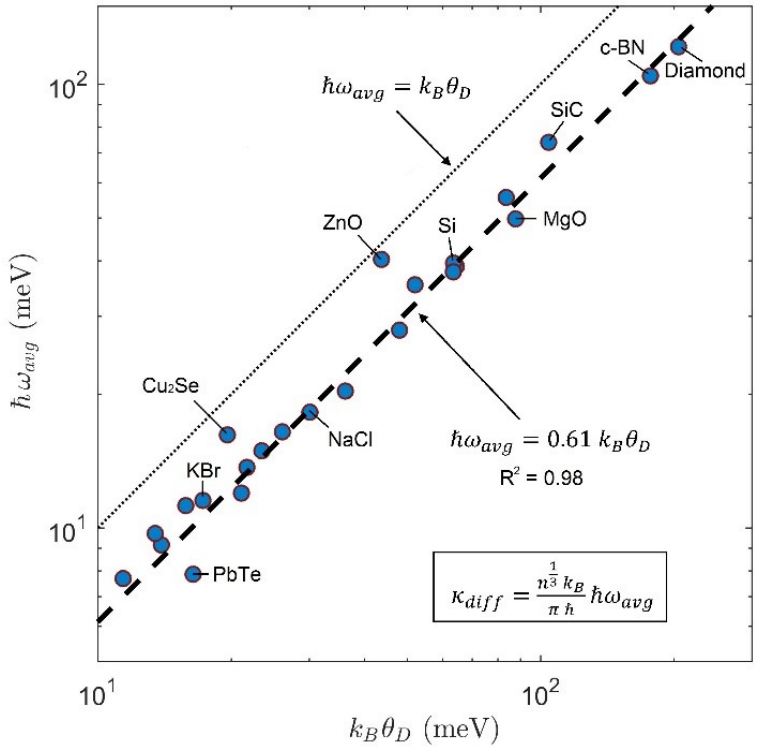

Figure 6.2: **Estimation of the average frequency of vibration.** A log-log plot demonstrating the linear correlation (Eq. 6.8) of the experimentally determined $\hbar\omega_{\text{avg}}$ (found from the vibrational density of states) with the Debye temperature ($k_{\text{B}}\theta_{\text{D}} = \hbar(6\,\pi^2 n)^{1/3} v_s$) calculated from the arithmetic average sound velocity ($v_{\text{s}} = \frac{1}{3}(2v_{\text{t}} + v_{\text{l}})$) using the values found in Table 6.1. A linear slope of 1 is shown for reference (thin dotted line). Note that the Debye model would predict a linear slope of 0.75, which is substantially higher than this heuristic finding.

reported in the literature with speeds of sound spanning an order of magnitude (Table 6.1), we found the linear correlation ($R^2 = 0.98$) (Fig. 6.2)

$$\hbar\omega_{\text{avg}} \approx 0.61\ k_{\text{B}}\theta_{\text{D}}\ , \tag{6.8}$$

having a normalized root-mean-square error of 3.6% (RMSE $\approx$ 4 meV). It should be noted that the harmonic average speed of sound is another option for calculating the scalar θ_{D} [244], which was found to give a slightly worse correlation ($R^2 = 0.97$, RMSE $\approx$ 5 meV), but would still lead to the same conclusions drawn below. Other methods of estimating θ_{D} (e.g., from low temperature heat capacity or inelastic neutron/x-ray scattering methods) are also expected to correlate with ω_{avg} .

Table 6.1: Experimental number density of atoms n calculated from ICSD reported unit cell volumes, and the longitudinal (v_l) and transverse (v_t) speeds of sound used to calculate the Debye temeprature (θ_D) from the arithmetic average speed of sound, as well as the experimental average energy ($\hbar\omega_\mathrm{avg}$) determined from the vibrational density of states. The speeds of sound for PbTe were measured herein by 5 MHz pulse-echo ultrasound, see ref. [2] for detailed methods.

Element/Compound	n/10^{28} (atoms m^{-3})	v_l (m s^{-1})	v_t (m s^{-1})	Debye Model $k_\mathrm{B}\theta_\mathrm{D}$ (meV)	Experimental $\hbar\omega_\mathrm{avg}$ (meV)
RbI	2.03	2411 [245]	1236 [245]	11.39	7.69 [246]
PbTe	2.67	3102	1662	16.42	7.85 [44]
RbBr	2.46	2580 [245]	1508 [245]	13.92	9.16 [246]
KI	2.3	2534 [245]	1501 [245]	13.47	9.71 [246]
NaI	2.78	2716 [245]	1688 [245]	15.79	11.23 [246]
KBr	2.69	3053 [245]	1843 [245]	17.26	11.52 [246]
RbCl	2.81	3078 [245]	2518 [245]	21.09	11.99 [246]
NaBr	3.7	3392 [245]	2112 [245]	21.71	13.70 [246]
KCl	3.22	3896 [245]	2366 [245]	23.48	14.92 [246]
Cu_2Se	6.02	3086 [247]	1381 [247]	19.6	16.20 [248]
RbF	4.46	3946 [245]	2333 [245]	26.12	16.46 [246]
NaCl	4.93	4470 [249]	2570 [249]	30.14	18.24 [246]
KF	6.98	4608 [245]	2842 [245]	36.24	20.35 [246]
NaF	8.03	5664 [245]	3673 [245]	48	27.89 [246]
FeO	10.06	6630 [250]	3230 [250]	52.07	35.31 [246]
CaO	7.17	8120 [251]	4880 [251]	63.51	37.78 [246]
SrTiO3	8.4	7860 [252]	4680 [252]	64.48	38.85 [246]
Si	5	8480 [253]	5860 [253]	63.62	39.55 [246]
ZnO	8.4	6000 [245]	2831 [245]	43.68	40.33 [254]
MgO	10.69	9576 [249]	6038 [249]	87.88	49.75 [246]
TiC	9.87	9429 [255]	5856 [255]	83.55	55.55 [246]
SiC	9.64	11730 [249]	7430 [249]	104.27	74.00 [254]
c-BN	16.92	16117 [256]	10653 [256]	177.01	104.40 [254]
Diamond	17.63	18120 [245]	12323 [245]	205.05	121.43 [254]

6.6 Comparison with Minimum Thermal Conductivity Models

Next, we compare our diffuson thermal conductivity, κ_diff, to previous models of κ_min based on the maximum phonon scattering approach. This comparison gives good justification to use κ_diff as a new formulation of κ_min. Consequently, κ_diff may thus be used to explain the experimental results of ultralow thermal conductivity materials. First, we point out that Eq. 6.8 can be used to further simplify Eq. 6.5 to depend solely on n and v_s:

$$\kappa_\mathrm{diff} \approx 0.76\ n^{\frac{2}{3}}\ k_\mathrm{B}\frac{1}{3}\left(2v_\mathrm{t} + v_\mathrm{l}\right)\ , \tag{6.9}$$

which makes this formulation of κ_diff directly comparable to the Cahill result,

$$\kappa_\mathrm{glass} = 1.21\ n^{\frac{2}{3}}\ k_\mathrm{B}\frac{1}{3}\left(2v_\mathrm{t} + v_\mathrm{l}\right)\ . \tag{6.10}$$

Here it is easily seen that κ_{diff} is approximately 37% lower than κ_{glass} on average. In fact, κ_{glass} is better used as a predictor for the experimental thermal conductivity of amorphous and disordered materials [43]. This is to say that, as a decent approximation, $\kappa_{\text{glass}} \approx \kappa_{\text{measured}}$ (within a factor of 2) and κ_{diff} may be a better estimation of κ_{min} (Fig. 6.3). The ideal κ_{min}would always predict a thermal conductivity that is lower than the measured value, and all of the data points in Fig. 6.3 would be to the left of that predicted line. Using κ_{diff} as κ_{min} very nearly satisfies this requirement, and only a few points remain to the right of the κ_{diff} line (shaded region in Fig. 6.3).

Further comparison shows that κ_{diff} is ≈18% lower than the κ_{min} equation presented by Clarke [40],

$$\kappa_{\text{min, Clarke}} \approx 0.93\, n^{\frac{2}{3}}\, k_{\text{B}} \frac{1}{3} \left(2v_{\text{t}} + v_{\text{l}}\right), \tag{6.11}$$

who also suggested that $v_s = \frac{1}{3}\left(2v_{\text{t}} + v_{\text{l}}\right) \approx 0.94\sqrt{Y/\rho}$ is a reasonable approximation (within 20%) for the speed of sound from Young's modulus, Y (N/m^2), and density, ρ (kg/m^3). As Eq. 6.11 is effectively a restatement of the Kittel κ_{min}, these comparisons suggest that the diffuson mechanism of thermal transport conducts heat more slowly than the maximum phonon scattering limit predicts. This leads to the implication that materials with thermal conductivities near to κ_{diff} are transporting heat at a rate analogous to the maximum rate if all of the atomic vibrations were diffusons. Experimental thermal conductivities that fall below κ_{diff} would tend to indicate that there is some interesting/exceptional mechanism that is influencing thermal conductivity. Thus, κ_{diff} provides a reference value for the upper limit of diffusive thermal conductivity and may give some physical insight to conduction mechanisms in ultralow thermal conductivity materials.

6.7 Temperature Dependence of Diffuson Model

Although most thermoelectric generators, thermal barrier coatings and thermal management devices are concerned with temperatures at or above room temperature, making the high temperature limit of κ_{diff} the primary focus, it is important to make some remarks about the temperature dependence of the model presented above. The sole temperature dependence is incorporated through the heat capacity term, which accounts for the thermal activation of higher energy atomic vibrations as the temperature is raised from 0 K.

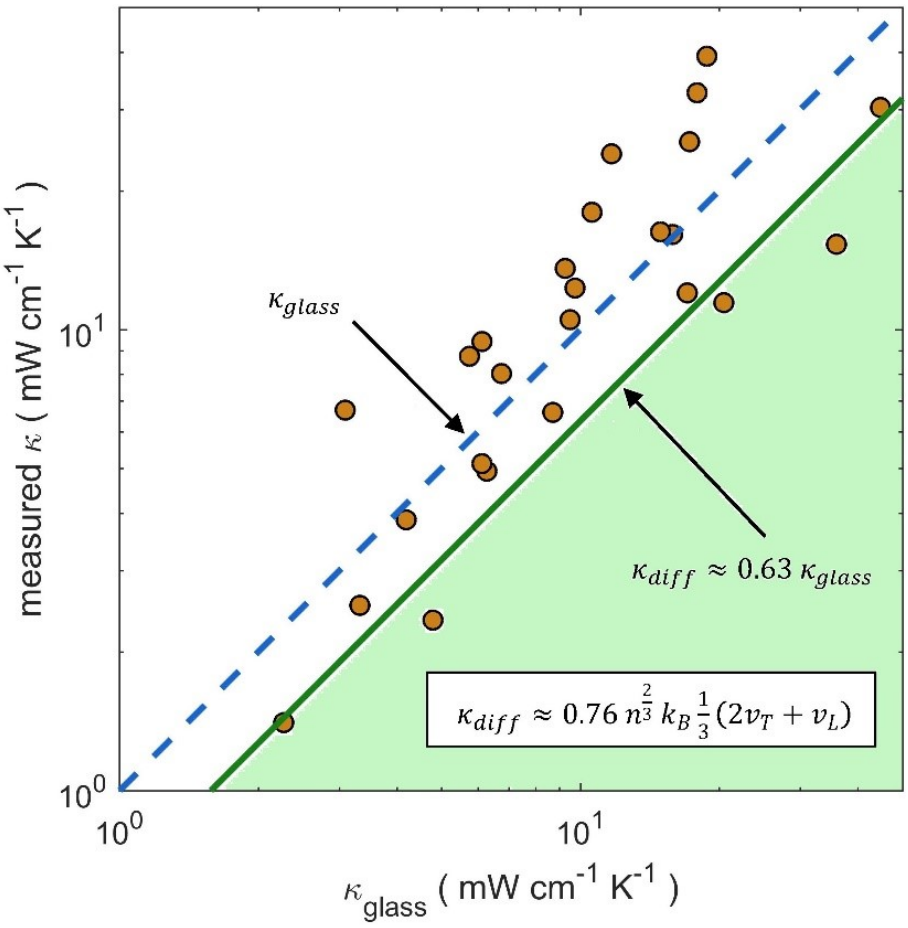

Figure 6.3: **Diffusons as a model of minimum thermal conductivity.** A comparison of κ_{diff} with the Cahill model, κ_{glass}, shows that κ_{glass} is a good estimate for the measured thermal conductivity (within a factor of 2), whereas κ_{diff} may be a better metric for estimating the minimum thermal conductivity. Plotted points are the same that appear in Fig. 7 of ref. [43].

Explicitly, Eq. 2.36 can be rewritten as

$$C(\omega) = k_{\text{B}} \left(\frac{\hbar\omega}{k_{\text{B}}T} \right)^2 \frac{e^{\frac{\hbar\omega}{k_{\text{B}}T}}}{\left(e^{\frac{\hbar\omega}{k_{\text{B}}T}} - 1 \right)^2} \tag{6.12}$$

which, in turn, can be used to incorporate a temperature dependence into Eq. 6.4:

$$\kappa_{\text{diff}}(T) = \frac{n^{\frac{1}{3}} k_{\text{B}}}{\pi} \int_0^{\infty} \left(\frac{g(\omega)}{3n} \right) \left(\frac{\hbar\omega}{k_{\text{B}}T} \right)^2 \frac{e^{\frac{\hbar\omega}{k_{\text{B}}T}}}{\left(e^{\frac{\hbar\omega}{k_{\text{B}}T}} - 1 \right)^2} \, \omega \, d\omega \, . \tag{6.13}$$

Here it is assumed that $g(\omega)$ and the diffusive mechanism of thermal transport are both reasonably independent of temperature. In effect, the integral in Eq. 6.13 is a temperature dependent average frequency, $\omega_{\text{avg}}(T)$, of the vibrational spectrum,

$$\kappa_{\text{diff}}(T) = \frac{n^{\frac{1}{3}} k_{\text{B}}}{\pi} \omega_{\text{avg}}(T) \ , \tag{6.14}$$

and $\omega_{\text{avg}}(T)$ converges, of course, to a constant value (ω_{avg} in Eq. 6.5) when the entire vibrational spectrum is thermally activated in the $T \to \infty$ limit.

However, it may be necessary to use $\kappa_{\text{diff}}(T)$ in the temperature range of interest if $T < \theta_{\text{D}}$. This is to say that high energy vibrations that are not yet thermally activated should not be included in the calculation of κ_{diff}. Considering PbTe as an example, $g(\omega)$ is fairly independent of temperature up to 500 K [44]. The INS data at 100 K (Fig. 6.4a) was used for all calculations, and numerical integration of Eq. 6.13 for temperatures up to 500 K reveals that $\kappa_{\text{diff}}(T)$ is converged to the high T value by 500 K (Fig. 6.4b). As the full vibrational spectrum (up to 16 meV in Fig. 6.4a) is excited by ~190 K ($k_{\text{B}}T \approx 16$ meV), the high temperature approximation is quite good for PbTe above room temperature.

The Einstein model of thermal conductivity, κ_E (see, e.g., ref. [239]), may be the most rudimentary equation for diffusive thermal transport, having a characteristic frequency, ω_E, that is constant with temperature and a density of states given by $g(\omega) = 3n\,\delta(\omega - \omega_E)$. Nevertheless, using $\omega_E = \omega_{\text{avg}}$ (gray lines in Fig. 6.5) results in an Einstein model that converges to the value of κ_{diff} at high temperatures and goes as $\kappa_E \propto e^{-\theta_E/T}$ at low temperatures ($\theta_E = \hbar\omega_E / k_{\text{B}}$). As ω_E is the only and ipso facto the maximum frequency of the Einstein density of states, κ_E converges to the high temperature value of κ_{diff} at a lower temperature than if there were a distribution to the density of states (Fig. 6.5b). In order to better approximate the temperature dependence of κ_{diff} found numerically, it is possible to utilize the correlation between ω_{avg} and θ_{D} (Eqs. 6.8 and 6.9), to estimate $\kappa_{\text{diff}}(T)$ using the Debye model $g(\omega)$ given by Eq. 3.8 (blue curve in Fig. 6.5a). However, to converge at the high temperature value given by Eq.6.9, the upper limit of integration has to be changed to compensate for the fact that the average frequency of the Debye model is higher than that found experimentally. Explicitly,

$$\kappa_{\text{diff}} \approx \frac{n^{\frac{1}{3}} k_{\text{B}}}{\pi\hbar}(0.61\ k_{\text{B}}\theta_{\text{D}}) = k_{\text{B}} \int_0^{f\omega_{\text{D}}} \left(\frac{3}{2\pi^2}\frac{\omega^2}{v_{\text{s}}^3}\right)\left(\frac{n^{-\frac{2}{3}}\omega}{3\pi}\right) d\omega \tag{6.15}$$

and equivalence with Eq. 6.9 is achieved when the upper limit of integration is defined by $f \approx 0.95$ (truncated Debye model, green curve in Fig. 6.5a). Switching to the reduced

variable, $x = \hbar\omega/k_{\mathrm{B}}\,T$, then $\kappa_{\mathrm{diff}}\,(T)$ may be approximated as

$$\kappa_{\mathrm{diff}}\,(T) \approx \frac{n^{-\frac{2}{3}}k_{\mathrm{B}}}{2\pi^3 v_s^3}\left(\frac{k_{\mathrm{B}}T}{\hbar}\right)^4 \int_0^{0.95\frac{\theta_{\mathrm{D}}}{T}} \frac{x^5 e^x}{\left(e^x-1\right)^2}dx\ , \tag{6.16}$$

which predicts κ_{diff} goes as T^4 at low temperatures (Fig. 6.5b). This temperature dependence is a direct result of using a parabolic density of states (typical of propagating lattice waves) with a diffusivity of diffusons that is linear in ω. The Cahill model of κ_{glass} uses a parabolic density of states, but assumes phonon scattering is inversely proportional to ω, giving a diffusivity that is proportional to ω^{-1}. Thus, κ_{glass} goes as T^2 at low temperatures, in better agreement with the thermal conductivity of amorphous materials (Fig. 6.5b). Consequently, the thermal conductivity of real materials is likely dominated by propagating (phonon-like) vibrations at low temperatures, whereas κ_{min} at high temperature may be better described by diffuson-like vibrations.

This conclusion is well-supported by a recent computational study on vibrations in a random $\mathrm{In_{1-x}Ga_xAs}$ alloy [231], as well as in defect-free crystalline $\mathrm{CePbBr_3}$ [92], $\mathrm{Yb_{14}MnSb_{11}}$ [93] and $\mathrm{Cu_{12}Sb_4S_{13}}$ [257].

It should be noted that although diffuson-like thermal transport is more likely in complex materials with low and ultralow thermal conductivity, correctly characterizing vibrational behavior is a non-trivial challenge. For example, the contribution of diffuson-like vibrations to the thermal conductivity of $\mathrm{Tl_3VSe_4}$ at high temperature is currently under investigation [258, 94, 259].

6.8 Summary

The Kittel, Slack, and Cahill (phonon-based) models, i.e. κ_{glass}, are good approximations for amorphous materials particularly at low temperatures. However, at high temperature, thermal conductivities are sometimes even lower, suggesting that κ_{diff} may be a better estimate for a minimum thermal conductivity, κ_{min}. Here we define κ_{diff} as the limit of thermal conductivity when vibrations are not propagating (not phonon-like) but also not localized (specifically, $P = 1$).

Additionally, by correlating ω_{avg} with the Debye temperature ($\hbar\omega_{\mathrm{avg}} \approx 0.61\ k_{\mathrm{B}}\theta_{\mathrm{D}}$) it is possible to estimate κ_{diff} from simple and accessible speed of sound measurements. From this correlation, we find that κ_{diff} is approximately 37% lower than the κ_{glass} estimate of Cahill using identical experimental inputs. In many cases, this may reconcile experimental ob-

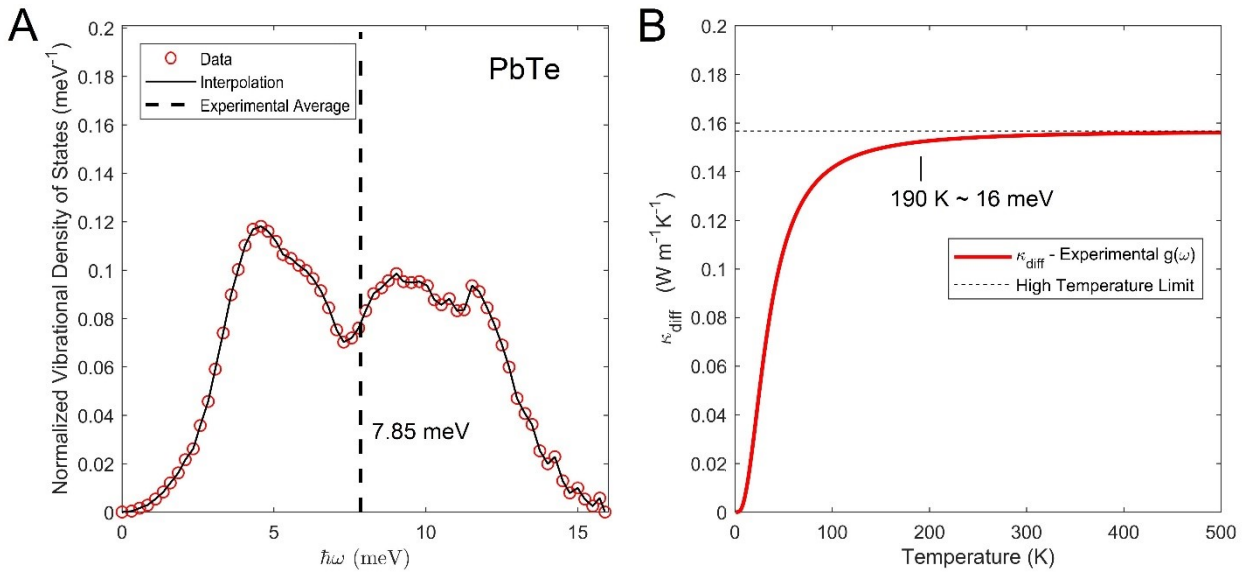

Figure 6.4: **Temperature dependent diffuson model.** The experimental vibrational density of states for PbTe at 100 K taken from [44] (panel A) and the temperature dependent $\kappa_{\text{diff}}(T)$ calculated numerically using Eq. 6.13, tending to $\kappa_{\text{diff}} = 0.157$ W/mK at high temperature when the entire density of states is thermally excited (panel B).

servations with the concept of minimum thermal conductivity. However, observations of thermal conductivities below the κ_{diff} value are not unexpected, and would tend to indicate extraordinary physics leading to ultralow thermal conductivity. For example, complex materials may have a large number of localized (locon-like) vibrations that do not contribute to thermal conductivity; or, anisotropy may give rise to the exceptional mechanism of phonon focusing.

Finally, in the context of our analysis of PbTe, using κ_{diff} as a benchmark for minimum thermal conductivity leads to the conclusion that further reductions in thermal conductivity may be possible in many good thermoelectric materials. Engineering the vibrational properties of these materials may lead to diffuson-like thermal transport, resulting in significant improvements to the thermoelectric figure of merit.

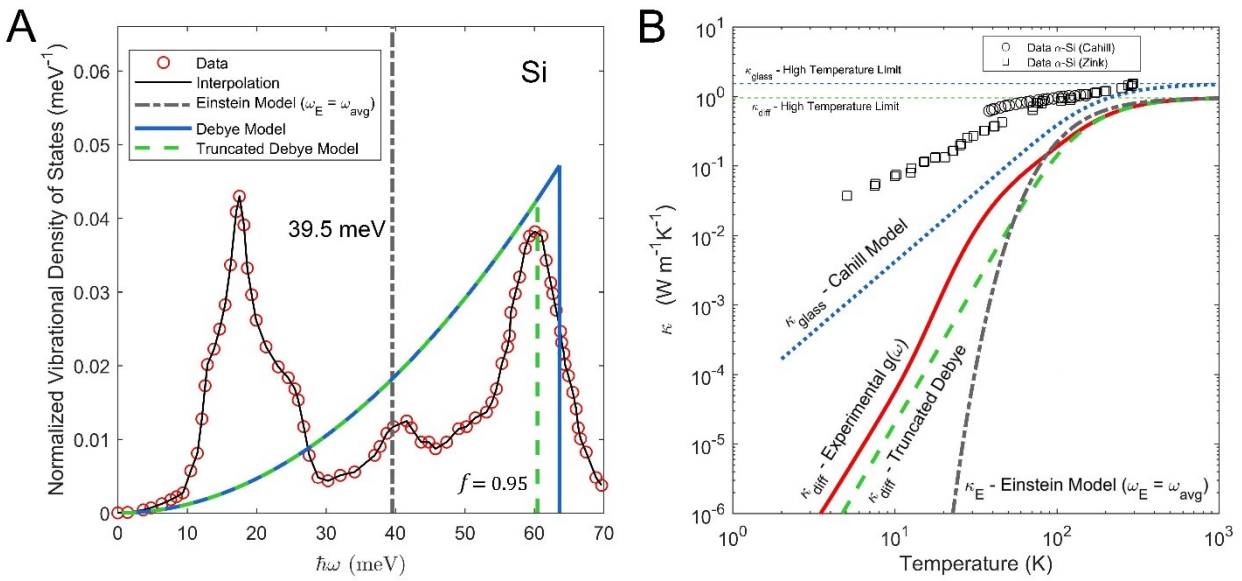

Figure 6.5: **Comparison of the temperature dependence of minimum thermal conductivity models.** The experimental vibrational density of states (red circles) for Si at 300 K taken from [45], the Debye density of states (blue curve) having a maximum energy $k_B\theta_D$ determined by the speed of sound (Table 6.1), and the truncated Debye density of states (green curve) with a maximum energy 0.95 $k_B\theta_D$ (panel A). $\kappa_{diff}(T)$ was calculated numerically (κ_{diff}-Experimental $g(\omega)$, red curve, using Eq. 6.13) and analytically (κ_{diff}-Truncated Debye, green curve, using Eq. 6.16), and compared with the Cahill (κ_{glass}, blue curve) and Einstein (κ_E, gray curve) models, with experimental thermal conductivity measurements of amorphous Si [46, 47] shown for reference (panel B). The low temperature behavior for each model is $\kappa_{diff} \propto T^4$, $\kappa_{glass} \propto T^2$, and $\kappa_E \propto e^{-\theta_E/T}$, respectively.

Chapter 7

Thermodynamic Stability in Mixed Conductors

7.1 Overview

Many superionic mixed ionic-electronic conductors with a liquid-like sublattice have been identified as high efficiency thermoelectric materials, but their applications are limited due to the possibility of decomposition when subjected to high electronic currents and large temperature gradients. Here, through systematically investigating electromigration in copper selenide thermoelectric materials, we reveal the mechanism for atom migration and deposition based on a critical chemical potential difference. Then, a strategy for stable use is proposed: constructing a series of electronically conducting, but ion-blocking barriers to reset the chemical potential of such conductors to keep it below the threshold for decomposition, even if it is used with a high electric currents and/or large temperature differences. This strategy not only opens the possibility of using such conductors in thermoelectric applications, but may also provide approaches to engineer perovskite photovoltaic materials and the experimental methods may be applicable to understanding dendrite growth in lithium ion batteries.

The bulk of this chapter was published as:

Qiu, Pengfei, Matthias T. Agne, et al. "Suppression of atom motion and metal deposition in mixed ionic electronic conductors." Nature Communications 9.1 (2018): 1-8.

7.2 Introduction to Superionic Conductors

Superionic conductors are solids in which at least one type of atom forms a rigid sublattice framework and another type of atom forms a "melted" liquid-like sublattice composed of highly mobile charged atoms, i.e. ions [260]. The description of the ensemble of highly mobile ions in terms of a "liquid" sublattice derives from the fact that the entropy change during transition into the superionic phase is comparable to the entropy change during a solid/liquid phase transition [260]. This unique liquid-like ion migration is the basis for many phenomena and applications in the fields of solid-state ionics, e.g. of solid electrolytes, batteries, fuel cells, and various types of sensors [261]. Ion migration also occurs in materials with much lower ion mobility, and is often the origin of electric field-driven degradation in hybrid organic-inorganic perovskite solar cell materials (e.g. $CH_3NH_3PbI_3$) and Cu-based photovoltaic materials [262, 263]. Ion migration and the redox-based formation of conducting paths in dielectrics is the basis for future information storage technologies (atomic switching and memristive devices) [264].

Recently, the application of superionic mixed ionic-electronic conductors (MIECs) with a liquid-like sublattice has been extended to the field of thermoelectrics. A concept named as "Phonon-Liquid Electron-Crystal" (PLEC) has been proposed to design and develop high-performance thermoelectric (TE) materials that conduct phonons like a liquid and electrons like a crystal [157]. A large family of novel Cu-, Ag- and Zn-based superionic MIECs have been identified satisfying this concept – with typical examples being $Cu_{2-\delta}X$ (X = S, Se, Te), Ag_2Se, CuAgSe, Zn_4Sb_3, Cu_5FeS_4, Cu_7PSe_6, and $Cu_{12}Sb_4S_{13}$, etc. [157, 265, 266, 267, 268, 155, 269].

In a MIEC, both the ions and electrons (or holes) are mobile such that atom (rather than ion) migration is possible, which may lead to composition changes within the MIECs [270]. Many new and unusual electrical and thermal transport properties, such as the reduced specific heat, ultralow and temperature independent lattice thermal conductivity, and extremely high TE figure of merit zT > 2.0 have been observed and reported in these MIECs [271]. The high TE performance and the fact that Cu is relatively non-toxic and earth-abundant has attracted much attention to these MIECs for both fundamental studies and industrial applications.

Despite the high performance, the stability and reliability of MIECs are key concerns for long-term service in real applications for batteries, photovoltaics, and thermoelectrics. In Li-ion batteries, for instance, the Li dendrite growth can result in catastrophic failure leading to combustion or explosion [272]. In CdTe-Cu_xTe solar cells, Cu atoms can mi-

grate into the CdTe absorber and CdS window layers to form carrier traps that reduce device performance [263]. In thermoelectrics, the added potential risk using MIECs contributed to the discontinuation of $Cu_{2-\delta}Se$ development for aeronautics and space applications [273, 274].

The mobile Cu species in Cu-based MIECs are prone to deposit on the surface at the cathode to form Cu metal when an external electric field or temperature gradient is applied (Fig. 7.1a). If Cu is not supplied at the anode, the Cu metal deposition at the cathode will change the initial material's composition and degrade TE performance as the metal deficiency in MIECs is optimized for a high zT. In TE devices with MIECs, Cu metal deposition on the sample surface may also damage the contact between the TE material and the electrode by forming cracks to increase electrical/thermal resistance and degrade the power output and conversion efficiency [82]. In addition, the plating of Cu at the cathode may lead to the evaporation of chalcogenides at the anode, resulting in the breakage of the thermolegs [81]. This is partly why NASA stopped the program of $Cu_{1.97}Ag_{0.03}Se_{1+y}$-based radioisotope thermal generators in 1981 after more than 10 years of research activity [82]. Therefore, metal deposition caused by ion flux must be restricted to improve the stability and reliability of TE devices consisting of MIECs before the use in any industrial application.

In this study, through systematically investigating the behavior of various MIECs with a liquid-like ionic sublattice in an electric field with or without a temperature gradient, we reveal the relations of ion migration, metal deposition, and materials degradation in MIECs for thermoelectric application. A general model is proposed to reveal the thermodynamic threshold for decomposition of MIECs. With this understanding, we develop a strategy to improve the MIECs' stability and reliability by adding electronically conducting, but ion-blocking interfaces in the material.

7.3 Mechanism of Ion Transport in Mixed Conductors

The physical and chemical processes of atom migration and metal deposition in MIECs are presented in Fig. 7.1b-f. The mobile ions (Cu^+ in Cu_2S and Cu_2Se) possess high diffusivities, as they have relatively low activation energies for migration, E_a (e.g. 0.19 eV in Cu_2S and 0.14 eV in Cu_2Se [275, 276]. Simply, neighboring sites are energetically close and jumps are frequent (Fig. 7.1b). If there is no directional force or field applied to the uniform material, the random motion of ions is equal in all directions and there

will be no net mass transport in a specific direction (Fig. 7.1c). In response to an external driving force (an electric field or temperature gradient) the charge carriers (ions and electronic species) flow (Fig. 7.1d). If the electrodes do not allow for ion transfer, there can be no net ionic current in the stationary state, and a concentration gradient of ions will form within the material. For reasons of electroneutrality, this concentration gradient will lead to an equal concentration gradient of electrons, and in essence, a chemical composition gradient is formed. If the concentration variation remains within the stability limits of the material, i.e. within the homogeneous phase field defined by the phase diagram of the MIEC, the concentration gradient of the mobile component acts as diffusion force opposing the external applied force on the mobile component, and a steady-state condition is achieved, i.e., there is no driving force for further migration of the neutral component (Fig. 7.1e). In the following, we describe transport of the neutral metal component as transport of atoms for the sake of simplicity. In the steady-state condition with ion blocking electrodes, the material can still transport a net flux of electric charge (via electrons or holes in the presence of an electric field) and heat (via electrons or holes and phonons in the presence of a temperature gradient), but the net flux of atoms is zero. This steady-state condition of vanishing atom transport, also called the Soret steady state [277], is similar to the condition in a conventional TE material (e.g. Bi_2Te_3, PbTe, and SiGe) [278, 279, 280].

However, the change in the chemical potential of the migrating atom may lead to decomposition of the MIEC and prevent the formation of a steady-state condition. At the electrode interface, a critical chemical potential may be reached where a decomposition (product) phase is favored. For instance, in $Cu_{2-\delta}$(Se,S), when the chemical potential of Cu at the cathode is equal to or higher than the chemical potential of Cu metal, the reduction of Cu^+ to Cu metal at the cathode or the oxidation of selenium/sulfur anions to Se/S (solid and/or gaseous) at the anode can occur [273, 274, 82, 81]. The chemical potential beyond which decomposition occurs also corresponds to a "solubility limit" of Cu in the MIEC. The maximum solubility of Cu precedes Cu metal deposition and the minimum solubility of Cu precedes Se/S oxidation. When the Cu concentration increases beyond this "solubility limit", Cu metal will deposit at the cathode if the kinetics of metal crystallization allows (Fig. 7.1f). Once this happens, the material and the interface in the device can be permanently altered. We note that the deposition of Cu metal is also hindered by a nucleation barrier. For Cu deposition the chemical potential of Cu needs then to be slightly higher than its standard potential, μ^0(Cu), but all the general conclusions above remain the same.

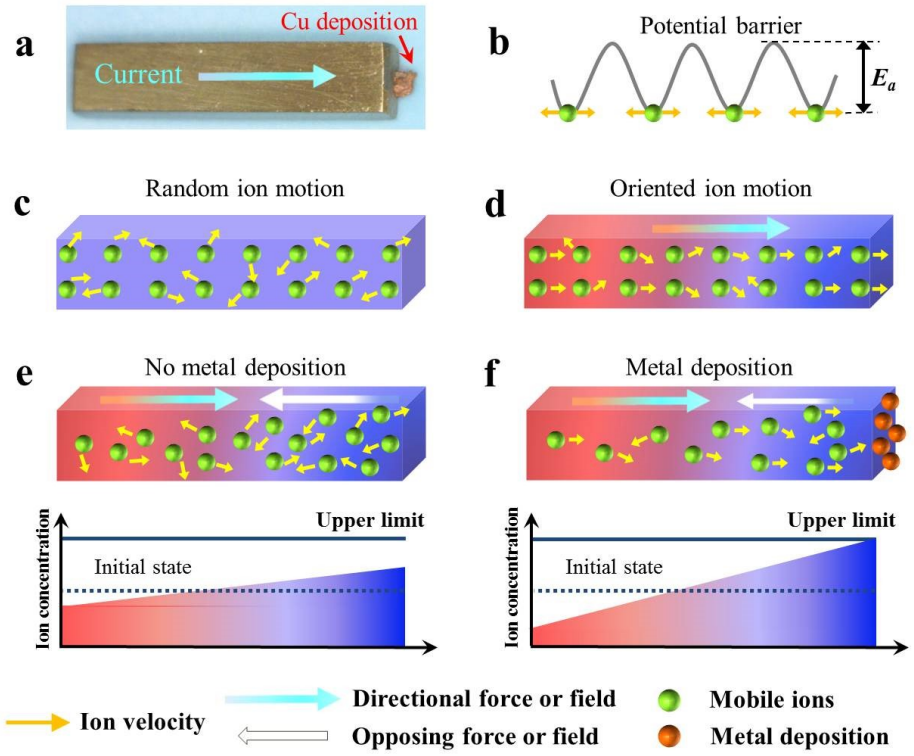

Figure 7.1: **Physical and chemical processes of ion migration and metal deposition in MIECs**. (a) Metallic Cu deposition on the surface of a Cu_2S sample induced by a current. (b-e) Schematic of (b) the energy landscape for ions; (c) random ion motion without net flux; and (d) net ion flux under directional force or field. Due to a directional force or field and depending on the electrode constraints, MIECs may either reach a (e) steady-state without net ion transport (and without metal deposition) or (f) continuous metal deposition (or other decomposition), if the local Cu concentration reaches a critical level determined by the stability range of the MIECs.

The thermodynamic threshold for the maximum or minimum solubility in Cu-based MIECs can be reached if there is a sufficient change in the chemical potential of Cu atoms due to applied forces (electric field and temperature gradient). In steady state, the net change in chemical potential of Cu atoms can be determined from the sum of the change in electrochemical potentials of the constituent ions and electronic carriers. Because copper atoms are in equilibrium with copper ions and electrons, the electrochemical potentials ($\tilde{\mu}$) are related by

$$\mu_{\mathrm{Cu}} = \tilde{\mu}_{\mathrm{Cu}^+} + \tilde{\mu}_{\mathrm{e}^-} \ . \tag{7.1}$$

Thus the change in chemical potential across the material (defined by the electrodes each

end is in contact with),

$$\Delta\mu_{\mathrm{Cu}} = \mu_{\mathrm{Cu}}^{\mathrm{anode}} - \mu_{\mathrm{Cu}}^{\mathrm{cathode}} = \Delta\widetilde{\mu}_{\mathrm{Cu^+}} + \Delta\widetilde{\mu}_{\mathrm{e^-}} \ . \tag{7.2}$$

Consequently, our goal is to relate experimental parameters to μ_{Cu} in order to explain the critical condition of Cu metal deposition in Cu-based MIECs.

From the flux equation of linear non-equilibrium thermodynamics (see section 2.2.2) [89, 281], the electronic current density, J, is driven by the gradient of the electrochemical potential of the electronic species and the temperature gradient through the relation

$$J = -\sigma \left[\frac{1}{z_e F} \nabla\widetilde{\mu}_{\mathrm{e^-}} + S_e \nabla T \right], \tag{7.3}$$

where z_e defines the charge (-1 for electrons or +1 for holes), F is Faraday's constant, and σ is the specific electrical conductivity. S_e which has the sign and units of the electronic Seebeck coefficient, captures the effect of thermodiffusion due to the temperature gradient ∇T. Using the analogous flux equation for ions, considering the case when ion blocking electrodes are used (i.e., there is no ion flux, $J_{\mathrm{Cu^+}} = 0$), then the electrochemical potential driving force exactly cancels the thermal driving force for ion migration. Explicitly,

$$\nabla\widetilde{\mu}_{\mathrm{Cu^+}} = -z_{\mathrm{Cu^+}} \ F \ S_{\mathrm{Cu^+}} \nabla T \ , \tag{7.4}$$

and $S_{\mathrm{Cu^+}}$ similarly relates to the thermodiffusion of Cu ions. When the gradients in Eqs. 7.3 and 7.4 only apply in the x-direction they can be integrated, which for linearly varying systems (such as MIECs [282]) is equivalent to being multiplied through by $\Delta x = L$ (L is the effective length between electrodes), and used in the relation defined by Fig. 7.2. Upon rearranging, we arrive at

$$V = \frac{JL}{\sigma} = -\frac{1}{z_e F} \Delta\mu_{\mathrm{Cu}} - S^* \Delta T \ , \tag{7.5}$$

where S^* accounts for the net effect of thermodiffusion and V is the experimental parameter (in units of voltage, calculated from J) of this study.

Because there are bounds to the chemical potential range over which the material can exist, there must be some critical chemical potential difference ($\Delta\mu_{\mathrm{Cu}}^{\mathrm{crit}}$) at which Cu metal deposition occurs. From Eq. 7.5, it is straightforward to find the voltage corresponding to this critical chemical potential difference:

1. in the isothermal case:

$$V_{\mathrm{c}} = -\frac{1}{z_e F}\,\Delta\mu_{\mathrm{Cu}}^{\mathrm{crit}}\,, \tag{7.6}$$

where V_{c} is a critical voltage that results from a critical applied current density J_{c}, and,

2. in a temperature difference,

$$V_{\mathrm{c}} = -\frac{1}{z_e F}\,\Delta\mu_{\mathrm{Cu}}^{\mathrm{crit}} - S^{*}\Delta T\,, \tag{7.7}$$

where it is important to note that the sign of ΔT (=$T_{\mathrm{anode}} - T_{\mathrm{cathode}}$) is important, as will be discussed.

From this analysis it is expected that a voltage difference, not current density, is the critical parameter for Cu deposition. We also note that in open circuit conditions (no electronic or ionic current) the thermodynamics predicts a critical ΔT resulting in Cu deposition at the cathode (when $V_{\mathrm{c}} = 0$ in Eq. 7.7).

Further consideration of the isothermal condition (Eq. 7.6) reveals that V_{c} only depends on the composition of the compound relative to the "solubility limit". This allows for the use of a microscopic defect model to relate off-stoichiometry, δ, in $Cu_{2-\delta}X$ (X=S, Se) to the critical chemical potential in Cu-based MIECs. A parameter named as the critical off-stoichiometry (δ_{c}) is introduced here, corresponding to the "solubility limit" of Cu concentration at the cathode of the MIEC. Based on the theory proposed by Yokota and Korte et al. [283],

$$V_{\mathrm{c}} = -\frac{RT}{F}\left(\operatorname{arcsinh}\left(\frac{\delta_c}{2\sqrt{K_e}}\right) - \operatorname{arcsinh}\left(\frac{2\delta - \delta_{\mathrm{c}}}{2\sqrt{K_e}}\right)\right). \tag{7.8}$$

K_e is the equilibrium constant for electrons and holes that is independent of stoichiometry, R is the gas constant, and T is the temperature. The thermodynamic theory developed herein predicts that a given off-stoichiometry and temperature gradient will result in limitations on the electrical potential difference that is stable across the material. Using this knowledge, the latter part of this paper will address possible ways to engineer stability in these materials for thermoelectric applications.

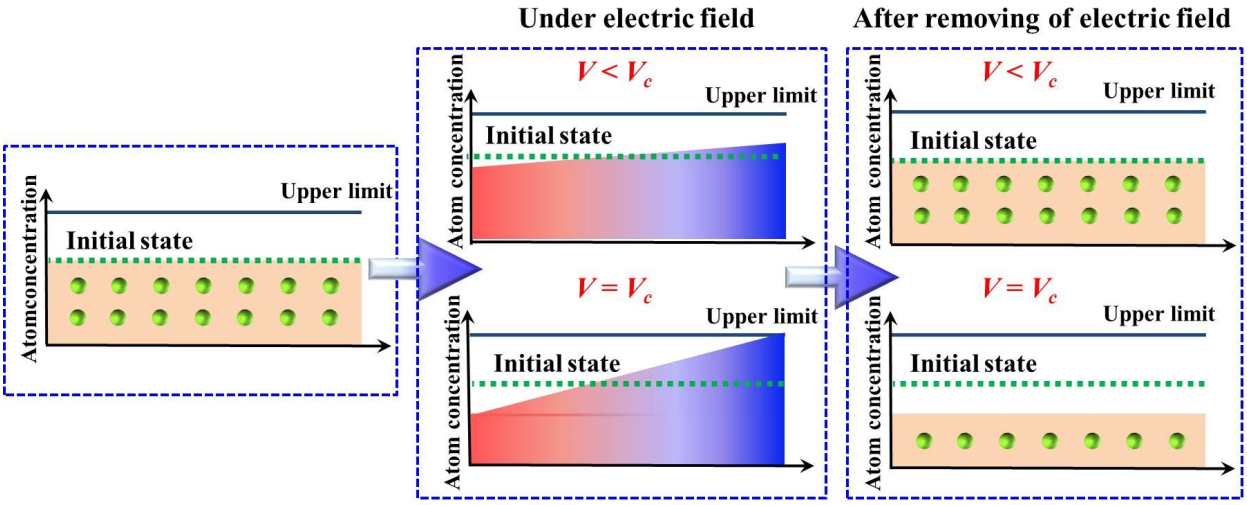

Figure 7.2: **Schematic of material behavior under experimental conditions leading to the determination of the critical voltage V_c.**

7.4 Isothermal Ion Transport in Mixed Conductors

Taking the family of Cu-based TE MIECs as an example, the determination of V_c is introduced for the isothermal case. When an externally applied electric field does not raise V between the two ends of the sample to the critical V_c value, the Cu atoms simply redistribute inside the sample to form a steady-state gradient of Cu concentration without metal deposition at the cathode (Fig. 7.1e). After removing the electric field, the Cu concentration gradient gradually returns to the initial homogeneous state (Figs. 7.1 and 7.2). Thus, for $V < V_c$, the Cu redistribution under the external electric field is temporary, with no lasting effect on the MIEC. However, when the external electric field reaches V_c (Fig. 7.1f), Cu metal will deposit. Although metallic Cu is not thermodynamically stable after the electric field is removed, many of the metallic deposits cannot immediately diffuse back into the sample (kinetically limited). In this case, the average Cu concentration inside the MIEC is reduced (Fig. 7.2), which causes measureable changes of the resistivity (Fig. 7.3a).

The V_c values for several Cu-based TE MIECs, including $Cu_{2-\delta}S$ (δ = 0, 0.01, 0.03, 0.04, 0.06, and 0.1), Cu_2Se, and $Cu_2S_{0.5}Se_{0.5}$, are experimentally determined at a constant temperature of 750 K (Table 7.1) by using the apparatus and method shown in Figs. 7.4 and 7.5.

The details can be found in Appendix G. The maximum V_c value for all samples is only 0.11 V (Fig. 7.3b). Such small values are consistent with the ease of observing Cu-metal

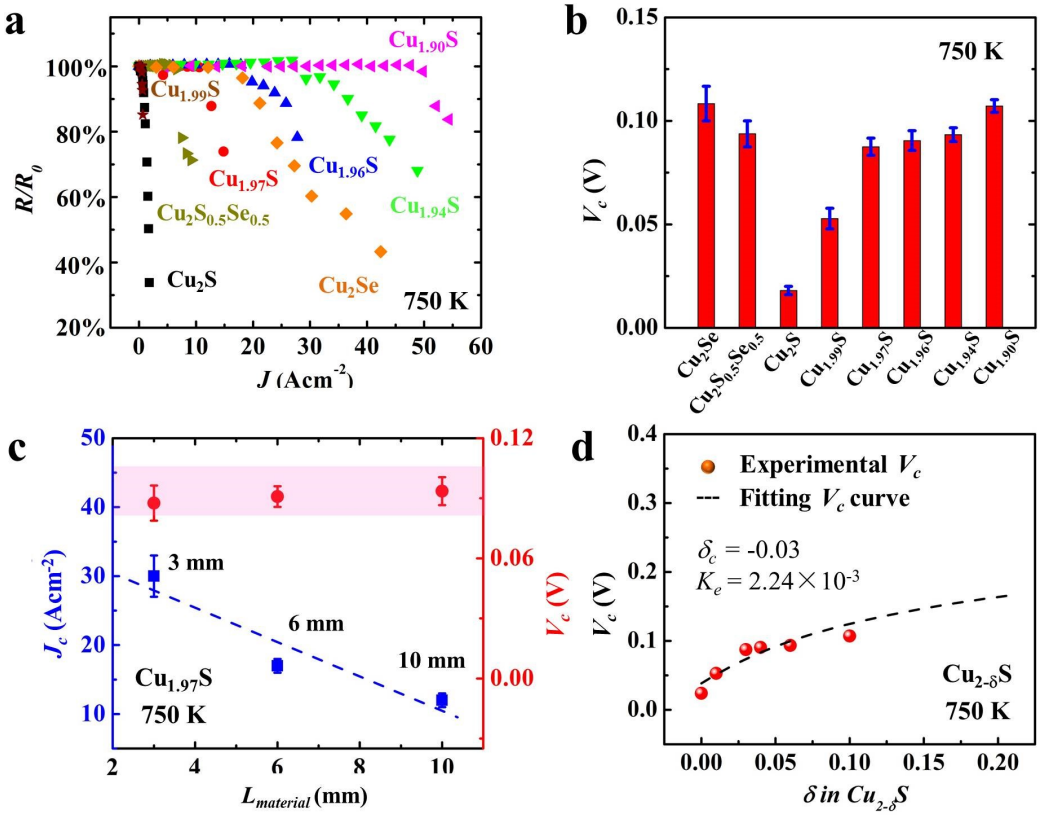

Figure 7.3: **Critical electric potential difference V_c for several Cu-based TE MIECs in the isothermal case.** (a) Current density dependence of relative electrical resistance variation R/R_0) for several Cu-based TE MIECs with L = 10 mm. (b) Experimentally determined V_c (L = 10 mm). (c) Material length L dependences of V_c and the critical current density J_c for $Cu_{1.97}S$. The dashed line is a guide to the eyes. (d) V_c as a function of Cu off-stoichiometry δ in the $Cu_{2-\delta}S$ (δ = 0, 0.01, 0.03, 0.04, 0.06, and 0.1) samples with L = 10 mm. The dashed line represents the V_c curve based on Eq. 7.8. All measurements were carried out at 750 K.

deposition in these TE MIECs [273, 274]. Notice that V_c is constant for a series of $Cu_{1.97}S$ samples with various material lengths, L, whereas J_c decreases with increasing L (Fig. 7.3c). This agrees well with Eqs. 7.5-7.7 in which V_c is not dependent on length but J_c is. Thus, although it may seem natural to be concerned about metal deposition due to high current density in a TE generator device, it is the voltage and not the current density that defines the critical quantity, which is in agreement with the insight of Eq. 7.5.

Furthermore, we found experimentally (Fig. 7.3d) that V_c gradually increases with increasing Cu off-stoichiometry (δ in $Cu_{2-\delta}S$). Intuitively, this coincides with a reduction in the chemical potential of Cu as the off-stoichiometric material is more willing to accept

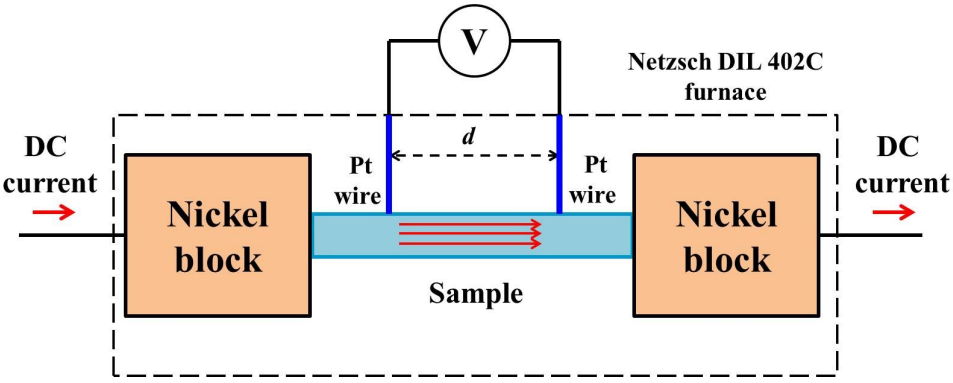

Figure 7.4: **Schematic of the experimental setup used to determine the critical electric potential difference in the isothermal case.**

Table 7.1: Experimental critical current density J_c, critical electronic potential difference V_c, and electrical conductivity σ for several typical Cu-based TE MIECs at 750 K. The compositions determined by electron probe microanalysis (EPMA) are also included.

Composition	**EPMA Composition**	**Sample Length (cm)**	J_c **(A cm^{-2})**	V_c **(V)**	σ**/10^4 (S m^{-1})**
Cu_2Se	$Cu_{2.004}Se$	10	18-21	0.103(±0.008)	1.74
$Cu_2S_{0.5}Se_{0.5}$	$Cu_{1.990}S_{0.5}Se_{0.501}$	10	7-8	0.096 ±0.006	0.52
Cu_2S	$Cu_{2.009}S$	10	0.14-0.21	0.024(±0.003)	0.02
$Cu_{1.99}S$	$Cu_{1.992}S$	10	0.47-0.57	0.053(±0.005)	0.14
$Cu_{1.97}S$	$Cu_{1.975}S$	10	11-13	0.087(±0.004)	1.14
$Cu_{1.96}S$	$Cu_{1.961}S$	10	18-20	0.090(±0.005)	2.01
$Cu_{1.94}S$	$Cu_{1.939}S$	10	27-29	0.093(±0.003)	2.86
$Cu_{1.90}S$	$Cu_{1.904}S$	10	51-54	0.107(±0.003)	4.67
$Cu_{1.97}S$	$Cu_{1.975}S$	6	16-18	0.090(±0.005)	1.74
$Cu_{1.97}S$	$Cu_{1.975}S$	3	28-32	0.093(±0.007)	0.52

Cu atoms. This trend can be well explained by Eq. 7.8. According to the Cu-S binary equilibrium phase diagram [284], $Cu_{2-\delta}S$ has a wide composition range ($0 < \delta < 0.27$) at 750 K. Thus, for these $Cu_{2-\delta}S$ (δ = 0, 0.01, 0.03, 0.04, 0.06, and 0.1) samples, constant values for δ_c (=-0.03) and K_e(=2.24×10^{-3}) fit the experimental data well using Eq. 7.8 (Fig. 7.3d). In theory, δ_c should correspond to the Cu-rich phase boundary composition found on the phase diagram, but here it is used as a phenomenological constant. Since $K_e = x_n x_p = \exp(-\Delta G_e/RT)$, where x_n and x_p are the molar fractions of intrinsic electrons and holes, respectively [283], the electron-hole pair free energy of formation, ΔG_e, is estimated to be 0.4 eV; consistent with the band gap of cubic Cu_2S reported by Lukashev et al [285]. In addition, it was found experimentally that the V_c values for both Cu_2S and Cu_2Se increase with increasing temperature (Fig. 7.6), which corresponds to an increase in $\Delta\mu_{Cu}^{crit}$ associated with the increase in phase width of these MIECs with temperature [284, 286].

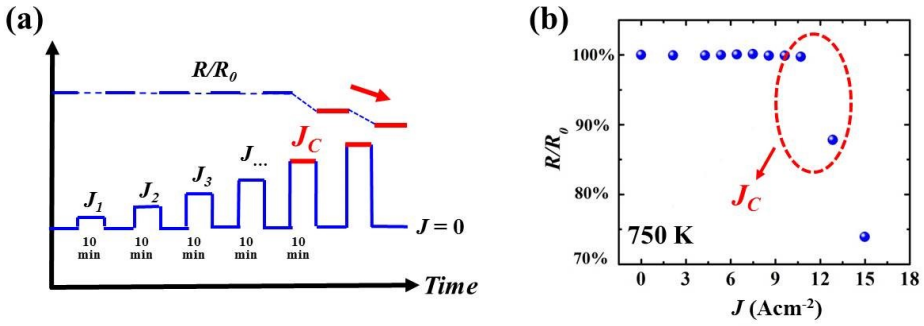

Figure 7.5: **Procedure for determining the critical voltage.** (a) Illustration of the measurement procedure for the critical electric potential difference in the isothermal case. The red lines depict the case when Cu deposits. (b) Current density dependence of the variation of relative electrical resistance for the $Cu_{1.97}S$ sample at 750 K. The points in the red circle depict the case when Cu deposits.

An illustration of how the atomic chemical potential changes across the single phase region and how the critical voltage is intuitively connected to off-stoichiometry is shown in Appendix F.1.

7.5 Ion Transport of Mixed Conductors in Temperature Gradient

In the non-isothermal case, the relative directions of the electric current and the heat flux are expected to have dramatic effects on V_c (Eq. 7.7). If the current direction is the same as the heat flux direction (i.e., $T_{\text{anode}} > T_{\text{cathode}}$), the electrical potential and temperature gradient work together to drive atom migration to the cathode. Conversely, when the direction of the electric current is opposite to the heat flux (i.e., $T_{\text{anode}} < T_{\text{cathode}}$), the current and temperature gradient have opposed driving forces for atom migration. Although the necessary condition for metallic Cu to plate out is that the chemical potentials of Cu in the MIEC are that of Cu metal at the cathode, this is a necessary but not sufficient condition because some degree of overpotential may be required to initiate and drive the electrodeposition reaction. The rate of deposition is not addressed in the thermodynamics analysis here.

Nevertheless, irrespective of overpotential effects, $\Delta\mu_{\text{Cu}}^{\text{crit}}$ is expected to be constant for a given temperature difference, regardless of the relative flux directions. This is because the range of chemical potentials corresponds to the range in compositional phase space, which is negligibly impacted by the electric field. For engineering applications, this allows us to contrast the critical current densities that can be applied relative to the temperature

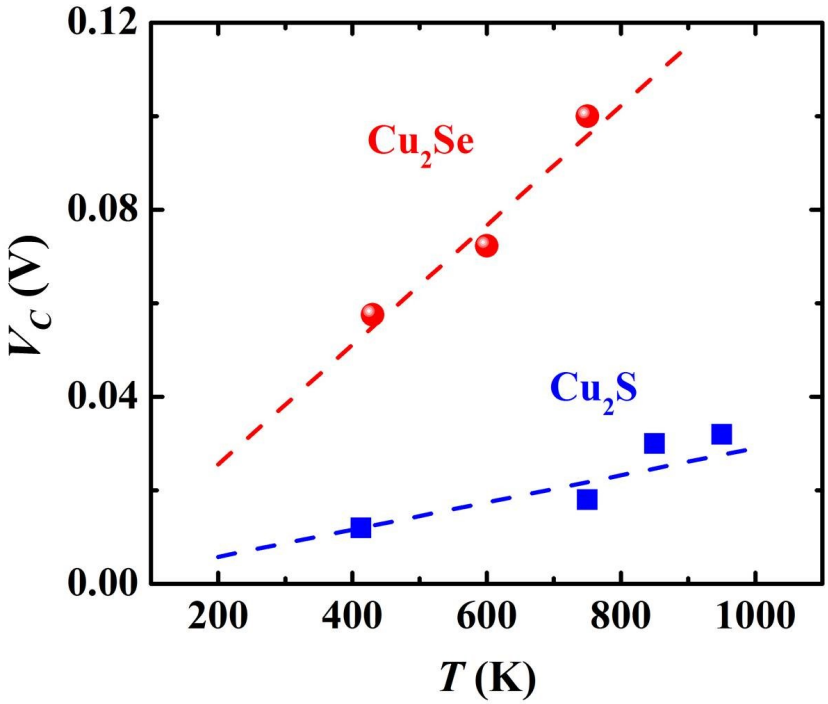

Figure 7.6: **Temperature dependence of the critical voltage.** Experimental critical electric potential difference for Cu_2Se and Cu_2S superionic phases at different temperatures. The dashed lines are guides to the eyes.

gradient. For a constant magnitude of $|\Delta T|$ and $\Delta\mu_{\text{Cu}}^{\text{crit}}$ in Eq. 7.7, we can write

$$V_{\text{c,same}} = \frac{J_{\text{c,same}} L}{\sigma_{\text{avg}}} = -\frac{1}{F}\,\Delta\mu_{\text{Cu}}^{\text{crit}} - S^*|\Delta T| \tag{7.9}$$

when the current is applied in the same direction as the temperature gradient ($J_{\text{c,same}}$), or

$$V_{\text{c, opposite}} = \frac{J_{\text{c,opposite}} L}{\sigma_{\text{avg}}} = -\frac{1}{F}\,\Delta\mu_{\text{Cu}}^{\text{crit}} + S^*|\Delta T| \tag{7.10}$$

when the current is applied in the opposite direction as the temperature gradient ($J_{\text{c,opposite}}$). Here, L and σ_{avg} are the effective length and average electrical conductivity across the superionic phase on the sample, respectively. Put another way, $V_{\text{c,same}}$ and $V_{\text{c,opposite}}$ are different from the isothermal case due to the additional potential that results from the thermodiffusion of charged species (generalized Seebeck effect).

Taking $Cu_{1.97}S$ as an example, the critical current density in the non-isothermal case

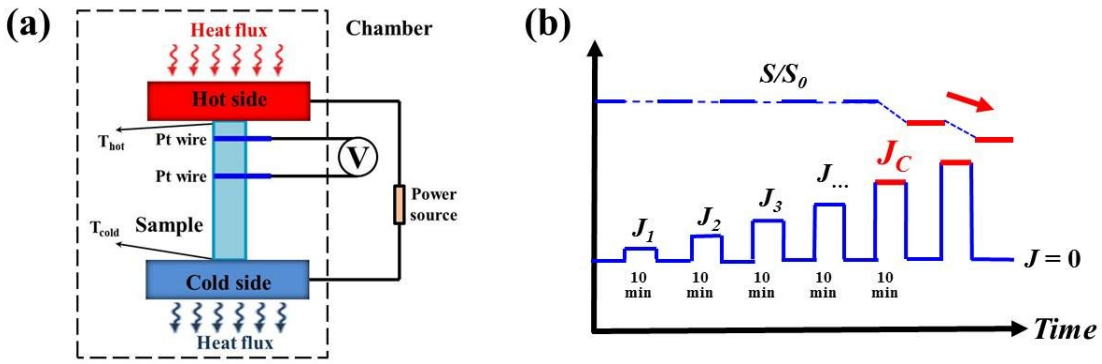

Figure 7.7: **Determination of the critical voltage in the presence of a temperature gradient.** (a) Schematic of the experimental setup used for determining the critical electric potential difference under a thermal gradient. (b) The measurement process illustrated for the critical electric potential difference in thermal gradient. The red lines depict the case when Cu deposits.

Table 7.2: The average electrical conductivity σ_{avg} of $Cu_{1.97}S$ for different temperature ranges.

	350–473 K	350–523	350–573 K	350–623 K	350–673 K
$\sigma_{avg}/10^4$ (S m^{-1})	1.01	0.96	0.94	0.98	1.03

is measured by using the apparatus and method shown in Fig. 7.7. The details can be found in Appendix G. At a constant ΔT(=673 K−300 K), a significant difference in critical current density is required depending on the relative flux directions (Fig. 7.8a). If the current direction is the same as the heat flux direction, $J_{c,same} \approx 0.3$ A cm^{-2} is large enough to obtain metallic Cu deposition near the cold side. However, if the current direction is reversed, $J_{c,opposite} \approx 20$ A cm^{-2} is required to obtain metallic Cu deposition at the hot side. This observation is in agreement with the thermodynamic expectations, although overpotential effects may contribute. To further demonstrate the trend predicted by Eq. 7.7, $V_{c,same}$ and $V_{c,opposite}$ were evaluated as a function of increasing $|\Delta T|$ by using the σ_{avg} data shown in Table 7.2 (Fig. 7.8b). As expected, $V_{c,opposite}$ is found to increase with $|\Delta T|$ and $V_{c,same}$ is found to decrease with $|\Delta T|$ (Fig. 7.8b).

7.6 Strategy to Improve Stability in Mixed Conductors

In real TE generators the direction of the current flowing through the p-type legs is always the same as the direction of the heat flux. Consequently, the thermodynamic understanding validated through the temperature gradient experiments is very helpful to design stable TE devices based on these high performance MIECs. Eq. 7.5 and Fig. 7.3c

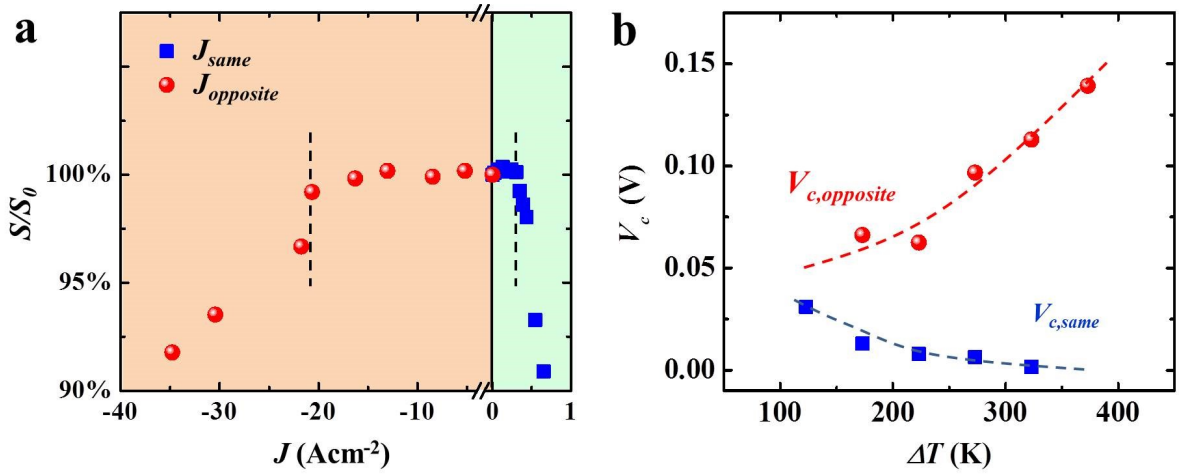

Figure 7.8: **Critical electric potential difference V_c measurements for the TE MIECs under thermal gradient.** (a) The relative Seebeck coefficient variation (S/S_0) as a function of the current density for $Cu_{1.97}S$ at $T_{cathode}$ = 300 K and T_{anode} = 673 K. The positive J means that the current direction is the same as the heat flux direction. The negative J means that the current direction is opposite to the heat flux direction. (b) Experimentally determined $V_{c,same}$ and $V_{c,opposite}$ as a function of $|\Delta T|$, showing qualitative agreement with Eq. 7.7. The temperatures at the anode and cathode for each flux direction can be found in text. The length of all measured samples is 6 mm. The dashed lines are guides to the eyes.

clearly show that V_c is length independent; thus, $V_{c,same}$ in Eq. 7.7 is length independent as well. Changing the geometry cannot change the critical chemical potential – it is fixed for a given temperature, temperature gradient, and off-stoichiometry. However, the total voltage across a thermoelectric leg can be increased by using a series connection of several segments of MIEC material, in which electrically-conducting, but ion-blocking interfaces are used between the individual segments. The reason for this is simple: the total voltage across the series-segmented leg, V_{leg}, is the sum of voltages across each segment, V_{seg} as

$$V_{leg} = \sum_{segments} V_{seg}. \tag{7.11}$$

When n segments are approximately the same length, and each segment has the same critical voltage, $V_{seg,c}$, the critical voltage for the entire leg is $V_{leg,c} = nV_{seg,c}$.

The schematic of this strategy is shown in Fig. 7.9a. These interfaces limit the ion movement but allow the free movement of the electrons or holes. Schematically, the ion concentration distribution rises linearly (as in Fig. 7.1e) in each segment, but because the chemical potential is reset by the ion-blocking interfaces a saw-tooth like pattern can

be obtained. Engineering the number of segments n can allow for high voltages (and corresponding current densities) without reaching the critical chemical potential that results in the degradation of the material.

Initially, we test this strategy at a constant temperature of 750 K. The unsegmented $Cu_{1.97}S$ leg exhibits a critical applied current density of ≈11 A cm^{-2}. However, for a three-segment $Cu_{1.97}S$ leg, the critical applied current density is ≈30 A cm^{-2} (Fig. 7.9c). This is in excellent agreement with the thermodynamic theory. The critical chemical potential for Cu at 750 K is then equivalent to $V_{\text{seg,c}} = 0.09$ V, as determined from the unsegmented leg. Because V_{c} is geometry independent, each segment has this same critical voltage. When the three segments are connected in series the critical voltage across the leg rises to $V_{\text{leg,c}}$ =0.27 V, exactly as expected.

Series segmentation is also effective in the case of a temperature gradient. As before, the critical voltage for the leg is the sum of critical voltages for each segment. However, the temperature dependencies of $\Delta\mu_{\text{Cu}}^{\text{crit}}$ and S^* may lead to different critical voltages for each segment. Nevertheless, the unsegmented leg can only substantiate a small current density of $J_{\text{c,same}} = 0.3$ A cm^{-2} (Fig. 7.9d). A three-segment leg, was found to sustain a significantly larger current density, $J_{\text{c,same}} \approx 3.0$ A cm^{-2}, about one order of magnitude higher than the unsegmented $Cu_{1.97}S$ leg (Fig. 7.9d). Correspondingly, the critical voltage across the leg is increased from $V_{\text{c,same}} = 0.002$ V to about 0.018 V. If more Cu-atom blocking layers are added, the critical total voltage across the leg can be expected to continue to increase. Therefore, the present data strongly suggests that MIECs can indeed sustain large current densities and achieve high stability whenever the local chemical potential is engineered to be lower than the corresponding critical chemical potential.

7.7 Summary

By understanding the thermodynamic principles behind ion and atom migration and metal deposition in TE MIECs, we derive a thermodynamic model to understand the critical electrical potential difference for decomposition of non-stoichiometric MIECs at constant temperature, and demonstrate that it is a critical voltage, not current, that is the limiting factor. In the more complicated case of concurrent electrical and thermal fluxes, the experimental observations are in excellent qualitative agreement with the thermodynamic predictions. Furthermore, we propose the use of ion-blocking but electrically conducting interfaces to enhance the critical electric potential difference in engineering

applications. This is most efficiently done with a grain-boundary engineered microstructure. This study clearly shows that ion migration and metal deposition can be effectively suppressed in MIECs, which has been an overwhelming concern, but not solved before. Consequently, the technique demonstrated herein to increase the critical potential opens a new possibility of using these TE MIECs in real applications. Recently, we have developed a geometric design strategy (at the device level) to avoid the critical voltage of mixed conductors, which resulted in a stable high-efficiency thermoelectric device [77]. We expect that the mechanism and strategies proposed in this study for TE materials should also be valid for other ionic conductors, and thus can be used in the research areas of, photovoltaics, solid electrolytes, and various sensors. Although the strategy of blocking ion transport is not applicable for batteries, the experimental and theoretical methods for characterizing and understanding atom deposition in MIECs should be applicable to Li batteries.

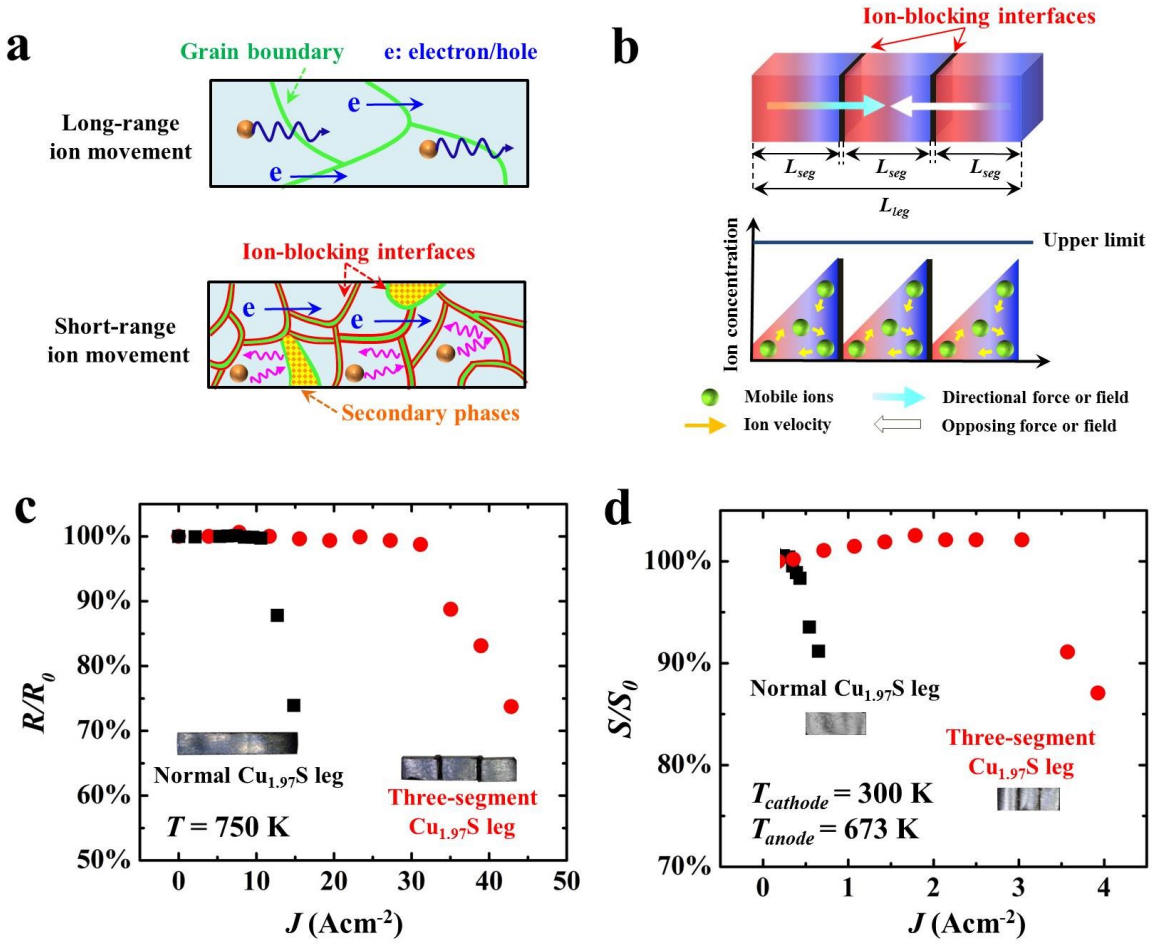

Figure 7.9: **Strategy to improve the service stability and reliability of TE MIECs.** (a) Schematic for limiting the ion movement by including thin electron-conducting and ion-blocking interfaces; either grain boundaries (red areas) or a secondary phase (yellow areas). (b) Schematic of ion-blocking electrically conducting interfaces that allow the concentration profile to be reset at each interface so that the ion concentration does not ever reach the upper limit. (c) Relative resistance variation (R/R_0) as a function of current density for different $Cu_{1.97}S$ samples at a constant temperature of 750 K without a thermal gradient. (d) Relative Seebeck coefficient variation (S/S_0) as a function of current density for different $Cu_{1.97}S$ samples under the condition of thermal gradient (T_{anode} = 673 K and $T_{cathode}$ = 300 K). The insets in (c) and (d) show the optical images of the measured $Cu_{1.97}S$ samples. The critical current density was measured across the segment in the middle.

Chapter 8

Energetic Considerations of Fracture

8.1 Overview

Fracture mechanics is a fundamental topic to materials science. Fracture toughness, in particular, is a material property of great technological importance for device design. The relatively low fracture toughness of many semiconductor materials, including many electronic and energy materials, makes it difficult to use these materials in applications with large external stresses. Here, it is shown how the ideal strength of crystalline materials, which can be obtained from density functional theory calculations, is a direct method to probe fracture behavior and fracture toughness. Specifically, the integral stress-displacement method is used to estimate the energy (work) of fracture that is needed for the calculation of fracture toughness. While fracture is assumed to occur in the weakest crystallographic direction, other idealized cases (including those with defects) could easily be adapted. By comparison with experimental fracture toughness values, the calculated fracture toughness values provide realistic estimates for bulk materials and are predictive of experimental single crystal results. Consequently, ideal strength calculations may be useful for benchmarking experimental measurements and can serve as a starting point for the construction of multi-scale fracture models and the computational design of new materials and devices.

8.2 Fracture Criterion

The resilience of a material to fracture is defined in part by its fracture toughness, which describes the conditions for crack growth to occur. Since even ambient stresses present in

everyday devices can be problematic for some materials, fracture toughness is an important engineering design metric. In particular, the utility of semiconductor materials for applications having applied stresses often requires clever engineering solutions. Thermal and vibrational stresses are often present in electronic [287, 288] and energy materials [289, 290] (including those used for efficient gas turbines [70]) during operation. Additionally, new, strong materials are desired for modern applications, like internet-of-things devices [291].

8.2.1 Definition of Fracture Toughness

The mechanical failure of materials by fracture (or rupture) is an inevitable result of the finite strength of atomic bonds. Although bonding is the fundamental material property that determines fracture conditions, defects (e.g. cracks) are often the primary focus since they serve to amplify local stresses well beyond the nominal external stress applied to the material. Griffith [292] was the first to recognize that material properties (i.e. bonding) and system properties (i.e. stress state and defect geometry) were connected through a thermodynamic criteria for fracture. Later, Irwin [293] and Orowan [294, 295] expounded upon Griffith's work and defined fracture toughness, K, as the inherent material property which determines fracture conditions. For plane strain conditions, the mode I (tensile force acting to open the crack) fracture toughness, K_{Ic}, is given by

$$K_{\mathrm{Ic}}^2 = G_{\mathrm{Ic}} E/(1-\nu^2) = \phi \sigma_{\mathrm{f}}^2 a_{\mathrm{c}} \tag{8.1}$$

where E and ν are the Young's modulus and Poisson's ratio for an isotropic material, G_{Ic} is the work of fracture per unit area, σ_{f} is the nominal stress needed for fracture to occur in a material with critical crack length, a_{c}, and ϕ is a numeric factor depending on the geometry of the crack. For brittle materials having an elliptical crack, Griffith found that $\phi = \pi$ and $G_{\mathrm{Ic}} = 2\gamma_{\mathrm{s}}$, where γ_{s} is the surface energy and the factor of 2 arises because 2 surfaces are created. Orowan and Irwin generalized the Griffith result to include ductile fracture, but the form of Eq. 8.1 is retained. In the general sense, G_{Ic} is the energy per unit area needed to create additional surfaces.

For mode II (shear force in the plane of the crack, parallel to the crack direction) in the plane strain condition, Rice [296] derived the fracture toughness K_{IIc} as

$$K_{\mathrm{IIc}}^2 = 2 G_{\mathrm{IIc}} \mu/(1-\nu) \tag{8.2}$$

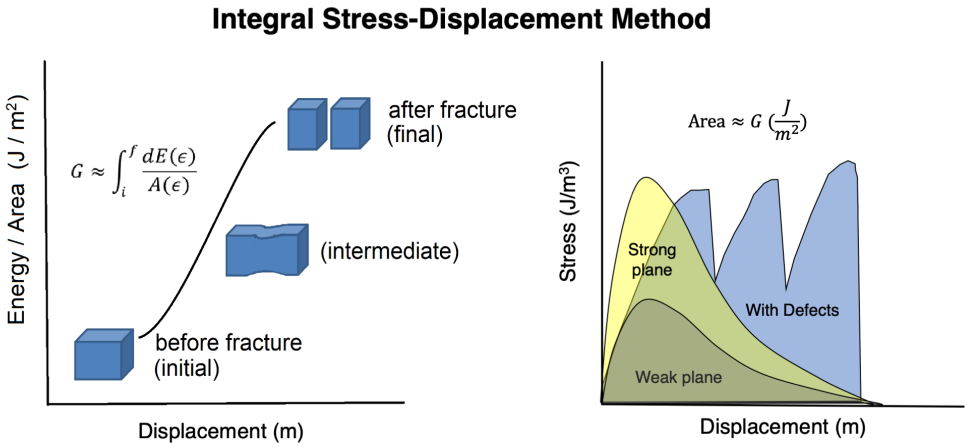

Figure 8.1: **The integral stress-displacement method of determining the fracture energy, G.** The physics of fracture is captured by the continuous deformation of the atomic structure in the computational simulation (left). The work required to create two new surfaces is found by integrating the stress-displacement curve (right). The stress-displacement curve is different for different crystallographic directions within a material and can be changed by adding defects such as twins to the crystallographic structure. These defect structures can be investigated using this method which may or may not increase fracture energy.

where μ is the shear modulus and $G_{\mathrm{IIc}} = \gamma_{\mathrm{us}}$, which Rice calls the unstable stacking energy corresponding to the nucleation of a full dislocation.

Although fracture toughness is defined by material properties, it is experimentally more accessible to estimate K by finding the critical crack length for a given applied stress. This is largely because G is difficult to obtain experimentally. While it is straight-forward to find relaxed surface energies (e.g. the Boettger method [297, 298] or other "slab methods"), a distinction should be made between surface energy (e.g. the excess energy due to the dangling bonds of a relaxed surface) and the energy required to make a surface.

8.2.2 The Work of Fracture

The "surface energy" relevant to fracture is, in fact, the energy (work) required to break atomic bonds and form a new surface (i.e. $G/2$). While having units of [J/m^2], this is not necessarily the same surface energy as γ_{s}. Griffith made the approximation that the frac-

ture energy was twice the surface energy ($G = 2\gamma_s$) for brittle materials. This approximation is valid when surfaces are made via thermodynamically reversible processes, which is not necessarily the case due to the complexity of fracture (e.g. plasticity). This misunderstanding has led to widespread estimates (of varying complexity) of fracture toughness based on relaxed surface energies found computationally [299, 300, 301, 302, 303]. However, the ability to investigate fracture directly via computational methods no longer requires such an approximation to be made. The integral under any stress-strain curve is the total mechanical energy stored in the material per unit volume (i.e. energy density). When the material is strained to failure, the integral under the stress-strain curve describes how much work was done to the material to fracture it. This is often called toughness [304]. Alternatively, the integral of a stress-displacement curve has units of energy per unit area and describes the energy required to create the new surfaces formed when the material fractures (Fig. 8.1). These quantities can be evaluated at the atomic scale using computational methods to determine the "ideal" stress-strain or "ideal" stress-displacement relations for atomic structures (e.g. the unit cell of a crystalline material).

Herein, it is shown that the fracture energy G (specifically G_{Ic} and G_{IIc}) can be estimated from the integral stress-displacement method using the ideal stress-displacement curves obtained by density functional theory calculations (Fig. 8.1). From this estimation of G the fracture toughness can be calculated. By comparison with experimental reports, this method gives realistic estimates for fracture toughness that may provide insights into the fundamental nature of fracture beyond the atomic scale.

8.3 Ideal Strength of Titanium Carbide and Nitride

Ideal strength calculations were undertaken for TiC and TiN using density functional theory methods (see Appendix I). In both cases, a tensile stress was applied along the [100] crystallographic direction. Their stress-displacement curves are shown in Fig. 8.2. The ideal strength (i.e. the maximum stress that the material can obtain) is 33.8 GPa for TiC and 31.4 GPa for TiN.

We extracted the bond length changes to determine the response of the bonds to tensile strain, as shown in Fig. 8.3. The Ti-C and Ti-N bonds along the [100] direction linearly increase with increasing tensile strain. This suggests the structure uniformly resists the deformation. The softening and breakage of these bonds gradually release the internal stress, leading to structural failure.

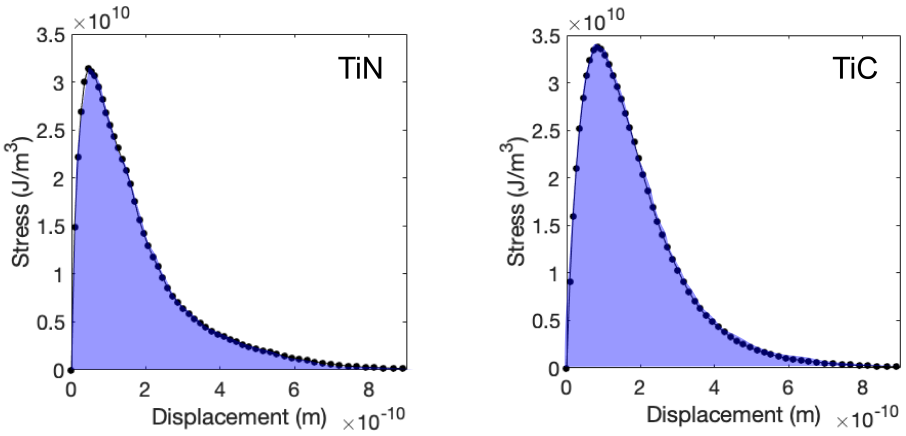

Figure 8.2: **Ideal stress-displacement curves for titanium carbide and titanium nitride.** Here, the tensile loading is in the [100] crystallographic direction. Note that displacement can be converted to strain using the relevant lattice parameters (4.34 Å for TiC and 4.25 Å for TiN).

Specifically, the atomic structures and bond lengths against tensile strain were extracted to determine the bond-responding processes. As the tensile strain increases to 0.104 which corresponds to the ideal tensile stress of 31.38 GPa for TiN (Fig. 8.3b), the strong covalent Ti-N1 bond along the [100] direction is uniformly stretched from 2.15 to 2.37 Åwith a stretching ratio of 10.2%. While the Ti-N2 bond along the [001] direction is slightly shrunk from 2.15 to 2.09 Åwith a shrinking ratio of 2.8%. With further increasing tensile strain, the Ti-N1 bond starts to soften, with a linearly increased length, while the Ti-N2 bond length remains unchanged. This leads to the structural yielding and gradually released internal stress. At 1.208 tensile strain (Fig. 8.3c), the Ti-N1 length increases to 4.74 Å. This highly stretched length indicates a highly softened or non-interaction bonding, leading to a very low internal stress of 2.02 GPa. The softening and breakage of these covalent Ti-N1 bonds gradually release the internal stress, leading to the structural failure. In TiC, the atomic configurations and bond-responding process is similar with that in TiN, as shown in Fig. 8.3d.

Using the integral stress-displacement method (illustrated in Fig. 8.1), we estimated the fracture energy G from the weakest crystallographic direction for both our TiC and TiN calculations and several previously reported ideal strength calculations [305, 306, 307, 308, 53, 309, 310, 311, 312, 313, 314, 315, 316, 317]. From the estimate of G, and the bulk elastic properties also found from DFT, fracture toughness values were calculated using Eq. 8.1 or 8.2 (depending on the mode of fracture). Surface energies of relaxed structures were also calculated for several materials and used to estimate the fracture energy (Table 8.2).

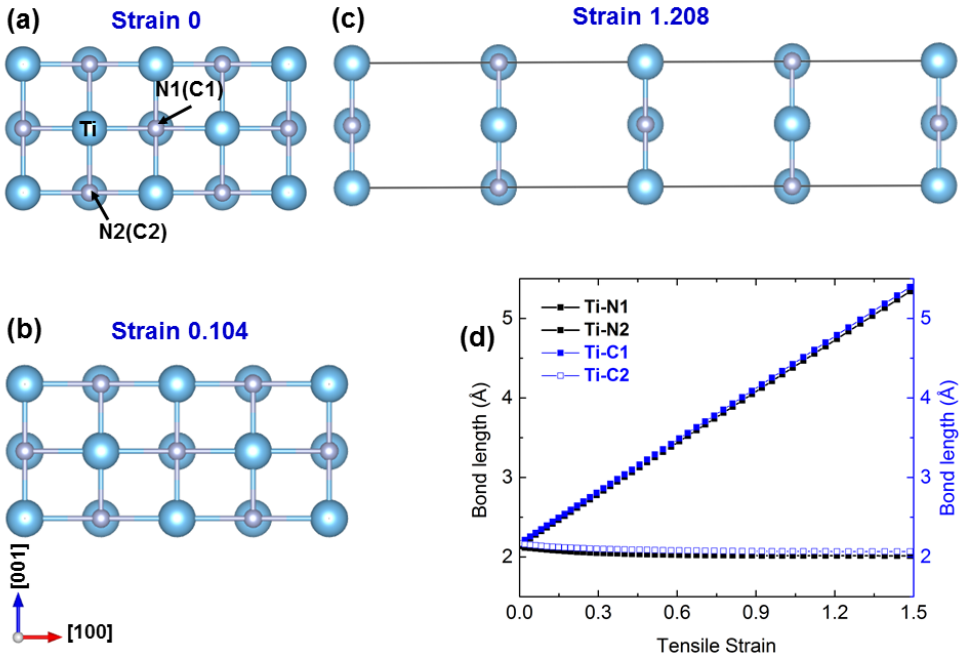

Figure 8.3: **Bond deformations in titanium carbide and titanium nitride.** Bond length as a function of tensile strain for TiC and TiN along the [100] direction in tension.

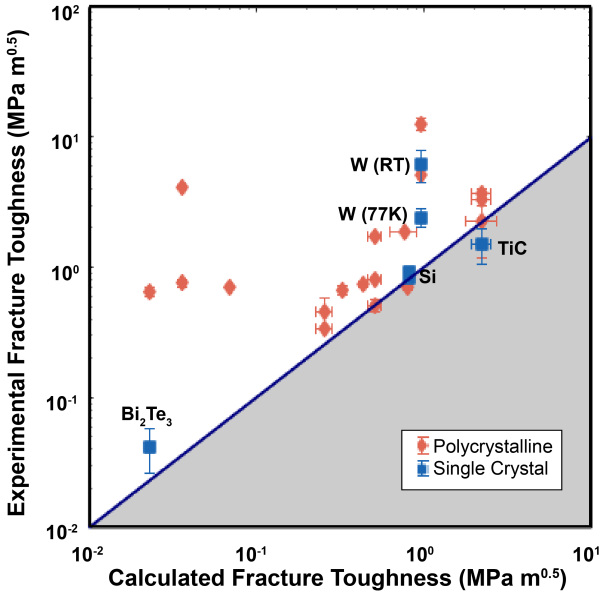

Figure 8.4: **Calculated fracture toughness compared to experimental values.** Specifically, the comparison of experimental fracture toughness values [48, 49, 50, 51, 52, 53, 54, 55, 56, 57, 58, 59, 60, 61, 62, 63, 64, 65, 66] to fracture toughness values calculated using fracture energies estimated from the integral stress-displacement method. This calculated fracture toughness is an estimate of the experimental fracture toughness in bulk materials using the idealized case where fracture occurs in the weakest crystallographic direction and without consideration of any additional toughening mechanisms. In this sense, the fracture toughness calculated herein is a realistic lower limit of experimental values. Both mode I and mode II fracture toughness calculations are plotted (see Table 8.1).

In order to obtain the fracture energy, G, the integral of the stress-displacement curve is needed. Knowledge of the unit cell, was utilized for each material in order to convert strain to absolute displacement. Using the crystallographic direction in which the crystal is being pulled as well as the DFT calculated lattice parameters, the relevant lattice parameter was determined. For instance, for a cubic material being pulled in the <100> direction, the relevant lattice parameter was simply the lattice parameter, a. Likewise, for a BCC material being pulled in the <111> direction, the relevant lattice parameter is $\frac{\sqrt{3}}{2}a$. In order to convert the stress-strain curve to a stress-displacement curve, the strain was multiplied by this relevant lattice parameter.

Numerical integration was performed in MATLAB, using interpolant fitting between data points. In cases where the DFT created stress-displacement curve did not include data points for the zero of stress at complete material failure, linear extrapolations were intro-

duced to complete the area under the curve, introducing some subjectivity to the estimation of G. This procedure may affect the estimate of G by a few percent. The values for unit cell parameters, modulii, Poisson's ratio and estimated fracture toughness for all of the materials in this study are compiled in Table 8.1.

8.4 Comparison of Calculated Fracture Toughness with Experiment

Fracture toughness is an important limiting factor for device implementation and lifetime. The desire for computational materials design necessarily includes having estimates of fracture toughness, K, that can be used in engineering purposes. Herein, K is calculated from the fracture energy, G, estimated from ideal strength calculations. This integral stress-displacement method aims to capture the physics of fracture within the idealized case of fracture occurring on the weakest crystallographic plane.

The physics of fracture on the atomic scale is the breaking of and/or rearrangement of atomic bonds. While the loading geometries and distribution of internal stresses within bulk materials is vastly more complicated, computational materials techniques (DFT or molecular dynamics) are well-suited to investigate specified loading conditions on local atomic structures. In particular, the "ideal" strength of crystalline solids can be investigated, which is found from the stress-strain behavior of a defect-free "perfect" crystal. The magnitude of the ideal strength depends on the loading geometry and crystallographic direction. A pure tensile stress results in the cleavage of atomic planes. Shear stress results in the formation of a dislocation. Generally, ideal shear strengths are lower than ideal tensile strengths, reflecting the experimental evidence that dislocations tend to govern deformation in crystals. Furthermore, for a particular applied stress, certain crystallographic directions are stronger than others. "Cleavage planes" are typically planes of high atomic density that are the first to fracture in brittle materials.

In general, crack propagation will depend on the local stress state near the crack tip relative to the crystal orientation. Consequently, the weakest crystallographic plane may not always be the preferential crack growth direction. This is particularly relevant for bulk polycrystalline materials where the relative orientation of adjacent grains can influence crack propagation. Here, fracture toughness is calculated using the fracture energy G estimated from the weakest crystallographic plane in either shear and/or tensile loading. This is representative of the idealized case of fracture occurring along the weakest crystallographic plane, without crack deflection or toughening mechanisms present. This calculation of K can thus be expected to capture the magnitude of experimental results

for polycrystalline samples, but is more aptly a lower bound. As seen in Fig. 8.4 this is generally the case. Even though fracture toughness values can vary drastically for the same material, the estimated K provides a realistic magnitude of the observed fracture toughness in most cases, and is predictive of the lowest values reported for a given material. Experimental values much larger than these estimates are likely due to additional toughening mechanisms not captured by the present method, such as the effects of polycrystallinity.

8.4.1 Titanium Carbide

TiC has well-studied mechanical properties due to its high melting point and high hardness making it valuable in high temperature applications such as components for jet engines and rocket nozzles [323]. Our fracture toughness calculations were able to capture the magnitude of fracture toughness quite well. The single crystal fracture toughness is reported to be $\sim$1.5 MPa $\sqrt{\text{m}}$ in the [100] direction [59]. Our fracture toughness estimate along that same direction was calculated to be 1.9 MPa $\sqrt{\text{m}}$, demonstrating good agreement between experiment and this method. The dependence of fracture toughness on crystal orientation as well as polycrystallinity is well-demonstrated in TiC. As illustrated in Fig. 8.1, the area under the curve, G, can vary between the weak and strong crystallographic directions. Thus, if a material is not fracturing along the weakest direction, it can be expected that the fracture toughness would be greater. For example, while the weakest crystallographic direction of the single crystal has an experimental fracture toughness as low as $\sim$1.5 MPa $\sqrt{\text{m}}$, this increases to $\sim$3.6 MPa $\sqrt{\text{m}}$ in the strongest crystallographic direction [59]. Polycrystalline experiments of fracture toughness report values around 3.6 MPa $\sqrt{\text{m}}$ [59, 315]. Further efforts using alloying and introducing nanostructures have been found to increase the fracture toughness to $\sim$ 7 MPa $\sqrt{\text{m}}$ [323, 324].

8.4.2 Titanium Nitride

Thin film TiN is incredibly useful for microelectronics [325, 326, 327], corrosion protective coatings [328, 329], and energy material applications [330, 331, 332]. These applications often include high stress states which necessitates understanding of mechanical properties including fracture behavior. Thin film TiN has been reported experimentally to have a fracture toughness of about 1.72-2.9 MPa $\sqrt{\text{m}}$ [329, 333], in excellent agreement with our calculation of 1.76 MPa $\sqrt{\text{m}}$. The strong agreement between our calculations using

the integral stress-displacement and experimental values for TiC and TiN suggests that this method may work well for other technical ceramics and semiconductors.

8.4.3 Bismuth Telluride

In fact, these same insights gained from the well-studied TiC and TiN materials are also demonstrated in the fracture toughness of the layered material Bi_2Te_3, which relevant for thermoelectric applications near room temperature [334]. Our calculated fracture toughness ($\sim$ 0.02 MPa $\sqrt{\text{m}}$) corresponds to the lower bound of the experimental value for a single crystal (0.042 $\pm$ 0.016 MPa $\sqrt{\text{m}}$ [48]). Given the particularly brittle nature of Bi_2Te_3 the fracture toughness of polycrystalline materials can be $\sim$10$\times$ higher than the single crystal value due to crack blunting and deflection at grain boundaries. Particularly for highly anisotropic materials, grain orientation can be expected to play a significant role [49].

8.4.4 Considerations of Temperature Dependence

The close agreement with single crystal data is not surprising since the DFT calculations are representative of 0 K conditions for a perfect single crystal. Toughening mechanisms (e.g. defects) introduced at higher temperatures or polycrystalline conditions are not taken into account and thus we would expect our calculated fracture toughness values to be at the lower bound of experimental work. For instance, it has been shown experimentally that tungsten and vanadium undergo ductile to brittle transitions causing the fracture toughness to decrease with temperature [335, 62]. Our estimation for the fracture toughness of single crystal W is in strong agreement with measurements at 77 K, and shows the embrittlement with temperature down to 0 K (Fig. 8.5). Thus, while the ideal strength calculations reported here correspond to the 0 K condition, they may be used as a basis for understanding temperature dependent fracture mechanics.

Nevertheless, even though the temperature dependence of W had to be taken into consideration, the single crystal experimental data was well predicted by the present method. In addition to TiC and Bi_2Te_3, the calculated fracture toughness of Si also showed good agreement with single crystal experiments. These were all room temperature fracture toughness values that do not have the same strong temperature dependence as W. The overall agreement of our calculated K with single crystal experimental values (compare solid line with blue squares in Fig. 8.4) is a strong indication that the essential physics of fracture is being captured by the computational technique.

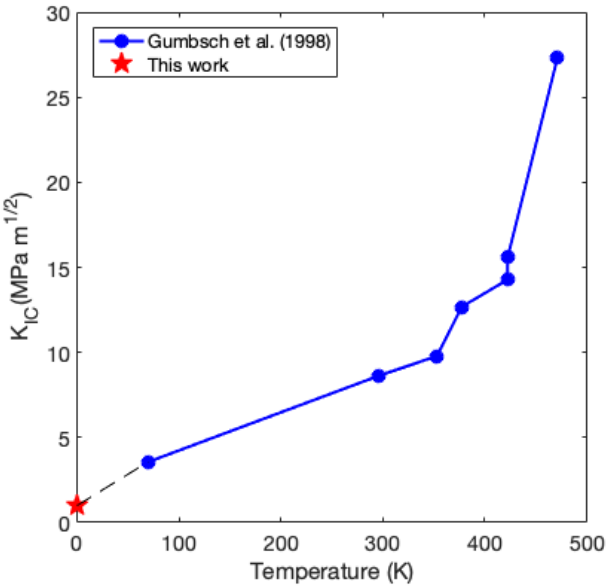

Figure 8.5: **Ductile to brittle behavior of fracture toughness in BCC tungsten.** The ductile to brittle transition in tungsten results in a drastic reduction in fracture toughness as the temperature is lowered from room temperature. Here, our 0 K calculation of fracture toughness is in agreement with the experimental trend in fracture toughness. This behavior is somewhat common in BCC metals, but not others, so while the 0 K DFT calculation is a starting point for understanding the temperature dependence of materials like tungsten, in general the 0 K calculation is in agreement with room temperature experimental values of fracture toughness.

8.4.5 Extension to Defect Structures

Although the "ideal" strength of solids may not include defects [336], it is still possible to investigate the effects of defect structures on fracture toughness using this method [307, 305]. This is shown schematically in Fig. 8.1. In the case of Bi_2Te_3, a factor of 2 to 4 improvement in fracture toughness may be possible by introducing nanotwinning to the structure. This was estimated by considering the DFT calculated stress-strain relations for atomic arrangements having a nanotwinned structure [305, 307]. In general, computational techniques may provide a unique insight into the physics of fracture when point defects (e.g. vacancies or atomic substitutions), dislocations or defect structures (like grain boundaries) are included in the calculation. It has been shown experimentally [337, 338, 339] that the presence of defects can have varying degrees of impact on the fracture toughness depending on factors such as dislocation structure, grain boundary geometries, and defect pinning. The generality of the integral stress-displacement method lends itself to computationally probing the fracture behavior of many atomic ar-

rangements, allowing for greater insight to fracture mechanisms on the atomistic scale.

8.4.6 Comparison to Relaxed Surface Energies

Lastly, it should be noted that the estimates of fracture energy G found from slab calculations of surface energy (Eq. I.0.1) and from the integral stress-displacement method were not always in agreement (Table 8.2). The surface energy found by the slab method is for a relaxed structure and does not probe the continuous deformation of the material during fracture. Thus, while further investigation is needed to understand the discrepancy between the two methods, the integral stress-displacement method (Fig. 8.1) is expected to be a better probe into the actual fracture mechanics, which are not necessarily thermodynamically reversible.

8.5 Summary

Ideal strength calculations provide insights into fracture behavior at the atomic level. The fracture energies obtained from the weakest crystallographic directions result in fracture toughness estimates whose magnitude are consistent with experimental reports and provide a basis for more-involved studies of fracture. The effects of defects like vacancies, interstitials, dislocations and grain boundaries may also be investigated within the framework of the integral stress-displacement method. Although fracture is inherently complicated, realistic values of fracture toughness can be calculated that can be used for computation based materials design [226], multi-scale fracture models, or other engineering applications where a baseline approximation of fracture toughness is necessary. Since this work relies only on first principles, it could be used to calculate the anticipated fracture toughness of new materials, allowing for reverse engineering towards the development of next-generation technologies.

Table 8.1: Parameters used in estimating fracture toughnesses where E is the Young's modulus, μ is the shear modulus, ν is Poisson's ratio, and G is the estimated fracture energy.

Material	Tensile (T) or Shear (S)	Calculated fracture toughness ($MPa\sqrt{m}$)	Unit cell parameter(s) (Å)	E (GPa)	μ (GPa)	ν	G (J/m^2)
Bi_2Te_3	S	0.02	a=4.47, c=31.15 [305]	15 [305]	11 [305]	0.21 [305]	0.02
$CaMg_2Sb_2$	S	0.17	a= 4.69, c= 7.59 [310]	69 [310]	28 [310]	0.22 [310]	0.40
$CaZn_2Sb_2$	S	0.13	a=4.50, c= 7.51 [310]	52 [310]	20[310]	0.30 [310]	0.30
$CoSb_3$	S	0.46	a=9.048 [306]	145 [306]	59 [306]	0.23 [306]	1.38
$CoSb_3$	T	0.56	a=9.048 [306]	145 [306]	59 [306]	0.23 [306]	2.04
Ge	T	0.80	a=4.075 [318]	155 [61]	45 [318]	0.19 [318]	3.95
InSb	S	0.24	a=6.648 [307]	49 [307]	19 [307]	0.28 [307]	1.07
La_3Te_4	S	0.07	a= 9.686 [308]	64 [308]	25 [308]	0.29 [308]	0.07
Mg_3Sb_2	S	0.10	a= 4.59, c= 7.27 [310]	48 [310]	18 [310]	0.31 [310]	0.18
PbS	S	0.44	a= 5.994 [53]	77 [53]	30 [53]	0.27 [53]	2.29
PbSe	S	0.33	a=6.207 [53]	70 [53]	28 [53]	0.26 [53]	1.44
PbTe	S	0.23	a=6.56 [53]	60 [53]	24 [53]	0.24 [53]	0.82
PbTe	T	0.28	a=6.56 [53]	60 [53]	24 [53]	0.24 [53]	1.27
Si	T	0.82	3.686 [318]	169 [319]	61 [318]	0.2 [318]	3.81
SnSe	S	0.04	a=11.790, b=4.219, c=4.524 [309]	41 [309]	17 [309]	0.21 [309]	0.03
TiC	T	1.94	a=4.3372	429	176 [318]	0.22	8.35
TiN	T	1.76	a=4.2551	437	180 [318]	0.24	6.69
TiNiSn	S	0.63	a=5.912 [311]	172 [311]	67 [311]	0.28 [311]	2.12
TiNiSn	T	0.90	a=5.912 [311]	172 [311]	67 [311]	0.28 [311]	4.31
V	T	0.40	a=2.98 [320]	130 [320]	48 [320]	0.36 [320]	6.14
W	T	1.00	a=3.17 [312]	540 [321]	161 [322]	0.28 [314]	1.70

Table 8.2: Calculated surface energies for $CoSb_3$,TiNiSn, PbTe, TiC, and TiN surfaces and the comparison of fracture energy G values estimated from slab calculations of surface energy and the integral stress-displacement method utilized in this study.

	$CoSb_3$	TiNiSn	PbTe	TiC	TiN
Surface Plane	(100)	(111)	(100)	(100)	(100)
$G = 2\gamma_s$ (using Eq.I.0.1) (J/m^2)	2.36	5.14	0.31	3.22	2.44
G (using integral method) (J/m^2)	1.38	4.31	1.27	8.35	6.69

Chapter 9

Outlook and Conclusions

The ability to control bulk material properties at an engineering level is essential to the development of next generation technologies. The progress made in tuning electrical transport properties (e.g. semiconductor devices) has revolutionized human capabilities through computational power. Now, it seems that our ability to harness thermal transport will be fundamental to the further advancement of current technologies, and may hold the key to unlocking new technologies presently unattainable. The present efforts in developing electro-mechanical devices, opto-electronic devices, thermo-mechanical and thermo-electric devices may be only the starting point for technologies that combine these various effects. The current trend in internet-of-things technologies would suggest that materials with multi-sensory capabilities are in our future.

The ultimate goal of becoming independent of fossil fuels and using sustainable energy harvesting and storage methods is also limited by our ability to develop efficient and stable materials-based devices. The recent breakthrough in solar efficiency [340] is one such stepping stone. However, a fundamental understanding of the physics of ionic transport, battery thermodynamics, as well as the mechanisms of electro-catalysis are all subjects that can directly lead to improvements in energy sustainability. These, among many others, are the promise of 21^{st} Century materials science.

The thermoelectrics-motivated problems considered in this work, aim to direct the field towards improvements in thermoelectric efficiency by reconsidering the fundamental nature of vibrations in solids, which may lead to new engineering design principles for reducing (tuning) thermal conductivity. Additionally, insights into the operational stability of materials and devices gives direct guidance for mitigating chemical decomposition in mixed conductors and assessing fracture toughness computationally. In all respects, this work provides a path forward for the computational design of materials from the atomic

scale to device-level thermodynamic considerations.

Specifically, a great deal of effort was put forth to characterize the nature of heat capacity in solids, both with and without phase transitions, and its implications for estimations of thermal conductivity. From the analysis presented herein, phase transitions do not significantly impact thermal conductivity, and are not likely to significantly improve thermoelectric performance. Furthermore, the complicated effects that phase transitions may have on material properties measurements can make the interpretation of these measurements difficult in general (i.e. beyond thermal properties). Thus, caution is advised in the characterization of thermoelectric properties (and zT) when phase transformations are present. This includes temperature dependent solubility, as in dynamic doping. These effects should also be considered as other materials, like electrode materials in batteries, are characterized as they undergo phase transformations.

Nevertheless, the work put forth to characterize anharmonicity and the nature of vibrations in complex crystals has far reaching implications for thermoelectrics and other disciplines of solid-state science. The connection of the thermodynamic Grüneisen parameter to thermal conductivity and phonon scattering is directly impacted by these results connecting the harmonic (e.g. elastic) properties of solids to anharmonic (e.g. thermal expansion) properties. Understanding and interpreting the vibrational behaviors of solids is essential to developing higher level transport models in ionics, as recent results suggest. Furthermore, engineering design principles based on a diffuson theory of thermal transport may lead to novel strategies for controlling thermal conductivity. As a "minimum" thermal conductivity, the model of diffuson transport developed herein provides a benchmark for experimental observations and may thus be used to assess the nature of ultralow thermal conductivity in some solids. Rethinking anharmonicity and the nature of vibrations in solids may also lead to insights regarding high temperature superconductors, which have yet to be well-explained.

At the device level, chemical stability and resistance to fracture are crucial to engineering design and implementation. Here, it is demonstrated that it is, in fact, a critical voltage that determines the decomposition condition of the material, which is not the same as "high current density" as is prevalently discussed. This understanding leads directly to design strategies for the stable operation of mixed conducting thermoelectric materials. The systematic trouble of decomposition in halide perovskite solar cells is governed by the same underlying thermodynamic conditions. Thus, the work presented here may also guide the development of stable devices in that field. The generality of this thermodynamics approach is likely beneficial to the characterization of phenomena in battery

materials, such as characterizing the formation of lithium dendrites.

Lastly, energetic considerations of fracture suggest that ideal strength calculations from first principles can capture the essential physics of fracture. From these calculations, the magnitude of experimental fracture toughness values can be obtained. The present results are more indicative of the experimental lower limit of fracture toughness, which is useful as an engineering design parameter for technological devices, but the method is easily adapted to explore the complexities of fracture at the atomic scale. The importance of defect structures in many materials, especially for structural applications, makes this method particularly useful for exploratory computational materials design.

As far as future directions are concerned, there are many straight-forward progressions alluded to within this text. An accurate characterization of the phase diagram and nature of the phase transition in SnSe, for example. Also, consideration of the spectral (time-dependence) of heat capacity through phase transitions using molecular dynamics simulations (for example) may provide a more quantitative description of the impacts of phase transitions on thermal properties measurements. These investigations would be useful for latent heat storage materials as well. This work on diffusons in solids has already motivated inelastic neutron scattering studies of large unit cell crystals to look for signatures of diffuson character in vibrational measurements. Certainly this is a completely new area of exploration for crystalline solids and both theoretical and experimental work to understand the effects of crystalline disorder on vibrational character are required. In what limit is phonon scattering theory still applicable? Furthermore, the mechanical concept of phonon (vibrational) pressure as it is related to anharmonicity in solids, there remain many questions as to how this ties into current theories of anharmonicity, as well as how it may be used to explain transport behavior in solids (like phonon and diffuson thermal transport, or even ionic conduction). Also, the marriage of the concept of phonon pressure with ideal strength calculations suggests there may be a mechanical description of melting. The theory and methods developed to characterize decomposition in mixed conductors is largely predictive of trends and not magnitudes presently. The characterization (experimental and/or computational) of the thermodynamic parameters needed to assess stability in these materials, and their temperature dependence, will be hugely beneficial to the design of thermoelectric devices, solar cells and others.

The culmination of work developed here is intended as a stepping stone along the path to greater technological and humanitarian achievements. Its purpose to answer immediate questions and to inspire curiosities among the thermoelectrics community is hoped to

have a broader impact on solid-state materials research through the inherent transference of thermodynamic principles and these microscopic insights to other energy materials.

Bibliography

[1] John Frederick Nye et al. *Physical properties of crystals: their representation by tensors and matrices*. Oxford university press, 1985.

[2] Riley Hanus, Matthias T Agne, Alexander JE Rettie, Zhiwei Chen, Gangjian Tan, Duck Young Chung, Mercouri G Kanatzidis, Yanzhong Pei, Peter W Voorhees, and G Jeffrey Snyder. Lattice softening significantly reduces thermal conductivity and leads to high thermoelectric efficiency. *Advanced Materials*, 31(21):1900108, 2019.

[3] Hong Yoon. *I. Low temperature lattice heat capacities of alloys: InPb, AuCd, Mg_3Sb_2. II. Effect of ordering on lattice heat capacity: $AuCu_3$*. Ph.D. thesis, 1971.

[4] Jing Shuai, Yumei Wang, Hee Seok Kim, Zihang Liu, Jingying Sun, Shuo Chen, Jiehe Sui, and Zhifeng Ren. Thermoelectric properties of Na-doped Zintl compound: $Mg_{3-x}Na_xSb_2$. *Acta Materialia*, 93:187–193, 2015.

[5] Hiromasa Tamaki, Hiroki K Sato, and Tsutomu Kanno. Isotropic conduction network and defect chemistry in $Mg_{3+\delta}Sb_2$-based layered Zintl compounds with high thermoelectric performance. *Advanced Materials*, 28(46):10182–10187, 2016.

[6] A Bhardwaj and DK Misra. Enhancing thermoelectric properties of a p-type Mg_3Sb_2-based Zintl phase compound by Pb substitution in the anionic framework. *Rsc Advances*, 4(65):34552–34560, 2014.

[7] Xiaoxi Chen, Haijun Wu, Juan Cui, Yu Xiao, Yang Zhang, Jiaqing He, Yue Chen, Jian Cao, Wei Cai, and Stephen J Pennycook. Extraordinary thermoelectric performance in n-type manganese doped Mg_3Sb_2 Zintl: High band degeneracy, tuned carrier scattering mechanism and hierarchical microstructure. *Nano Energy*, page In Press, 2018.

[8] Sankalp Kota, Matthias Agne, Eugenio Zapata-Solvas, Olivier Dezellus, Diego Lopez, Bruno Gardiola, Miladin Radovic, and Michel W Barsoum. Elastic proper-

ties, thermal stability, and thermodynamic parameters of MoAlB. *Physical Review B*, 95(14):144108, 2017.

[9] S Bhattacharya, RP Hermann, Veerle Keppens, TM Tritt, and GJ Snyder. Effect of disorder on the thermal transport and elastic properties in thermoelectric Zn_4Sb_3. *Physical Review B*, 74(13):134108, 2006.

[10] Eric S Toberer, Protima Rauwel, Sylvain Gariel, J Taftø, and G Jeffrey Snyder. Composition and the thermoelectric performance of β-Zn_4Sb_3. *Journal of materials chemistry*, 20(44):9877–9885, 2010.

[11] Stephen Dongmin Kang, Sergey A Danilkin, Umut Aydemir, Maxim Avdeev, Andrew Studer, and G Jeffrey Snyder. Apparent critical phenomena in the superionic phase transition of $Cu_{2-x}Se$. *New Journal of Physics*, 18(1):013024, 2016.

[12] David R Brown, Tristan Day, Kasper A Borup, Sebastian Christensen, Bo B Iversen, and G Jeffrey Snyder. Phase transition enhanced thermoelectric figure-of-merit in copper chalcogenides. *APL Materials*, 1(5):052107, 2013.

[13] JD Chung, AJH McGaughey, and M Kaviany. Role of phonon dispersion in lattice thermal conductivity modeling. *J. Heat Transfer*, 126(3):376–380, 2004.

[14] Massoud Kaviany. *Heat transfer physics*. Cambridge University Press, 2014.

[15] Yudong Cheng, Junyou Yang, Qinghui Jiang, Dongsheng He, Jiaqing He, Yubo Luo, Dan Zhang, Zhiwei Zhou, Yangyang Ren, and Jiwu Xin. New insight into InSb-based thermoelectric materials: from a divorced eutectic design to a remarkably high thermoelectric performance. *Journal of Materials Chemistry A*, 5(10):5163–5170, 2017.

[16] Huili Liu, Xun Yuan, Ping Lu, Xun Shi, Fangfang Xu, Ying He, Yunshan Tang, Shengqiang Bai, Wenqing Zhang, and Lidong Chen. Ultrahigh thermoelectric performance by electron and phonon critical scattering in $Cu_2Se_{1-x}I_x$. *Advanced Materials*, 25(45):6607–6612, 2013.

[17] Cheng Chang, Minghui Wu, Dongsheng He, Yanling Pei, Chao-Feng Wu, Xuefeng Wu, Hulei Yu, Fangyuan Zhu, Kedong Wang, and Yue Chen. 3D charge and 2D phonon transports leading to high out-of-plane *z*T in n-type SnSe crystals. *Science*, 360(6390):778–783, 2018.

[18] Franck Gascoin and Antoine Maignan. Order–disorder transition in $AgCrSe_2$: a new route to efficient thermoelectrics. *Chemistry of Materials*, 23(10):2510–2513, 2011.

[19] Yang Wu, Johanna Nylén, Craig Naseyowma, Nathan Newman, Francisco J Garcia-Garcia, and Ulrich Haussermann. Comparative study of the thermoelectric properties of amorphous $Zn_{41}Sb_{59}$ and crystalline Zn_4Sb_3. *Chemistry of Materials*, 21(1):151–155, 2008.

[20] Il Ho Kim, JB Park, Tae Whan Hong, Soon Chul Ur, Young Geun Lee, Sung Lim Ryu, G Nakamoto, and M Kurisu. Low-temperature thermoelectric properties of Zn_4Sb_3 prepared by hot pressing. In *Materials science forum*, volume 510, pages 1070–1073. Trans Tech Publ.

[21] Johanna Nylen, Sven Lidin, Magnus Andersson, Hongxue Liu, Nate Newman, and Ulrich Häussermann. Effect of metal doping on the low-temperature structural behavior of thermoelectric β-Zn_4Sb_3. *Journal of Solid State Chemistry*, 180(9):2603–2615, 2007.

[22] Kostyantyn Korniyenko and Materials Science International Team, MSIT®. The In-Sb phase diagram: Datasheet from msi eureka in springermaterials (https://materials.springer.com/msi/phase-diagram/docs/sm_msi_r_10_013409_01_full_lnkdia0). Copyright 2005 MSI, Materials Science International Services GmbH, Stuttgart.

[23] Li You, Jiye Zhang, Shanshan Pan, Ying Jiang, Ke Wang, Jiong Yang, Yanzhong Pei, Qing Zhu, Matthias T Agne, G Jeffrey Snyder, et al. Realization of higher thermoelectric performance by dynamic doping of copper in n-type PbTe. *Energy & Environmental Science*, 12(10):3089–3098, 2019.

[24] Li-Dong Zhao, Shih-Han Lo, Yongsheng Zhang, Hui Sun, Gangjian Tan, Ctirad Uher, Christopher Wolverton, Vinayak P Dravid, and Mercouri G Kanatzidis. Ultralow thermal conductivity and high thermoelectric figure of merit in SnSe crystals. *Nature*, 508(7496):373, 2014.

[25] D Li, JC Li, XY Qin, J Zhang, CJ Song, L Wang, and HX Xin. Thermoelectric performance for SnSe hot-pressed at different temperature. *Journal of Electronic Materials*, 46(1):79–84, 2017.

[26] S Sassi, C Candolfi, J-B Vaney, V Ohorodniichuk, P Masschelein, A Dauscher, and B Lenoir. Assessment of the thermoelectric performance of polycrystalline p-type SnSe. *Applied Physics Letters*, 104(21):212105, 2014.

[27] Xin-Ke Wang, Igor Veremchuk, Matej Bobnar, Jing-Tai Zhao, and Yuri Grin. Solid solution $Pb_{1-x}Eu_xTe$: constitution and thermoelectric behavior. *Inorganic Chemistry Frontiers*, 3(9):1152–1159, 2016.

[28] Yasumasa Okada and Yozo Tokumaru. Precise determination of lattice parameter and thermal expansion coefficient of silicon between 300 and 1500 K. *Journal of applied physics*, 56(2):314–320, 1984.

[29] B. A. Efimova Ravich, IUrii Isaakovich and I. A. Smirnov. *Semiconducting lead chalcogenides*, volume 5. Springer Science & Business Media, 2013.

[30] Yu I Vesnin and Yu V Shubin. On the constancy of the "average" crystal lattice parameter in the decay of the solid solutions PbS–PbTe. *Materials research bulletin*, 19(10):1355–1359, 1984.

[31] Orson L. Anderson. A simplified method for calculating the Debye temperature from elastic constants. *Journal of Physics and Chemistry of Solids*, 24(7):909–917, 1963.

[32] M. J. Druyvesteyn. An approximate calculation of the thermal expansion of solids II. *Physica*, 8(8):862–867, 1941.

[33] Albert Einstein. Elementare betrachtungen über die thermische molekularbewegung in festen körpern. *Annalen der Physik*, 340(9):679–694, 1911.

[34] Philip B Allen and Joseph L Feldman. Thermal conductivity of glasses: Theory and application to amorphous Si. *Physical review letters*, 62(6):645, 1989.

[35] Philip B Allen and Joseph L Feldman. Thermal conductivity of disordered harmonic solids. *Physical Review B*, 48(17):12581, 1993.

[36] Philip B Allen, Joseph L Feldman, Jaroslav Fabian, and Frederick Wooten. Diffusons, locons and propagons: Character of atomic vibrations in amorphous Si. *Philosophical Magazine B*, 79(11-12):1715–1731, 1999.

[37] Joseph L Feldman, Philip B Allen, and Scott R Bickham. Numerical study of low-frequency vibrations in amorphous silicon. *Physical Review B*, 59(5):3551, 1999.

[38] Joseph L Feldman, Mark D Kluge, Philip B Allen, and Frederick Wooten. Thermal conductivity and localization in glasses: Numerical study of a model of amorphous silicon. *Physical Review B*, 48(17):12589, 1993.

[39] Charles Kittel. Interpretation of the thermal conductivity of glasses. *Physical Review*, 75(6):972–974, 1949.

[40] David R Clarke. Materials selection guidelines for low thermal conductivity thermal barrier coatings. *Surface and Coatings Technology*, 163:67–74, 2003.

[41] David G Cahill, Susan K Watson, and Robert O Pohl. Lower limit to the thermal conductivity of disordered crystals. *Physical Review B*, 46(10):6131, 1992.

[42] Glen A Slack. The thermal conductivity of nonmetallic crystals. *Solid state physics*, 34:1–71, 1979.

[43] RO Pohl. Lattice vibrations of glasses. *Journal of non-crystalline solids*, 352(32):3363–3367, 2006.

[44] CW Li, J Ma, HB Cao, AF May, DL Abernathy, G Ehlers, C Hoffmann, X Wang, T Hong, and A Huq. Anharmonicity and atomic distribution of SnTe and PbTe thermoelectrics. *Physical Review B*, 90(21):214303, 2014.

[45] Tania Claudio, Gabi Schierning, Ralf Theissmann, Hartmut Wiggers, Helmut Schober, Michael Marek Koza, and Raphaël P Hermann. Effects of impurities on the lattice dynamics of nanocrystalline silicon for thermoelectric application. *Journal of Materials Science*, 48(7):2836–2845, 2013.

[46] David G Cahill, Henry E Fischer, Tom Klitsner, ET Swartz, and RO Pohl. Thermal conductivity of thin films: measurements and understanding. *Journal of Vacuum Science & Technology A: Vacuum, Surfaces, and Films*, 7(3):1259–1266, 1989.

[47] BL Zink, R Pietri, and F Hellman. Thermal conductivity and specific heat of thin-film amorphous silicon. *Physical review letters*, 96(5):055902, 2006.

[48] Caterina Lamuta, Anna Cupolillo, Antonio Politano, Ziya S Aliev, Mahammad B Babanly, Evgueni V Chulkov, and Leonardo Pagnotta. Indentation fracture toughness of single-crystal Bi_2Te_3topological insulators. *Nano Research*, 9(4):1032–1042, 2016.

[49] Chi Ma, Hongquan Liu, Ruxue Chen, Qiang Su, Hongzhi Cui, and Yijie Gu. Anisotropy thermoelectric and mechanical property of polycrystalline SnSe prepared under different processes. *Journal of Materials Science: Materials in Electronics*, 30(7):6403–6410, 2019.

[50] Kriti Tyagi, Bhasker Gahtori, Sivaiah Bathula, Niraj Kumar Singh, Swati Bishnoi, S. Auluck, A. K. Srivastava, and Ajay Dhar. Electrical transport and mechanical properties of thermoelectric tin selenide. *RSC Advances*, 6(14):11562–11569, 2016.

[51] Rui Shu, Yecheng Zhou, Qi Wang, Zhijia Han, Yongbin Zhu, Yong Liu, Yuexing Chen, Meng Gu, Wei Xu, Yu Wang, Wenqing Zhang, Li Huang, and Weishu Liu. $Mg_{3+\delta}Sb_xBi_{2-x}$Family: A Promising Substitute for the State-of-the-Art n-Type Thermoelectric Materials near Room Temperature. *Advanced Functional Materials*, 29(4):1807235, 2019.

[52] James M Ma, Samad A Firdosy, Richard B Kaner, Jean Pierre Fleurial, and Vilupanur A Ravi. Hardness and fracture toughness of thermoelectric La3-x Te 4. *Journal of Materials Science*, 49(3):1150–1156, 2014.

[53] Guodong Li, Umut Aydemir, Bo Duan, Matthias T. Agne, Hongtao Wang, Max Wood, Qingjie Zhang, Pengcheng Zhai, William A Goddard, and G Jeffrey Snyder. Micro- and Macromechanical Properties of Thermoelectric Lead Chalcogenides. *ACS Applied Materials and Interfaces*, 9(46):40488–40496, 2017.

[54] Qihao Zhang, Zhenxing Zhou, Maxwell Dylla, Matthias T Agne, Yanzhong Pei, Lianjun Wang, Yunshan Tang, Jincheng Liao, Juan Li, Shengqiang Bai, Wan Jiang, Lidong Chen, and Gerald Jeffrey Snyder. Realizing high-performance thermoelectric power generation through grain boundary engineering of skutterudite-based nanocomposites. *Nano Energy*, 41:501–510, 2017.

[55] V. Ravi, S. Firdosy, T. Caillat, B. Lerch, A. Calamino, R. Pawlik, M. Nathal, A. Sechrist, J. Buchhalte, and S. Nutt. Mechanical properties of thermoelectric skutterudites. In *AIP Conference Proceedings*, volume 969, pages 656–662, 2008.

[56] James Eilertsen, M. A. Subramanian, and J. J. Kruzic. Fracture toughness of Co_4Sb_{12} and $In_{0.1}Co_4Sb_{12}$ thermoelectric skutterudites evaluated by three methods. *Journal of Alloys and Compounds*, 552:492–498, 2013.

[57] Wesley Everhart and Joseph Newkirk. Mechanical properties of Heusler alloys, 2019.

[58] Toru Ono and Masanori Ueki. *Effect of Graphite Addition on the Microstructure and Mechanical Properties of Hot-pressed Titanium Carbide*, pages 585–588. 12 1994.

[59] C. Maerky, M. O. Guillou, J. L. Henshall, and R. M. Hooper. Indentation hardness and fracture toughness in single crystal $TiC_{0.96}$. *Materials Science and Engineering A*, 209(1-2):329–336, 1996.

[60] Xueping Li, Takashi Kasai, Shigeki Nakao, Hiroshi Tanaka, Taeko Ando, Mitsuhiro Shikida, and Kazuo Sato. Measurement for fracture toughness of single crystal silicon film with tensile test. *Sensors and Actuators, A*, 119(1):229–235, 2005.

[61] Rogers R. Salem, J. and E. Baker. Structural design parameters for germanium. Technical Report 20160012342, 2017.

[62] T. D. Joseph, M. Tanaka, A. J. Wilkinson, and S. G. Roberts. Brittle-ductile transitions in vanadium and iron-chromium. *Journal of Nuclear Materials*, 367-370 A(SPEC. ISS.):637–643, 2007.

[63] Jennifer E. Ni, Eldon D. Case, Kristen N. Khabir, Ryan C. Stewart, Chun I. Wu, Timothy P. Hogan, Edward J. Timm, Steven N. Girard, and Mercouri G. Kanatzidis. Room temperature Young's modulus, shear modulus, Poisson's ratio and hardness of PbTe- PbS thermoelectric materials. *Materials Science and Engineering B: Solid-State Materials for Advanced Technology*, 170(1-3):58–66, 2010.

[64] A. Hohenwarter and S. Wurster. Deformation and fracture characteristics of ultrafine-grained vanadium. *Materials Science and Engineering A*, 650:492–496, 2016.

[65] B. Gludovatz, S. Wurster, A. Hoffmann, and R. Pippan. Fracture toughness of polycrystalline tungsten alloys. *International Journal of Refractory Metals and Hard Materials*, 28(6):674–678, 2010.

[66] R. W. Margevicius, J. Riedle, and P. Gumbsch. Fracture toughness of polycrystalline tungsten under mode I and mixed mode I/II loading. *Materials Science and Engineering A*, 270(2):197–209, 1999.

[67] MS Dresselhaus and IL Thomas. Alternative energy technologies. *Nature*, 414(6861):332–337, 2001.

[68] Perry Sadorsky. Renewable energy consumption and income in emerging economies. *Energy policy*, 37(10):4021–4028, 2009.

[69] Perry Sadorsky. The impact of financial development on energy consumption in emerging economies. *Energy policy*, 38(5):2528–2535, 2010.

[70] David R. Clarke, Matthias Oechsner, and Nitin P. Padture. Thermal-barrier coatings for more efficient gas-turbine engines. *MRS Bulletin*, 37(10):891–898, 2012.

[71] Eric Pop. Energy dissipation and transport in nanoscale devices. *Nano Research*, 3(3):147–169, 2010.

[72] Christian Monachon, Ludger Weber, and Chris Dames. Thermal Boundary Conductance: A Materials Science Perspective. *Annual Review of Materials Research*, 46:433–463, 2016.

[73] S Mei, C J Foss, L N Maurer, O Jonasson, Z Aksamija, and I Knezevic. Boundaries, interfaces, point defects, and strain as impediments to thermal transport in nanostructures. *IEEE*, pages 1–10, 2017.

[74] Young-Ik Sohn, Srujan Meesala, Benjamin Pingault, Haig A Atikian, Jeffrey Holzgrafe, Mustafa Gündoğan, Camille Stavrakas, Megan J Stanley, Alp Sipahigil, Joonhee Choi, et al. Controlling the coherence of a diamond spin qubit through its strain environment. *Nature communications*, 9(1):1–6, 2018.

[75] G. Jeffrey Snyder and Eric S. Toberer. Complex thermoelectric materials. *Nature Materials*, 7(2):105–114, 2008.

[76] Pengfei Qiu, Matthias T Agne, Yongying Liu, Yaqin Zhu, Hongyi Chen, Tao Mao, Jiong Yang, Wenqing Zhang, Sossina M Haile, Wolfgang G Zeier, et al. Suppression of atom motion and metal deposition in mixed ionic electronic conductors. *Nature communications*, 9(1):1–8, 2018.

[77] Pengfei Qiu, Tao Mao, Zhongfu Huang, Xugui Xia, Jincheng Liao, Matthias T Agne, Ming Gu, Qihao Zhang, Dudi Ren, Shengqiang Bai, et al. High-efficiency and stable thermoelectric module based on liquid-like materials. *Joule*, 3(6):1538–1548, 2019.

[78] Chia-Chi Yu, Hsin-jay Wu, Ping-Yuan Deng, Matthias T Agne, G Jeffrey Snyder, and Jinn P Chu. Thin-film metallic glass: An effective diffusion barrier for Se-doped $AgSbTe_2$ thermoelectric modules. *Scientific reports*, 7:45177, 2017.

[79] Chia-Chi Yu, Hsin-jay Wu, Matthias T Agne, Ian T Witting, Ping-Yuan Deng, G Jeffrey Snyder, and Jinn P Chu. Titanium-based thin film metallic glass as diffusion

barrier layer for PbTe-based thermoelectric modules. *APL Materials*, 7(1):013001, 2019.

[80] MC Chang, MT Agne, RA Michi, David C Dunand, and Gerald Jeffrey Snyder. Compressive creep behavior of hot-pressed GeTe based TAGS-85 and effect of creep on thermoelectric properties. *Acta Materialia*, 158:239–246, 2018.

[81] G Stapfer, P Rouklove, and L Garvey. Progress report No. 23 for a program of thermoelectric generator testing and RTG degradation mechanisms evaluation. Technical report, Jet Propulsion Lab., Pasadena, CA (USA), 1977.

[82] JD Hinderman. Thermoelectric materials evaluation program. annual technical report for fiscal years 1980/1981. Technical report, Minnesota Mining and Mfg. Co., St. Paul (USA). Industrial Electrical, 1981.

[83] Xuning Feng, Minggao Ouyang, Xiang Liu, Languang Lu, Yong Xia, and Xiangming He. Thermal runaway mechanism of lithium ion battery for electric vehicles: A review. *Energy Storage Materials*, 10:246–267, 2018.

[84] Sybren Ruurds De Groot and Peter Mazur. *Non-equilibrium thermodynamics*. Courier Corporation, 2013.

[85] Jean Baptiste Joseph Baron Fourier. *The analytical theory of heat*. The University Press, 1878.

[86] Horatio Scott Carslaw and John Conrad Jaeger. *Conduction of heat in solids*. Clarendon Press, 1960.

[87] WJ Parker, RJ Jenkins, CP Butler, and GL Abbott. Flash method of determining thermal diffusivity, heat capacity, and thermal conductivity. *Journal of applied physics*, 32(9):1679–1684, 1961.

[88] Kasper A Borup, Johannes De Boor, Heng Wang, Fivos Drymiotis, Franck Gascoin, Xun Shi, Lidong Chen, Mikhail I Fedorov, Eckhard Müller, and Bo B Iversen. Measuring thermoelectric transport properties of materials. *Energy & Environmental Science*, 8(2):423–435, 2015.

[89] Carl Wagner. The thermoelectric power of cells with ionic compounds involving ionic and electronic conduction. *Progress in Solid State Chemistry*, 7:1–37, 1972.

[90] Hyun-Sik Kim, Zachary M Gibbs, Yinglu Tang, Heng Wang, and G Jeffrey Snyder. Characterization of lorenz number with seebeck coefficient measurement. *APL materials*, 3(4):041506, 2015.

[91] G Jeffrey Snyder, Matthias T Agne, and Ramya Gurunathan. Thermal conductivity of complex materials. *National Science Review*, 6(3):380–381, 2019.

[92] Michele Simoncelli, Nicola Marzari, and Francesco Mauri. Unified theory of thermal transport in crystals and glasses. *Nature Physics*, 15(8):809–813, 2019.

[93] Riley Hanus, Janine George, Max Wood, Yongqiang Cheng, Douglas L Abernathy, Michael E Manley, Geoffroy Hautier, G Jeffrey Snyder, and Raphaël P Hermann. Transition from crystal-like to amorphous-like heat conduction in structurally-complex crystals. 2020.

[94] Yixiu Luo, Xiaolong Yang, Tianli Feng, Jingyang Wang, and Xiulin Ruan. Vibrational hierarchy leads to dual-phonon transport in low thermal conductivity crystals. *Nature Communications*, 11(1):1–10, 2020.

[95] Georg KH Madsen and David J Singh. BoltzTraP. a code for calculating band-structure dependent quantities. *Computer Physics Communications*, 175(1):67–71, 2006.

[96] Nevill Francis Mott. The resistance and thermoelectric properties of the transition metals. *Proceedings of the Royal Society of London. Series A-Mathematical and Physical Sciences*, 156(888):368–382, 1936.

[97] Sokseiha Muy, John C Bachman, Livia Giordano, Hao-Hsun Chang, Douglas L Abernathy, Dipanshu Bansal, Olivier Delaire, Satoshi Hori, Ryoji Kanno, Filippo Maglia, et al. Tuning mobility and stability of lithium ion conductors based on lattice dynamics. *Energy & Environmental Science*, 11(4):850–859, 2018.

[98] Thorben Krauskopf, Sokseiha Muy, Sean P Culver, Saneyuki Ohno, Olivier Delaire, Yang Shao-Horn, and Wolfgang G Zeier. Comparing the descriptors for investigating the influence of lattice dynamics on ionic transport using the superionic conductor $Na_3PS_{4-x}Se_x$. *Journal of the American Chemical Society*, 140(43):14464–14473, 2018.

[99] James Male, Matthias T Agne, Anuj Goyal, Shashwat Anand, Ian T Witting, Vladan Stevanović, and G Jeffrey Snyder. The importance of phase equilibrium for doping efficiency: iodine doped PbTe. *Materials Horizons*, 6(7):1444–1453, 2019.

[100] Eric S. Toberer, Alex Zevalkink, and G. Jeffrey Snyder. Phonon engineering through crystal chemistry. *Journal of Materials Chemistry*, 21(40):15843, 2011.

[101] Zhenxing Zhou, Matthias T Agne, Qihao Zhang, Shun Wan, Qingfeng Song, Qing Xu, Xiaofang Lu, Shijia Gu, Yuchi Fan, Wan Jiang, et al. Microstructure and composition engineering Yb single-filled $CoSb_3$ for high thermoelectric and mechanical performances. *Journal of Materiomics*, 5(4):702–710, 2019.

[102] Ramya Gurunathan, Riley Hanus, Maxwell Dylla, Ankita Katre, and G Jeffrey Snyder. Analytical models of phonon–point-defect scattering. *Physical Review Applied*, 13(3):034011, 2020.

[103] Riley Hanus, Anupam Garg, and G Jeffery Snyder. Phonon diffraction and dimensionality crossover in phonon-interface scattering. *Communications Physics*, 1(1):1–11, 2018.

[104] Matthias T Agne, Kazuki Imasato, Shashwat Anand, Kathleen Lee, Sabah K Bux, Alex Zevalkink, Alexander JE Rettie, Duck Young Chung, Mercouri G Kanatzidis, and G Jeffrey Snyder. Heat capacity of Mg_3Sb_2, Mg_3Bi_2, and their alloys at high temperature. *Materials Today Physics*, 6:83–88, 2018.

[105] Chas G Maier and KK Kelley. An equation for the representation of high-temperature heat content data. *Journal of the American chemical society*, 54(8):3243–3246, 1932.

[106] Saneyuki Ohno, Kazuki Imasato, Shashwat Anand, Hiromasa Tamaki, Stephen Dongmin Kang, Prashun Gorai, Hiroki K Sato, Eric S Toberer, Tsutomu Kanno, and G Jeffrey Snyder. Phase boundary mapping to obtain n-type Mg_3Sb_2-based thermoelectrics. *Joule*, 2(1):141–154, 2018.

[107] Fivos Drymiotis, Tristan W Day, David R Brown, Nicholas A Heinz, and G Jeffrey Snyder. Enhanced thermoelectric performance in the very low thermal conductivity $Ag_2Se_{0.5}Te_{0.5}$. *Applied Physics Letters*, 103(14):143906, 2013.

[108] Stéphane Gorsse, Solange Vivès, Philippe Bellanger, D Riou, Laetitia Laversenne, Salvatore Miraglia, and David R Clarke. Multi-scale architectured thermoelectric materials in the Mg_2(Si, Sn) system. *Materials Letters*, 166:140–144, 2016.

[109] Rachel J Korkosz, Thomas C Chasapis, Shih-han Lo, Jeff W Doak, Yoon Jun Kim, Chun-I Wu, Euripidis Hatzikraniotis, Timothy P Hogan, David N Seidman, and

Chris Wolverton. High ZT in p-type $(PbTe)_{1-2x}(PbSe)_x(PbS)_x$ thermoelectric materials. *Journal of the American Chemical Society*, 136(8):3225–3237, 2014.

[110] Anil Kumar, Paul A Vermeulen, Bart J Kooi, Jiancun Rao, Lambert van Eijck, Stefan Schwarzmüller, Oliver Oeckler, and Graeme R Blake. Phase transitions of thermoelectric TAGS-85. *Inorganic chemistry*, 56(24):15091–15100, 2017.

[111] Chun-Wan Timothy Lo, Volodymyr Svitlyk, Dmitry Chernyshov, and Yurij Mozharivskyj. The updated Zn–Sb phase diagram. How to make pure $Zn_{13}Sb_{10}$ ("Zn_4Sb_3"). *Dalton Transactions*, 47(33):11512–11520, 2018.

[112] Quentin Lognoné and Franck Gascoin. Reactivity, stability and thermoelectric properties of n-Bi_2Te_3 doped with different copper amounts. *Journal of Alloys and Compounds*, 610:1–5, 2014.

[113] Johanna Nylén, Sven Lidin, Magnus Andersson, Bo Brummerstedt Iversen, Nate Newman, and Ulrich Häussermann. Low-temperature structural transitions in the phonon-glass thermoelectric material β-Zn_4Sb_3: Ordering of Zn interstitials and defects. *Chemistry of Materials*, 19(4):834–838, 2007.

[114] Brenden R Ortiz, Jesse M Adamczyk, Kiarash Gordiz, Tara Braden, and Eric S Toberer. Towards the high-throughput synthesis of bulk materials: thermoelectric PbTe–PbSe–SnTe–SnSe alloys. *Molecular Systems Design & Engineering*, 2019.

[115] Yanzhong Pei, Andrew F May, and G Jeffrey Snyder. Self-tuning the carrier concentration of PbTe/Ag_2Te composites with excess Ag for high thermoelectric performance. *Advanced Energy Materials*, 1(2):291–296, 2011.

[116] Suresh Perumal, Subhajit Roychowdhury, and Kanishka Biswas. High performance thermoelectric materials and devices based on GeTe. *Journal of Materials Chemistry C*, 4(32):7520–7536, 2016.

[117] Yuting Qiu, Lili Xi, Xun Shi, Pengfei Qiu, Wenqing Zhang, Lidong Chen, James R Salvador, Jung Y Cho, Jihui Yang, and Yuan-chun Chien. Charge-compensated compound defects in Ga-containing thermoelectric skutterudites. *Advanced Functional Materials*, 23(25):3194–3203, 2013.

[118] Jong-Soo Rhyee, Kyu Hyoung Lee, Sang Mock Lee, Eunseog Cho, Sang Il Kim, Eunsung Lee, Yong Seung Kwon, Ji Hoon Shim, and Gabriel Kotliar. Peierls distortion as a route to high thermoelectric performance in $In_4Se_{3-\delta}$ crystals. *Nature*, 459(7249):965, 2009.

[119] Manisha Samanta and Kanishka Biswas. Low thermal conductivity and high thermoelectric performance in $(GeTe)_{1-2x}(GeSe)_x(GeS)_x$: Competition between solid solution and phase separation. *Journal of the American Chemical Society*, 139(27):9382–9391, 2017.

[120] Michael Schwall and Benjamin Balke. Phase separation as a key to a thermoelectric high efficiency. *Physical Chemistry Chemical Physics*, 15(6):1868–1872, 2013.

[121] Yinglu Tang, Sinn-wen Chen, and G Jeffrey Snyder. Temperature dependent solubility of Yb in Yb–$CoSb_3$ skutterudite and its effect on preparation, optimization and lifetime of thermoelectrics. *Journal of Materiomics*, 1(1):75–84, 2015.

[122] Yinglu Tang, Xiaoshuang Li, Lukas HJ Martin, Eduardo Cuervo Reyes, Toni Ivas, Christian Leinenbach, Shashwat Anand, Matthew Peters, G Jeffrey Snyder, and Corsin Battaglia. Impact of Ni content on the thermoelectric properties of half-heusler TiNiSn. *Energy & Environmental Science*, 11(2):311–320, 2018.

[123] Hsin-jay Wu, Sinn-wen Chen, Teruyuki Ikeda, and G Jeffrey Snyder. Reduced thermal conductivity in Pb-alloyed $AgSbTe_2$ thermoelectric materials. *Acta Materialia*, 60(17):6144–6151, 2012.

[124] Hsin-jay Wu, Tian-Wey Lan, Sinn-wen Chen, Yang-Yuan Chen, Tristan Day, and G Jeffery Snyder. State of the art $Ag_{50-x}Sb_xSe_{50-y}Te_y$ alloys: Their high zT values, microstructures and related phase equilibria. *Acta Materialia*, 93:38–45, 2015.

[125] Sima Aminorroaya Yamini, Teruyuki Ikeda, Aaron Lalonde, Yanzhong Pei, Shi Xue Dou, and G Jeffrey Snyder. Rational design of p-type thermoelectric PbTe: temperature dependent sodium solubility. *Journal of Materials Chemistry A*, 1(31):8725–8730, 2013.

[126] Sima Aminorroaya Yamini, Heng Wang, Zachary M Gibbs, Yanzhong Pei, Shi Xue Dou, and G Jeffrey Snyder. Chemical composition tuning in quaternary p-type Pb-chalcogenides — a promising strategy for enhanced thermoelectric performance. *Physical Chemistry Chemical Physics*, 16(5):1835–1840, 2014.

[127] Kazuki Imasato, Stephen Dongmin Kang, Saneyuki Ohno, and G Jeffrey Snyder. Band engineering in Mg_3Sb_2 by alloying with Mg_3Bi_2 for enhanced thermoelectric performance. *Materials Horizons*, 5(1):59–64, 2018.

[128] Kazuki Imasato, Saneyuki Ohno, Stephen Dongmin Kang, and G Jeffrey Snyder. Improving the thermoelectric performance in $Mg_{3+x}Sb_{1.5}Bi_{0.49}Te_{0.01}$ by reducing excess Mg. *APL Materials*, 6(1):016106, 2018.

[129] Tsutomu Kanno, Hiromasa Tamaki, Hiroki K Sato, Stephen Dongmin Kang, Saneyuki Ohno, Kazuki Imasato, Jimmy Jiahong Kuo, G Jeffrey Snyder, and Yuzuru Miyazaki. Enhancement of average thermoelectric figure of merit by increasing the grain-size of $Mg_{3.2}Sb_{1.5}Bi_{0.49}Te_{0.01}$. *Applied Physics Letters*, 112(3):033903, 2018.

[130] Jimmy Jiahong Kuo, Stephen Dongmin Kang, Kazuki Imasato, Hiromasa Tamaki, Saneyuki Ohno, Tsutomu Kanno, and G Jeffrey Snyder. Grain boundary dominated charge transport in Mg_3Sb_2-based compounds. *Energy & Environmental Science*, 11(2):429–434, 2018.

[131] Jun Mao, Jing Shuai, Shaowei Song, Yixuan Wu, Rebecca Dally, Jiawei Zhou, Zihang Liu, Jifeng Sun, Qinyong Zhang, and Clarina dela Cruz. Manipulation of ionized impurity scattering for achieving high thermoelectric performance in n-type Mg_3Sb_2-based materials. *Proceedings of the National Academy of Sciences*, 114(40):10548–10553, 2017.

[132] Jun Mao, Yixuan Wu, Shaowei Song, Jing Shuai, Zihang Liu, Yanzhong Pei, and Zhifeng Ren. Anomalous electrical conductivity of n-type te-doped $Mg_{3.2}Sb_{1.5}Bi_{0.5}$. *Materials Today Physics*, 3:1–6, 2017.

[133] Jun Mao, Yixuan Wu, Shaowei Song, Qing Zhu, Jing Shuai, Zihang Liu, Yanzhong Pei, and Zhifeng Ren. Defect engineering for realizing high thermoelectric performance in n-type Mg_3Sb_2-based materials. *ACS Energy Letters*, 2(10):2245–2250, 2017.

[134] Wanyue Peng, Guido Petretto, Gian-Marco Rignanese, Geoffroy Hautier, and Alexandra Zevalkink. An unlikely route to low lattice thermal conductivity: Small atoms in a simple layered structure. *Joule*, page In Press, 2018.

[135] Jing Shuai, Jun Mao, Shaowei Song, Qinyong Zhang, Gang Chen, and Zhifeng Ren. Recent progress and future challenges on thermoelectric Zintl materials. *Materials Today Physics*, 1:74–95, 2017.

[136] Jing Shuai, Jun Mao, Shaowei Song, Qing Zhu, Jifeng Sun, Yumei Wang, Ran He, Jiawei Zhou, Gang Chen, and David J Singh. Tuning the carrier scattering mecha-

nism to effectively improve the thermoelectric properties. *Energy & Environmental Science*, 10(3):799–807, 2017.

[137] Jiawei Zhang, Lirong Song, Steffen Hindborg Pedersen, Hao Yin, Le Thanh Hung, and Bo Brummerstedt Iversen. Discovery of high-performance low-cost n-type Mg_3Sb_2-based thermoelectric materials with multi-valley conduction bands. *Nature communications*, 8:13901, 2017.

[138] Kazuki Imasato, Chenguang Fu, Yu Pan, Max Wood, Jimmy Jiahong Kuo, Claudia Felser, and G Jeffrey Snyder. Metallic n-type Mg_3Sb_2 single crystals demonstrate the absence of ionized impurity scattering and enhanced thermoelectric performance. *Advanced Materials*, 32(16):1908218, 2020.

[139] Fan Zhang, Chen Chen, Honghao Yao, Fengxian Bai, Li Yin, Xiaofang Li, Shan Li, Wenhua Xue, Yumei Wang, Feng Cao, et al. High-performance n-type Mg_3Sb_2 towards thermoelectric application near room temperature. *Advanced Functional Materials*, page 1906143, 2019.

[140] Maxwell Wood, Jimmy Jiahong Kuo, Kazuki Imasato, and Gerald Jeffrey Snyder. Improvement of low-temperature zT in a Mg_3Sb_2–Mg_3Bi_2 solid solution via Mg-vapor annealing. *Advanced Materials*, 31(35):1902337, 2019.

[141] Jimmy Jiahong Kuo, Yuan Yu, Stephen Dongmin Kang, Oana Cojocaru-Mirédin, Matthias Wuttig, and G Jeffrey Snyder. Mg deficiency in grain boundaries of n-type Mg_3Sb_2 identified by atom probe tomography. *Advanced Materials Interfaces*, 6(13):1900429, 2019.

[142] Max Wood, Kazuki Imasato, Shashwat Anand, Jiong Yang, and G Jeffrey Snyder. The importance of the Mg-Mg interaction in Mg_3Sb_2-Mg_3Bi_2 shown through cation site alloying. *Journal of Materials Chemistry A*, 2020.

[143] Jun Mao, Hangtian Zhu, Zhiwei Ding, Zihang Liu, Geethal Amila Gamage, Gang Chen, and Zhifeng Ren. High thermoelectric cooling performance of n-type Mg_3Bi_2-based materials. *Science*, 365(6452):495–498, 2019.

[144] Yu Pan, Mengyu Yao, Xiaochen Hong, Yifan Zhu, Fengren Fan, Kazuki Imasato, Yangkun He, Christian Hess, Jörg Fink, Jiong Yang, et al. $Mg_3(Bi,Sb)_2$ single crystals towards high thermoelectric performance. *Energy & Environmental Science*, 2020.

[145] Wanyue Peng, Sevan Chanakian, and Alexandra Zevalkink. Crystal chemistry and thermoelectric transport of layered AM 2×2 compounds. *Inorganic Chemistry Frontiers*, 5:1744–1759, 2018.

[146] Hsin Wang, Wallace D Porter, Harald Böttner, Jan König, Lidong Chen, Shengqiang Bai, Terry M Tritt, Alex Mayolet, Jayantha Senawiratne, and Charlene Smith. Transport properties of bulk thermoelectrics: An international round-robin study, part II: Thermal diffusivity, specific heat, and thermal conductivity. *Journal of electronic materials*, 42(6):1073–1084, 2013.

[147] Alex Zevalkink, David M Smiadak, Jeff L Blackburn, Andrew J Ferguson, Michael L Chabinyc, Olivier Delaire, Jian Wang, Kirill Kovnir, Joshua Martin, and Laura T Schelhas. A practical field guide to thermoelectrics: Fundamentals, synthesis, and characterization. *Applied Physics Reviews*, 5(2):021303, 2018.

[148] Yanzhong Pei, Aaron LaLonde, Shiho Iwanaga, and G Jeffrey Snyder. High thermoelectric figure of merit in heavy hole dominated PbTe. *Energy & Environmental Science*, 4(6):2085–2089, 2011.

[149] Max Wood, Umut Aydemir, Saneyuki Ohno, and G Jeffrey Snyder. Observation of valence band crossing: the thermoelectric properties of $CaZn_2Sb_2$–$CaMg_2Sb_2$ solid solution. *Journal of Materials Chemistry A*, 6(20):9437–9444, 2018.

[150] Anubhav Jain, Shyue Ping Ong, Geoffroy Hautier, Wei Chen, William Davidson Richards, Stephen Dacek, Shreyas Cholia, Dan Gunter, David Skinner, and Gerbrand Ceder. Commentary: The materials project: A materials genome approach to accelerating materials innovation. *Apl Materials*, 1(1):011002, 2013.

[151] Otfried Madelung. *Semiconductors: data handbook*. Springer Science & Business Media, 2012.

[152] Michel W Barsoum. *MAX phases: Properties of Machinable Ternary Carbides and Nitrides*. John Wiley & Sons, 2013.

[153] Sankalp Kota, Eugenio Zapata-Solvas, Alexander Ly, Jun Lu, Omar Elkassabany, Amanda Huon, William E. Lee, Lars Hultman, Steve J. May, and Michel W. Barsoum. Synthesis and characterization of an alumina forming nanolaminated boride: MoAlB. *Scientific Reports*, 6(1):26475, 2016.

[154] Matthias T Agne and Michel W Barsoum. Enthalpy of formation and thermodynamic parameters of the MAX phase V_2AlC. *Journal of Alloys and Compounds*, 665:218–224, 2016.

[155] G Jeffrey Snyder, Mogens Christensen, Eiji Nishibori, Thierry Caillat, and Bo Brummerstedt Iversen. Disordered zinc in Zn_4Sb_3 with phonon-glass and electron-crystal thermoelectric properties. *Nature materials*, 3(7):458–463, 2004.

[156] T Caillat, J-P Fleurial, and A Borshchevsky. Preparation and thermoelectric properties of semiconducting Zn_4Sb_3. *Journal of Physics and Chemistry of Solids*, 58(7):1119–1125, 1997.

[157] Huili Liu, Xun Shi, Fangfang Xu, Linlin Zhang, Wenqing Zhang, Lidong Chen, Qiang Li, Ctirad Uher, Tristan Day, and G Jeffrey Snyder. Copper ion liquid-like thermoelectrics. *Nature materials*, 11(5):422, 2012.

[158] Matthias T Agne, Peter W Voorhees, and G Jeffrey Snyder. Phase transformation contributions to heat capacity and impact on thermal diffusivity, thermal conductivity, and thermoelectric performance. *Advanced Materials*, 31(35):1902980, 2019.

[159] Zhiwei Chen, Binghui Ge, Wen Li, Siqi Lin, Jiawen Shen, Yunjie Chang, Riley Hanus, G Jeffrey Snyder, and Yanzhong Pei. Vacancy-induced dislocations within grains for high-performance PbSe thermoelectrics. *Nature communications*, 8(1):1–8, 2017.

[160] Jiaqing He, Steven N Girard, Mercouri G Kanatzidis, and Vinayak P Dravid. Microstructure-lattice thermal conductivity correlation in nanostructured $PbTe_{0.7}S_{0.3}$ thermoelectric materials. *Advanced Functional Materials*, 20(5):764–772, 2010.

[161] John Androulakis, Kuei Fang Hsu, Robert Pcionek, Huijun Kong, Ctirad Uher, Jonathan J D'Angelo, Adam Downey, Tim Hogan, and Mercouri G Kanatzidis. Nanostructuring and high thermoelectric efficiency in p-type $Ag(Pb_{1-y}Sn_y)_mSbTe_{2+m}$. *Advanced Materials*, 18(9):1170–1173, 2006.

[162] Hongyi Chen, Zhongmou Yue, Dudi Ren, Huarong Zeng, Tianran Wei, Kunpeng Zhao, Ronggui Yang, Pengfei Qiu, Lidong Chen, and Xun Shi. Thermal conductivity during phase transitions. *Advanced Materials*, page 1806518, 2018.

[163] D Vasilevskiy, MK Keshavarz, J-M Simard, RA Masut, S Turenne, and GJ Snyder. Assessing the thermal conductivity of $Cu_{2-x}Se$ alloys undergoing a phase transition via the simultaneous measurement of thermoelectric parameters by a Harman-based setup. *Journal of Electronic Materials*, 47(6):3314–3319, 2018.

[164] D Vasilevskiy, RA Masut, and S Turenne. A phenomenological model of unconventional heat transport induced by phase transition in $Cu_{2-x}Se$. *Journal of Electronic Materials*, pages 1–6, 2018.

[165] Ilya Prigogine, Raymond Defay, and DH Everett. *Chemical thermodynamics*, volume 32. Longmans London, 1954.

[166] AA Minakov, SA Adamovsky, and C Schick. Advanced two-channel ac calorimeter for simultaneous measurements of complex heat capacity and complex thermal conductivity. *Thermochimica Acta*, 403(1):89–103, 2003.

[167] Yu Xiao, Haijun Wu, Dongyang Wang, Changlei Niu, Yanling Pei, Yang Zhang, Ioannis Spanopoulos, Ian Thomas Witting, Xin Li, and Stephen J Pennycook. Amphoteric indium enables carrier engineering to enhance the power factor and thermoelectric performance in n-type $Ag_nPb_{100}In_nTe_{100+2n}$ (LIST). *Advanced Energy Materials*, page 1900414, 2019.

[168] Lu Chen, Jun Liu, Chao Jiang, Kunpeng Zhao, Hongyi Chen, Xun Shi, Lidong Chen, Chenghua Sun, Shengbai Zhang, and Yong Wang. Nanoscale behavior and manipulation of the phase transition in single-crystal Cu_2Se. *Advanced Materials*, 31(4):1804919, 2019.

[169] Y Feutelais, M Majid, B Legendre, and SG Frics. Phase diagram investigation and proposition of a thermodynamic evaluation of the tin-selenium system. *Journal of phase equilibria*, 17(1):40–49, 1996.

[170] David R Brown, Richard Heijl, Kasper A Borup, Bo B Iversen, Anders Palmqvist, and GJ Snyder. Relating phase transition heat capacity to thermal conductivity and effusivity in Cu_2Se. *physica status solidi (RRL)–Rapid Research Letters*, 10(8):618–621, 2016.

[171] Cheng-Lung Chen, Heng Wang, Yang-Yuan Chen, Tristan Day, and G Jeffrey Snyder. Thermoelectric properties of p-type polycrystalline SnSe doped with Ag. *Journal of Materials Chemistry A*, 2(29):11171–11176, 2014.

[172] Yong Kyu Lee, Kyunghan Ahn, Joonil Cha, Chongjian Zhou, Hyo Seok Kim, Garam Choi, Sue In Chae, Jae-Hyuk Park, Sung-Pyo Cho, and Sang Hyun Park. Enhancing p-type thermoelectric performances of polycrystalline SnSe via tuning phase transition temperature. *Journal of the American Chemical Society*, 139(31):10887–10896, 2017.

[173] Yong Kyu Lee, Zhongzhen Luo, Sung Pyo Cho, Mercouri G Kanatzidis, and In Chung. Surface oxide removal for polycrystalline SnSe reveals near-single-crystal thermoelectric performance. *Joule*, 2019.

[174] Hua-Qian Leng, Min Zhou, Jie Zhao, Ye-Mao Han, and Lai-Feng Li. The thermoelectric performance of anisotropic SnSe doped with Na. *Rsc Advances*, 6(11):9112–9116, 2016.

[175] Kunling Peng, Xu Lu, Heng Zhan, Si Hui, Xiaodan Tang, Guiwen Wang, Jiyan Dai, Ctirad Uher, Guoyu Wang, and Xiaoyuan Zhou. Broad temperature plateau for high ZTs in heavily doped p-type SnSe single crystals. *Energy & Environmental Science*, 9(2):454–460, 2016.

[176] Li-Dong Zhao, Gangjian Tan, Shiqiang Hao, Jiaqing He, Yanling Pei, Hang Chi, Heng Wang, Shengkai Gong, Huibin Xu, and Vinayak P Dravid. Ultrahigh power factor and thermoelectric performance in hole-doped single-crystal SnSe. *Science*, 351(6269):141–144, 2016.

[177] Xiao-Lei Shi, Xinyong Tao, Jin Zou, and Zhi-Gang Chen. High-performance thermoelectric SnSe: Aqueous synthesis, innovations, and challenges. *Advanced Science*, 2020.

[178] JY Cho, M Siyar, SH Bae, JS Mun, MY Kim, SH Hong, and C Park. Effect of sintering pressure on electrical transport and thermoelectric properties of polycrystalline SnSe. *Bulletin of Materials Science*, 43(1):63, 2020.

[179] Joonil Cha, Chongjian Zhou, Yong Kyu Lee, Sung-Pyo Cho, and In Chung. High thermoelectric performance in n-type polycrystalline SnSe via dual incorporation of Cl and PbSe and dense nanostructures. *ACS applied materials & interfaces*, 11(24):21645–21654, 2019.

[180] J Gainza, F Serrano-Sánchez, M Gharsallah, F Carrascoso, J Bermúdez, OJ Dura, FJ Mompean, N Biskup, JJ Meléndez, JL Martínez, et al. Evidence of nanostructuring and reduced thermal conductivity in n-type Sb-alloyed SnSe thermoelectric polycrystals. *Journal of Applied Physics*, 126(4):045105, 2019.

[181] Sushmita Chandra and Kanishka Biswas. Realization of high thermoelectric figure of merit in solution synthesized 2D SnSe nanoplates via Ge alloying. *Journal of the American Chemical Society*, 141(15):6141–6145, 2019.

[182] Bowen Cai, Li-Dong Zhao, Jing-Feng Li, et al. High thermoelectric figure of merit ZT>1 in SnS polycrystals. *Journal of Materiomics*, 6(1):77–85, 2020.

[183] Ziyao Wang, Dongyang Wang, Yuting Qiu, Jiaqing He, and Li-Dong Zhao. Realizing high thermoelectric performance of polycrystalline SnS through optimizing carrier concentration and modifying band structure. *Journal of Alloys and Compounds*, 789:485–492, 2019.

[184] Hong Wu, Kunling Peng, Bin Zhang, Xiangnan Gong, Zhenzhen Feng, Xuemei Zhang, Ming Xi, Xiangmei Yan, Yongsheng Zhang, Guoyu Wang, et al. Realizing high thermoelectricity in polycrystalline SnS via manipulating fermi surface anisotropy and phonon dispersion. *Materials Today Physics*, page 100221, 2020.

[185] Dipanshu Bansal, Jiawang Hong, Chen W Li, Andrew F May, Wallace Porter, Michael Y Hu, Douglas L Abernathy, and Olivier Delaire. Phonon anharmonicity and negative thermal expansion in SnSe. *Physical Review B*, 94(5):054307, 2016.

[186] Pai-Chun Wei, Sriparna Bhattacharya, Yu-Fei Liu, Fengjiao Liu, Jian He, Yung-Hsiang Tung, Chun-Chuen Yang, Cheng-Rong Hsing, Duc-Long Nguyen, and Ching-Ming Wei. Thermoelectric figure-of-merit of fully dense single-crystalline SnSe. *ACS Omega*, 4(3):5442–5450, 2019.

[187] Qian Zhang, Eyob Kebede Chere, Jingying Sun, Feng Cao, Keshab Dahal, Shuo Chen, Gang Chen, and Zhifeng Ren. Studies on thermoelectric properties of n-type polycrystalline $SnSe_{1-x}S_x$ by iodine doping. *Advanced Energy Materials*, 5(12):1500360, 2015.

[188] Yoichi Takashi. Recent developments in experimental methods for heat-capacity measurements. *Pure and Applied Chemistry*, 47(4):323 – 331, 1976.

[189] L Balde, B Legendre, C Souleau, P Khodadad, and JR Didry. Capacité calorifique de l'alliage $Sn_{0.5}Se_{0.5}$ à l'état solide entre 375 et 1135 K. *Journal of the Less Common Metals*, 80(1):45–50, 1981.

[190] AS Pashinkin, AS Malkova, VA Fedorov, and MS Mikhailova. Heat capacity of tin monoselenide. *Inorganic Materials*, 42(6):593–595, 2006.

[191] Katsunori Yamaguchi, Kazuo Kameda, Yoichi Takeda, and Kimio Itagaki. Measurements of high temperature heat content of the II–VI and IV–VI (II: Zn, Cd IV: Sn, Pb VI: Se, Te) compounds. *Materials Transactions, JIM*, 35(2):118–124, 1994.

[192] Michal Kövér, Mária Behúlová, Marián Drienovský, and Petr Motyčka. Determination of the specific heat using laser flash apparatus. *Journal of Thermal Analysis and Calorimetry*, 122(1):151–156, 2015.

[193] Michael E Manley, Jason R Jeffries, Hohyun Lee, Nicholas P Butch, A Zabalegui, and DL Abernathy. Multiple high-temperature transitions driven by dynamical structures in NaI. *Physical Review B*, 89(22):224106, 2014.

[194] ND Milošević and KD Maglić. Thermophysical properties of solid phase zirconium at high temperatures. *International journal of thermophysics*, 27(4):1140–1159, 2006.

[195] Matthias T Agne, Riley Hanus, and G Jeffrey Snyder. Minimum thermal conductivity in the context of *diffuson*-mediated thermal transport. *Energy & Environmental Science*, 11(3):609–616, 2018.

[196] Tian-Ran Wei, Chao-Feng Wu, Wei Sun, Yu Pan, and Jing-Feng Li. Is Cu_3SbSe_3 a promising thermoelectric material? *RSC Advances*, 5(53):42848–42854, 2015.

[197] Albert Einstein. Die plancksche theorie der strahlung und die theorie der spezifischen wärme. *Annalen der Physik*, 327(1):180–190, 1907.

[198] Peter Debye. Zur theorie der spezifischen wärmen. *Annalen der Physik*, 344(14):789–839, 1912.

[199] John M Ziman. *Electrons and phonons: the theory of transport phenomena in solids*. Oxford university press, 2001.

[200] Brent Fultz. Vibrational thermodynamics of materials. *Progress in Materials Science*, 55(4):247–352, 2010.

[201] John Bardeen, Leon N Cooper, and John Robert Schrieffer. Theory of superconductivity. *Physical review*, 108(5):1175, 1957.

[202] Barbara Romanowicz. Using seismic waves to image earth's internal structure. *Nature*, 451(7176):266–268, 2008.

[203] Steven A Cummer, Johan Christensen, and Andrea Alù. Controlling sound with acoustic metamaterials. *Nature Reviews Materials*, 1(3):16001, 2016.

[204] Charles Kittel, Paul McEuen, and Paul McEuen. *Introduction to solid state physics*, volume 8. Wiley New York, 1996.

[205] Wolfgang G Zeier, Alex Zevalkink, Zachary M Gibbs, Geoffroy Hautier, Mercouri G Kanatzidis, and G Jeffrey Snyder. Thinking like a chemist: intuition in thermoelectric materials. *Angewandte Chemie International Edition*, 55(24):6826–6841, 2016.

[206] Samuel A. Miller, Prashun Gorai, Brenden R. Ortiz, Anuj Goyal, Duanfeng Gao, Scott A. Barnett, Thomas O. Mason, G. Jeffrey Snyder, Qin Lv, Vladan Stevanović, and Eric S. Toberer. Capturing anharmonicity in a lattice thermal conductivity model for high-throughput predictions. *Chemistry of Materials*, 29(6):2494–2501, 2017.

[207] Matthias T Agne, Riley Hanus, and G Jeffrey Snyder. Minimum thermal conductivity in the context of diffuson-mediated thermal transport. *Energy & Environmental Science*, 11(3):609–616, 2018.

[208] Atsushi Togo and Isao Tanaka. First principles phonon calculations in materials science. *Scripta Materialia*, 108:1–5, 2015.

[209] Alan JH McGaughey, Ankit Jain, Hyun-Young Kim, and Bo Fu. Phonon properties and thermal conductivity from first principles, lattice dynamics, and the Boltzmann transport equation. *Journal of Applied Physics*, 125(1):011101, 2019.

[210] Philip B Allen. Theory of thermal expansion: Quasi-harmonic approximation and corrections from quasi-particle renormalization. *Modern Physics Letters B*, 34(02):2050025, 2020.

[211] Duane C. Wallace. *Thermodynamics of Crystals*. Dover, New York, 1998.

[212] Michael E Manley, O Hellman, Nina Shulumba, Andrew F May, Paul J Stonaha, Jeffrey W Lynn, Vasile O Garlea, Ahmet Alatas, Raphael P Hermann, John D Budai, et al. Intrinsic anharmonic localization in thermoelectric PbSe. *Nature communications*, 10(1):1–9, 2019.

[213] Jose J Plata, Pinku Nath, Demet Usanmaz, Jesús Carrete, Cormac Toher, Maarten de Jong, Mark Asta, Marco Fornari, Marco Buongiorno Nardelli, and Stefano Curtarolo. An efficient and accurate framework for calculating lattice thermal conductivity of solids: AFLOW–AAPL automatic anharmonic phonon library. *npj Computational Materials*, 3(1):1–10, 2017.

[214] Rinkle Juneja, George Yumnam, Swanti Satsangi, and Abhishek K. Singh. Coupling the high-throughput property map to machine learning for predicting lattice thermal conductivity. *Chemistry of Materials*, 31(14):5145–5151, 2019.

[215] Arthur Ashkin. Applications of laser radiation pressure. *Science*, 210(4474):1081–1088, 1980.

[216] FE Borgnis. Acoustic radiation pressure of plane compressional waves. *Reviews of Modern Physics*, 25(3):653, 1953.

[217] Olivier Delaire, Jie Ma, Karol Marty, Andrew F May, Michael A McGuire, Mao-Hua Du, David J Singh, A Podlesnyak, G Ehlers, MD Lumsden, et al. Giant anharmonic phonon scattering in PbTe. *Nature materials*, 10(8):614–619, 2011.

[218] Sangyeop Lee, Keivan Esfarjani, Tengfei Luo, Jiawei Zhou, Zhiting Tian, and Gang Chen. Resonant bonding leads to low lattice thermal conductivity. *Nature communications*, 5(1):1–8, 2014.

[219] W Miller, CW Smith, DS Mackenzie, and KE Evans. Negative thermal expansion: a review. *Journal of materials science*, 44(20):5441–5451, 2009.

[220] David Wendt, Emil Bozin, Joerg Neuefeind, Katharine Page, Wei Ku, Limin Wang, Brent Fultz, Alexei V Tkachenko, and Igor A Zaliznyak. Entropic elasticity and negative thermal expansion in a simple cubic crystal. *Science advances*, 5(11):eaay2748, 2019.

[221] G. N. Greaves, A. L. Greer, R. S. Lakes, and T. Rouxel. Poisson's ratio and modern materials. *Nature Materials*, 10(11):823–837, 2011.

[222] KL Leont'ev. O svyazi uprugikh i teplovykh svoistv veshchestv [bonding of elastic and thermal properties of substances]. *Akusticheskii zhurnal-Acoustical Physics*, pages 554–561, 1981.

[223] Vladimir Nikolaevich Belomestnykh. The acoustical grüneisen constants of solids. *Technical Physics Letters*, 30(2):91–93, 2004.

[224] K. G. Bansigir. Evaluation of the gruneisen constant. *Journal of Applied Physics*, 39(8):4024–4026, 1968.

[225] Matthias T Agne, Kazuki Imasato, Shashwat Anand, Kathleen Lee, Sabah K Bux, Alex Zevalkink, Alexander JE Rettie, Duck Young Chung, Mercouri G Kanatzidis,

and G Jeffrey Snyder. Heat capacity of Mg_3Sb_2, Mg_3Bi_2, and their alloys at high temperature. *Materials Today Physics*, 6:83–88, 2018.

[226] Wei Xiong and Gregory B. Olson. Integrated computational materials design for high-performance alloys. *MRS Bulletin*, 40(12):1035–1044, 2015.

[227] O. Hellman, I. A. Abrikosov, and S. I. Simak. Lattice dynamics of anharmonic solids from first principles. *Physical Review B*, 84:180301, 2011.

[228] Olle Hellman, Peter Steneteg, I. A. Abrikosov, and S. I. Simak. Temperature dependent effective potential method for accurate free energy calculations of solids. *Physical Review B*, 87:104111, 2013.

[229] A. H. Romero, E. K. U. Gross, M. J. Verstraete, and Olle Hellman. Thermal conductivity in PbTe from first principles. *Physical Review B*, 91:214310, 2015.

[230] L. Brillouin. *Tensors in mechanics and elasticity*. Academic Press, 1964.

[231] Hamid Reza Seyf, Luke Yates, Thomas L Bougher, Samuel Graham, Baratunde A Cola, Theeradetch Detchprohm, Mi-Hee Ji, Jeomoh Kim, Russell Dupuis, and Wei Lv. Rethinking phonons: The issue of disorder. *npj Computational Materials*, 3(1):49, 2017.

[232] Hamid Reza Seyf and Asegun Henry. A method for distinguishing between propagons, diffusions, and locons. *Journal of Applied Physics*, 120(2):025101, 2016.

[233] Wei Chen, Jan-Hendrik Pöhls, Geoffroy Hautier, Danny Broberg, Saurabh Bajaj, Umut Aydemir, Zachary M Gibbs, Hong Zhu, Mark Asta, and G Jeffrey Snyder. Understanding thermoelectric properties from high-throughput calculations: trends, insights, and comparisons with experiment. *Journal of Materials Chemistry C*, 4(20):4414–4426, 2016.

[234] Catalin Chiritescu, David G Cahill, Ngoc Nguyen, David Johnson, Arun Bodapati, Pawel Keblinski, and Paul Zschack. Ultralow thermal conductivity in disordered, layered WSe_2 crystals. *Science*, 315(5810):351–353, 2007.

[235] G. A. Slack. *CRC handbook of thermoelectrics*. CRC press, 1995.

[236] G. A. Slack. Thermoelectric materials-new directions and approaches. In *Mater. Res. Soc. Symp. Proc.*, volume 478, page 47.

[237] Li-Dong Zhao, Shih-Han Lo, Yongsheng Zhang, Hui Sun, Gangjian Tan, Ctirad Uher, Christopher Wolverton, Vinayak P Dravid, and Mercouri G Kanatzidis. Ultralow thermal conductivity and high thermoelectric figure of merit in SnSe crystals. *Nature*, 508(7496):373, 2014.

[238] Albert Francis Birch and Harry Clark. The thermal conductivity of rocks and its dependence upon temperature and composition. *American Journal of Science*, 238(8):529–558, 1940.

[239] David G Cahill and RO Pohl. Heat flow and lattice vibrations in glasses. *Solid State Communications*, 70(10):927–930, 1989.

[240] AF Ioffe and AR Regel. Non-crystalline, amorphous and liquid electronic semiconductors. *Prog. Semicond*, 4:237–291, 1960.

[241] Wei Lv and Asegun Henry. Examining the validity of the phonon gas model in amorphous materials. *Scientific reports*, 6, 2016.

[242] Philip B Allen, Xiaoqun Du, Laszlo Mihaly, and Laszlo Forro. Thermal conductivity of insulating $Bi_2Sr_2YCu_2O_8$ and superconducting $Bi_2Sr_2CaCu_2O_8$: Failure of the phonon-gas picture. *Physical Review B*, 49(13):9073, 1994.

[243] Zhen Chen and Chris Dames. An anisotropic model for the minimum thermal conductivity. *Applied Physics Letters*, 107(19):193104, 2015.

[244] Orson L. Anderson. A simplified method for calculating the debye temperature from elastic constants. *Journal of Physics and Chemistry of Solids*, 24(7):909–917, 1963.

[245] O. L. Anderson. *Determination and Some Uses of Isotropic Elastic Constants of Polycrystalline Aggregates Using Single-Crystal Data*, volume 3, part B, pages 43–95. Academic Press, 1965.

[246] Heinz Bilz and Winfried Kress. *Phonon dispersion relations in insulators*, volume 10. Springer Science & Business Media, 2012.

[247] Stephen Dongmin Kang, Jan-Hendrik Pöhls, Umut Aydemir, Pengfei Qiu, Constantinos C Stoumpos, Riley Hanus, Mary Anne White, Xun Shi, Lidong Chen, and Mercouri G Kanatzidis. Enhanced stability and thermoelectric figure-of-merit in copper selenide by lithium doping. *Materials Today Physics*, 2017.

[248] Huili Liu, Jiong Yang, Xun Shi, Sergey A Danilkin, Dehong Yu, Chao Wang, Wenqing Zhang, and Lidong Chen. Reduction of thermal conductivity by low energy multi-Einstein optic modes. *Journal of Materiomics*, 2(2):187–195, 2016.

[249] Stanley P Marsh. *LASL shock Hugoniot data*, volume 5. Univ of California Press, 1980.

[250] R Freer. Debye temperatures of oxides with the NaCl structure. *Journal of Materials Science*, 16(11):3225–3227, 1981.

[251] Calcium oxide (CaO) sound velocities, elastic moduli: Datasheet from Landolt-Börnstein - Group III Condensed Matter · Volume 41B: "II-VI and I-VII Compounds; Semimagnetic Compounds" in springermaterials (https://doi.org/10.1007/10681719_226). Copyright 1999 Springer-Verlag Berlin Heidelberg.

[252] KS Aleksandrov, AI Krupny, VJ Fritzberg, and AN Rubulis. Phase transitions in ceramics on the basis of $SrTiO_3$. *physica status solidi (a)*, 15(2), 1973.

[253] KS Dubey and GS Verma. Lattice thermal conductivity of Si in the temperature range 2-1400 K. *Physical Review B*, 7(6):2879, 1973.

[254] Roland Pässler. Moments of phonon density of states spectra and characteristic phonon temperatures of wide band gap materials. *physica status solidi (b)*, 243(12):2719–2727, 2006.

[255] SP Dodd, M Cankurtaran, and B James. Ultrasonic determination of the elastic and nonlinear acoustic properties of transition-metal carbide ceramics: TiC and TaC. *Journal of materials science*, 38(6):1107–1115, 2003.

[256] Jin S Zhang, Jay D Bass, Takashi Taniguchi, Alexander F Goncharov, Yun-Yuan Chang, and Steven D Jacobsen. Elasticity of cubic boron nitride under ambient conditions. *Journal of Applied Physics*, 109(6):063521, 2011.

[257] Yi Xia, Vidvuds Ozolins, and Chris Wolverton. Microscopic mechanisms of glass-like lattice thermal transport in cubic $cu_{12}sb_4s_{13}$ tetrahedrites, 2020.

[258] Saikat Mukhopadhyay, David S. Parker, Brian C. Sales, Alexander A. Puretzky, Michael A. McGuire, and Lucas Lindsay. Two-channel model for ultralow thermal conductivity of crystalline Tl_3VSe_4. *Science*, 360(6396):1455–1458, 2018.

[259] Yi Xia, Koushik Pal, Jiangang He, Vidvuds Ozoliņš, and Chris Wolverton. Particlelike phonon propagation dominates ultralow lattice thermal conductivity in crystalline tl 3 vse 4. *Physical Review Letters*, 124(6):065901, 2020.

[260] James B Boyce and Bernardo A Huberman. Superionic conductors: Transitions, structures, dynamics. *Physics Reports*, 51(4):189–265, 1979.

[261] Philippe Knauth and Harry L Tuller. Solid-state ionics: roots, status, and future prospects. *Journal of the American Ceramic Society*, 85(7):1654–1680, 2002.

[262] Christopher Eames, Jarvist M Frost, Piers RF Barnes, Brian C O'regan, Aron Walsh, and M Saiful Islam. Ionic transport in hybrid lead iodide perovskite solar cells. *Nature communications*, 6(1):1–8, 2015.

[263] Aea Rohatgi, HC Chou, A Bhat, and R Sudharsanan. An improved understanding of efficiency limiting defects in polycrystalline CdTe/CdS solar cells. In *AIP Conference Proceedings*, volume 268, pages 243–249. American Institute of Physics, 1992.

[264] Rainer Waser and Masakazu Aono. Nanoionics-based resistive switching memories. In *Nanoscience And Technology: A Collection of Reviews from Nature Journals*, pages 158–165. World Scientific, 2010.

[265] Chong Xiao, Jie Xu, Kun Li, Jun Feng, Jinlong Yang, and Yi Xie. Superionic phase transition in silver chalcogenide nanocrystals realizing optimized thermoelectric performance. *Journal of the American Chemical Society*, 134(9):4287–4293, 2012.

[266] S Ishiwata, Y Shiomi, JS Lee, MS Bahramy, T Suzuki, M Uchida, R Arita, Y Taguchi, and Y Tokura. Extremely high electron mobility in a phonon-glass semimetal. *Nature materials*, 12(6):512–517, 2013.

[267] Pengfei Qiu, Tiansong Zhang, Yuting Qiu, Xun Shi, and Lidong Chen. Sulfide bornite thermoelectric material: a natural mineral with ultralow thermal conductivity. *Energy & Environmental Science*, 7(12):4000–4006, 2014.

[268] Kai S Weldert, Wolfgang G Zeier, Tristan W Day, Martin Panthofer, G Jeffrey Snyder, and Wolfgang Tremel. Thermoelectric transport in Cu_7PSe_6 with high copper ionic mobility. *Journal of the American Chemical Society*, 136(34):12035–12040, 2014.

[269] Xu Lu, Donald T Morelli, Yi Xia, Fei Zhou, Vidvuds Ozolins, Hang Chi, Xiaoyuan Zhou, and Ctirad Uher. High performance thermoelectricity in earth-abundant compounds based on natural mineral tetrahedrites. *Advanced Energy Materials*, 3(3):342–348, 2013.

[270] I Riess. Mixed ionic–electronic conductors—material properties and applications. *Solid State Ionics*, 157(1-4):1–17, 2003.

[271] X Shi, L Chen, and C Uher. Recent advances in high-performance bulk thermoelectric materials. *International Materials Reviews*, 61(6):379–415, 2016.

[272] Nan Chen, Yujuan Dai, Yi Xing, Lili Wang, Cui Guo, Renjie Chen, Shaojun Guo, and Feng Wu. Biomimetic ant-nest ionogel electrolyte boosts the performance of dendrite-free lithium batteries. *Energy & Environmental Science*, 10(7):1660–1667, 2017.

[273] David R Brown, Tristan Day, Thierry Caillat, and G Jeffrey Snyder. Chemical stability of (Ag,Cu)$_2$Se: a historical overview. *Journal of electronic materials*, 42(7):2014–2019, 2013.

[274] Gilles Dennler, Radoslaw Chmielowski, Stéphane Jacob, Frédéric Capet, Pascal Roussel, Sebastian Zastrow, Kornelius Nielsch, Ingo Opahle, and Georg KH Madsen. Are binary copper sulfides/selenides really new and promising thermoelectric materials? *Advanced Energy Materials*, 4(9):1301581, 2014.

[275] M Kh Balapanov, IG Gafurov, U Kh Mukhamed'Yanov, RA Yakshibaev, and R Kh Ishembetov. Ionic conductivity and chemical diffusion in superionic $Li_xCu_{2-x}S$ ($0 \leq x \leq 0.25$). *physica status solidi (b)*, 241(1):114–119, 2004.

[276] RA Yakshibaev, VN Konev, and M Kh Balapanov. Ionic conductivity and diffusion in superionic conductor α-$Cu_{2-\delta}Se$. *Fiz. Tverd. Tela*, 26:3641–3645, 1984.

[277] Alan R Allnatt and Alan B Lidiard. *Atomic transport in solids*. Cambridge University Press, 2003.

[278] Sang Il Kim, Kyu Hyoung Lee, Hyeon A Mun, Hyun Sik Kim, Sung Woo Hwang, Jong Wook Roh, Dae Jin Yang, Weon Ho Shin, Xiang Shu Li, Young Hee Lee, et al. Dense dislocation arrays embedded in grain boundaries for high-performance bulk thermoelectrics. *Science*, 348(6230):109–114, 2015.

[279] Kanishka Biswas, Jiaqing He, Ivan D Blum, Chun-I Wu, Timothy P Hogan, David N Seidman, Vinayak P Dravid, and Mercouri G Kanatzidis. High-performance bulk thermoelectrics with all-scale hierarchical architectures. *Nature*, 489(7416):414–418, 2012.

[280] Giri Joshi, Hohyun Lee, Yucheng Lan, Xiaowei Wang, Gaohua Zhu, Dezhi Wang, Ryan W Gould, Diana C Cuff, Ming Y Tang, Mildred S Dresselhaus, et al. Enhanced thermoelectric figure-of-merit in nanostructured p-type silicon germanium bulk alloys. *Nano letters*, 8(12):4670–4674, 2008.

[281] Werner Köhler and Simone Wiegand. *Thermal nonequilibrium phenomena in fluid mixtures*, volume 584. Springer, 2008.

[282] Isaaki Yokota. On the electrical conductivity of cuprous sulfide: a diffusion theory. *Journal of the Physical Society of Japan*, 8(5):595–602, 1953.

[283] Carsten Korte and Jürgen Janek. Nonisothermal transport properties of α-$Ag_{2+\delta}S$: Partial thermopowers of electrons and ions, the soret effect and heats of transport. *Journal of Physics and Chemistry of Solids*, 58(4):623–637, 1997.

[284] DJ Chakrabarti and DE Laughlin. The Cu-S (copper-sulfur) system. *Bulletin of Alloy Phase Diagrams*, 4(3):254, 1983.

[285] Pavel Lukashev, Walter RL Lambrecht, Takao Kotani, and Mark van Schilfgaarde. Electronic and crystal structure of $Cu_{2-x}S$: full-potential electronic structure calculations. *Physical Review B*, 76(19):195202, 2007.

[286] TB Massalski, H Okamoto, PR Subramanian, and L Kacprzak. Cu-Ni phase diagram. *Binary Alloy Phase Diagrams, 2nd ed.; ASM International: Materials Park, OH, USA*, 2:1442–1445, 1990.

[287] Sukwon Choi, Eric Heller, Donald Dorsey, Ramakrishna Vetury, and Samuel Graham. The impact of mechanical stress on the degradation of AlGaN/GaN high electron mobility transistors. *Journal of Applied Physics*, 114(16):164501, 2013.

[288] B. L. Hancock, M. Nazari, J. Anderson, E. Piner, F. Faili, S. Oh, D. Twitchen, S. Graham, and M. Holtz. Ultraviolet micro-Raman spectroscopy stress mapping of a 75-mm GaN-on-diamond wafer. *Applied Physics Letters*, 108(21):211901, 2016.

[289] Zhanqi Zhang, Zhongjun Yin, Tian Han, and Andy C.C. Tan. Fracture analysis of wind turbine main shaft. *Engineering Failure Analysis*, 34:129–139, 2013.

[290] Seungbae Park and Chin-Teh Sun. Fracture Criteria for Piezoelectric Ceramics. *Journal of the American Ceramic Society*, 78(6):1475–1480, 1995.

[291] Jayavardhana Gubbi, Rajkumar Buyya, Slaven Marusic, and Marimuthu Palaniswami. Internet of things (iot): A vision, architectural elements, and future directions. *Future generation computer systems*, 29(7):1645–1660, 2013.

[292] A. A. Griffith. The phenomena of rupture and flow in solids. *Philosophical Transactions of the Royal Society of London. Series A, Containing Papers of a Mathematical or Physical Character*, 221:163–198, 1921.

[293] George R Irwin. Analysis of stresses and strains near the end of a crack transversing a plate. *Trans. ASME, Ser. E, J. Appl. Mech.*, 24:361–364, 1957.

[294] E. Orowan. Fracture and strength of solids. *Reports on Progress in Physics*, 12(1):185–232, 1949.

[295] Egon Orowan. Energy criteria of fracture. *Welding Journal*, 34:157–160, 1955.

[296] James R. Rice. Dislocation nucleation from a crack tip: An analysis based on the Peierls concept. *Journal of the Mechanics and Physics of Solids*, 40(2):239–271, 1992.

[297] J C Boettger, John R Smith, Uwe Birkenheuer, Notker Rösch, S B Trickey, John R Sabin, and S Peter Apell. Extracting convergent surface formation energies from slab calculations. *Journal of Physics: Condensed Matter*, 10(4):893–894, 1998.

[298] Vincenzo Fiorentini and M Methfessel. Extracting convergent surface energies from slab calculations. *Journal of Physics: Condensed Matter*, 8(36):6525–6529, 1996.

[299] Pär A.T. Olsson, Matous Mrovec, and Martin Kroon. First principles characterisation of brittle transgranular fracture of titanium hydrides. *Acta Materialia*, 118:362–373, 2016.

[300] C. E. Dreyer, A. Janotti, and C. G. Van De Walle. Brittle fracture toughnesses of GaN and AlN from first-principles surface-energy calculations. *Applied Physics Letters*, 106(21), 2015.

[301] Jens Emmerlich, Niklas Thieme, Moritz To Baben, Denis Music, and Jochen M. Schneider. Stability, elastic properties and fracture toughness of $Al_{0.75}X_{0.75}B_{14}$ (X=Sc, Ti, V, Cr, Y, Zr, Nb, Mo) investigated using ab initio calculations. *Journal of Physics Condensed Matter*, 25(33), 2013.

[302] P. A.T. Olsson, K. Kese, M. Kroon, and A. M.Alvarez Holston. Ab initio-based fracture toughness estimates and transgranular traction-separation modelling of zirconium hydrides. *Modelling and Simulation in Materials Science and Engineering*, 23(4):45015, 2015.

[303] Zenong Ding, Shujia Zhou, and Yusheng Zhao. Hardness and fracture toughness of brittle materials: A density functional theory study. *Physical Review B*, 70(18):1–6, 2004.

[304] Yip Wah Chung. *Introduction to Materials Science and Engineering*. CRC Press, 2007.

[305] Guodong Li, Umut Aydemir, Sergey I. Morozov, Max Wood, Qi An, Pengcheng Zhai, Qingjie Zhang, William A. Goddard, and G. Jeffrey Snyder. Superstrengthening Bi_2Te_3 through Nanotwinning. *Physical Review Letters*, 119(8):1–6, 2017.

[306] Guodong Li, Qi An, Wenjuan Li, William A. Goddard, Pengcheng Zhai, Qingjie Zhang, and G. Jeffrey Snyder. Brittle failure mechanism in thermoelectric Skutterudite $CoSb_3$. *Chemistry of Materials*, 27(18):6329–6336, 2015.

[307] Guodong Li, Sergey I. Morozov, Qingjie Zhang, Qi An, Pengcheng Zhai, and G. Jeffrey Snyder. Enhanced Strength Through Nanotwinning in the Thermoelectric Semiconductor InSb. *Physical Review Letters*, 119(21):1–6, 2017.

[308] Guodong Li, Umut Aydemir, Max Wood, William A. Goddard, Pengcheng Zhai, Qingjie Zhang, and G. Jeffrey Snyder. Mechanical properties of thermoelectric lanthanum telluride from quantum mechanics. *Journal of Physics D: Applied Physics*, 50(27), 2017.

[309] Guodong Li, Umut Aydemir, Max Wood, William A. Goddard, Pengcheng Zhai, Qingjie Zhang, and G. Jeffrey Snyder. Ideal Strength and Deformation Mechanism in High-Efficiency Thermoelectric SnSe. *Chemistry of Materials*, 29(5):2382–2389, 2017.

[310] Guodong Li, Umut Aydemir, Max Wood, Qi An, William A. Goddard, Pengcheng Zhai, Qingjie Zhang, and G. Jeffrey Snyder. Deformation mechanisms in high-efficiency thermoelectric layered Zintl compounds. *Journal of Materials Chemistry A*, 5(19):9050–9059, 2017.

[311] Guodong Li, Qi An, Umut Aydemir, William A. Goddard, Max Wood, Pengcheng Zhai, Qingjie Zhang, and G. Jeffrey Snyder. Enhanced ideal strength of thermoelectric half-Heusler TiNiSn by sub-structure engineering. *Journal of Materials Chemistry A*, 4(38):14625–14636, 2016.

[312] David Roundy and Marvin L. Cohen. Ideal strength of diamond, Si, and Ge. *Physical Review B*, 64(21):2–4, 2001.

[313] Xiaoqing Li, Stephan Schönecker, Jijun Zhao, Börje Johansson, and Levente Vitos. Ideal strength of random alloys from first principles. *Physical Review B*, 87(21):1–12, 2013.

[314] C. R. Krenn, D. Roundy, J. W. Morris, and Marvin L. Cohen. Ideal strengths of bcc metals. *Materials Science and Engineering A*, 2001.

[315] T Ono, H Endo, and M Ueki. Hot-Pressing of TiC-Graphite Composite Materials. Technical report, 1993.

[316] An Ni Wang, Ge Ping Yu, and Jia Hong Huang. Fracture toughness measurement on TiN hard coatings using internal energy induced cracking. *Surface and Coatings Technology*, 239:20–27, 2014.

[317] Shigenobu Ogata, Ju Li, Yoji Shibutani, and Sidney Yip. Ab initio study of ideal shear strength. In *IUTAM Symposium on Mesoscopic Dynamics of Fracture Process and Materials Strength*, pages 401–410. Springer, 2004.

[318] Anubhav Jain, Shyue Ping Ong, Geoffroy Hautier, Wei Chen, William Davidson Richards, Stephen Dacek, Shreyas Cholia, Dan Gunter, David Skinner, Gerbrand Ceder, and Kristin a. Persson. The Materials Project: A materials genome approach to accelerating materials innovation. *APL Materials*, 1(1):011002, 2013.

[319] Jongpal Kim, Dong-il (Dan) Cho, and Richard S Muller. Why is (111) Silicon a Better Mechanical Material for MEMS? In Ernst Obermeier, editor, *Transducers '01 Eurosensors XV*, pages 662–665, Berlin, Heidelberg, 2001. Springer Berlin Heidelberg.

[320] Yue Lin Liu, Hong Bo Zhou, and Ying Zhang. Ideal mechanical properties of vanadium by a first-principles computational tensile test. *Journal of Nuclear Materials*, 416(3):345–349, 2011.

[321] P. Lazar and R. Podloucky. Cleavage fracture of a crystal: Density functional theory calculations based on a model which includes structural relaxations. *Physical Review B*, 78(10), 2008.

[322] D Roundy, C R Krenn, M L Cohen, and J W Morris Jr. The ideal strength of tungsten. *Philosophical Magazine A*, 81(7):1725–1747, 2001.

[323] M. Sribalaji, Biswajyoti Mukherjee, Srinivasa Rao Bakshi, P. Arunkumar, K. Suresh Babu, and Anup Kumar Keshri. In-situ formed graphene nanoribbon induced toughening and thermal shock resistance of spark plasma sintered carbon nanotube reinforced titanium carbide composite. *Composites Part B: Engineering*, 123:227–240, 2017.

[324] Shaocun Liu, Wentao Hu, Jianyong Xiang, Fusheng Wen, Bo Xu, Dongli Yu, Julong He, Yongjun Tian, and Zhongyuan Liu. Mechanical properties of nanocrystalline TiC–ZrC solid solutions fabricated by spark plasma sintering. *Ceramics International*, 40(7, Part B):10517–10522, 2014.

[325] Henry G Leduc, Bruce Bumble, Peter K Day, Byeong Ho Eom, Jiansong Gao, Sunil Golwala, Benjamin A Mazin, Sean McHugh, Andrew Merrill, David C Moore, et al. Titanium nitride films for ultrasensitive microresonator detectors. *Applied Physics Letters*, 97(10):102509, 2010.

[326] Amine Achour, Raul Lucio Porto, Mohamed-Akram Soussou, Mohammad Islam, Mohammed Boujtita, Kaltouma Ait Aissa, Laurent Le Brizoual, Abdou Djouadi, and Thierry Brousse. Titanium nitride films for micro-supercapacitors: effect of surface chemistry and film morphology on the capacitance. *Journal of Power Sources*, 300:525–532, 2015.

[327] Lili Gui, Shahin Bagheri, Nikolai Strohfeldt, Mario Hentschel, Christine M Zgrabik, Bernd Metzger, Heiko Linnenbank, Evelyn L Hu, and Harald Giessen. Nonlinear refractory plasmonics with titanium nitride nanoantennas. *Nano letters*, 16(9):5708–5713, 2016.

[328] Eleonora Santecchia, AMS Hamouda, Farayi Musharavati, Erfan Zalnezhad, Marcello Cabibbo, and Stefano Spigarelli. Wear resistance investigation of titanium nitride-based coatings. *Ceramics International*, 41(9):10349–10379, 2015.

[329] Yang Hu, Jia Hong Huang, and Jian Min Zuo. In situ characterization of fracture toughness and dynamics of nanocrystalline titanium nitride films. *Journal of Materials Research*, 31(3):370–379, 2016.

[330] Peter Chen and Wan-Yu Wu. The use of sputter deposited tin thin film as a surface conducting layer on the counter electrode of flexible plastic dye-sensitized solar cells. *Surface and Coatings Technology*, 231:140–143, 2013.

[331] Byung Gon Kim, Changshin Jo, Jaeho Shin, Yeongdong Mun, Jinwoo Lee, and Jang Wook Choi. Ordered mesoporous titanium nitride as a promising carbon-free cathode for aprotic lithium-oxygen batteries. *ACS nano*, 11(2):1736–1746, 2017.

[332] Bharat Avasarala and Pradeep Haldar. Durability and degradation mechanism of titanium nitride based electrocatalysts for pem (proton exchange membrane) fuel cell applications. *Energy*, 57:545–553, 2013.

[333] Julian Buchinger, L Löfler, J Ast, PH Mayrhofer, D Holec, M Bartosik, et al. Fracture properties of tin at elevated temperatures. *Available at SSRN 3458123*.

[334] Ian T. Witting, Thomas C. Chasapis, Francesco Ricci, Matthew Peters, Nicholas A. Heinz, Geoffroy Hautier, and G. Jeffrey Snyder. The Thermoelectric Properties of Bismuth Telluride. *Advanced Electronic Materials*, 5(6):1800904, 2019.

[335] Peter Gumbsch, Joachim Riedle, Alexander Hartmaier, and Hellmut F Fischmeister. Controlling Factors for the Brittle-to-Ductile Transition in Tungsten Single Crystals. *Science*, 282(November):1293–1295, 1998.

[336] A Kelly and N. H Macmillan. *Strong solids*. Monographs on the physics and chemistry of materials. Clarendon Press, Oxford, 3rd edition, 1986.

[337] Zhang Jiuxing, Liu Lu, Zhou Meiling, Hu Yancao, and Zuo Tieyong. Fracture toughness of sintered Mo-La_2O_3 alloy and the toughening mechanism. *International Journal of Refractory Metals and Hard Materials*, 17(6):405–409, 1999.

[338] M. Danylenko, Yu Podrezov, and S. Firstov. Effect of dislocation structure on fracture toughness of strained BCC-metals. *Theoretical and Applied Fracture Mechanics*, 32(1):9–14, 1999.

[339] A. A. Kaminskiĭ, M. Sh Akchurin, R. V. Gaĭnutdinov, K. Takaichi, A. Shirakava, H. Yagi, T. Yanagitani, and K. Ueda. Microhardness and fracture toughness of Y_2O_3- and $Y_3Al_5O_{12}$-based nanocrystalline laser ceramics. *Crystallography Reports*, 50(5):869–873, 2005.

[340] John F Geisz, Ryan M France, Kevin L Schulte, Myles A Steiner, Andrew G Norman, Harvey L Guthrey, Matthew R Young, Tao Song, and Thomas Moriarty. Six-junction

III–V solar cells with 47.1% conversion efficiency under 143 Suns concentration. *Nature Energy*, pages 1–10, 2020.

[341] MA Korzhuev. Mixed conduction and ultrafast chemical diffusion in superionic $Cu_{2-x}Se$. *Fizika Tverdogo Tela*, 31(10):25–32, 1989.

[342] Richard Dalven. A review of the semiconductor properties of PbTe, PbSe, PbS and PbO. *Infrared Physics*, 9(4):141–184, 1969.

[343] David R Poirier and G Geiger. *Transport phenomena in materials processing*. Springer, 2016.

[344] WK Chen, NL Peterson, and WT Reeves. Isotope effect for cation self-diffusion in CoO crystals. *Physical Review*, 186(3):887, 1969.

[345] Lada Yashina and Volkmar Leute. The phase diagrams of the quasibinary systems (Pb, Ge)Te and (Ge, Sn)Te. *Journal of alloys and compounds*, 313(1-2):85–92, 2000.

[346] Ken Ando and Yasumichi Oishi. Diffusion characteristics of actinide oxides. *Journal of nuclear science and technology*, 20(12):973–982, 1983.

[347] Mark Sneeringer, Stanley R Hart, and Nobumichi Shimizu. Strontium and samarium diffusion in diopside. *Geochimica et Cosmochimica Acta*, 48(8):1589–1608, 1984.

[348] A Atkinson and RI Taylor. The diffusion of Ni in the bulk and along dislocations in NiO single crystals. *Philosophical Magazine A*, 39(5):581–595, 1979.

[349] Derek Shaw. *Atomic diffusion in semiconductors*. Springer Science & Business Media, 2012.

[350] DJ Cherniak. Lead diffusion in titanite and preliminary results on the effects of radiation damage on Pb transport. *Chemical Geology*, 110(1-3):177–194, 1993.

[351] Chia-Chi Yu, Hsin-jay Wu, Ping-Yuan Deng, Matthias T. Agne, G. Jeffrey Snyder, and Jinn P. Chu. Thin-film metallic glass: an effective diffusion barrier for Se-doped $AgSbTe_2$ thermoelectric modules. *Scientific Reports*, 7:45177, 2017.

[352] Gary G Tibbetts. Diffusivity of carbon in iron and steels at high temperatures. *Journal of Applied Physics*, 51(9):4813–4813, 1980.

[353] Baohua Zhang and Xiaoping Wu. Calculation of self-diffusion coefficients in diamond. *Applied Physics Letters*, 100(5):051901, 2012.

[354] Jan W Jaeken and Stefaan Cottenier. Solving the christoffel equation: Phase and group velocities. *Computer Physics Communications*, 207:445–451, 2016.

[355] Walter Kohn, Axel D Becke, and Robert G Parr. Density functional theory of electronic structure. *The Journal of Physical Chemistry*, 100(31):12974–12980, 1996.

[356] Stefano Baroni, Stefano De Gironcoli, Andrea Dal Corso, and Paolo Giannozzi. Phonons and related crystal properties from density-functional perturbation theory. *Reviews of Modern Physics*, 73(2):515, 2001.

[357] Georg Kresse and Jürgen Furthmüller. Efficient iterative schemes for ab initio total-energy calculations using a plane-wave basis set. *Physical Review B*, 54(16):11169, 1996.

[358] John P Perdew, Adrienn Ruzsinszky, Gábor I Csonka, Oleg A Vydrov, Gustavo E Scuseria, Lucian A Constantin, Xiaolan Zhou, and Kieron Burke. Restoring the density-gradient expansion for exchange in solids and surfaces. *Physical review letters*, 100(13):136406, 2008.

[359] John P Perdew, Kieron Burke, and Matthias Ernzerhof. Generalized gradient approximation made simple. *Physical Review Letters*, 77(18):3865, 1996.

[360] G. Kresse and J. Furthmüller. Efficiency of ab-initio total energy calculations for metals and semiconductors using a plane-wave basis set. *Computational Materials Science*, 6(1):15–50, 1996.

[361] G. Kresse and J. Furthmüller. Efficient iterative schemes for ab initio total-energy calculations using a plane-wave basis set. *Physical Review B*, 54:11169–11186, 1996.

[362] G. Kresse and D. Joubert. From ultrasoft pseudopotentials to the projector augmented-wave method. *Physical Review B*, 59:1758–1775, 1999.

[363] Shiqiang Hao, Bernard Delley, and Catherine Stampfl. Structure and properties of $\mathrm{TiN}(111)/\mathrm{Si}_x\mathrm{N}_\mathrm{y}/\mathrm{TiN}(111)$ interfaces in superhard nanocomposites: First-principles investigations. *Physical Review B*, 74:035402, 2006.

[364] Shiqiang Hao, Bernard Delley, Stan Veprek, and Catherine Stampfl. Superhard nitride-based nanocomposites: Role of interfaces and effect of impurities. *Physical Review Letters*, 97:086102, 2006.

Appendix A

Extracting the Sommerfeld Coefficient

The dependence of the value of the Sommerfeld coefficient is dependent on the linear fit region that is chosen (Fig. A.1). Here, the fit region starts from the first data point (at 4.0 K) through data points at progressively higher temperatures (plotted here by their squared value). At first, the R-squared value is low due to the small number of data points that are sampled, but the value of γ_e remains consistent up until $T^2 \sim 200$ K at which point the estimate of γ_e decreases due to deviations from the T^3 law as the density of states rises faster than the Debye model predicts. The R-squared value remains high, however, such that careful attention should be paid in how the fit region is selected. The dashed line ($\gamma_e = 1.94$ mJ mol^{-1}K^{-2}) was determined by averaging the individual γ_e values determined by the different fit regions, excluding the first two points (having low R-squared values) and the last two points (which are clearly decreasing due to deviations from linearity).

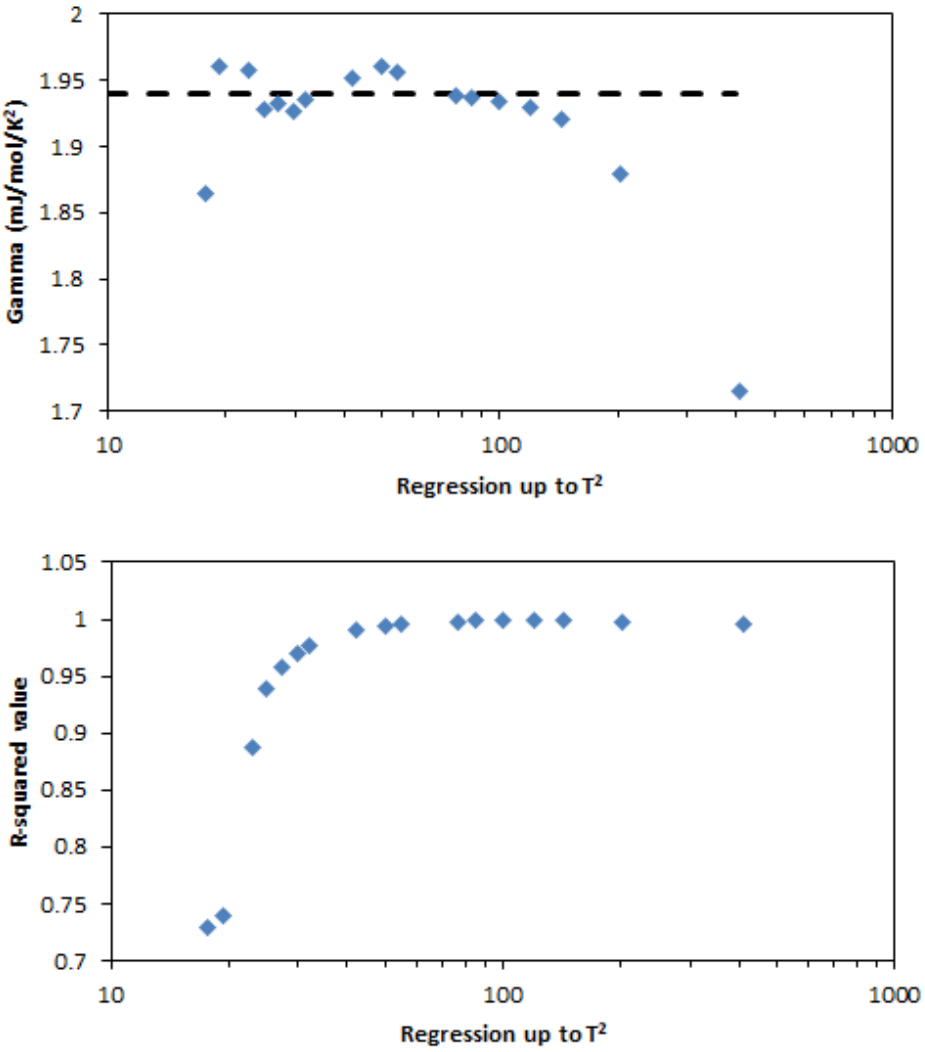

Figure A.1: **Regression analysis to determine the Sommerfeld coefficient.** The dependence of the value of the Sommerfeld coefficient in relation to how large the linear fit region is. Here, the fit region starts from the first data point (at 4.0 K) through data points at progressively higher temperatures (plotted here by their squared value). At first, the R-squared value is low due to the small number of data points that are sampled, but the value of γ_e remains consistent up until $T^2 \sim 200$ K at which point the estimate of γ_e decreases due to deviations from the T^3 law as the density of states rises faster than the Debye model predicts. The R-squared value remains high, however, such that careful attention should be paid in how the fit region is selected. The dashed line ($\gamma_e = 1.94$ mJ mol^{-1}K^{-2}) was determined by averaging the individual γ_e values determined by the different fit regions, excluding the first two points (having low R-squared values) and the last two points (which are clearly decreasing due to deviations from linearity).

Appendix B

Sommerfeld Coefficient of Mn_2AlB_2 and Fe_2AlB_2

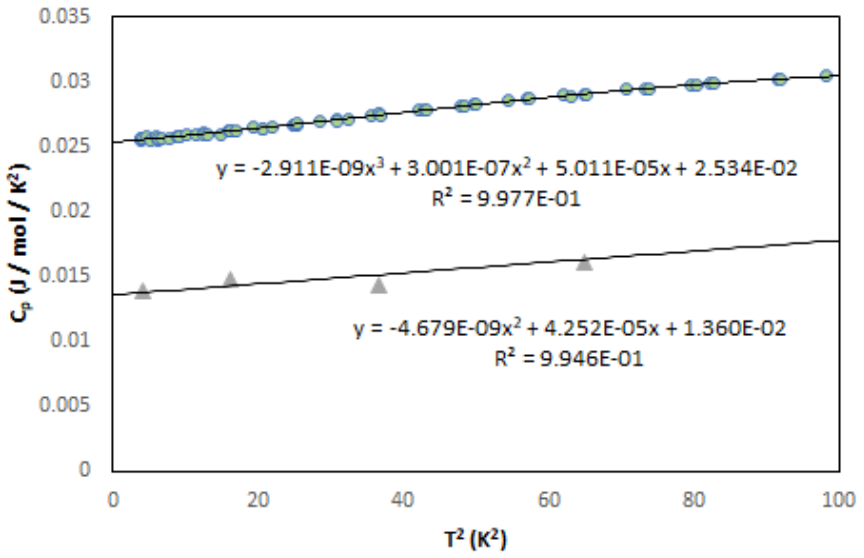

Figure B.1: **Estimation of the Sommerfeld coefficient in MAB phases.** The Sommerfeld coefficient γ_e of the MAB phases Mn_2AlB_2 (upper curve) and Fe_2AlB_2 (lower curve) can be estimated assuming an arbitrary polynomial to the low temperature C_P data. Since magnetic contributions at low temperature do not have the same temperature dependence as the electronic contriubiton (i.e. linear with T), then a plot of C_P/T vs T^2 is still expected to give a reasonable estimate of γ_e as the intercept of the y-axis.

Appendix C

Atomic Diffusion Times

Table C.1: Parameters used to calculate the relative atomic diffusion times presented in Fig. 4.3. Number density of atoms was approximated from crystallographic information available through the ICSD database. Diffusion time is defined as $t_a = D_a^{-1} n^{-2/3}$.

Reference	**Diffusion of:**	**In the system:**	**Atomic diffusion coefficient, D_a ($cm^2\ s^{-1}$)**	**Density of atomic sites, n (m^{-3})**	**Temperature (K)**	**Diffusion time, t_a (s)**
[341]	Cu	Cu_2Se	5.50E-04	6.02E+28	673	1.20E-12
[342]	Ag	PbSe	1.26E-05	3.52E+28	1000	7.40E-11
[343]	Ag	Cu_2S	1.22E-06	6.97E+28	400	4.90E-10
[342]	Na	PbSe	5.35E-08	3.52E+28	1000	1.70E-08
[344]	Co	CoO	9.70E-10	1.03E+29	1250	4.70E-07
[342]	Sb	PbTe	8.19E-10	2.96E+28	1000	1.30E-06
[342]	Na	PbTe	3.85E-11	2.96E+28	1000	2.70E-05
[342]	Sb	PbSe	2.70E-11	3.52E+28	1000	3.40E-05
[343]	Ag	Cu_2Te	9.54E-12	5.58E+28	400	7.20E-05
[345]	Ge	PbTe	1.30E-11	2.96E+28	893	8.00E-05
[346]	O	UO_2	1.00E-12	7.34E+28	1000	5.70E-04
[347]	Sr	$CaMgSi_2O_6$ (diopside)	3.89E-14	1.09E+29	1400	1.10E-02
[348]	Ni	NiO	2.80E-15	1.10E+29	1000	1.60E-01
[349]	Al	Si	3.40E-17	5.00E+28	1000	2.20E+01
[350]	Pb	$CaTiSiO_5$ (titanite)	7.74E-18	8.65E+28	1000	6.60E+01
[351]	Se	$Zr_{60}Cu_{24}Al_{11}Ni_5$	1.20E-20	3.25E+28	673	8.20E+04
[352]	C	Steel	6.57E-24	8.20E+28	300	8.10E+07
[353]	C	C (diamond)	1.11E-27	1.76E+29	1200	2.90E+11

Appendix D

Scaling of Thermal Diffusivity

Thermal diffusivities for $InSb_{1.04}$ [15], Cu_2Se [12], $AgCrSe_2$ [18], and SnSe [17] were either taken directly from reported values of thermal diffusivity, or calculated from the reported thermal conductivity using the heat capacity and density provided by the authors. The thermal diffusivity of Zn_4Sb_3 was measured using the laser flash method in this study. In order to show the universality of the decrease in thermal diffusivity through the phase transition, and subsequent increase above the maximum phase transition temperature, the thermal diffusivity was scaled by the magnitude of this step-wise increase (ΔD_{step}) as:

$$D_{\text{scaled}} = \frac{D - D_{\text{min}}}{\Delta D_{\text{step}}} \ , \tag{D.0.1}$$

where D_{min} is the lowest value of thermal diffusivity. Similarly, the temperature values were scaled so that the phase transition regions are comparable. This relies on either reported temperature ranges of the phase transition or knowledge of the phase diagram. Then,

$$T_{\text{scaled}} = \frac{T - T_{\text{PT,max}}}{T_{\text{PT,max}} - T_{\text{PT,min}}} \ , \tag{D.0.2}$$

where $T_{\text{PT,max}}$ is approximately the maximum temperature of the phase transition and $T_{\text{PT,min}}$ is considered to be the onset temperature of the phase transition.

Appendix E

Phonon Pressure Calculations

E.0.1 Phonon Pressure Model

The sum of stresses acting on an atom due to a phonon mode (having frequency ω, wave vector k and branch index s) is zero at equilibrium. Thus, analogous to Eq. 5.5, the vibrational (kinetic) stress of this phonon mode is compensated by its corresponding elastic stress. Explicitly, the total stress $\sigma_{\mathbf{k}s}$ in the $\hat{n}$-direction acting on atom α and pertaining to the ks vibrational mode is derived here to be

$$\sigma_{\mathbf{k}s} = \frac{\hbar\omega_{\mathbf{k}s}}{V_{\mathrm{a}}} f_{\mathrm{BE}}(\omega_{\mathbf{k}s}, T)|\hat{e}_{\mathbf{k}s} \cdot \hat{n}|^2 - \rho v_{\mathrm{p}}^2 |\hat{e}_{\mathbf{k}s} \cdot \hat{n}| \epsilon_{\mathbf{k}s} = 0. \tag{E.0.1}$$

Here, the vibrational stress exerted by an atom on a plane (whose normal direction is defined by the $\hat{n}$ unit vector) by a vibration (having the unit eigenvector $\hat{e}_{\mathbf{k}s}$ that determines the motion of atom α) is proportional to the kinetic energy of each phonon mode ($\hbar\omega_{\mathbf{k}s}/2$) as well as the number of phonons that are excited according to the Bose-Einstein distribution,

$$f_{\mathrm{BE}}\left(\omega_{\mathbf{k}s}, T\right) = \frac{1}{\exp\left(\frac{\hbar\omega_{\mathbf{k}s}}{k_{\mathrm{B}}T}\right) - 1}, \tag{E.0.2}$$

and V_{a} is the atomic volume. This relation can be found from momentum flux considerations analogous to an ideal gas (Fig. 5.2).

The elastic stress acting against (compensating) the vibrational stress is defined by the elastic modulus (ρv_{p}^2) governing the vibration, where ρ is the mass density of the solid and $v_{\mathrm{p}} = \omega_{\mathbf{k}s}/||\mathbf{k}||$ is the magnitude of the phase velocity of the phonon. Then, the strain response due to the ks vibrational mode, $\epsilon_{\mathbf{k}s}$, is also in the $\hat{n}$ direction, and achieves

equilibrium when

$$\epsilon_{\mathbf{k}s} = \frac{\hbar\omega_{\mathbf{k}s}}{V_\mathrm{a}} \frac{f_\mathrm{BE}\left(\omega_{\mathbf{k}s}, T\right)\ \left|\hat{e}_{\mathbf{k}s}\cdot\hat{n}\right|}{\rho v_\mathrm{p}^2}. \tag{E.0.3}$$

Thermal expansion in the $\hat{n}$-direction due to the ks vibrational mode is found using Eq. E.0.1 and the thermodynamic relation

$$\left(\frac{\partial\epsilon_{\mathbf{k}s}}{\partial T}\right)_{\sigma_{\mathbf{k}s}} = -\frac{(\partial\sigma_{\mathbf{k}s}/\partial T)_{\epsilon_{\mathbf{k}s}}}{(\partial\sigma_{\mathbf{k}s}/\partial\epsilon_{\mathbf{k}s})_\mathrm{T}} \tag{E.0.4}$$

and the total thermal expansion in the $\hat{n}$-direction is found by summing over all vibrational modes,

$$\left(\frac{\partial\epsilon_{ij}}{\partial T}\right)_{\sigma} = \sum_{\mathbf{k},s}\left(\frac{\partial\epsilon_{\mathbf{k}s}}{\partial T}\right)_{\sigma_{\mathbf{k}s}}. \tag{E.0.5}$$

It should be noted that σ and ϵ considered throughout Eqs. E.0.1 to E.0.5 are tensors ($\sigma_{ij}, \epsilon_{ij}$), the elements of which are defined by the unit vector $\hat{n}$. When $\hat{n}$ points only in the x-, y-, or z-direction, Eq. E.0.5 corresponds to the linear thermal expansion coefficient α_L in that direction. The volumetric thermal expansion coefficient is the summation of the three linear thermal expansions, or in the case of materials with cubic symmetry like PbTe, $\alpha = 3\alpha_\mathrm{L}$. The above derivation is written explicitly for materials with one atom per primitive unit cell, but is easily generalized to many-atom unit cells by considering the partial pressures contributed by each atom.

The Grüneisen parameter can be calculated from the volumetric thermal expansion coefficient according to Eq. 5.6 and can be used to renormalize the frequencies $\omega_{\mathbf{k}s}$ within the single Grüneisen parameter approximation (i.e. all vibrational modes have the same γ_i). This process can be done iteratively with temperature and, thus, phenomenologically accounts for the gentle increase in the thermal expansion coefficient at high temperatures (as shown in Fig. 5.3).

The "harmonic Grüneisen parameter" used in Fig. 5.4 did not consider any renormalization of vibrational frequencies and was calculated using Eqs. E.0.1, E.0.4 and E.0.5 in the $T \to \infty$ limit.

A simplified analytic description of thermal expansion can also be derived from the concept of vibrational pressure (Eq. 5.7). Here, an approximation for the frequency distribution of vibrational modes must be made, as well as the vibration direction. The Debye model of phonons as a dispersive continuum is often used to approximate the distribution of vibrational modes in solids and is applicable here. In the isotropic approximation the

elastic properties of the solid are independent of direction and the atoms vibrate equally in all directions (i.e. the average incidence cosine $|\hat{e}_{\mathbf{k}s} \cdot \hat{n}|$ is $1/2$). Making use of these approximations, the linear thermal expansion coefficient α_{L} can be written as

$$\alpha_L \approx \frac{3k_{\mathrm{B}}}{4\pi^2 \rho v_{\mathrm{s}}^5} \int_0^{\omega_{\mathrm{D}}} \omega^2 \left(\frac{\hbar\omega}{k_{\mathrm{B}}T}\right)^2 \frac{\exp\left(\frac{\hbar\omega}{k_{\mathrm{B}}T}\right)}{\left(\exp\left(\frac{\hbar\omega}{k_{\mathrm{B}}T}\right)-1\right)^2} d\omega, \tag{E.0.6}$$

where ρ is the density (kg m^{-3}), v_{s} is the average speed of sound (m s^{-1}), and $\omega_{\mathrm{D}} = \left(6\pi^2 n\right)^{1/3} v_{\mathrm{s}}$ is the Debye frequency, which uses v_{s} and the number density of atoms n (atoms m^{-3}) to approximate the maximum frequency of vibration in the solid.

E.0.2 Density Functional Theory Calculations

Harmonic eigenmodes (phonons) and corresponding mode Grüneisen parameters γ_i were found using density function theory methods. The compounds shown in Fig. 5.4a were previously reported [214]. Additional calculations were undertaken to calculate thermodynamically averaged Grüneisen parameter for compounds with varied $v_{\mathrm{t}}/v_{\mathrm{l}}$ ratios as shown in Fig. 5.4b. The isotropically averaged speed of sounds (v_{t} and v_{l}) were calculated using the christoffel code.[354] The elastic modulus tensor input for the code was calculated from the Density Functional Perturbation Theory (DFPT) [355, 356] capabilities implemented in the VASP code.[357] We used the PBEsol [358] formulation of the exchange–correlation energy functional derived under a generalized-gradient approximation (GGA).[359] Plane-wave basis sets were truncated at an energy cutoff of 500 eV, and a Γ- centered k-point mesh with a density of $\sim$8000 k-points per reciprocal atom (KPPRA) was used. The electronic degrees of freedom in the self-consistent loop were converged to 10^{-8} eV. All structures were relaxed with respect to cell vectors and their internal degrees of freedom until forces on all atoms were less than 0.1 eV nm^{-1}. "DFT Grüneisen parameters" were found by thermodynamically averaging the mode Grüneisen parameters γ_i in the high temperature limit such that they are weighted equally at all frequencies. The mode Grüneisen parameters were calculated using a finite difference method as implemented in Phonopy.[208] For this, the phonon calculations of the compounds were performed on structures where the cell parameters were strained by +/- 0.02%.

Appendix F

Critical Chemical Potential

In two phase regions (e.g. A+AB or B+AB) the atomic chemical potentials are fixed (constant) by Gibbs phase rule. However the chemical potential changes continuously across the single phase region (green dashed curve in Fig. F.1). As the sample made with some initial off-stoichiometry (grey point in the AB single phase region) is subjected to progressively higher electric fields, the composition (as well as local chemical potential) also changes across the sample. The critical point corresponds to when the material has reached its maximimum (or minimum) solubility and the chemical potential inside the sample is equivalent to the chemical potential of the adjacent phase, shown here as the case when the chemical potential of atom A in compound AB is equivalent to the chemical potential of pure A.

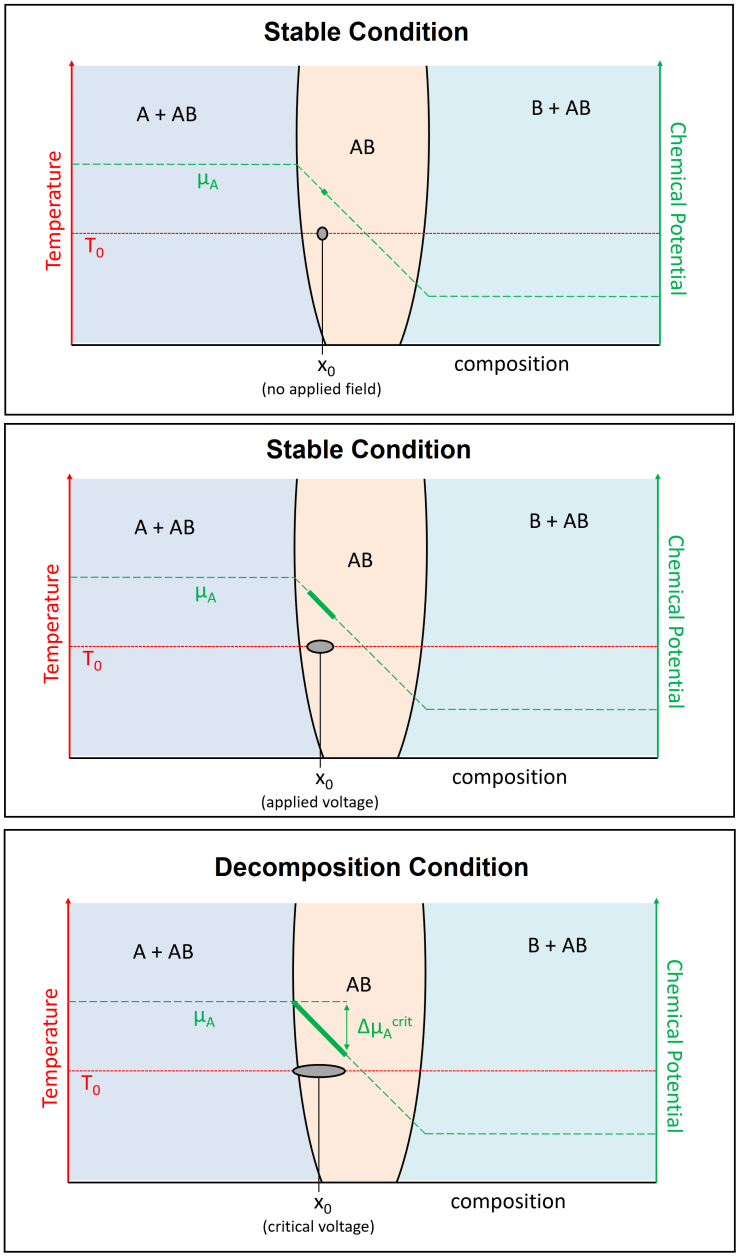

Figure F.1: **The connection of critical chemical potential to composition.** In two phase regions (e.g. A+AB) the atomic chemical potentials are fixed (constant), however the chemical potential changes continuously across the single phase region (green dashed curve). The sample made with some initial off-stoichiometry (grey point in the AB single phase region) is subjected to progressively higher electric fields, causing the composition (as well as local chemical potential) to change across the sample. The critical point corresponds to when the material has reached its maximimum (or minimum) solubility and the chemical potential inside the sample is equivalent to the chemical potential of the adjacent phase (shown here as the case when the chemical potential of atom A in compound AB is equivalent to the chemical potential of pure A).

Appendix G

Measurement of Critical Voltage in MIECs

G.0.1 Overview

The detailed preparation process of the Cu-based TE MIECs used in the present study can be found elsewhere [271]. The experimental work of this particular project was headed by Pengfei Qiu.

The experimental parameter, V_c, was ascertained by monitoring the electronic properties (e.g. electrical resistance R and Seebeck coefficient S) of the material after applying different electric currents or temperature gradients. Because the TE properties of the MIEC, especially the electrical resistance R and (electronic) Seebeck coefficient S, are very sensitive to the chemical composition, by monitoring the variation of the relative electrical resistance (R/R_0, where R_0 is the initial electrical resistance) or relative Seebeck coefficient (S/S_0, where S_0 is the initial Seebeck coefficient) under different current densities, the critical V_c can be determined. The critical current density, J_c, corresponds to the point when R/R_0 (or S/S_0) begins to decrease, is shown in Fig. 7.3a.

In the isothermal case, the chemical potential of Cu atoms is determined by the voltage on the sample generated by the electric current (see Eq. 7.5), which is determined experimentally as $V = \frac{J\ L}{\sigma}$, where J is the applied electric current density, and σ and L are the electrical conductivity and effective length of the MIEC, respectively. In the evaluation of V_c, the temperature is set 750 K. The length of the measured sample is 10 mm. The typical 4-point electrical conductivity at the experimental temperature is used for resistance measurement.

In the non-isothermal case and $T_{\text{anode}} > T_{\text{cathode}}$ (Eq. 7.6), the electrical potential and temperature gradient work together to drive atom migration to the cathode. In this case,

the Cu metal deposition will occur at the superionic-phase/normal-phase interface if T_{cathode} is lower than the superionic phase transition temperature of the MIEC; or, at the cathode if T_{cathode} is above the superionic phase transition temperature. When the relative fluxes are opposed (T_{cathode} is the hot side), Cu metal deposits at the cathode so long as T_{cathode} is above the superionic phase transition temperature. This was accounted for in the effective length, L, used to calculate V_{c}. In the evaluation of $V_{\text{c,same}}$, the cathode temperature T_{cathode} was fixed at 300 K, but $|\Delta T|$ was calculated relative to the superionic phase transition temperature of $Cu_{1.97}S$ ($\approx$ 350 K). The anode temperatures, T_{anode}, were 473 K, 523 K, 573 K, 623 K, and 673 K, respectively. To determine $V_{\text{c,opposite}}$, T_{anode} was fixed at 300 K and T_{cathode} was set to 473 K, 523, 573, 623 K, and 673 K, respectively. The length of the measured sample is 6 mm.

G.0.2 Segmented Leg Construction

The J_{c} and $V_{\text{leg,c}}$ values for a n = 3 segmented $Cu_{1.97}S$ leg (total length is L_{leg} = 10 mm) are experimentally obtained. The leg is made by bonding three $L_{\text{seg}} \approx$ 3.3 mm pieces together by using conductive carbon paste as the Cu-atom blocking layer. The data of this three-segment $Cu_{1.97}S$ leg are compared with those of the unsegmented $Cu_{1.97}S$ leg ($L_{\text{leg}} = L =$ 10 mm). Fig. 4d shows the relative Seebeck coefficient variation S/S_0 values for a three-segment $Cu_{1.97}S$ leg with L_{seg} = 2 mm, T_{anode} = 673 K, and T_{cathode} = 300 K. The leg was fabricated in the same manner previously described. The data for the unsegmented $Cu_{1.97}S$ leg (L_{leg} = L = 6 mm) is included for comparison.

G.0.3 Isothermal Condition

The schematic of the critical electric potential difference measurement apparatus in isothermal case is shown in Figure 7.4. Two nickel blocks (10×5 mm^3) are used as the electrodes to conduct the electric current flowing through the measured samples. These high thermal-conductive nickel blocks can also weaken the temperature variation on the sample caused by the Peltier effect when stressing current on the sample. Two Pt wires are pasted on the sample to record the potential variation induced by the DC current. The electrodes, sample, and Pt wires are packaged into the furnace chamber of the Netzsch DIL 402C equipment. All measurements are carried out in static Ar atmosphere.

In order to simplify the experiments, we use nickel blocks as Cu ion blocking electrodes. The external electric field is generated by drawing a constant current across the sample. The magnitude of the build-up electric potential difference along the sample can

be adjusted via tuning the value of current density. In order to sufficiently polarize the sample by diffusion of Cu atoms, the duration for each current pulse is 10 minutes. After switching off the current, we wait for 10 minutes to let the Cu atoms sufficiently diffuse back and reach again equilibrium. Then, the electrical resistance R is measured by using a 4-point method and a small DC current. The measured resistance R is then compared with the initial value R0 before the next current pulse. If R is unchanged, the current density J is enhanced to further raise the electric potential difference across the sample, followed by repeating the above measurement processes. In this way, the critical current density and critical electric potential difference corresponding to the onset of Cu-metal deposition can be identified as the case when R shows an abrupt decrease (see Figure 7.5a). Because we use a 4-point resistance measurement, the electric potential difference reported here does not include any potential drop across the electrodes where the Cu-metal deposition may or may not occur. Thus even if there is an over-potential drop across the electrodes to deposit Cu this potential drop is not included in the electric potential difference measured here. Take $Cu_{1.97}S$ as an example, Figure 7.5b shows the measurement results at 750 K.

G.0.4 Temperature Gradient Condition

The measured sample is located between a Cu block and a heater inside a nickel block (Fig. 7.7). Good thermal contact is maintained at the interfaces using one compression spring. The Cu block is used as the cold side and its temperature is controlled by the circulating water. A program based on LabView software is used to control the input power to the heater. Two Pt wires are pasted on the sample near the hot end to record the Seebeck coefficient variation (S/S_0) induced by the temperature gradient and the DC current. The measurement is conducted inside a chamber that is filled with argon. This apparatus allows for simultaneous measurement of electric potential and temperature and application of current of up to 2 A. The length of the measured sample is 6 mm.

When the temperature at the hot side is raised to the specified value, we wait for two hours to let the sample reach the stationary state. After the initial Seebeck coefficient S_0 (= $V_0/\Delta T$, where V_0 and ΔT are the electropotental and the temperature difference between the two Pt wires, respectively) is recorded, a constant current is stressed on the sample. In order to sufficiently polarize the sample by diffusion of Cu atoms, the duration for each time current stress is 10 minutes. After switching off the current, we wait for 10 minutes to let the Cu atoms sufficiently diffuse back and reach again equilibrium. Then, the Seebeck coefficient S is recorded again and compared with the

initial value S_0 before the next time current test. If S is unchanged, the current density J is increased to further raise the electric potential difference across the sample, followed by repeating the above measurement processes. In this way, the critical current density corresponding to the onset of Cu-metal deposition can be identified as the case when S shows an abrupt decrease (see Figure 7.7b). The critical electric potential difference can then be calculated. Similar with the above measurements in isothermal case, the over-potential drop across the electrodes is also not included here.

Appendix H

Estimation of Fracture Energy

In some cases the DFT calculations did not consider the extreme strains needed for the stress to return to zero. In these cases, a linear extrapolation was utilized (e.g. Fig. H.1). These extrapolations introduce a degree of uncertainty into the estimation of the fracture energy G, but are not expected to affect the conclusions drawn from the calculated fracture toughness.

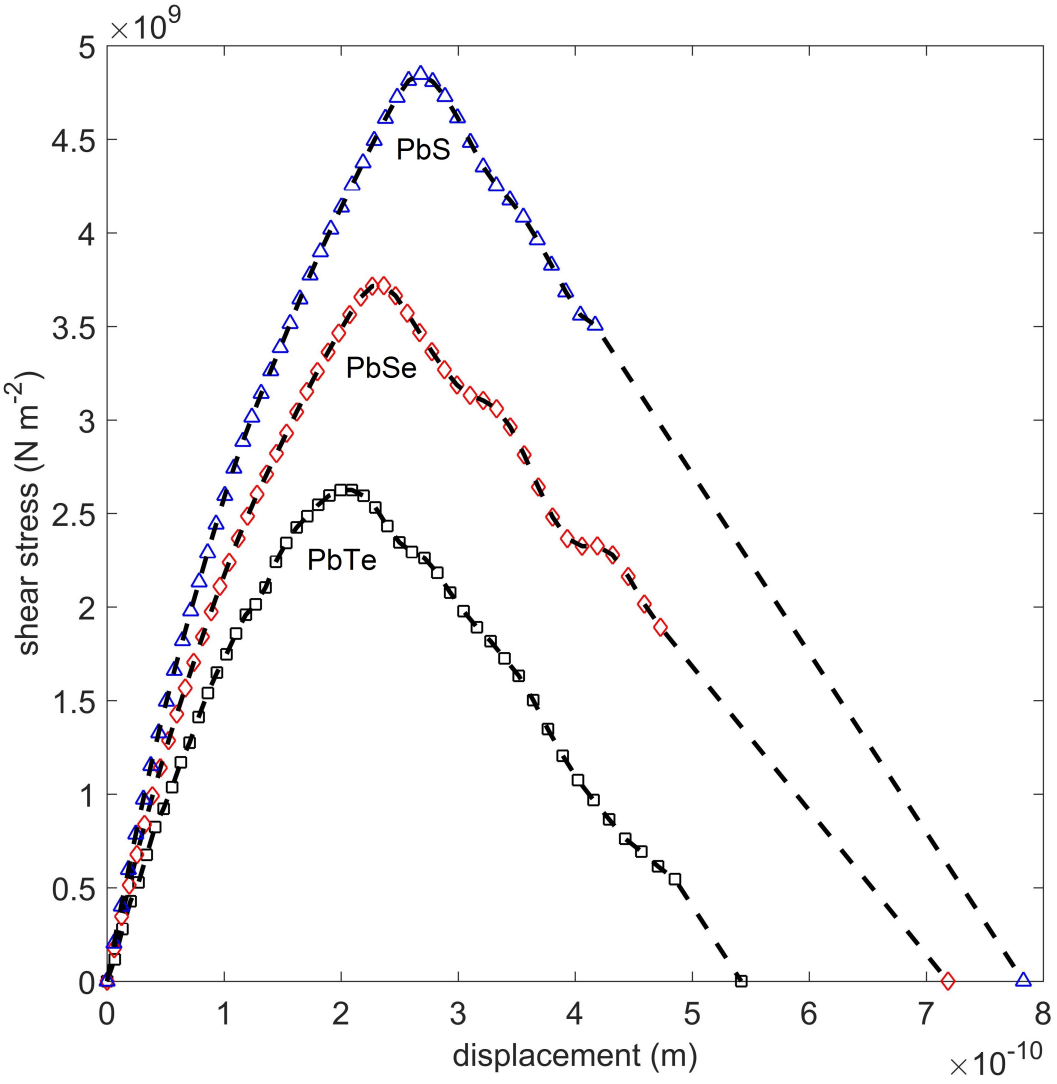

Figure H.1: **Uncertainty in fracture energy estimations.** The fracture energy was sometimes estimated from extrapolations of the ideal strength curves. In all cases, a linear regression was utilized. Although this introduces some subjectivity to the process, it is unlikely to affect the estimate of G by more than a few percent and certainly not more than a factor of 2. As fracture toughness goes as $\sqrt{G}$, small uncertainties in G have negligible consequences for the conclusions drawn from the resulting calculation of fracture toughness.

Appendix I

Ideal Strength Calculations

Ideal strength calculations were undertaken for TiC and TiN using the following procedure. All density functional theory (DFT) calculations were performed by the Vienna ab initio Simulation Package (VASP). The Perdew-Burke-Ernzerhof (PBE) exchange-correlation functional with the projector augmented wave (PAW) method was used to account for the core-valence interactions [360, 361, 362]. A plane wave cutoff energy of 500 eV gives good convergence for the total energies. The convergence criteria were set to 1×10^{-6} eV energy difference for solving the electronic wave function and 1×10^{-2} eV/Å force for geometry optimization. All calculations used the -centered Monkhorst-Pack scheme with a fine resolution of $2\pi \times 1/40$ Å^{-1} in the k-point reciprocal space sampling. The detailed quasi-static mechanical loading setup of TiC and TiN is similar with our previous calculations on thermoelectric materials [311, 53, 309].

We calculated the surface energy, γ_{s}, from the following formula [363, 364],

$$\gamma_{\mathrm{s}} = \frac{E_{\mathrm{slab}} - N \cdot E_{\mathrm{bulk}}}{2A}, \tag{I.0.1}$$

where E_{slab} is the total energy of surface slab obtained from density functional theory calculations, N is the number of atoms in the surface slab, E_{bulk} is the bulk energy per atom, and A is the surface area. In all the slab calculations, the slab direction is surrounded by a vacuum region of 10 Å to decouple the slabs. All the surface atoms are fully relaxed to optimize the surface structure. The calculated slab energies for $CoSb_3$, TiNiSn, PbTe, TiC, and TiN surfaces are listed in Table 8.2.